Sapienza Università di Roma

"Vito Volterra" Doctoral School in Astronomical, Chemical,
Earth, Mathematical and Physical Sciences

The mechanics of phyllosilicates-bearing faults: insights from field examples and rock deformation experiments

by

Carolina Giorgetti

A Dissertation in

Structural Geology and Rock Mechanics
submitted in fulfillment of the
Requirements for the Degree of

Doctor of Philosophy

December 2017

The dissertation of Carolina Giorgetti was reviewed and approved by

Cristiano Collettini
Associate Professor of Structural Geology
Sapienza University of Rome, Italy
Dissertation Advisor

Marie Violay
Assistant Professor of Rock Mechanics
EPFL Lausanne, Switzerland
External Reviewer

Tom M. Mitchell
Reader in Earthquake Geology and Rock Physics
UCL London, United Kingdom
External Reviewer

Abstract

Faults in the brittle crust are zones of weakness, whose reactivation depends on their friction and stress field acting on them. Over the last few decades, increasingly attention has been paid to characterize the frictional properties of phyllosilicates. These layer-structured minerals are indeed particularly weak, if compared with earliest laboratory experiments conducted on a vast gamut of crustal rocks showing friction almost independent of rock type and in the range of μ = 0.6-0.85. Phyllosilicates are not only inherently weak, but also unable to re-gain strength during inter-seismic period and to host earthquake nucleation. Moreover, previous studies have reported that even small amounts of phyllosilicates can drastically affect the overall frictional properties of fault rocks. These observations have strong implications for natural faults that involve different lithologies, including phyllosilicates-bearing rocks, and thus develop geometrical and lithological heterogeneities along dip and strike. The influence of these heterogeneities on fault mechanics is still poorly constrained.

Here, I integrate field observations and laboratory experiments on phyllosilicate-bearing faults to address different aspects regarding the role of phyllosilicates in fault mechanics. I examine questions such as: what is the minimum amount of phyllosilicates that drastically affects fault frictional properties? What is the mechanics of incipient faults within phyllosilicate-rich mechanical multilayers? What is the role of stress field orientation in the reactivation of phyllosilicate-bearing faults?

In Chapter 1, I experimentally investigate the frictional properties of talc-bearing faults in carbonates. Although talc has been found along carbonate-bearing faults, little is known about the amount of talc able to effectively weaken calcite fault gouges. In Chapter 2, I integrate field data and laboratory deformation experiments to study fault initiation and growth within clay-rich mechanical multilayers. Thus I give insight into the mechanics of clay-rich multilayers that is still poorly understood. In Chapter 3, I report on laboratory deformation experiments designed to evaluate the reactivation of pre-existing clay-bearing faults depending on their orientation within the stress field. The reactivation of pre-existing faults can be theoretically predicted assuming a zero-thickness fault. I attempt to validate frictional reactivation for a finite-thickness fault.

This dissertation provides insight into the mechanics of phyllosilicate-bearings faults. Firstly, I show that small amounts of talc fully weaken calcite-rich faults, developing an interconnected network of talc lamellae, and that even minor amounts of talc result in the evolution from velocity-neutral to velocity-strengthening behavior and in the reduction of

50% in frictional healing. Secondly, I demonstrate that the complex geometry of faults affecting mechanical multilayers results from the interplay between the mechanical properties of the involved lithologies and the presence of pre-existing discontinuities. Finally, I show that misoriented faults of finite thickness are weaker than theoretically predicted and that the assumption of a zero-thickness plane provides an upper bound for the stress required for the reactivation of a finite-thickness fault.

Riassunto

Faglie situate nella porzione fragile della crosta terrestre costituiscono zone di debolezza la cui riattivazione dipende dal loro attrito e dal campo dello sforzo che agisce su di esse. Negli ultimi decenni un'attenzione crescente è stata rivolta alla caratterizzazione delle proprietà frizionali dei fillosilicati. Tali minerali, caratterizzati da una struttura a strati, risultano infatti particolarmente deboli se paragonati con la maggior parte dei minerali costituenti la crosta terrestre. Inoltre i fillosilicati non sono capaci di riacquistare resistenza durante i periodi intersismici né di generare terremoti.

In aggiunta studi sperimentali riportano che la presenza di piccole quantità di fillosilicati può drasticamente influenzare le proprietà frizionali di rocce di faglia. Forti sono le implicazioni che questi studi sperimentali hanno sul comportamento di faglie naturali che contengono fillosilicati. Il coinvolgimento di diverse litologie in fenomeni di fagliamento comporta lo sviluppo di rocce di faglia fortemente eterogenee, il cui comportamento meccanico è ancora non del tutto compreso.

Nel presente lavoro integro osservazioni di terreno con esperimenti di laboratorio su faglie contenenti fillosilicati allo scopo di rispondere alle domande che seguono. Qual è il minimo quantitativo di fillosilicato che altera in modo significativo le proprietà frizionali della roccia di faglia? Qual è il comportamento meccanico di faglie incipienti in multistrati meccanici? Qual è il ruolo dell'orientazione del campo dello sforzo nella riattivazione di faglie contenenti fillosilicati?

Nel Capitolo 1 studio le proprietà frizionali di rocce di faglia contenenti talco che si sviluppano in carbonati. Nonostante il talco sia un fillosilicato particolarmente debole rinvenuto in faglie naturali in carbonati, non è noto come la sua presenza influenzi il comportamento meccanico della faglia. Nel Capitolo 2 descrivo l'inizio e lo sviluppo di faglie in multistrati meccanici ricchi in argilla, integrando dati di terreno con esperimenti di deformazione condotti in laboratorio. Il comportamento meccanico di tali multistrati è ad oggi scarsamente compreso. Nel Capitolo 3 riporto i risultati di esperimenti di deformazione sviluppati per studiare il ruolo dell'orientazione del campo dello sforzo sulla riattivazione di faglie contenenti argilla. Nonostante la riattivazione di faglie preesistenti sia spesso modellata analiticamente assumendo che la faglia sia un piano di spessore nullo, in natura la presenza di rocce di faglia fa sì che questa abbia uno spessore concreto. Per validare tali modelli analitici, ho simulato in laboratorio faglie di spessore finito

Questa tesi apporta ulteriori chiarimenti nella meccanica di faglie contenenti fillosilicati. Nel Capitolo 1, mostro che il 20% di talco abbassa significativamente l'attrito di faglie in carbonati, a seguito della concentrazione delle lamelle di talco lungo i piani di taglio. Inoltre l'aggiunta del 5% di talco comporta la transizione da un comportamento *velocity-neutral* ad uno *velocity-strengthening* ed una riduzione del 50% del *frictional healing*. Nel Capitolo 2 dimostro che le geometrie complesse sviluppate da faglie in multistrati meccanici risulta dall'interazione delle proprietà meccaniche del multistrato con discontinuità preesistenti. Infine nel Capitolo 3 mostro che faglie male orientate di spessore finito sono più deboli di quanto teoricamente previsto, pertanto assumere che la faglia sia un piano di spessore nullo può condurre ad una sovrastima dello sforzo necessario alla riattivazione.

Preface

The work presented in the main chapters of the dissertation is a result of collaboration with Sapienza University of Rome, INGV (Istituto Nazionale di Geofisica e Vulcanologia) and University of Perugia. The data collection, analysis, and writing are my own work. Chapters 1 and 2 have been peer-reviewed and can be found in the literature with the following citations:

> Giorgetti, C., B. M. Carpenter, and C. Collettini (2015), Frictional behavior of talc-calcite mixtures, Journal of Geophysical Research Solid Earth, 120, 6614-6633, doi:10.1002/2015JB011970.
>
> Giorgetti, C., C. Collettini, M. M. Scuderi, M. R. Barchi, and T. Tesei (2016), Fault geometry and mechanics of marly carbonate multilayers: An integrated field and laboratory study from the Northern Apennines, Italy, Journal of Structural Geology, 93, 1-16, doi:10.1016/j.jsg.2016.10.001.

Chapter 3 is currently being prepared for submission with the following author list:

> Giorgetti, C., T. Tesei, M. M. Scuderi and C. Collettini.

“Nell’analisi delle idee (ben inteso nel campo delle scienze naturali) non è sempre proficuo seguire l’ordine in cui esse si presentano storicamente. Molto spesso noi poniamo il piede nell’edificio sconosciuto d’un nuovo ordine di idee per una porticina secondaria, arriviamo dapprima in un’ala laterale e ci vuole molto tempo prima di essere orientati, prima di aver trovato l’entrata principale e di aver scelto una posizione che ci permetta di contemplare l’architettura dell’insieme dalla giusta prospettiva.”

“Der Geist der Naturwissenschaft”
Erwin Schrödinger, 1947

Table of Contents

Introduction **1**

Chapter 1. Frictional behavior of talc-calcite mixtures **6**

Abstract **6**

1.1. Introduction **7**

1.2. Experimental method **9**

1.2.1. Sample description 9

1.2.2. Experimental procedure 9

1.2.3. Microscopy Observations 14

1.3. Results **15**

1.3.1. Mechanical data 15

1.3.1.1. Frictional behavior at 5 MPa normal stress 15

1.3.1.2. Frictional behavior at 20 and 50 MPa normal stress 17

1.3.2. Microstructural observations 20

1.4. Discussion **23**

1.4.1 Integration of mechanical data and microstructures 23

1.4.2 Comparison to previous data 27

1.4.3 The Mechanisms of frictional healing 31

1.5. Conclusion **35**

Acknowledgments **35**

1.6. Supporting information **37**

Chapter 2. Fault geometry and mechanics of marly carbonate multilayers: an integrated field and laboratory study from the Northern Apennines, Italy **44**

Abstract **44**

2.1. Introduction **45**

2.2. Geological framework **47**

2.3. Investigation methods **49**

2.3.1. Theoretical framework for field observations 49

2.3.2 Laboratory investigations 50

2.3.2.1 Triaxial deformation experiments 52

2.3.2.2 Biaxial deformation experiments 54

2.4. Structural data 56

2.4.1. Fault architecture: from incipient to "mature" faults 57

2.4.2. Stress field orientation and angles of faulting 61

2.5. Laboratory rock deformation data 63

2.5.1. Strength and fracture permeability of cohesive limestones 63

2.5.2. Strength of incohesive marls 64

2.6. Discussion 66

2.6.1. Fault initiation 66

2.6.1.1 Fault initiation in limestone 66

2.6.1.2 Fault initiation in marls 67

2.6.1.3 Fault initiation in the mechanical multilayer 68

2.6.2. Fault growth and angles of fault reactivation 68

2.6.3. Fluid flow controlled by fracture and fault permeability 71

2.7. Conclusions 72

Acknowledgments 73

Chapter 3. Fault reactivation: insights from triaxial saw-cut experiments 74

Abstract 74

3.1. Introduction 75

3.2. Methods 77

3.2.1. Triaxial experiments 77

3.2.2. Friction experiments 79

3.2.3. Triaxial saw-cut experiments 81

3.3 Results 83

3.3.1. Sandstone strength and marl friction 83

3.3.2. Stress versus displacement evolution curves in triaxial saw-cut experiments: saw-cut reactivation versus new fracture development 84

3.3.3. Microstructural evolution during reactivation 87

3.4. Discussion 89

3.4.1. Integration of mechanical data and microstructures 89

3.4.2. Fault reactivation: theory versus experimental data 89

3.4.3. The dynamics of fault reactivation..... 92

3.4.4. Implications for natural faults 95

3.5 Conclusions 96

Acknowledgments..... 96

Conclusion 97

Bibliography 99

Appendix A. Technical corrections to mechanical data from triaxial and triaxial saw-cut experiments 117

A.1. Elastic stretch of the load frame on the vertical axis as a function of confining pressure 117

A.2. Strength of the polyolefin jacket used in triaxial saw-cut experiments..... 118

Appendix B. Python scripts developed to analyze field and laboratory data 120

B.1. Local stress field and angle between faults and maximum principal stress from field data 120

B.2. Data analysis of triaxial saw-cut experiments in which slip occurs within the saw-cut 123

Appendix C. Friction and scale-dependent deformation processes of large experimental carbonate faults 126

Appendix D. Structural Disorder of Graphite and Implications for Graphite Thermometry 139

Appendix E. Dynamics of fault slip near the stability transition combining laboratory and numerical experiments..... 159

Appendix F. List of experiments..... 160

Introduction

Faults in the brittle crust are the expression of localized strain mostly due to tectonic loading. Accumulated strain, clearly observable in exhumed faults, is the evidence of slip experienced by faults. How this slip is accommodated ranges from sudden and repeated to continuous and stable. Particularly, a sudden slip on a fault results from an abrupt release of stored elastic energy that generates an earthquake (*Reid*, 1910; *Brace and Byerlee*, 1966). This elastic energy is released only when the decrease of fault frictional strength with displacement exceeds the elastic unloading of the surrounding (*Rice*, 1983; *Scholz*, 2002). Additionally, the occurrence of repeated earthquakes on a fault requires that the fault re-strengthens after each sudden slip (e.g., *Dieterich*, 1972; *Marone*, 1998a; *Tadokoro and Ando*, 2002; *Li et al.*, 2003). Stable versus unstable slip behavior significantly depends on the frictional properties of the fault and the mechanical properties of its surrounding and, consequently, by the lithology involved in the deformation processes.

Laboratory experiments on rock mechanics effectively simulate slip on fault portions at small scale. Over the last few decades, increasingly attention has been paid to characterize the frictional properties of phyllosilicates and phyllosilicates-bearing fault rocks. These layer-structured minerals are particularly weak (e.g., *Brown et al.*, 2003; *Moore and Lockner*, 2008; *Ikari et al.*, 2009a; *Lockner et al.*, 2011), if compared with earliest laboratory experiments, conducted on a vast gamut of crustal rocks showing friction almost independent of rock type and in the range of $\mu = 0.6 - 0.85$ (*Byerlee*, 1978).

Early laboratory investigations revealed that rock sliding friction at sub-seismic velocity depends on sliding velocity (*Dieterich*, 1978) and that static friction depends on time of stationary contact (*Dieterich*, 1972). Both these aspects are well constrained in a laboratory-derived empirical relation called the rate- and state-dependent friction law (*Dieterich*, 1979; *Ruina*, 1983). In the framework of the rate- and state- friction, the velocity dependence of sliding friction describes fault seismic potential and the time dependence of static friction (i.e. the healing rate) describes inter-seismic fault re-strengthening. Velocity-weakening behavior (i.e. an increase in sliding velocity induces a decrease in sliding friction) implies earthquake rupture nucleation during pre-seismic fault acceleration. Contrarily, velocity strengthening behavior (i.e. an increase in sliding velocity induces an increase in sliding friction) favors rupture arrest and aseismic creep. In addition, earthquake nucleation requires the re-strengthening of the fault during the inter-seismic locking. In general, high friction (i.e., $\mu = 0.6 - 0.85$) in rocks is associated with velocity-weakening behavior and high healing rate (e.g.,

Ikari et al., 2011; *Carpenter et al.*, 2016b). Oppositely, phyllosilicates are characterized by velocity-strengthening and near-zero healing rate (e.g., *Ikari et al.*, 2009a; *Tesei et al.*, 2012; *Carpenter et al.*, 2016b). Experimental studies have not only shown the intrinsic weakness of phyllosilicates but also the significant influence that even small amounts of them in fault rocks exert on the overall fault frictional properties (e.g., *Collettini et al.*, 2009a; *Tembe et al.*, 2010; *Moore and Lockner*, 2011; *Tesei et al.*, 2014). Striking similarity between microstructures produced during experiments and microstructures of natural fault rocks suggests that shear experiments well reproduce processes occurring on natural faults.

However, faults are much more complex structure whose reactivation not only depends on rock frictional properties but also on the orientation and the magnitude of the stress field (e.g., *Sibson*, 1985). Generally, fault architecture consists of a fault core, up to few meter thick, surrounded by complex damage zones (e.g., *Caine et al.*, 1996; *Ben-Zion and Sammis*, 2003; *Faulkner et al.*, 2011). In turn, the fault core consists of lenses of fault rocks bounded by localized slip zones no more than few centimeters thick (e.g., *Sibson*, 1977; *Koopman et al.*, 1983; Sibson, 2003; *Tesei et al.*, 2013; *Collettini et al.*, 2014a). Differently, phyllosilicate-rich fault rocks develop fault cores up to 1 km thick containing high strain zones up to few meters thick where the deformation is homogeneously distributed (e.g., *Collettini and Holdsworth*, 2004; *Faulkner* et al., 2003; *Tesei et al.*, 2013). As a consequence, a layered crust characterized by the presence of different lithologies, including phyllosilicates-rich layer, involve the development of faults in which localized and distributed deformation coexist. Geometrical and lithological heterogeneities along fault dip and strike results in frictional properties variability within the fault core. In addition, fault evolution with accumulating strain results in frictional properties that change over time.

Similarly, on a smaller scale, stratigraphy exerts a major control on fault geometry (e.g., *Peacock and Sandersons*, 1992; *Ferrill* and *Morris*, 2008). The stratigraphic alternation of lithologies, with variable content of phyllosilicates, results in the alternation of layers with differing mechanical properties. Faults affecting these mechanical multilayers, especially at incipient stages, develop complex geometries resulting from the interplay between the strength and the thickness of the layers and the orientation of the stress field with respect to the layering. Again, the high heterogeneity of these faults in space and time strongly influences their frictional properties and their slip behavior.

The influence of lithological heterogeneities on fault mechanics in phyllosilicates-bearing rocks is still poorly constrained. The present thesis strives to integrate field observations on

natural faults and laboratory experiments to contribute towards filling this knowledge gap. The thesis comprises three chapters in which I present my own research developed during the PhD. In Appendices I report technical details of the methodologies that I used and scientific collaborations in which I took part. Rock deformation experiments reported in Chapters 1, 2 and 3 and Appendices C, D and E were conducted with the BRAVA apparatus (*Collettini et al.*, 2014b) installed at the High Pressure - High Temperature laboratory of INGV (Rome, Italy).

In Chapter 1 I investigate the role of increasing talc content on the frictional properties of calcite-rich experimental faults. Talc is one of the weakest amongst phyllosilicates and it has been found along many mature faults. In particular, the precipitation of talc and calcite, due to the stress-induced dissolution of dolomite in the presence of silica-rich fluids, has been documented along the Zuccale low-angle normal fault in Italy (*Collettini et al.*, 2009a). The development of talc in magnesium-rich carbonates may significantly weaken faults in the brittle crust. To constrain the minimum amount of talc that can effectively weaken calcite fault gouge, I conducted shear experiments on binary mixtures of talc and calcite powders, systematically increasing the talc content. I examine the frictional strength, the velocity dependence and the frictional healing of the mixtures, integrating the mechanical results with microstructures of the sheared gouges. I show that an interconnected network of talc, developed by adding a 20% wt. talc, significantly weakens the calcite gouge, causing a reduction of 70% wt. in strength, a markedly velocity-strengthening behavior and an almost zero frictional healing. Interestingly, 5 % wt. talc dispersed in the calcite gouge results in a reduction of 50% in frictional healing, pointing out the possible contribution of chemical mechanisms to frictional healing even at shallow conditions.

In Chapter 2 I explore brittle faulting in mechanical multilayers through the integration of structural geology in the field and rock mechanics in the laboratory. Despite the complex geometries of faults in multilayers have been largely documented in outcrop, their mechanics is still a matter of debate and considered as a frontier research topic due to their economical and societal impact. Clay-rich multilayers potentially constitute both seals for hydrocarbons or unconventional reservoirs and a comprehensive understanding of their mechanical behavior is required to assess the risks associated to human activity, as drilling, well exploitation or injection. Here, I present a new approach that combines the structural characterization of outcropping faults in multilayers with the laboratory deformation of involved lithologies. The studied outcrop consists of clay-rich multilayers characterized by the alternation of pelagic limestone and clay-rich marl, affected by mesoscale faults from millimetric to decametric

displacement. The local stress field was reconstructed from the orientation of faults, fractures and kinematic indicators. The angle between the faults and the maximum principle stress provides a mechanical characterization of the outcropping faults. After collecting representative samples of limestone and marl, the strength of the limestone was evaluated via triaxial experiments and the sliding friction of marl via shear experiments. I constrained the mechanical evolution of faults from incipient complex staircase geometry to well-developed core with SCC' fabric through the integration of field and laboratory data. The angles of fault initiation in limestone and marl layers are consistent with the respective failure and frictional strength or with the reactivation of pre-existing fractures in limestone and sedimentary foliation in clay-rich marl. The angles of reactivated faults characterized by a clay-rich fault core are consistent with the laboratory-derived sliding friction of marl. Furthermore, field observations demonstrate that brittle faulting enhances fluid circulation within low-permeability multilayers.

In Chapter 3 I investigate the role of stress field orientation on the reactivation of pre-existing faults. Theoretically the reactivation is controlled by the sliding friction of the fault plane, the orientation and the magnitude of the stress field and it is upper bounded by the strength of the surrounding rock. To investigate the reactivation of a pre-existing fault, I designed and developed the triaxial saw-cut configuration (e.g., *Byerlee*,1978) within BRAVA (*Collettini et al.*, 2014b). I placed a layer of granular clay-rich gouge within a saw-cut realized in a cylinder of intact sandstone to simulate a pre-existing fault in a rock volume. Systematically changing the orientation of the saw-cut to the maximum principal stress, I evaluated the role of stress field orientation in fault reactivation. In parallel with the collection of mechanical data, I performed microstructural analyses on sheared experimental faults at different amount of displacement to evaluate their micro-mechanical evolution during reactivation. I show that the reactivation occurs via stress drops and it is related to the transition from distributed to localized deformation along shear planes. Fault reactivation versus new fracture development observed during our triaxial saw-cut experiments is well predicted by the single plane of weakness theory (e.g., *Jaeger*,1960), that is a generalization of the Mohr-Coulomb failure criterion. However, I show that the assumption of a zero-thickness plane provides an upper bound on the stress required for the reactivation of finite thickness fault.

In Appendix A, I carefully describe technical corrections that I developed to analyze the data collected from triaxial and triaxial saw-cut experiments. Particularly, I evaluated the elastic stretch of the load frame on the vertical axis as a function of confining pressure to

correct the displacement applied to sample with or without saw-cut. Moreover, I evaluated the strength of the polyolefin jacket used in triaxial saw-cut experiments to correct the differential stress required to shear within the gouge layer. In Appendix B, I reported the code that I developed to analyze the data collected in the field described in Chapter 2 and the data recorded during triaxial saw-cut experiments in which shear occurs within the gouge layer described in Chapter 3.

Appendices C and D are papers, published and under review respectively, in which I am coauthor. In Appendices C, we reported on frictional behavior and deformation products of shear experiments on large faults, i.e. 20 cm x 20 cm bare surfaces. I contributed performing experiments and collecting microstructural observations. In Appendices D, we reported on shear experiments on highly-crystalline powdered graphite to investigate the disordering induced by brittle shear. I contributed planning and performing all the experiments. Appendix E is an abstract on an on-going project on the dynamics of fault slip near the stability transition. Finally, Appendix F is the complete list of the experiments that I performed during my PhD.

Chapter 1.
Frictional behavior of talc-calcite mixtures

Abstract

Faults involving phyllosilicates appear weak when compared to the laboratory-derived strength of most crustal rocks. Amongst phyllosilicates, talc, with very low friction, is one of the weakest minerals involved in various tectonic settings. As the presence of talc has been recently documented in carbonate faults, we performed laboratory friction experiments to better constrain how various amounts of talc could alter these fault's frictional properties. We used a biaxial apparatus to systematically shear different mixtures of talc and calcite as powdered gouge at room temperature, normal stresses up to 50 MPa and under different pore fluid saturated conditions, i.e. $CaCO_3$-equilibrated water and silicone oil. We performed slide-hold-slide tests, 1-3000 seconds, to measure the amount of frictional healing and velocity-stepping tests, 0.1-1000 μm/s, to evaluate frictional stability. We then analyzed microstructures developed during our experiments. Our results show that with the addition of 20% talc the calcite gouge undergoes a 70% reduction in steady-state frictional strength, a complete reduction of frictional healing and a transition from velocity-weakening to velocity-strengthening behavior. Microstructural analysis shows that with increasing talc content, deformation mechanisms evolve from distributed cataclastic flow of the granular calcite to localized sliding along talc-rich shear planes, resulting in a fully interconnected network of talc lamellae from 20% talc onwards. Our observations indicate that, in faults where talc and calcite are present, a low concentration of talc is enough to strongly modify the gouge's frictional properties and specifically to weaken the fault, reduce its ability to sustain future stress drops and stabilize slip.

1.1. Introduction

Geological studies show that mature fault zones can contain a variable amount of phyllosilicates (e.g., *Wintsch et al.*, 1995; *Vrolijk and van der Pluijm*, 1999; *Faulkner et al.*, 2003; *Collettini and Holdsworth*, 2004; *Jefferies et al.*, 2006; *Fagereng and Sibson*, 2010). Talc, in particular, has been documented in exhumed subduction thrust faults (e.g., *Peacock*, 1987; *Bebout and Barton*, 2002; *King et al.*, 2003), in oceanic transform faults (*d'Orazio et al.*, 2004) and in oceanic detachments (e.g., *Escartín et al.*, 2003; *Schroeder and John*, 2004). Drilling projects have reported the presence of talc within active traces of major faults at depth, such as the San Andreas fault in California (*Moore and Rymer*, 2007) and the Moresby fault in Papua New Guinea (e.g., *Floyd et al.*, 2001; *Kopf*, 2001; *Roller et al.*, 2001; *Taylor and Huchon*, 2002). Talc has also been found along exhumed low angle normal faults in Italy (*Collettini et al.*, 2009b; *Viti and Collettini*, 2009) and in the Cyclades (*Grasemann and Tschegg*, 2012). In subduction thrust faults, oceanic fracture zones and oceanic detachments, talc is typically derived from the metamorphic alteration of ultramafic rocks with silica-saturated hydrothermal fluids (e.g., *Manning*, 1995; *Boschi et al.*, 2006; *Moore and Rymer*, 2007). In sedimentary rocks, talc development is the result of dissolution of dolomite and interaction with silica-rich fluids (*Collettini et al*., 2009b).

The presence of talc and other phyllosilicates within mature fault zones strongly influences the strength and slip behavior of those faults. Early laboratory experiments conducted on a vast gamut of rocks showed that friction was almost independent of rock type and is in the range of μ = 0.6-0.85 (*Byerlee*, 1978). Hereafter, we referred to rocks and faults whose coefficient of friction is within this range as strong, as opposed to rocks and faults whose coefficient of friction is half of or less than the values in this range, that are thus considered weak. The laboratory prediction of strong faults, with high friction, seems to be consistent with measurements of crustal stress levels in deep boreholes (*Townend and Zoback*, 2000) and the analysis of earthquake focal mechanisms (*Collettini and Sibson*, 2001). However in the last decade there is growing evidence for the presence of mechanically weak faults: including strike-slip faults, like the San Andreas (*Hickman and Zoback*, 2004; *Moore and Rymer*, 2007; *Schleicher et al*., 2010; *Carpenter et al.*, 2011; *Lockner et al.*, 2011), low-angle normal faults (*Numelin et al.*, 2007; *Collettini et al.*, 2009b) and thrust faults (*Kopf and Brown*, 2003; *Ikari et al.*, 2009b; *Tesei et al.*, 2014). In all of these structures, fault weakness is inferred to result from the development of through-going phyllosilicate-rich zones within the fault zone at the expense of the strong mineral phases. The importance of the distribution of weak and strong minerals in fault rocks has been further confirmed by laboratory

experiments showing that intact, foliated samples are extremely weak when compared to powders derived from the same samples (e.g., *Collettini et al.*, 2009a). Phyllosilicates are characterized by a strong mechanical anisotropy, due their layered structure, that leads to the development of efficient planes of weakness, when the layers are favorably iso-oriented with respect to the shear.

Important questions for fault mechanics that remain are: what percent of a weak mineral phase is capable of changing fault strength and how does the presence of weak mineral phases influences fault slip behavior? Experimental studies conducted on intact cores of slightly serpetinized peridotites have shown that small amounts of weak phase, i.e. 9% of lizardite and chrysotile, strongly affect the mechanical properties of peridotite, resulting in a mechanical behavior characteristic of pure serpentinites (*Escartín et al.*, 2001). Similarly, metasomatic growth of talc observed during shear experiments strongly weakens gouges, developing through-going shear surfaces (*Hirauchi et al.*, 2013). Previous experiments on mixtures of strong granular materials and weak platy minerals have highlighted the role of phyllosilicates in weakening granular fault gouges (e.g., *Bos and Spiers*, 2000; *Tembe et al.*, 2010; *Moore and Lockner*, 2011). For example in quartz/montmorillonite mixtures, 50% of montmorillonite reduces friction, measured at about 9 mm of shear displacement, from 0.75 to 0.26 (*Tembe et al.*, 2010). In quartz/talc mixtures, 50% of talc is responsible of a friction drop, measured at about 3.5 mm of shear displacement, from 0.7 to 0.3 and promotes velocity-strengthening behavior, i.e. increasing friction with increasing velocity (*Moore and Lockner*, 2011). The presence of weak platy minerals also reduces the ability of gouges to regain strength during non-shearing periods (*Niemeijer and Spiers*, 2006; *Carpenter et al.*, 2011; *Tesei et al.*, 2012).

In this manuscript we investigate the effect of increasing talc content on the frictional and healing properties of calcite by running experiments on binary mixtures of calcite and talc and looking at the microstructures developed within the experimental faults. Our study provides insights on fault slip behavior, not only for talc rich-faults developed within carbonates, but also for those forming from serpentinites where calcite can be present along the fault zone due to hydrothermal cementation (e.g., *Bernoulli and Weissert*, 1985).

1.2. Experimental method

1.2.1. Sample description

Synthetic gouge mixtures used in this study were prepared from calcite and talc minerals in various proportions by weight. Calcite gouge was prepared from locally sourced Carrara Marble (>98% $CaCO_3$) that was crushed and sieved to < 125 μm grain size (Figures S1 and S2). Talc was prepared by separating talc grains from a talc-rich schist from Balmat, New York, and was provided by Ward's Science. It was also crushed and sieved to < 125 μm grain size (Figures S1 and S2).

We performed friction experiments in a servo-controlled biaxial testing apparatus installed in the High Pressure-High Temperature Laboratory at the INGV in Rome, Italy (*Collettini et al.*, 2014b). Stainless steel load cells continuously measure applied force with 0.03 kN resolution and LVDT sensors continuously measure load point displacements with 0.1 μm resolution. Two layers of simulated fault gouge were placed in-between three grooved sliding blocks, in a double-direct shear configuration (e.g., *Dieterich*, 1972; *Mair and Marone*, 1999; *Ikari et al.*, 2011). The two gouge layers, each with an initial ~5-mm uniform thickness measured before the samples were loaded, were constructed in order to have a 5×5-cm uniform area, that is maintained constant throughout the experiment (Figure 1.1a, inset).

1.2.2. Experimental procedure

Experiments were performed at room temperature and under $CaCO_3$-equilibrated water saturated conditions, except for two experiments, which were saturated with silicone oil. Initially, we ran a suite of 14 friction experiments under a constant normal stress of 5 MPa, in which talc content was systematically increased from 0% to 100%, in order to characterize the frictional behavior of the binary mixtures. Subsequently, we ran 4 more experiments under higher normal stress, i.e. 20 MPa and 50 MPa, focusing on 5 % and 20 % talc samples.

The experimental sample assembly was loaded into the testing apparatus and placed within a plastic membrane that was filled with the saturating fluid after the application of an initial normal load. Our experiments were performed under drained conditions. Initially we applied a normal stress of 1 MPa and allowed the sample to saturate for 30 minutes with DI water that had been brought into equilibrium with $CaCO_3$.

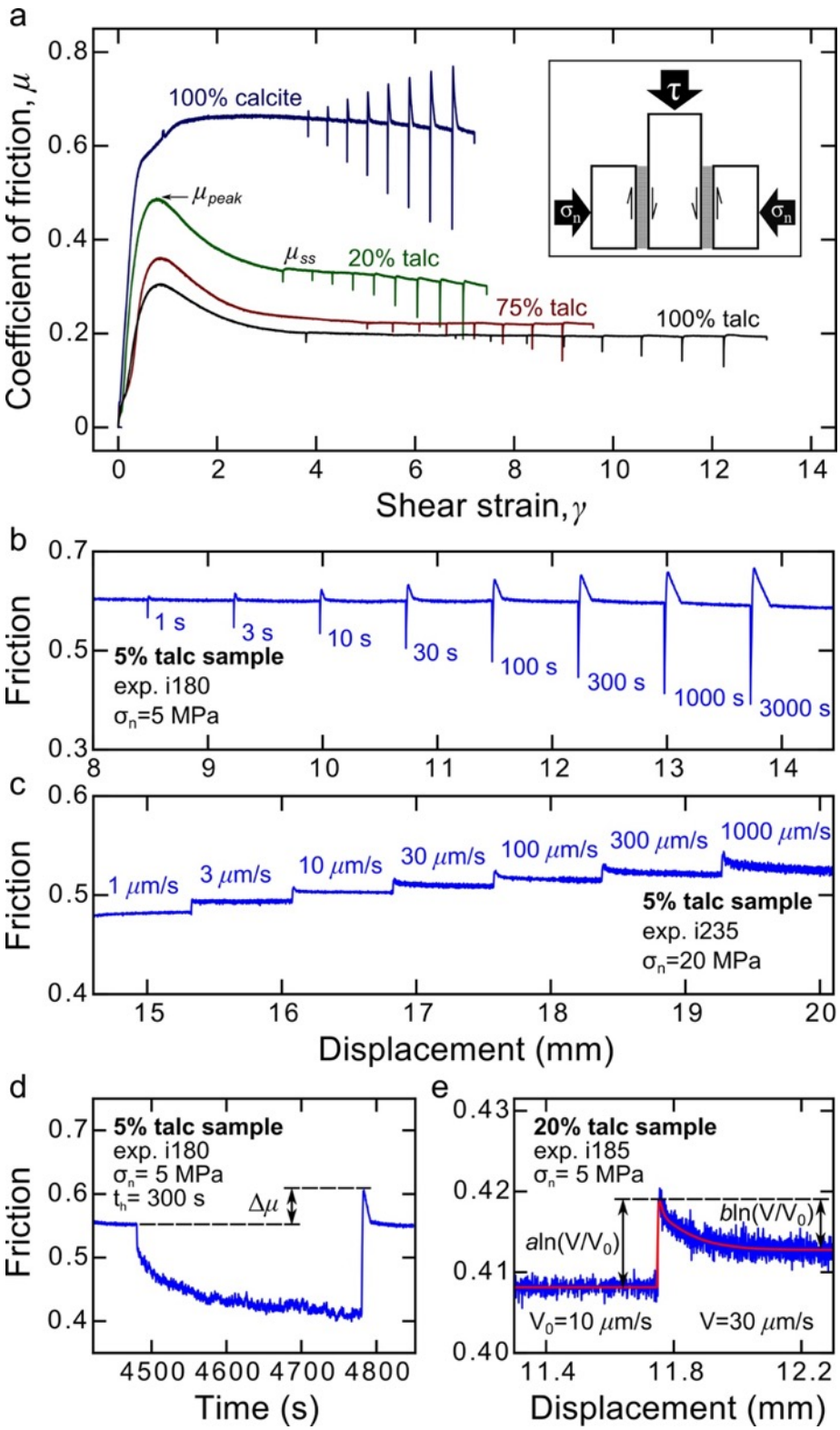

Figure 1.1. a) Friction plotted against shear strain for selected slide-hold-slide friction experiments, showing the evolution of friction for different talc contents. During the "run-in" phase, peak friction is attained (μ_{peak}) and then evolves to a steady-state value (μ_{ss}), as shown in the 20% talc sample. After the run-in, the slide-hold-slide and velocity step sequences are started. Inset shows the double-direct shear configuration in which three stainless steel forcing blocks sandwich two identical layers of experimental fault gouge. b) Details of friction versus displacement for a slide-hold-slide sequence. c) Details of friction versus displacement for a velocity step sequence. d) Details of friction versus time for a 300 s hold. $\Delta\mu$ is the difference between the peak value of friction upon re-shear and the pre-hold steady-state friction. e) Details of friction versus displacement for a 10-30 μm/s velocity step. a is proportional to the instantaneous change in friction and b is proportional to the subsequent drop to a new steady-state. The red line shows the modeled output of the velocity step.

Layer compaction was monitored checking, after 30 minutes, the achievement of a steady-state value of layer thickness, that depends on the amount of compaction each gouge undergoes. Subsequently, normal stress was increased to the target value, i.e. 5, 20 or 50 MPa, and the sample was subjected to a shear displacement "run-in" of ~7.5-8.5 mm by imposing a load velocity of 10 μm/s to the vertical piston. The "run-in" phase allows for the development of a steady-state friction (Figure 1.1a). Following steady shear, we imposed a series of computer-controlled changes in sliding velocity to test the time- and velocity-dependence of friction (Figure 1.1); we evaluated changes in friction in the context of rate- and state-dependent friction (e.g., *Marone*, 1998b).

The coefficient of friction (μ) was calculated from the Coulomb criterion by dividing half of the vertical load (two gouge layers) by the horizontal load, i.e. the shear stress by the normal stress, and assuming no cohesion. The average shear strain within the layer was calculated by dividing shear displacement increments by the measured layer thickness and summing. The displacement values of the vertical and horizontal load points were corrected for the elastic stretch of each load frame, taking into account that the machine stiffness is 1283 kN/mm on the horizontal axis and 928.5 kN/mm on the vertical axis.

Following steady shear, we performed slide-hold-slide and velocity-stepping sequences (Table 1.1). Slide-hold-slide tests consist of a sequence of slide-hold-slide cycles: 75 s of sliding at 10 μm/s was followed by a hold period, t_h, ranging from 1 to 3000 s, during which sliding is halted and subsequently resumed (Figure 1.1a, b and d), following the same procedure as in *Carpenter et al*. (2011) and *Tesei et al*. (2012). The amount of frictional healing ($\Delta\mu$) is measured as the difference between the peak friction measured upon re-shear after each hold and the pre-hold steady-state friction ($\Delta\mu$), as in previous work by *Marone* (1998), *Richardson and Marone* (1999), and *Frye and Marone* (2002). Steady-state friction is generally identical before and after the hold. However, few samples showed a slight strain related trend in plotting friction as a function of shear strain. We removed these trends in order to measure a more precise $\Delta\mu$. Frictional healing rates (β) was calculated as

$$\beta = \Delta\mu / \Delta \log_{10}(t_h) \quad (1.1)$$

During velocity-stepping tests, we imposed velocity step sequences of 0.1 to 1000 μm/s with a constant displacement of 750 μm at each step. In four experiments we also ran velocity step sequence of 1 to 1000 μm/s after the slide-hold-slide sequence. Each velocity step consists of a near instantaneous step changes in sliding velocity from V_0 to V (e.g., *Dieterich*, 1979; *Marone*, 1998b; *Scholz*, 1998). For each velocity step, the velocity was stepped up and

the new sliding velocity held constant until a new steady-state shear stress level was attained (Figure 1.1c and e). The instantaneous change in friction scales as the friction parameter $a\ln(V/V_0)$, where a is an empirical constant defined as the direct effect (e.g., *Ruina*, 1983). The subsequent drop to a new steady-state value of friction scales as the friction parameter $b\ln(V/V_0)$, where b is an empirical constant defined as the evolution effect (e.g., *Ruina*, 1983). The velocity dependence of steady-state friction (a-b) is defined as

$$a - b = \frac{\Delta\mu_{ss}}{\ln(V/V_0)} \tag{1.2}$$

where $\Delta\mu_{ss}$ is the change in steady-state friction. Positive values of (a-b), defining velocity-strengthening behavior, indicate that stable sliding should be expected. Negative values of (a-b), i.e. velocity-weakening behavior, are a requirement for the nucleation of slip instability (e.g., *Dieterich and Kilgore*, 1994; *Marone*, 1998b; *Scholz*, 1998).

The collected data were subsequently modeled with the Dieterich, time-dependent, version of the rate- and state- friction constitutive law and evolution equation (*Dieterich*, 1979)

$$\mu = \mu_0 + a\,ln\left(\frac{V}{V_0}\right) + b\,\ln\left(\frac{V_0\theta}{D_c}\right),\ \frac{d\theta}{dt} = 1 - \frac{\theta V}{D_c} \tag{1.3}$$

where V_0 is a reference velocity and μ_0 is the steady-state friction at $V = V_0$. D_c is the critical slip distance and θ is the state variable (units of time) that expresses the effective contact time derived from the ratio of a critical slip distance D_c to slip velocity V. The state variable θ is thought to represent the average lifetime of asperity contacts that control friction and the critical slip distance D_c represents the displacement over which the population of asperity contacts are renewed (*Marone and Kilgore*, 1993; *Scholz*, 1998). To model our data, the constitutive law and the evolution equation are coupled with an equation describing the compliant coupling between the frictional surface and its surroundings, i.e. the interaction of the sample with its elastic load frame

$$\frac{d\mu}{dt} = k\left(V_{lp}/V\right) \tag{1.4}$$

where V_{lp} is the velocity measured at the displacement control point and k is stiffness of the testing apparatus and the sample blocks, normalized by the normal stress, in units of coefficient of friction per displacement. We simultaneously solved the Dieterich constitutive law and evolution equation, with elastic coupling equation as a constraint, by using a fifth-order Runge-Kutta numerical integration. The constitutive parameters a, b and D_c were obtained as best-fit parameter values using an iterative, least-squares method to solve the

nonlinear inverse problem (e.g., *Reinen and Weeks*, 1993; *Blanpied et al.*, 1998; *Saffer and Marone*, 2003).

Table 1.1. List of experiments. All experiments were conducted at a background sliding velocity of 10 μm/s.

Experiment	Calcite/talc (wt.%)	σ_n (MPa)	Pore fluid	Sequence of hold times (s)	Sequence of velocity steps (μm/s)
i040	100/0	5	$CaCO_3$-saturated water	1, 3, 10, 30, 100, 300, 1000, 3000	-
i180	95/5	5	$CaCO_3$-saturated water	1, 3, 10, 30, 100, 300, 1000, 3000	-
i179	90/10	5	$CaCO_3$-saturated water	1, 3, 10, 30, 100, 300, 1000, 3000	-
i176	80/20	5	$CaCO_3$-saturated water	1, 3, 10, 30, 100, 300, 1000, 3000	-
i175	70/30	5	$CaCO_3$-saturated water	1, 3, 10, 30, 100, 300, 1000, 3000	-
i174	60/40	5	$CaCO_3$-saturated water	1, 3, 10, 30, 100, 300, 1000, 3000	-
i050	50/50	5	$CaCO_3$-saturated water	1, 3, 10, 30, 100, 300, 1000, 3000	-
i181	25/75	5	$CaCO_3$-saturated water	1, 3, 10, 30, 100, 300, 1000, 3000	-
i173	0/100	5	$CaCO_3$-saturated water	1, 3, 10, 30, 100, 300, 1000, 3000	-
i058	100/0	5	$CaCO_3$-saturated water	-	0.1, 0.3, 1, 3, 10, 30, 100, 300, 1000
i184	95/5	5	$CaCO_3$-saturated water	-	0.1, 0.3, 1, 3, 10, 30, 100, 300, 1000
i185	80/20	5	$CaCO_3$-saturated water	-	0.1, 0.3, 1, 3, 10, 30, 100, 300, 1000
i186	50/50	5	$CaCO_3$-saturated water	-	0.1, 0.3, 1, 3, 10, 30, 100, 300, 1000
i183	100/0	5	$CaCO_3$-saturated water	-	0.1, 0.3, 1, 3, 10, 30, 100, 300, 1000
i234	95/5	50	$CaCO_3$-saturated water	1, 3, 10, 30, 100, 300, 1000, 3000	1, 3, 10, 30, 100, 300, 1000
i235	95/5	20	$CaCO_3$-saturated water	1, 3, 10, 30, 100, 300, 1000, 3000	1, 3, 10, 30, 100, 300, 1000
i236	80/20	50	$CaCO_3$-saturated water	1, 3, 10, 30, 100, 300, 1000, 3000	1, 3, 10, 30, 100, 300, 1000
i237	80/20	20	$CaCO_3$-saturated water	1, 3, 10, 30, 100, 300, 1000, 3000	1, 3, 10, 30, 100, 300, 1000
i161	100/0	5	Silicone Oil	1, 3, 10, 30, 100, 300, 1000, 3000	-
i262	95/5	5	Silicone Oil	1, 3, 10, 30, 100, 300, 1000, 3000, 1000, 300, 100	-

At the end of the slide-hold-slide tests, parts of the gouge layers were collected, dried at room temperature and preserved in epoxy resin, in order to obtain thin sections parallel to the sense of shear for microstructural analysis.

1.2.3. Microscopy Observations

Microstructural observations were performed with a JEOL JSM-6500F thermal field emission scanning electron microscope, installed in the Electron Microscopy Laboratory at the INGV in Rome, Italy. All the micrographs presented in this manuscript are backscattered electron (BSE) images. Specifically, we collected photo mosaics at high magnification of the entire thin section thickness and micrographs of thin section details at higher magnification.

1.3. Results

1.3.1. Mechanical data

1.3.1.1. Frictional behavior at 5 MPa normal stress

Our strength results, with the exception of pure calcite, indicate an evolution curve of the coefficient of friction characterized by a distinct peak (μ_{peak}) and subsequent decay to a steady-state value (μ_{ss}) with increasing displacement (Figure 1.1a and Figure S3b). All the values of steady-state friction reported and discussed hereafter are measured during slide-hold-slide experiments. All the mixtures, at a sliding velocity of 10 μm/s, have values of the coefficient of friction that range between pure calcite value, i.e. $\mu_{peak} = \mu_{ss} \approx 0.66$, and pure talc value, i.e. $\mu_{peak} \approx 0.30$ and $\mu_{ss} \approx 0.20$ (Figure 1.2).

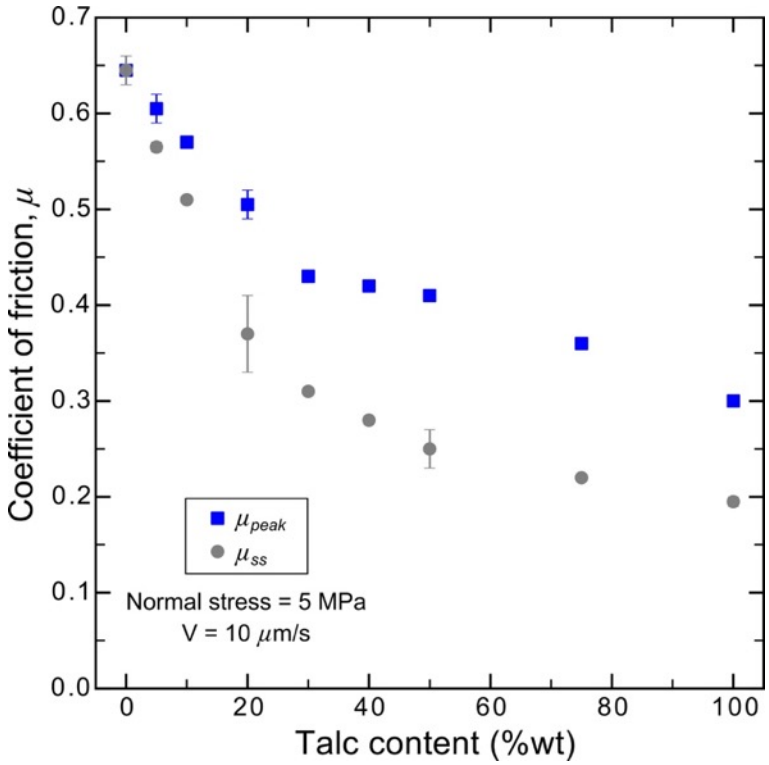

Figure 1.2. Friction of talc/calcite binary mixtures as function of talc content in experiments carried out at sliding velocity of 10 μm/s and at constant normal stress of 5 MPa. Friction systematically decreases with increasing talc content. The values reported for 0%, 5%, 20%, 50% and 100% are the average between slide-hold-slide experiments and velocity step experiments, the error bar thus indicates the difference between the two values. Whereas the values reported for all the other mixtures result from slide-hold-slide experiments. For the strain and the displacement at which the values were measured see Figure S3.

The coefficient of friction decreases systematically with increasing talc content, but the trend of friction reduction between the two end-members is not linear. There is a significant drop in friction (70% in μ_{ss}) between 0 and 20% talc, and a more gradual decrease at higher talc concentrations. In addition, the difference between peak friction and steady-state friction

tends to increase from 0 to 0.18 with the progressive addition of up to 50% talc and then to decrease slightly for higher talc contents. Strain at which the coefficient of friction reaches peak values tends to increase with increasing talc content, from $\gamma = 0.85$ to $\gamma = 1.88$, whereas strain at which friction reaches steady-state values tends to slightly decrease with increasing talc content, from $\gamma = 6.41$ to $\gamma = 1.88$ (Figure S3a).

Figure 1.3 shows healing results for our experiments at normal stress of 5 MPa. A content of 5% of talc is enough to cause a 50% drop in the rate of frictional healing, i.e. from $\beta \approx 0.0361$ to $\beta \approx 0.0196$. The healing rate of 10% talc sample is lower ($\beta \approx 0.0124$) and it is nearly zero for samples containing ≥ 20% talc. In samples with talc ranging from 20% to 50%, the rate of frictional healing ranges from $0.0021 < \beta < 0.0035$. For the gouges containing 75% and 100% talc the healing rate is $\beta \approx 0.0010$. Like for frictional strength, there is a significant and sharp, almost linear, drop in healing rate between 0 and 20% talc, and a slower degradation at higher talc contents.

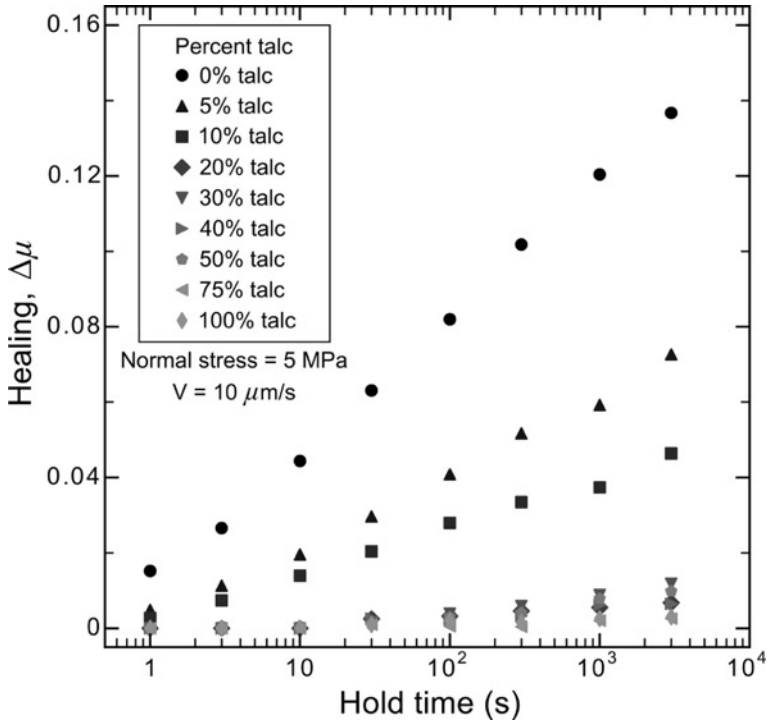

Figure 1.3. Frictional healing as function of hold time for different talc contents in experiments carried out at sliding velocity of 10 μm/s and at constant normal stress of 5 MPa. A small amount of talc strongly reduces frictional healing.

Concerning the velocity dependence of friction (Figure 1.4), pure calcite gouge shows variable behavior from velocity-strengthening to velocity-weakening, whereas all the other gouges exhibit a clear velocity strengthening behavior (Figure 1.4a). The trend of (a-b) with increasing talc content grows up to 20% talc, with maximum value (a-b) ≈ 0.0079 (velocity step 100-300 μm/s). Subsequently, (a-b) slowly decreases up to 50% talc ($0.0016 < (a\text{-}b) <$

0.0061), and then remains almost constant. The friction rate parameter *a*, as well as the friction rate parameter *b*, decreases with increasing talc content (Figure 1.4b and c). The major drop in *a* and *b* is recorded between 0 and 20% of talc. The *b* value then remains close to zero with some negative values for the velocity steps 30-100 μm/s, 100-300 μm/s and 300-1000 μm/s in the pure talc sample. In Figure 1.4d we show a velocity step, 300-1000 μm/s, conducted on the pure calcite and on the 20% talc gouges: here we can observe the decrease in *a* values and the reduction of the *b* values to zero in response to an addition of 20% talc to pure calcite.

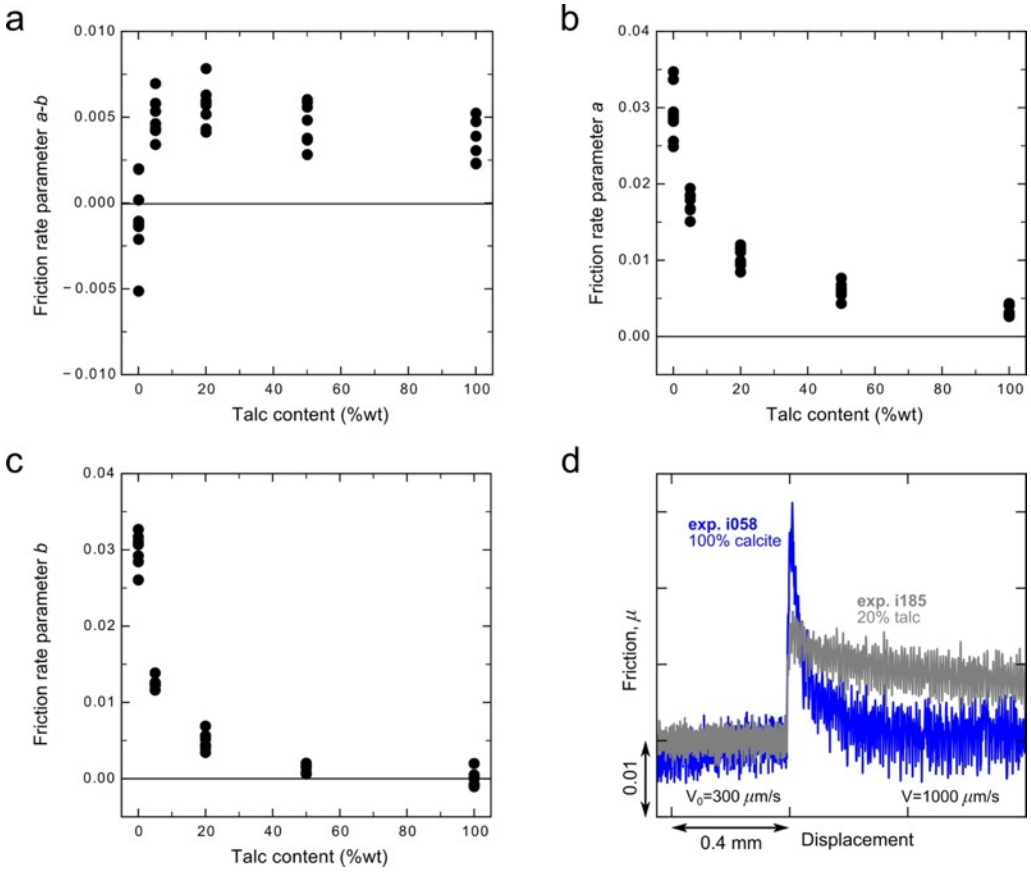

Figure 1.4. Friction rate parameters as function of talc content in experiments carried out at 5 MPa of normal stress. a) Talc/calcite mixtures are characterized by velocity-strengthening frictional behavior, i.e. positive (*a*-*b*). b) The "direct effect" *a* decreases with increasing talc content. c) The "evolution effect" *b* decreases with increasing talc content approaching negative values. d) A comparison between the velocity dependence of 100% calcite gouge (blue) and 20% talc gouge (gray) at 5 MPa for a velocity step of 300-1000 μm/s.

1.3.1.2. Frictional behavior at 20 and 50 MPa normal stress

Mechanical results from the first suite of 14 experiments at 5 MPa highlight the presence of a threshold value corresponding to a talc content of 20%. In the calcite/talc series, most of the degradation in friction, healing rate and *a* and *b* parameters occurs by 20% talc. Moreover, our slide-hold-slide experiments showed that a content of 5% talc is enough to halve the

healing rate of calcite gouge. In order to better constrain the frictional properties of 5 and 20% talc gouges, we performed 4 additional experiments at higher normal stresses (i.e. 20 or 50 MPa).

The coefficient of friction of the 5% talc sample is systematically reduced with increasing normal stress (Figure 1.5): the 5% talc sample at 5MPa has $\mu_{peak} \approx 0.59$ and $\mu_{ss} \approx 0.55$, whereas at 50 MPa has $\mu_{peak} \approx 0.50$ and $\mu_{ss} \approx 0.49$. The coefficient of friction of the 20% talc gouge shows a strong reduction in the difference between peak friction and steady-state friction with increasing normal stress. The peak friction of the 20% talc sample systematically decreases from $\mu_{peak} \approx 0.49$ at 5 MPa to $\mu_{peak} \approx 0.40$ at 50 MPa (Figure 1.5a), whereas the steady-state friction increases from $\mu_{ss} \approx 0.33$ at 5 MPa to $\mu_{ss} \approx 0.36$ (Figure 1.5b).

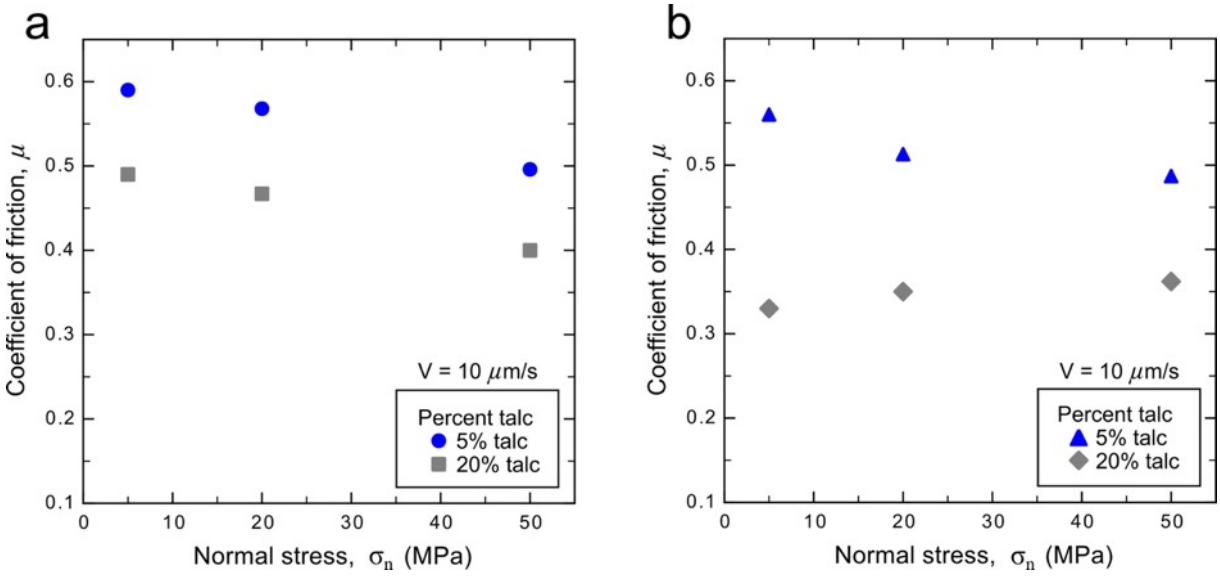

Figure 1.5. Peak friction (a) and steady-state (b) friction of talc/calcite binary mixtures as a function of normal stress at talc contents of 5 and 20%. Experiments were carried out at a sliding velocity of 10 μm/s.

In Figure 1.6a we show healing values of 5 and 20% talc samples at different normal stresses versus hold time. Gouges with 5% talc show remarkably different healing values, $\Delta\mu$, at higher normal stresses: the rate of frictional healing decreases with increasing normal stress ranging from $\beta \approx 0.0196$ at 5MPa to $\beta \approx 0.0032$ at 50 MPa. In Figure 1.6b, we report the different healing behavior of a 5% talc gouge at different normal stresses during a 3000 s hold: at 5 MPa $\Delta\mu \approx 0.07267$, whereas at 20 MPa $\Delta\mu \approx 0.01473$. The higher normal stress seems to suppress healing. Conversely, in sample with 20% talc, healing has no normal stress dependence: healing rate is almost constant with $\beta \approx 0.0021$ at 5 MPa and $\beta \approx 0.0018$ at both 20 and 50 MPa.

At 20 and 50 MPa, we observe velocity-strengthening behavior with (a-b) values similar to values obtained at 5 MPa (Figure 1.7a). Gouge with 5% talc at 50 MPa has the most variable

(*a*-*b*) values, ranging from 0.0042 to 0.0107. Moreover, at 50 MPa normal stresses, (*a*-*b*) systematically decreases with increasing velocity, whereas friction rate parameters *a* and *b* systematic increase with increasing velocity. In 5% talc sample, the friction rate parameter *a* (Figure 1.7b) slightly decreases with increasing normal stress, ranging from $0.0151 < a < 0.0194$ to $0.0082 < a < 0.0133$. In 20% talc sample, the reduction in *a* with increasing normal stress is less evident.

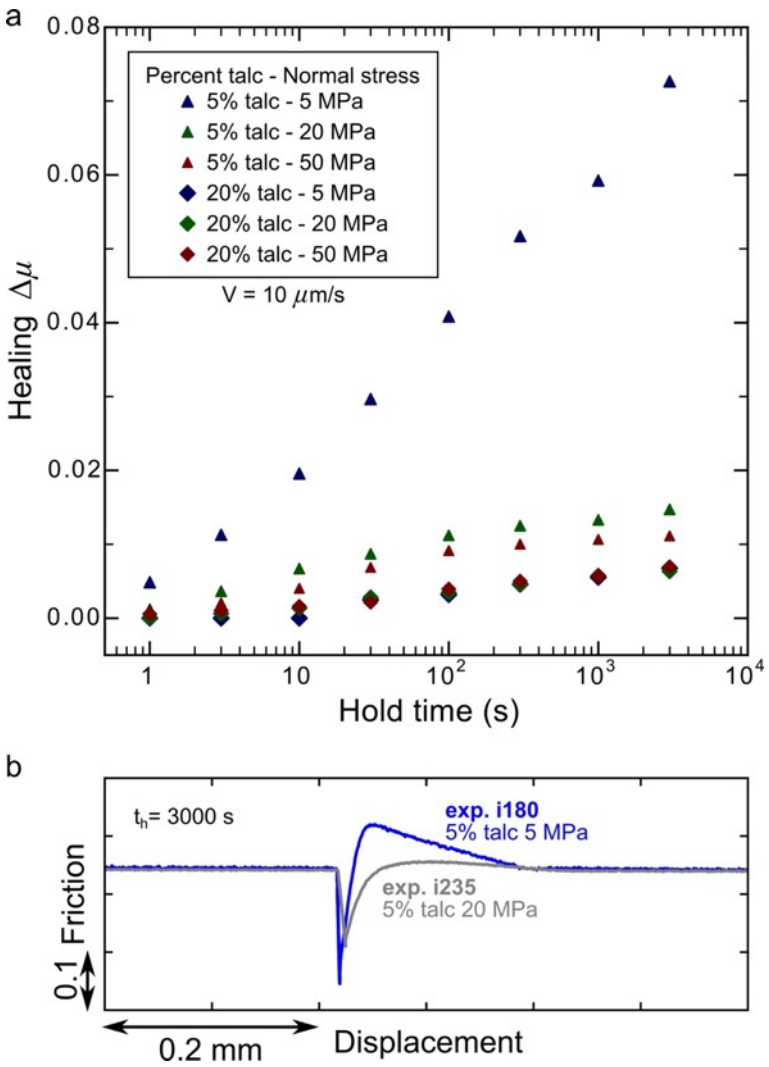

Figure 1.6. a) Frictional healing as function of hold time, talc content (5% and 20% talc) and normal stresses (5 MPa, 20 MPa and 50 MPa) in experiments carried out at a sliding velocity of 10 μm/s. Frictional healing of the 5% talc sample is strongly affected by changes in normal stress. b) Comparison between the healing of 5% talc gouge at 5 MPa normal stress (blue) and at 20 MPa normal stress (gray) in a 3000 s hold.

The parameter *b* (Figure 1.7c) shows a decrease between 5 and 20 MPa for both 5 and 20% talc gouges, whereas the *b* values at 50 MPa are more variable, becoming negative in some velocity steps ($b \approx -0.0025$ for 5% talc in velocity step 1-3 μm/s, $b \approx -0.0019$ for 20% talc in velocity step 1-3 μm/s). In Figure 1.7d we show two velocity steps conducted on the 5% talc gouge at different normal stresses: at 5MPa velocity-dependent behavior is characterized by

positive *a* and positive *b* in both velocity steps 1-3 μm/s and 100-300 μm/s, whereas at 50MPa velocity-dependent behavior shows different *b* parameter values, changing from negative *b* in velocity step 1-3 μm/s to positive *b* in velocity step 100-300 μm/s.

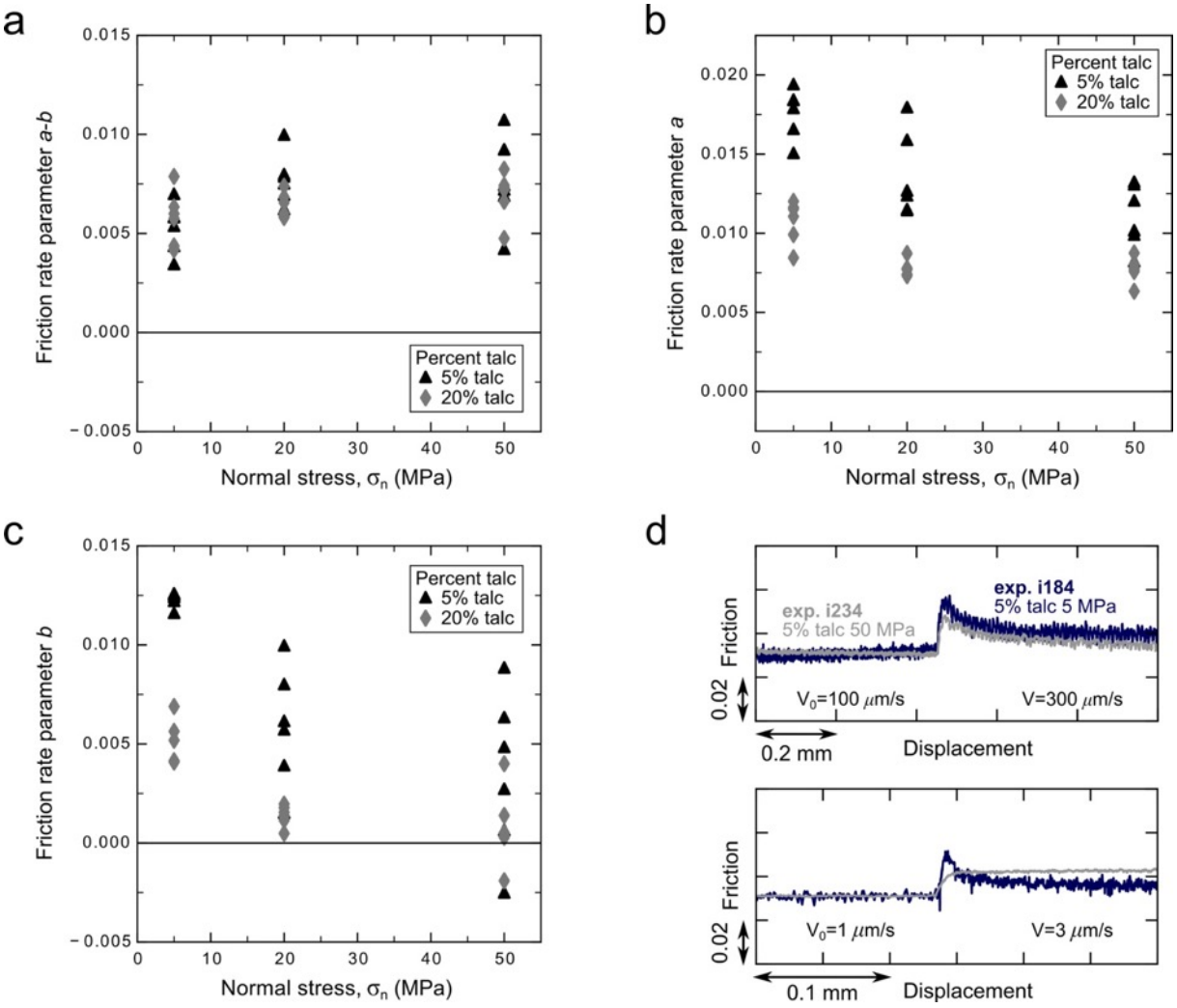

Figure 1.7. Friction rate parameters as function of normal stress (5 MPa, 20 MPa and 50 MPa) and talc content (5% and 20%). a) Talc/calcite mixtures are characterized by velocity-strengthening frictional behavior, i.e. positive *(a-b)*. b) The "direct effect" *a* decreases with increasing normal stress. c) The "evolution effect" *b* decreases with increasing normal stress approaching negative values. d) Comparison between the velocity dependence of 5% talc gouge at 5 MPa normal stress (blue) and at 50 MPa normal stress (gray) for velocity steps of 100-300 μm/s and 1-3 μm/s.

1.3.2. Microstructural observations

SEM investigations on the experimental faults at low normal stress, i.e. 5 MPa, indicate that deformation-induced microstructures are strongly controlled by the amount of talc. The texture of pure calcite sample (Figure 1.8a) is dominated by angular grains, isotropically distributed in a finer matrix. Overall, the structure is characterized by limited portions of fine-grained calcite, possibly derived from both localized cataclasis and/or starting material. We

observe limited fracturing and chipping (e.g., *Billi*, 2010) of larger calcite grains. The starting calcite grain size distribution shows a high concentration of fine material (50% of the volume is characterized by a grain size < 16 μm; Figure S1), which is clearly displayed in thin sections taken from samples after only the application of normal stress (Figure S2). We suggest that, in our saturated samples and at low normal stress, the deformation occurs via cataclastic flow, with grain rotation, translation and frictional sliding at grain contacts, with the development of few areas of fine-grained calcite. These discontinuous zones can develop from the portions of the starting material characterized by small grain sizes and do not testify a predominant role of grain size reduction during deformation.

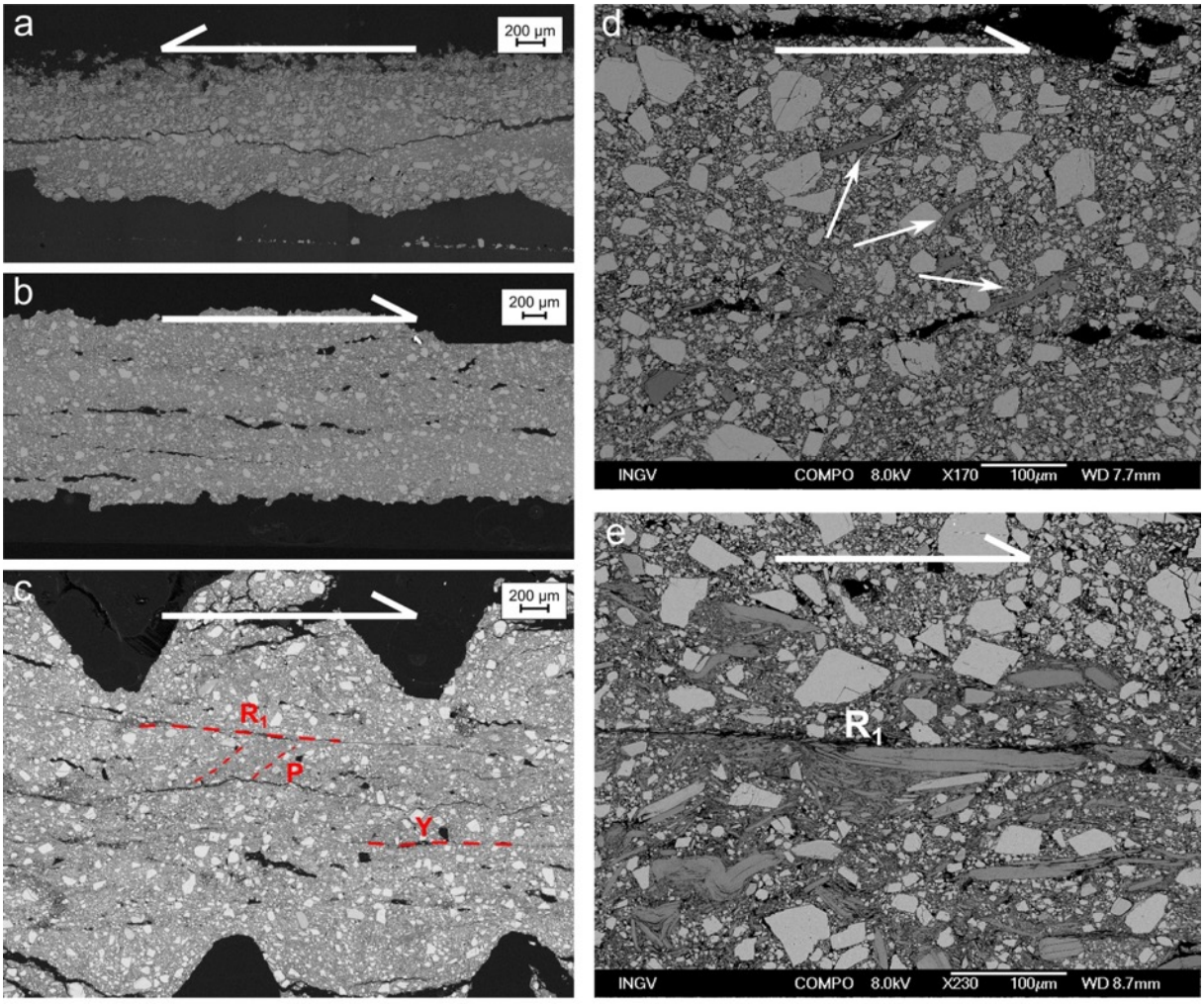

Figure 1.8. SEM micrograph showing microstructures developed in samples with variable talc content. (a) Distributed deformation characterizes the pure calcite sample, $\gamma \approx 7.1$. (b) The 5% talc sample deformed predominantly by cataclastic flow, $\gamma \approx 10.5$. (c) The 20% talc sample localizes deformation along shear zones, with the YPR fabric described by *Logan et al.* (1992). The shear strain is $\gamma \approx 7.4$. (d) Detail of the 5% talc sample showing talc lamellae iso-orientation (white arrows). (e) Detail of the 20% talc sample showing R_1 shear zone localized on talc lamellae.

In the 5% talc sample (Figure 1.8b and d), the texture is still homogeneous and dominated by a minor amount of large calcite grains (grain size > 100 μm). Calcite grains are more

rounded in comparison to the pure calcite gouge, suggesting a grain size reduction process such as chipping (*Billi*, 2010). Talc lamellae are scattered in the bulk microstructure, partially coating calcite grains and iso-orienting themselves forming a sort of "proto-foliation" (Figure 1.8d).

The microstructure of the 20% talc sample (Figure 1.8c and e) suggests a mixed mode of deformation with distributed deformation along the bulk microstructure and localization occurring along shear planes, defined on the basis of their geometric relationship to the YPR fabric described by *Logan et al.* (1992). Talc flakes scattered in the bulk microstructure are organized into foliation and are occasionally deformed by kinking and folding. R_1 shear planes show an enrichment of talc flakes and fine-grained calcite. The development of an interconnected network of talc lamellae around fine-grained calcite enables focusing of strain along shear planes. R_1 shear planes (Figure 1.8e), ~10°-clockwise oriented to the shear plane, are characterized by a high concentration of talc lamellae and the surrounding calcite grains display internal brittle deformation enhanced by the high strain condition. The continuity of R_1 planes is high, whereas Y planes, parallel to the shear plane, tend to be more discontinuous. Talc lamellae alignments can also be observed also along P foliation planes, ~145°-clockwise to the shear plane.

Our microstructural analysis shows that increasing talc content results in a progressive microstructural organization. The mechanism of deformation evolves from distributed cataclastic flow (0-5% of talc) to localized frictional sliding along talc-rich R_1 shear planes (20% of talc) with some grain size reduction and redistribution of finer calcite grains along shear planes, to distributed frictional sliding along talc-rich domains (50% of talc).

1.4. Discussion

1.4.1 Integration of mechanical data and microstructures

Peak and steady-state frictional strength decrease at two different rates (Figure 1.2). For both, a talc content of 20% is the value that marks a significant change in the degradation rate: a more rapid decrease at talc contents between 0%-20% is followed by a slower decrease from 20% to 100%. A talc content of 20% also strongly influences frictional healing (Figure 1.3) and velocity dependence (Figure 1.4). One possible explanation for this weakening trend is the generation of overpressure resulting from the decreasing permeability of gouges with increasing talc content. However, this mechanism unlikely provides a strong contribution to the weakening of our talc-bearing gouges, for mainly two reasons: our experiments were conducted under drained conditions, which allow the dissipation of any generated overpressure at least over the experiment time span, and the addition of only 5% of talc, which results in a decrease in friction, unlikely affects permeability parallel to the gouge such that overpressure would develop. Ruling out fluid overpressure as a weakening mechanism, on the grounds of microstructural observations we indicate the occurrence of shear localization on talc-enriched planes as the mechanism able to explain the variation in the frictional properties with increasing talc content.

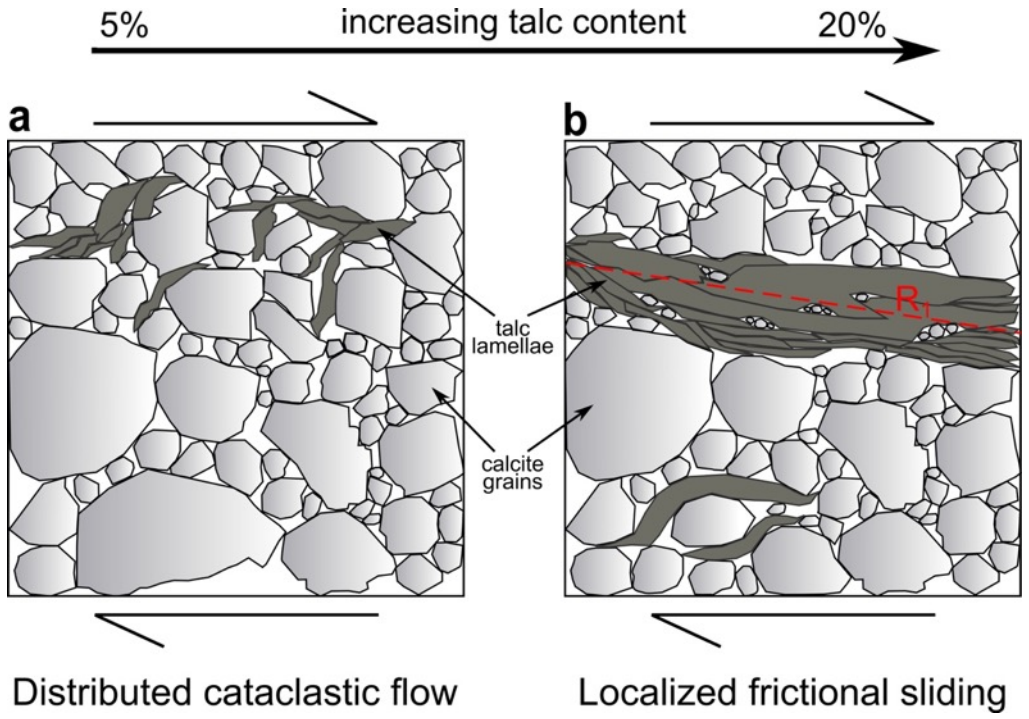

Figure 1.9. a) A stress-supporting framework of calcite grains, with talc lamellae (5% wt.) situated between some calcite grains, characterized by distributed deformation and resulting in high frictional strength, high frictional healing and high rate parameters. b) As the talc fraction increases, the development of interconnected talc network localizes deformation on planes (e.g., R_1) and reduces the frictional strength, the frictional healing and the rate parameters.

At low talc concentrations (0-10%), the absence of continuous gouge portions characterized by a concentration of small calcite grains suggests no localization of grain-size reduction nor grain-size redistribution along shear bands. The overall lower amount of 100 μm-sized calcite grains and their more rounded shape in the 5 and 10% talc samples, when compared to the pure calcite gouge, can be interpreted as an enhanced grain size reduction due to the incipient development of talc foliation. The progressive alignment of talc lamellae is favored in regions where calcite grain size is reduced, progressively localizing the strain. However, in our low talc concentration gouges, this mechanism seems to not have a predominant role as demonstrated by a limited number of intragrain fractures within calcite grains. In addition, short and discontinuous alignments of talc (Figures 1.8b and d) indicate that the amount of talc is not enough to localize the shear. On the basis of all these observations, we can infer that distributed cataclastic flow is the main deformation mechanism (Figure 1.9a). These gouges are relatively strong, with μ_{ss} ranging between 0.66 and 0.51 at 5 MPa, and the frictional healing is relatively high, with a healing rate β ranging between 0.036 and 0.012. The friction rate parameter a is high, with values ranging between 0.035 and 0.015. The direct effect a results from a change in gouge strength upon a velocity step, firstly attributed to a rate-dependence of contact strength (e.g., *Dieterich*, 1979). However, any porosity change in response to a velocity step influences gouge strength and consequently the a value. Moreover, different mechanisms, such as pressure solution and plasticity at grain contacts, can indirectly contribute to a values, influencing the properties of grain contacts and the porosity of our gouges. Dilatancy effects in gouge layers due to a step change in sliding velocity have long been recognized (e.g., *Marone et al.*, 1990; *Sammis and Steacy*, 1994; *Mair and Marone*, 1999). Dilation of gouges rich in calcite, resulting from the rearrangement of the microstructure in response to a step to higher sliding velocity, consists in grains sliding and rotation and involves an increase in friction due to work expended against the normal stress. In our mixtures, calcite dilation influences the mixture behavior during slide-hold-slide experiments (Figure S4): the dilation of the 5% and the 20% talc samples are reduced, respectively, of about 40% and 60%, when compared with the pure calcite sample. The high dilation values associated with high healing values upon re-shear suggests a possible contribution of dilation, related to granular calcite, in the evolution of the a values with increasing talc. Nonetheless, time dependent mechanisms, such as pressure solution and plasticity at contacts can contribute to the direct effect. Pressure solution, strengthening at grain contacts, correlates positively with a values. Conversely, plasticity limits dilation resulting in lower a values. However, as shown by other experiments that we performed on

calcite gouges (*Carpenter et al.*, 2016a), plasticity in calcite gouges, at room temperature, is an effective mechanism only at low slip velocities and high normal stresses, excluding an important contribution of plasticity in our low stress dataset. Furthermore, the large friction rate parameter *b* in calcite-rich gouges can be explained by the attainment of a new steady-state porosity following the microstructure rearrangement through granular dilation.

The 20% talc sample shows an YPR geometry (*Logan et al*., 1992) of the experimental gouge layer (e.g., Figure 1.8c) with talc lamellae concentrated along R_1 shear planes. This microstructure favors a deformation mechanism characterized by frictional sliding along the talc foliae (Figure 1.9b), typically observed in pure talc shear experiments (e.g., *Boutareaud et al.*, 2012; *Misra et al.*, 2014), promoting a decrease in the frictional strength to values of μ_{ss} ranging between 0.33 and 0.20. Similarly, *Moore and Lockner* (2011) in quartz/talc mixtures observed a marked weakening resulting from the formation of R_1 planes that cross the entire sample. Moreover, *Hirauchi et al.* (2013), shearing a mixture of antigorite and quartz at different experimental conditions generating different amounts of metasomatically grown talc, observed a weakening of the gouge associated with the progressive development of talc along through-going boundary shears. The almost zero healing of the gouges, with β smaller than 0.002, suggests that during hold periods the growing contact area, if it occurs, does not result in an increase in frictional strength. Talc lamellae, with their platy shape, can hinder growth of contact area. Following this interpretation, our data are in agreement with previous studies on phyllosilicates-rich fault rocks that have suggested real contact areas saturation in the actively slipping zone, due to crystal habit, as mechanism for inhibiting frictional healing (e.g., *Bos and Spiers*, 2001; *Saffer and Marone*, 2003; *Tesei et al.*, 2012). The localization of deformation along interconnected, talc-rich shear surfaces coincides with the onset of a strong velocity-strengthening behavior, as previously observed in phyllosilicate-bearing gouges that developed a strong foliation (e.g., *Bos and Spiers*, 2002; *Niemeijer and Spiers*, 2005; *Niemeijer and Spiers*, 2006). In these previous works, the strong foliation allowed the attainment of a steady-state microstructure that does not require dilation upon a step to higher shearing velocity. Similarly, the development of connected, talc-rich shear surfaces where deformation is highly localized does not require any significant rearrangement upon a sudden change in velocity, favoring velocity-strengthening behavior. Specifically, the friction rate parameters *a* and *b* decrease with increasing talc content (Figure 1.4b and c): again a 20% talc content marks the larger change in the evolution of the rate parameters. We suggest that, by adding more and more talc along the experimental fault, cataclastic flow of granular calcite is overcome by frictional sliding along the platy talc, resulting in a less pronounced dilatancy

effect, thus reducing *a* values. In addition, previous studies (*Beeler et al.*, 2007) proposed dislocation glide at room temperature as a possible mechanism operating in talc and other phyllosilicates. Such a mechanism possibly controls the value of the direct effect in our samples containing ≥ 20% of talc. Furthermore, in talc-rich samples, the talc lamellae are almost in complete contact, causing a decrease of *b* to near zero, implying that the real area of frictional contact does not change after a velocity step (e.g., *Scholz et al.*, 1990; *Niemeijer et al.*, 2010; *Collettini et al.*, 2011).

With increasing normal stress our experiments at 5 and 20 % talc contents show a more pronounced shift towards a pure talc-like behavior, that is: a) a reduction in the difference between peak and steady state friction in particular for 20% of talc (Figure 1.5); b) a close to zero healing rate for 5% of talc (Figure 1.6); and c) a reduction in the direct effect and an even stronger reduction in the evolution effect resulting in a stronger velocity-strengthening behavior (Figure 1.7). With increasing normal stress, the decrease in steady-state friction in the 5% talc versus the increase in steady-state friction in the 20% talc can result from the different contribution of grain size reduction to the deformation mechanisms operating in these gouges. Gouges with 5% talc, in which the deformation is predominantly accommodated by distributed cataclastic flow at low normal stress, can be weakened at higher normal stresses by the occurrence of grain size reduction that enhances the localization of deformation along shear bands. On the other hand, gouges with 20% talc, that deform by localized frictional sliding along talc-rich surfaces, can be strengthen by the involvement of small size grain, deriving from comminution, in the shear zones, as already proposed in previous studies on clay-rich gouges (*den Hartog et al.*, 2012). However, since the increase in steady-state friction in the 20% talc is rather slight and the values can be considered almost constant, another likely explanation for the two different trends in Figure 1.5b can be related to the effect of cohesion. Fitting the shear stress versus normal stress data with the Coulomb-Mohr failure criterion, we obtained a cohesion of C ≈ 0.5 MPa for the 5% talc sample and an almost zero cohesion for the 20% talc sample. Since we calculated the steady-state friction as the ratio between τ and σ_n, an amount of cohesion of ~0.5 for the 5% talc sample results in an apparent decrease of the friction value of ~0.09 between σ_n = 5 MPa and σ_n = 50 MPa, consistent with the measured steady-state values (Figure 1.5b). The 20% talc sample, having C ≈ 0 MPa, does not show any contribution of cohesion to the friction values.

To summarize, our results documented the significant drop in frictional strength, healing rate and rate parameters between 0% and 20% of talc due to the progressive localization of deformation on discrete talc-rich surfaces.

1.4.2 Comparison to previous data

The frictional strength for pure calcite is consistent with results from other studies on limestone and calcite-rich fault rock at low stress and room temperature (e.g., *Weeks and Tullis*, 1985; *Scuderi et al.*, 2013; *Carpenter et al.*, 2014; *Tesei et al.*, 2014; *Verberne et al.*, 2014). For pure talc, our data are in good agreement with results from other experiments conducted on synthetic talc gouges at variable normal stress and temperature representative of the shallow crustal conditions (e.g., *Escartín et al.*, 2008; *Moore and Lockner*, 2008; *Niemeijer et al.*, 2010; *Hirauchi et al*., 2013). Binary mixtures of calcite and talc show stress-strain curves characterized by a maximum value of strength reached during the "run-in" phase followed by a decrease in friction, up to 0.2, with increasing strain (Figures 1.1 and 1.2). This evolution is typical of clay-dominated gouges, and is generally explained by the alignment of clay particles with increasing deformation (e.g., *Lupini et al.*, 1981; *Chester and Logan*, 1987; *Bos and Spiers*, 2001; *Saffer et al.*, 2001; *Saffer and Marone*, 2003; *Moore and Lockner*, 2004; *Tembe et al.*, 2010).

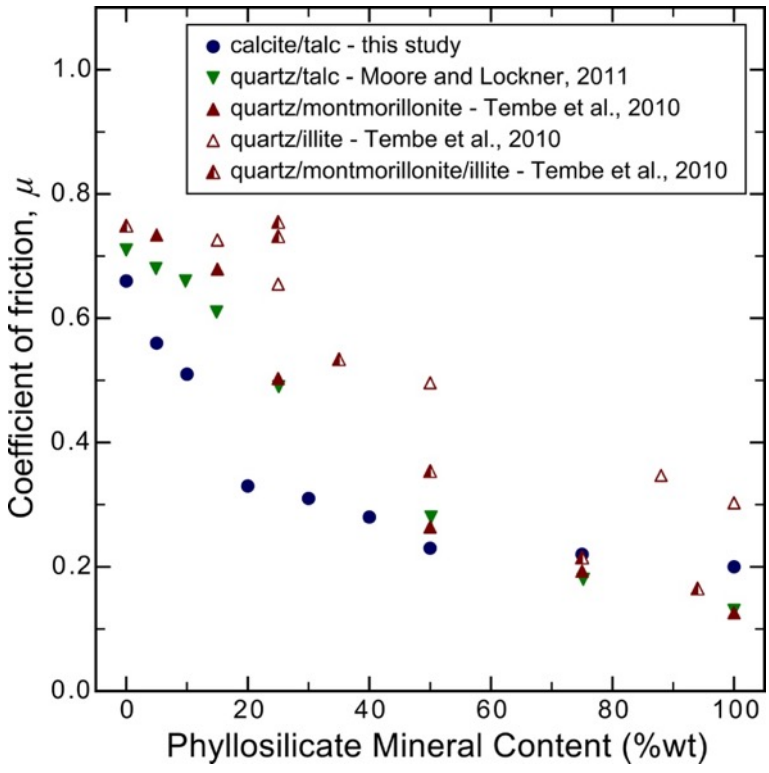

Figure 1.10. Comparison of friction degradation trends from different gouge mixtures. *Moore and Lockner* (2011) conducted experiments at high temperature (200°C); however, quartz solubility at high temperature is comparable to calcite solubility at room temperature (*Rimstidt*, 1997). Fault-parallel displacements are also comparable: *Moore and Lockner* (2011) measured the coefficient of friction at 4 mm, *Tembe at al.* (2010) at about 9 mm, whereas in our experiments the steady-state is reached between 5-8 mm. Quartz/talc (*Moore and Lockner*, 2011) and quartz/montmorillonite (*Tembe et al.*, 2010) mixtures show similar trends that differ from our calcite/talc mixtures for low phyllosilicates contents. Quartz/illite mixture (*Tembe et al.*, 2010) shows an almost linear trend.

In the following we present a comparison between our friction data on binary mixtures of talc and calcite with other frictional strength data of mixtures of quartz and various phyllosilicates (Figure 1.10) (*Tembe et al.*, 2010; *Moore and Lockner*, 2011). In this way we try to characterize the interplay between strong and angular material, such as quartz and calcite, and weak and platy minerals, such as talc and clays, in frictional strength. Comparing our 5 MPa dataset with studies conducted at higher normal stress is reasonable considering that: 1) the effect of normal stress on the coefficient of friction in our experiments is small, i.e. the variation of steady-state friction is less than 0.1 for different talc contents and normal stresses (Figure 1.5b); 2) we are presenting a conservative estimate of minimum talc amount able to weaken a fault, because for small talc percentages (5-20%) the increase of normal stress changes the rate and state parameters towards a more talc like-behavior (Figures 1.5-1.7).

Tembe et al. (2010) interpreted their strength data in term of three-regimes (*Lupini et al.,* 1981). Close to the end-members composition, the coefficient of friction is essentially the same of the respective end-member, whereas it decreases with increasing clay content at intermediate compositions. *Moore and Lockner* (2011) presented frictional data on quartz and talc mixtures showing that gouges containing low talc percentage fall on a straight line connecting the end-member values, whereas the rest of the mixtures follows a curved trend below the line. Our data mainly differ from these studies in the degradation trend at low talc content. In particular, we observe an initial linear rapid decrease in friction, between 0 and 20% talc, followed by a more gradual decrease at talc contents above 20%. Specifically, in these previous datasets, the onset of a fast degradation rate occurs with the addition of a certain amount of phyllosilicates to quartz gouges (i.e., 15% in the case of illite, montmorillonite and talc, and 25% in the case of montmorillonite/illite). Before these thresholds the degradation rate is slower. Our dataset is slightly different since the onset of the fast degradation rate coincides with the addition of low amounts of talc, i.e. 5%. Consequently, we do not observe a slower rate before the onset of the fast decrease in friction.

The grain size of starting materials can be a possible explanation for the different trends documented (Figure 1.10). *Tembe et al.* (2010) and *Moore and Lockner* (2011) used non-overlapping grain sizes of end-member minerals: respectively, < 175 μm-sized quartz and < 3 μm-sized montmorillonite, < 180 μm-sized quartz and < 90 μm-sized talc. The different frictional behavior of binary mixtures can be justified by an ideal packing model, as in previous works (*Lupini et al.* 1981; *Tembe et al.*, 2010). In mixtures characterized by non-overlapping grain sizes, at low clay concentrations the smaller-sized clay lamellae are isolated

and concentrated only in the void spaces. In this situation the stress-supporting framework of quartz grains determines high strength values. Instead, in our experiments all the starting materials were sieved to a size <125 μm and have a similar volumetric grain size distribution (Figure S1). In this case, even at very low phyllosilicate content, talc lamellae cannot be isolated in void spaces but they separate calcite grains interfering with the calcite grain-grain framework (Figure 1.9a) and thus reducing friction. As a result, the first, high frictional strength regime of *Lupini et al.* (1981) is not expressed in our samples that show a very rapid decrease in the first portion of the trend. This idea of different grain-sizes controlling the microstructure evolution and, thus, the frictional behavior of binary mixtures has been already suggested by *Niemeijer and Spiers* (2006) and *Moore and Lockner* (2011) for other types of binary mixtures.

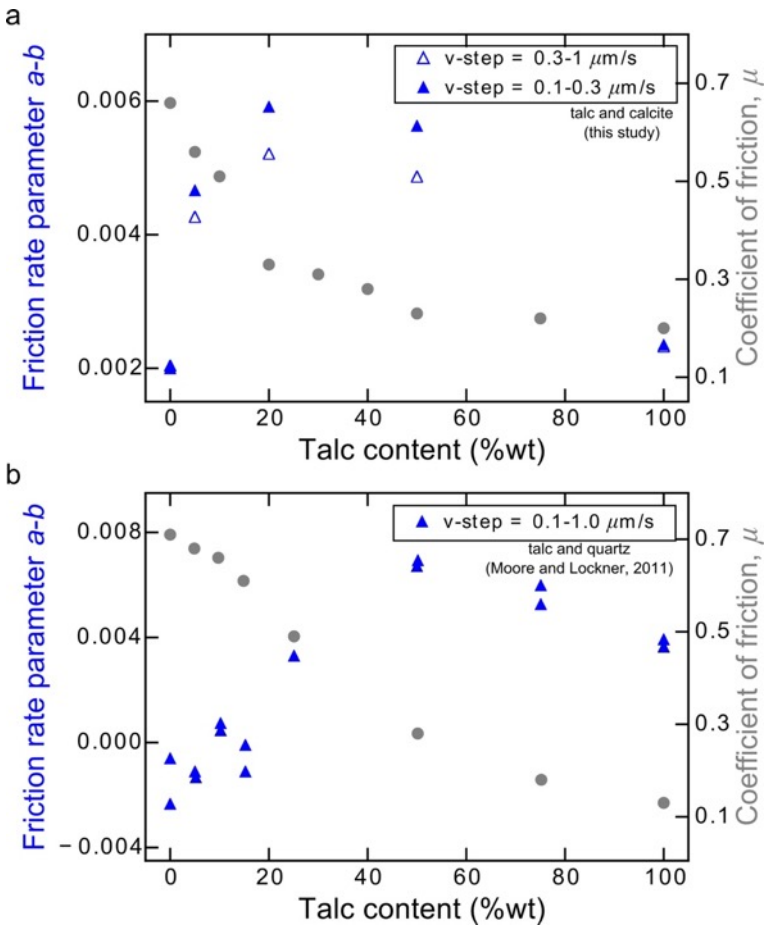

Figure 1.11. Comparison between friction reduction trend and (*a*-*b*) trend with increasing talc content. a) In our data, an initial fast drop in friction corresponds to an increase in (*a*-*b*) parameter. b) Data from *Moore and Lockner* (2011) also show that a rapid decrease in friction corresponds to an increase in (*a*-*b*) parameter. We selected the 0.1-0.3 μm/s and the 0.3-1.0 μm/s velocity steps from our data set in order to compare our results to *Moore and Lockner*'s (2011) 0.1-1.0 μm/s velocity steps.

The overlapping grain size of talc and calcite thus facilitates the effective interconnection of talc lamellae even with small amounts of talc, i.e. 20%. The importance of the topology of

the weakest mineral during deformation has been also suggested on the base of previous experiments on intact cores of serpentinized peridotites (*Escartín et al.*, 2001). In this study, serpentine coating olivine grain boundaries in the intact cores is interpreted as a key factor in controlling the nonlinear strength dependence on serpentinization. *Moore and Lockner* (2011) also performed velocity-stepping tests. In their experiments, at low talc content, the (*a*-*b*) parameter approaches zero value, further suggesting that quartz framework exercises a strong control over the frictional behavior of quartz-rich mixtures. Adding talc, they observed an increase in (*a*-*b*) in correspondence to the steeper portion of the friction degradation curve (Figure 1.11b). As observed also in other experimental studies on phyllosilicate-rich gouges (*den Hartog et al.*, 2014), an increase in the amount of quartz shifts (*a*-*b*) towards more negative values, promoting velocity-weakening behavior. However, the velocity dependence does not increase monotonically with increasing phyllosilicate content. In quartz/talc mixtures (*Moore and Lockner*, 2011) the value of (*a*-*b*) increases until a 50% talc content, the minimum amount of talc at which the localization of shear along talc-lined shears occurs. These results compare well with our velocity steps data that show the larger increase in (*a*-*b*) in correspondence of the steeper portion of friction degradation that for calcite-talc mixture is achieved at 20% of talc (Figure 1.11a). We suggest a progressively stabilization of gouge, towards more positive (*a*-*b*) values, with increasing talc content, as R_1 shears on talc alignments develop and increase in length, until a fully interconnected talc framework is reached. In addition, we noticed that, whereas at 5 MPa normal stress the velocity-dependence does not show a clear trend as a function of velocity, at 50 MPa (*a*-*b*) values systematically decrease with increasing step velocity. From a theoretical point of view, the rate- and state-friction law states that *a* and *b* are constitutive properties of the material and independent of sliding velocity (e.g., *Dieterich*, 1979), however our experiments, as well as previous studies, show that a velocity-dependence of the *a* and *b* parameters exists (e.g., *Ikari et al.*, 2007; *Niemeijer et al.*, 2010; *Ikari et al.*, 2011; *Moore and Lockner*, 2011; *Carpenter et al.*, 2014; *Verberne et al.*, 2014). We suggest that in our experiments this rate-dependence of (*a*-*b*) can derive in part from a low temperature plastic deformation of both talc lamellae (*Beeler et al.*, 2007) and calcite (e.g., *De Bresser et al.*, 2002; *Schubnel et al*., 2006), being more efficient at higher normal stresses. On this basis, lower sliding velocity, at which plasticity is more efficient, correspond to higher (*a*-*b*). Moreover, increasing normal stress (from 20 to 50 MPa) and increasing talc content (from 5 to 20%) we observe a switch towards negative values of *b*, resulting in a transition from a peak evolution of friction to a monotonic evolution of friction upon a velocity step. This behavior can be interpreted as the result of the interplay between

brittle and plastic behavior, possibly framed in a transition from a rate- and state-friction law, that can explain the peak evolution of pure calcite, to a flow law, that can explain the monotonic evolution of 20% talc gouge at high stress, as suggested from theoretical model by *Noda and Shimamoto* (2010) and *Shimamoto and Noda* (2014). However further investigation is required to discriminate the predominant deformation mechanism.

1.4.3 The Mechanisms of frictional healing

Frictional healing is a complex combination of different phenomena arising from the interplay of physical-mechanical and chemical processes occurring inside the gouge layer. Frictional strengthening of a granular gouge may result from porosity loss, due to mechanical and chemical compaction, and contact strengthening (e.g., *Scholz*, 2002). At shallow-crustal conditions, compaction of binary mixtures of strong and weak minerals results from mechanical compaction, due to inter-granular sliding, comminution, and clay particle plasticity, and chemical compaction, due to fluid-assisted processes such as pressure solution, cementation and contact area growth (*Evans et al*., 1999). Under low pressure and low temperature conditions, mechanical compaction consists of a time-independent process that develops a locked aggregate (*Evans et al.*, 1999; *Zhang and Spiers*, 2005). Contrarily, chemical compaction consists of a time-dependent creep (e.g., *Bos et al.*, 2000; *Bos and Spiers*, 2000; *Bos and Spiers*, 2001). Previous experiments on the healing of binary mixtures have been conducted on a mixture of kaolinite and halite (*Bos and Spiers*, 2000), which is in a first approximation, the basis of comparison for mixtures of phyllosilicates and higher-strength minerals. Our results are consistent with their results that showed a decrease of ~1 order of magnitude in the healing rate with the addition of 25% kaolinite content in the halite gouge. Our slide-hold-slide experiments outline the key role played by talc in drastically reducing the re-strengthening of the gouges. We suggest that talc strongly reduces fault healing by both mechanical processes via contact area saturation, and chemical processes via the inhibition of dissolution and cementation of calcite.

Our previous experiments on calcite gouges conducted with different saturation fluids (*Carpenter et al.*, 2016a) show different restrengthening behavior (Figure 1.12). Calcite samples were saturated both with brine and silicone oil, chosen due to the fact that it is an inert pore fluid inhibiting chemical processes. The healing of pure calcite sample in $CaCO_3$-equilibrated water solution increases linearly with the logarithm of hold time, a feature often observed in experiments conducted at room temperature and first described by *Dieterich*

(1972). Conversely, the healing of pure calcite in silicone oil is significantly lower and has a different trend with the logarithm of hold time: after an initial linear increase, healing stabilizes to a constant value, which appears to saturate at long hold times, possibly suggesting the maximum porosity reduction, due to only mechanical compaction of the layer, occurred via inter-granular sliding. Thus, these experiments give insight into the contribution of mechanical compaction, in silicone oil-saturated condition, versus the contribution of chemical compaction, in brine-saturated conditions, in relation to frictional healing. Such contributions have been previously explored in experimental works on calcite deformed with different pore fluids (*Zhang and Spiers*, 2005; *Zhang et al.*, 2010). On the basis of these considerations, a possible mechanism able to explain the high frictional healing under brine-saturated conditions is a fluid-assisted inter-granular cementation.

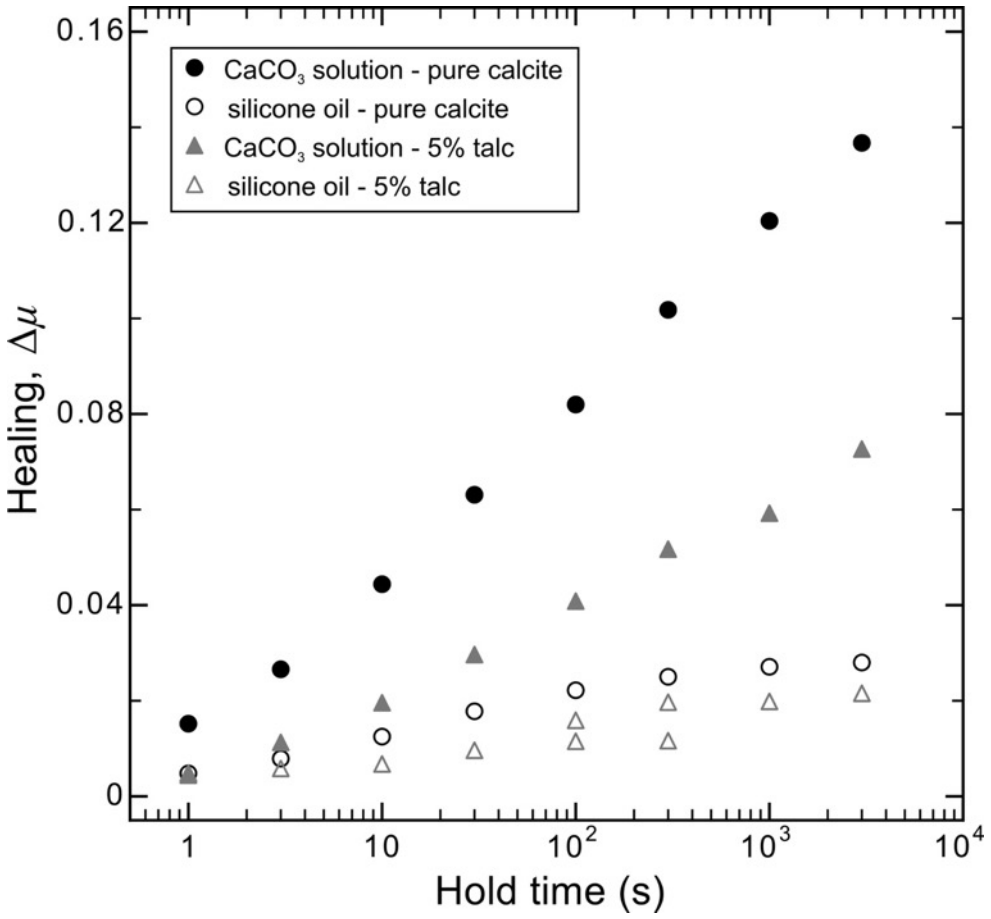

Figure 1.12. Comparison between frictional healing data from this study on 5% talc mixture and previous work on pure calcite (*Carpenter et al.*, 2016a) resulting from experiments conducted with different pore fluids ($CaCO_3$-equilibrated water and silicone oil). All the plotted experiments are carried out at 5 MPa normal stress and 10 μm/s sliding velocity. The difference between the pure calcite samples at different saturation conditions suggests an important role of water-assisted processes, as solution and cementation, in enhancing the healing rate. The difference between the pure calcite and 5% talc sample in $CaCO_3$-water possibly results from the inhibition of calcite solution and cementation exerted by the presence of talc. The frictional healing of 5% talc sample in silicone oil is similar to that of pure calcite under the same saturation conditions.

The development of an interconnected network of cemented calcite grains leads to high healing values, consistent with the mechanism identified in previous works, such as the strengthening of welded contacts by hydrothermal reaction (*Tenthorey et al.* 2003; *Yasuhara et al.*, 2005) and the gain in cohesion induced by grain cementation due to pressure solution (*Olsen et al.*, 1998; *Bos et al.*, 2000; *Kanagawa et al.*, 2000; *Bos and Spiers*, 2002). Another time-dependent compaction mechanism that we cannot rule out is water-assisted stress corrosion crack growth (*Yasuhara and Elsworth*, 2008). Also this process, the activation of which is essentially enhanced by the presence of pore water (*Atkinson and Meredith*, 1989), can be inhibited under silicone oil saturation. However, due to the abundance of fine-grained calcite in the starting material, stress corrosion crack growth is less-favored. This mechanism is indeed more efficient with coarser grains, whereas cementation and pressure-solution are more efficient with finer grains.

In contrast to the healing behavior of angular materials described above, in phyllosilicates, such as talc, the phyllosilicate foliation allows quick saturation of the contact area and thus no re-strengthening (e.g., *Bos and Spiers*, 2000; *Niemeijer et al.*, 2008; *Ikari et al.*, 2009a; *Tesei et al.*, 2012). We suggest this mechanism as the main control for the almost zero healing value in our 20% talc experiments (Figures 1.3 and 1.6), in which, as shown by microstructures, deformation occurs along talc-rich planes incapable of increasing their contact area or strength.

Interestingly, our mechanical data show that adding a talc content of 5% to pure calcite results in a drop is the healing rate from $\beta \approx 0.0361$ to $\beta \approx 0.0196$. At the same time this value is still significantly higher with respect to the pure calcite value under silicone oil-saturated condition ($\beta \approx 0.0071$) (Figure 1.12). If the difference in the healing rate between calcite in $CaCO_3$-equilibrated water and calcite in silicone oil is due to calcite cementation or stress corrosion cracking along grains contacts, our result suggests an important role of talc in limiting such chemical process of calcite and reducing it by about 60%. In order to have more insights into the frictional healing of 5% talc gouges, we ran one additional experiment under silicone oil-saturated conditions. The healing of 5% talc with silicone oil (Figure 1.12) shows a trend similar to pure calcite under the same conditions, but with slightly lower values ($\beta \approx 0.0053$). These lower values may indicate a certain, even if minimal, mechanical effect of talc on gouge compaction. In these tests, talc is not pervasive enough throughout the gouge layer to strongly affect the mechanical behavior of pure calcite by preventing the contact of calcite grains, but at the same time, talc lamellae, even if present in a small quantity, do not contribute to the progressive mechanical compaction of calcite grains, thus limiting healing.

Moreover, whereas in brine-saturated experiments dilation and compaction data show a linearly increasing trend, in silicone oil saturation experiments they are characterized by lower values that saturate at long hold times (Figure S5), further supporting the idea of a water-assisted chemical process operating in the gouges.

In order to explain the 50% of reduction in healing properties of calcite induced by the addition of 5% talc, we suggest the release of magnesium ions from talc into the pore water may play a key role. This process occurs at room temperature, as suggested by the increase in magnesium content of our saturating solution (see Table S1). Since it is known that magnesium ions in the pore fluid inhibits calcite precipitation (*Reddy and Wang*, 1980; *Davis et al*, 2000), we propose cementation as a plausible re-strengthening mechanism in our calcite gouges and partial cementation inhibition due to magnesium ions as a plausible mechanism in our 5% talc gouge. The operation of such a mechanism is supported by recent experiments documenting the effect of fluid presence on the re-strengthening of carbonate fault gouge (e.g., *Chen et al.*, 2015) and the effect of fluid composition on calcite compaction (e.g., *Zhang and Spiers*, 2005) and demonstrating that magnesium ions slow pressure solution processes (e.g., *Zhang and Spiers*, 2005).

To summarize we show that 5% of talc within calcite-rich fault gouges reduces frictional healing of 50% and, since little to no healing can be explained by the physical role of 5% talc in saturating the contact areas of deformation zones, we suggest this is accomplished by the chemical role exerted by talc in hindering cementation processes.

1.5. Conclusion

We systematically investigated the frictional sliding behavior of calcite gouges containing different amounts of talc, performing a suite of 20 friction experiments conducted at room temperature, normal stresses up to 50 MPa and saturated under different pore fluid, i.e. $CaCO_3$-equilibrated water and silicone oil, conditions. Our experiments highlight the role of even small amounts of talc in reducing the strength of natural faults and altering their mechanical behavior.

The shear strength of simulated calcite gouges is strongly affected by the presence of minor amounts of talc. The addition of 20% talc is responsible for a reduction of 70% in steady-state friction, a marked increase in the velocity-strengthening behavior and a decrease in the amount of frictional healing to nearly zero. Microstructural observations show that 20% talc is the minimum amount of talc that allows the interconnection of talc lamellae throughout the entire sample, thus localizing deformation on talc-rich R_1 shear planes and substantially weakening the gouge. We propose that the change in the mechanical properties of talc/calcite mixture occurring by about 20% talc content results from a switch in the deformation mechanism from distributed cataclastic flow for pure calcite to localized sliding on talc-rich shear planes.

Amounts of talc that only partially affected the frictional strength are able to drastically influence the healing behavior at normal stress of 5 MPa. The rate of frictional healing of a synthetic calcite gouge is halved with the addition of only 5% talc (from $\beta \approx 0.0361$ to $\beta \approx 0.0196$). Moreover, under silicone oil saturated conditions the healing rate of 5% talc sample further decreases from $\beta \approx 0.0196$ to $\beta \approx 0.0053$, suggesting that some water-assisted re-strengthening of the gouge happens in $CaCO_3$-equilibrated water experiments. We propose that the drop in healing, due to the addition of 5% talc, is not only related to the presence of talc between adjacent calcite grains that prevent contact area growth, but also to the presence of talc-derived magnesium ions in water that inhibit calcite precipitation.

Our experimental data support the idea that talc-bearing mature fault zones in carbonates are mechanically weak, remain weak over geologic time periods and fail via stable, aseismic creep, even if talc is present in limited amounts.

Acknowledgments

This research was carried out within the ERC Starting Grant GLASS (n° 259256). We thank Alexandre Schubnel, Andre Niemeijer, and one anonymous reviewer whose comments

helped strengthen this manuscript. We also thank Telemaco Tesei, Giuseppe Di Stefano, Andrea Cavallo and Daniele Cinti for fruitful discussions and assistance in the laboratory.

1.6. Supporting information

Auxiliary material for this article contains:

- grain-size characterization of starting materials (Figures S1 and S2);
- strain and displacement values at which peak friction and steady-state friction are measured (Figure S3);
- measurements of compaction and dilation percentage during slide-hold-slide sequences (Figures S4 and S5);
- chemical analysis on bench-top solution of talc in $CaCO_3$-equilibrated water (Table S1).

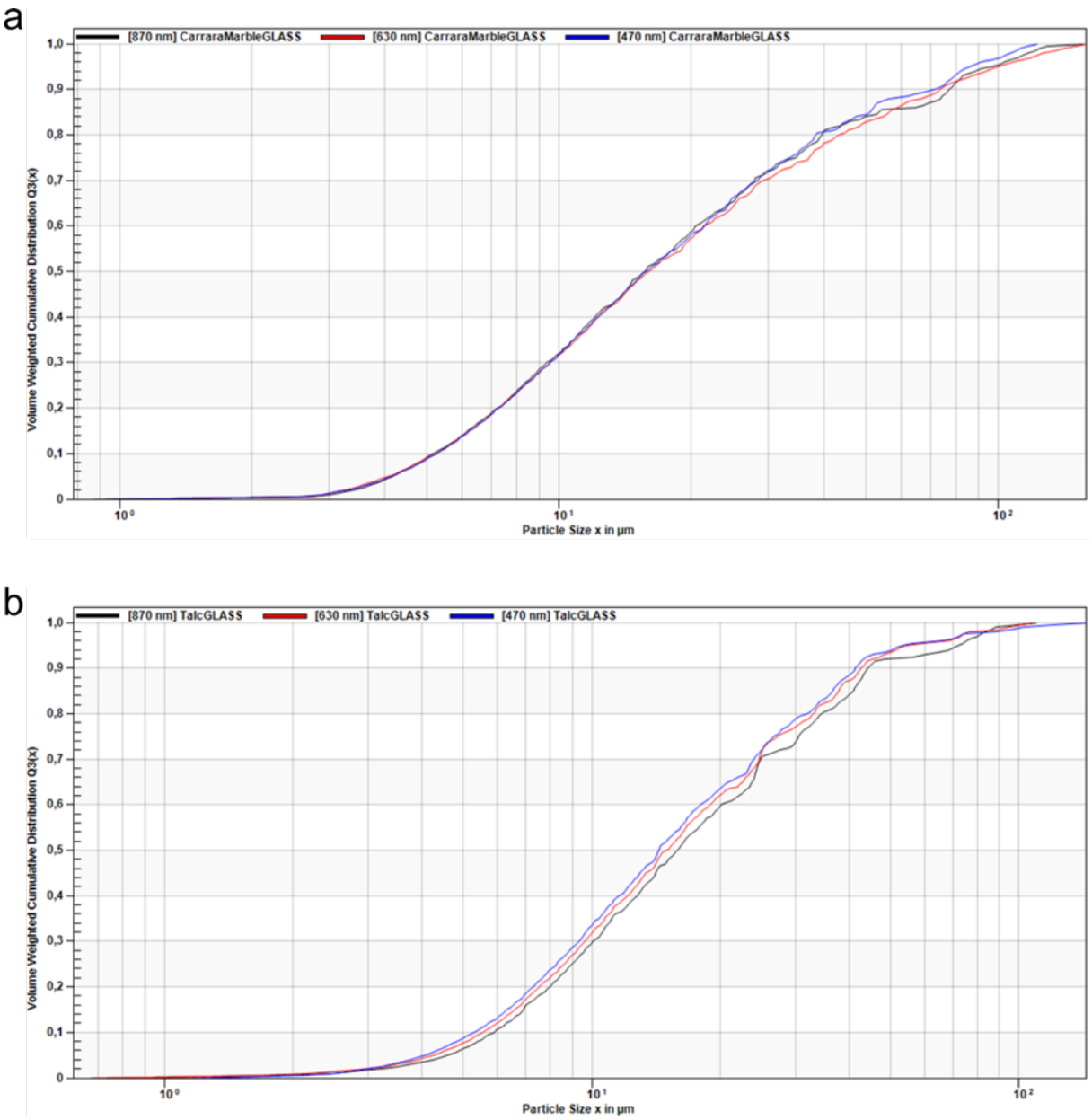

Figure S1. Volume weighted particle size distribution of starting material, namely (a) Carrara Marble powder and (b) talc powder. Analysis was conducted with a Separation Analyzer LUMiReader.

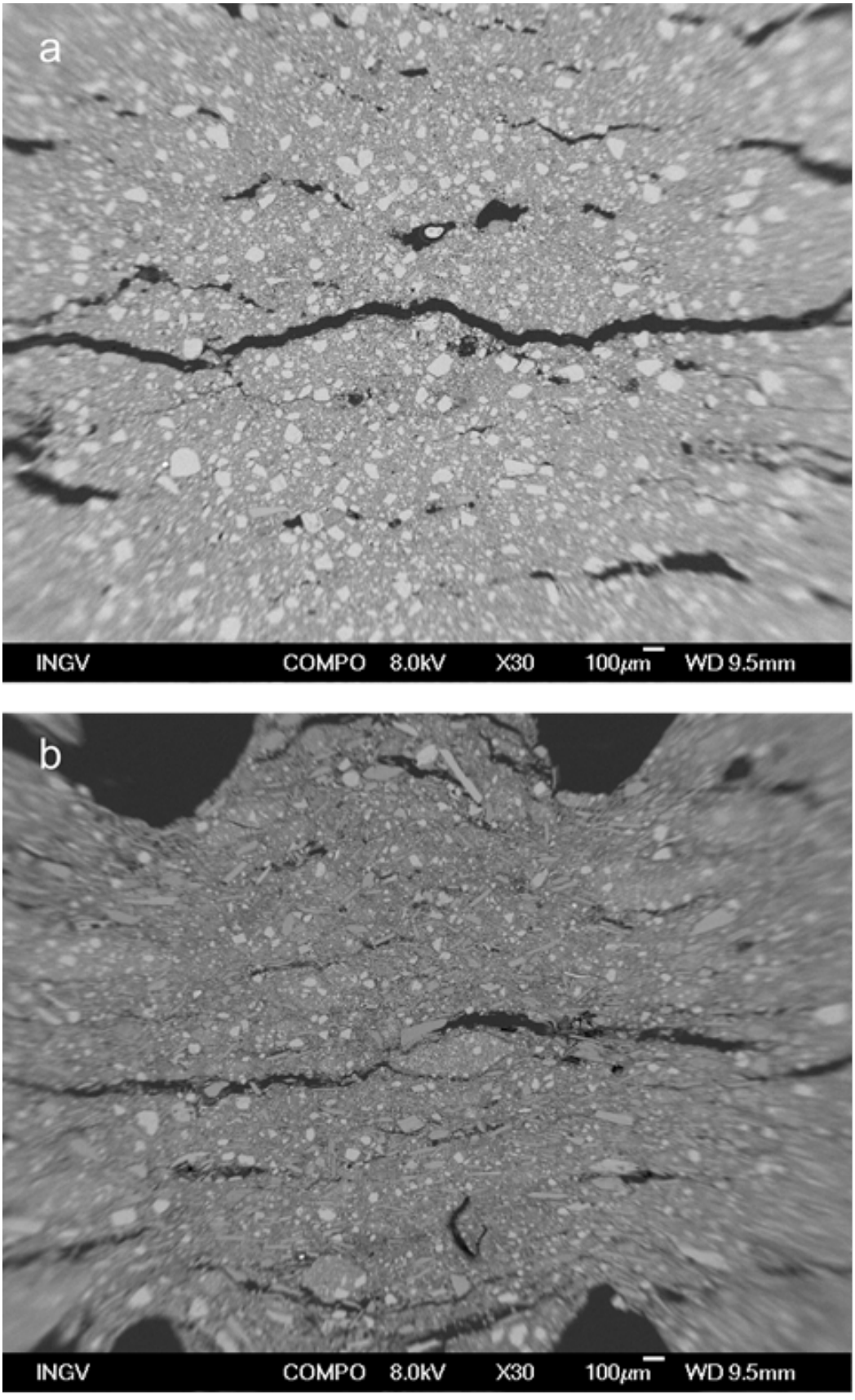

Figure S2. SEM micrograph showing 5% talc gouge (a) and 50% talc gouge (b) subjected to only 5 MPa normal load.

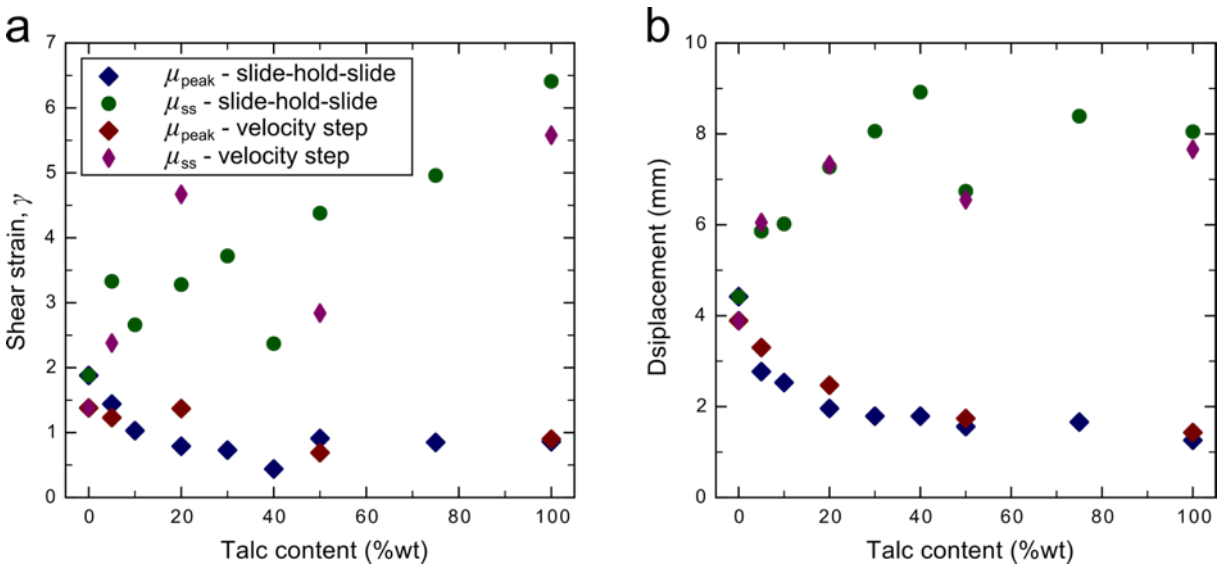

Figure S3. a) Shear strain at which peak and steady-state (measured at the onset of a steady-state sliding) friction values, reported in Figure 2, were measured. b) Displacement at which peak and steady-state friction are measured.

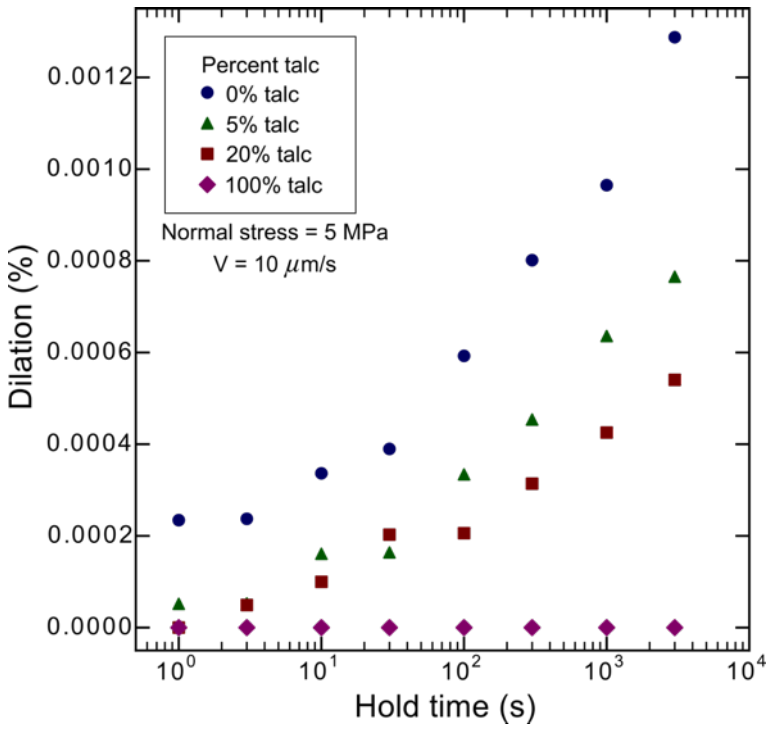

Figure S4. Percentage of layer dilation as function of hold time for different talc contents in experiments carried out at sliding velocity of 10 μm/s and at constant normal stress of 5 MPa. The value of dilation is calculated dividing the difference between the layer thickness before (minimum value reached during the hold period) and after the re-shear (maximum value reached upon re-shear) by the layer thickness before the re-shear. The calcite gouge shows high dilation (0.0013% during 3000 s hold). Adding talc dilation decreases towards zero values, characterizing the pure talc sample.

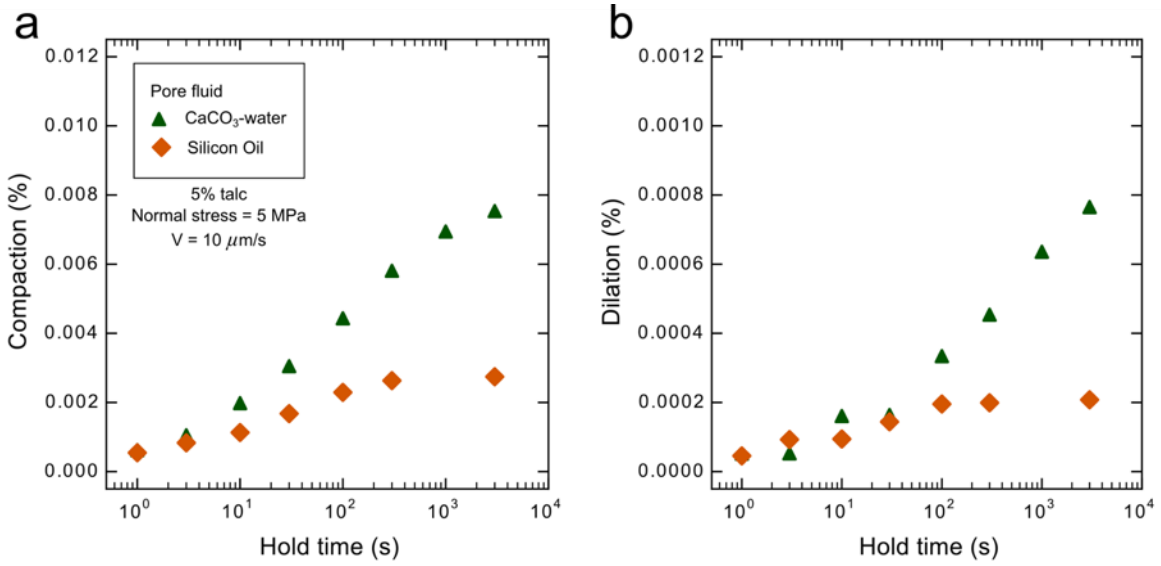

Figure S5. (a) Percentage of layer compaction as function of hold time for different pore fluids in 5% talc sample. The value of compaction is calculated dividing the difference between the layer thickness right before the beginning and right before the end of an hold period by the layer thickness right before the beginning of an hold. Compaction results enhanced by the presence of $CaCO_3$-water. (b) Percentage of layer dilation as function of hold time for different pore fluids in 5% talc sample. The value of dilation is calculated as in Figure S3. Experiments carried out at sliding velocity of 10 μm/s and at constant normal stress of 5 MPa. Dilation results enhanced by the presence of $CaCO_3$-water.

Sample	F^- (mg/l)	Cl^- (mg/l)	NO_3^- (mg/l)	SO_4^{2-} (mg/l)	HCO_3^- (mg/l)	Na^+ (mg/l)	K^+ (mg/l)	Mg^{2+} (mg/l)	Ca^{2+} (mg/l)
DI water	0.01	0.39	0.46	0.11	n.d.	3.21	0.92	0.17	0.40
$CaCO_3$-equilibrated water	0.13	1.32	0.43	3.56	n.d.	2.52	1.09	1.63	12.79
$CaCO_3$-water + talc (4.5h)	0.15	1.80	0.69	3.83	67.10	3.93	1.89	4.73	10.91

Table S1. Chemical analysis of DI water, $CaCO_3$-equilibrated, deriving from DI water and used to saturate our experiments, and a solution of $CaCO_3$-water and talc. The latter was analyzed in order to understand if at room temperature in our experiments the release of magnesium ions is plausible. We decided to mix talc and $CaCO_3$-water at room temperature on the bench-top and check if a change in water chemistry happens. We added 10.10g to 160 ml of CaCO3-water, we mixed and closed the mixture. After 4.5 hours we filtered the talc and we analyzed the water. After 4.5 hours, a time span comparable with our experiments duration, the water contains a considerably higher content of magnesium ions. Thus, the release of magnesium ions is possible on the bench, and probably it is enhanced under shear conditions.

Chapter 2.
Fault geometry and mechanics of marly carbonate multilayers: an integrated field and laboratory study from the Northern Apennines, Italy

Abstract

Sealing layers are often represented by sedimentary sequences characterized by alternating strong and weak lithologies. When involved in faulting processes, these mechanically heterogeneous multilayers develop complex fault geometries. Here we investigate fault initiation and evolution within a mechanical multilayer by integrating field observations and rock deformation experiments. Faults initiate with a staircase trajectory that partially reflects the mechanical properties of the involved lithologies, as suggested by our deformation experiments. However, some faults initiating at low angles in calcite-rich layers (θ_i = 5°-20°) and at high angles in clay-rich layers (θ_i = 45°-86°) indicate the important role of structural inheritance at the onset of faulting. With increasing displacement, faults develop well-organized fault cores characterized by a marly, foliated matrix embedding fragments of limestone. The angles of fault reactivation, which concentrate between 30° and 60°, are consistent with the low friction coefficient measured during our experiments on marls (μ_s = 0.39), indicating that clay minerals exert a main control on fault mechanics. Moreover, our integrated analysis suggests that fracturing and faulting are the main mechanisms allowing fluid circulation within the low-permeability multilayer, and that its sealing integrity can be compromised only by the activity of larger faults cutting across its entire thickness.

2.1. Introduction

The presence of directional heterogeneity (anisotropy) (e.g., *Peacock and Sanderson*, 1992) in sealing layers strongly affects their mechanical and hydrological properties. Low-permeability layers, acting as efficient seals, are often represented by sedimentary sequences characterized by the alternation of weak, clay-rich lithologies, e.g., marl and shale, and strong lithologies, e.g., sandstone and limestone. Directional heterogeneity is possibly associated with mechanical stratigraphy, defined as the presence in a given formation of stratigraphic layers with different mechanical properties (e.g., *Corbett et al.*, 1987; *Wilkins and Gross*, 2002). Within multilayers, these competence contrasts have a key role in fault initiation and growth (e.g., *Peacock and Sanderson*, 1992; *Schöpfer et al.*, 2006; *Schöpfer et al.*, 2007; *Ferrill and Morris*, 2008; *Childs et al.*, 2009; *Roche et al.*, 2012). In the incipient phase, faults hosted in multilayers develop a staircase trajectory with plane refraction at competence contrasts. This staircase trajectory results in a variable fault orientation that can be described by the angle of fault initiation. The angle of fault initiation θ_i is defined as the angle between the maximum principal stress and the fault plane and it depends on the failure strength of the faulted rocks (*Anderson*, 1951). In a mechanical multilayer, the strength heterogeneity results in different θ_i values within each different stratigraphic layer. The overall strength of a layer can also be influenced by the presence of pre-existing cohesionless surfaces, such as joints, that can further deflect the trajectory of the fault and thus change the θ_i value (e.g., *Peacock and Sanderson*, 1992; *Crider and Peacock*, 2004; *Roche et al.*, 2012). Furthermore, an additional directional heterogeneity is related to the intrinsic anisotropy of weak layers, i.e., the planes of weakness resulting from rock foliation (e.g., *Shea and Kronenberg*, 1993; *Massironi et al.*, 2011; *Bistacchi et al.*, 2012; *Misra et al.*, 2015). Deformation experiments on intact rocks show that the orientation of foliation with respect to the maximum principal stress strongly influences the strength of the rocks (e.g., *Jaeger*, 1960; *Donath*, 1961; *Jackson and Dunn*, 1974; *McCabe and Koerner*, 1975, *Bolognesi and Bistacchi*, 2016). Shear fractures in foliated rocks, developed during triaxial experiments, may reactivate the planes of weakness, even when the maximum principal stress is inclined at high angles, such as 45°-60°, to the pre-existing surface (*Donath*, 1961).

In the first stages of growth, slip along staircase faults causes the development of dilational jogs within competent layers (e.g., *Sibson*, 1996). The presence of dilational jogs has strong implications on fluid circulation in low-permeability multilayers, often promoting fluid flow in the direction parallel to the intersection of the fault plane and the bedding (e.g., *Sibson*, 1996; *Ferrill and Morris*, 2003). Structural studies on the distribution of displacement in

mechanical multilayers are essential in order to better understand fluid flow properties within fault zones (e.g., *Manzocchi et al.*, 2008; *Childs et al.*, 2009; *Manzocchi et al*., 2010). However, most of the previous field-based studies have only given a detailed geometrical description of complex faults within mechanical multilayers (e.g., *Peacock and Sanderson*, 1992; *Nicol et al.*, 1996; *Gross et al.*, 1997; *Wilkins and Gross*, 2002; *Soliva and Benedicto*, 2005; *Schöpfer et al.*, 2006; *Antonellini et al.*, 2008; *Ferrill and Morris*, 2008; *Childs et al.*, 2009; *Ferrill et al.*, 2011; *Roche et al.*, 2012; *Kristensen et al.*, 2013), while a complementary mechanical characterization is still lacking. In this paper we integrate field observations with rock deformation experiments to investigate fault evolution within a mechanical multilayer consisting of alternating limestones and clay-rich marls. We aim to better characterize the role of mechanical properties on the overall deformation style and fluid circulation.

2.2. Geological framework

We studied outcrops of faulted multilayers located in the northeastern limb of the Monte Montiego Anticline (Figure 2.1) in the Umbria-Marche Apennines that represent the outer part of the Northern Apennines (e.g., *Bally et al.*, 1986; *Barchi et al.*, 2012). The Northern Apennines are a complex, arc-shaped fold-and-thrust belt having an overall northeastward convexity and vergence (e.g., *Carmignani et al.*, 2001; *Barchi et al.*, 2001), developed in the framework of the Europe-Africa convergence (e.g., *Reutter et al.*, 1980; *Alvarez*, 1991; *Doglioni et al.*, 1998; *Carminati and Doglioni*, 2012). The Umbria-Marche Apennines are characterized by large asymmetric anticlines overturned eastward on tight synclines with fold axes trending NW-SE (e.g., *Abbate et al.*, 1970; *Lavecchia et al.*, 1988). Locally, the Monte Montiego Anticline has a fold axis trending WNW-ESE (*Engelder*, 1984).

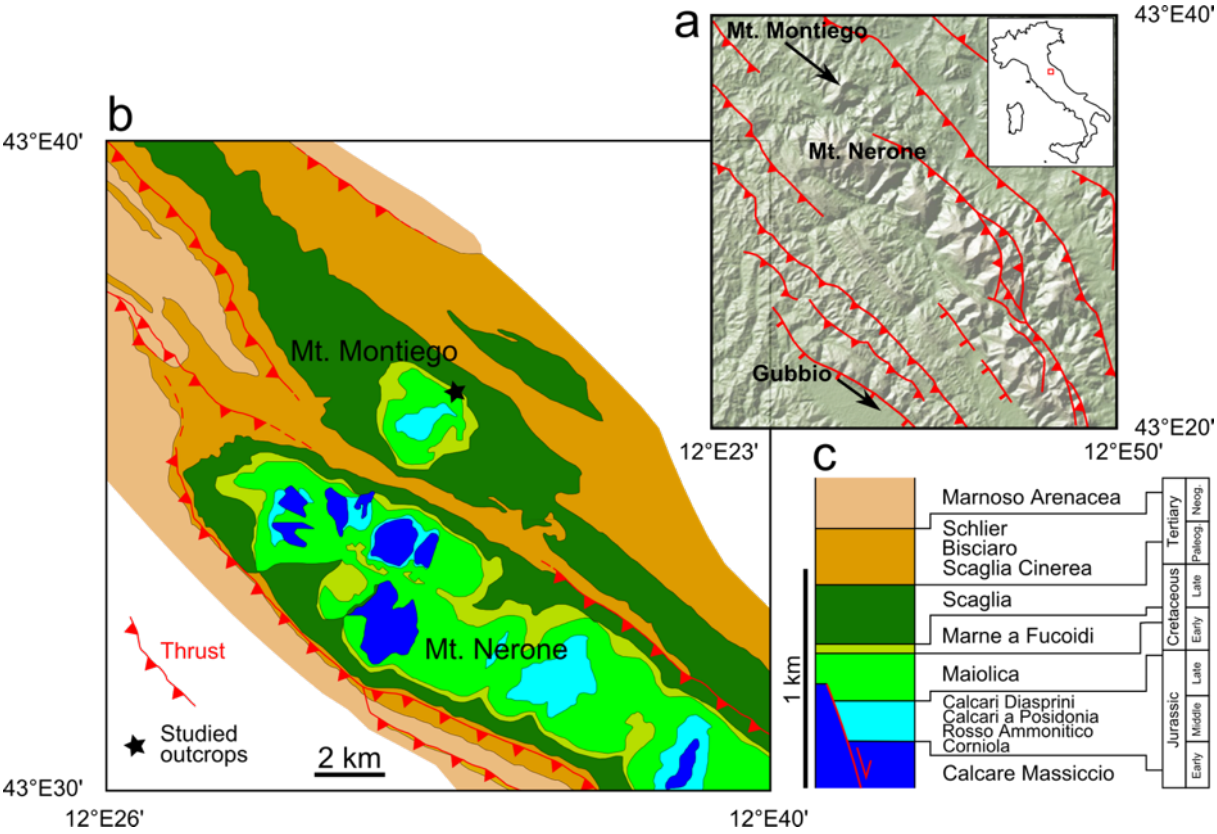

Figure 2.1. (a) Digital elevation model of the Northern Umbria-Marche Apennines created using GeoMapApp (http://www.geomapapp.org) displaying traces of main thrusts and normal faults. (b) Geological map of Mt. Montiego anticline area (after *Centamore et al.*, 1972; *Capuano et al.*, 2009), showing the location of the studied outcrops. (c) Stratigraphic succession in the study area.

The Mesozoic carbonates are folded coherently with the compressional regime and they are also affected by small-scale faulting. Specifically, we studied mesoscale faults showing subvertical dips with displacements ranging from less than 1 cm up to ~20 m. Kinematic indicators, i.e., bedding offsets, drag folds, and subhorizontal slickenfibers, indicate a strike-

slip movement. The relationship of fault-bedding intersections and the sense of displacement are consistent with fold-axis-parallel extension (e.g., *Marshak et al.*, 1982). Strike-slip faults are commonly found in fold-and-thrust belts (e.g., *Sylvester*, 1988; *Hindle and Burkhard*, 1999), including the anticlines of the Umbria-Marche Apennines (e.g., *Marshak et al.*, 1982; *Barchi et al.*, 1993). Moreover, a previous study (*Marshak et al.*, 1982) in the same area of the Apennines proposed that the activity of strike-slip faults is, at least in part, contemporaneous with the formation of the anticline.

The studied faults developed within the Lower Cretaceous Marne a Fucoidi Formation. The lithology of the Marne a Fucoidi Formation is highly variable in terms of composition, with $CaCO_3$ content ranging from 4% to 75% (*Giorgioni et al.*, 2017; *Li et al.*, 2016). The remaining percentage is made of a homogeneous clay mineral assemblage consisting of ~50% smectite, ~30% illite and ~20% mixed layer illite-smectite (*Coccioni et al*., 1989). The Marne a Fucoidi Formation is also highly variable in terms of thickness and spacing of competent limestone layers (e.g., *Tornaghi et al.*, 1989; *Coccioni et al.*, 1989). The high lithological variability of this formation results in high variability of mechanical properties, thus defining mechanical multilayers, prone to develop complex fault geometries. Despite this high variability, the alternation of layers with higher and lower $CaCO_3$ content is always evident. In the present work, we define competent layers as those characterized by relatively high $CaCO_3$ content and incompetent layers as those characterized by low $CaCO_3$ content and the presence of sedimentary foliation.

2.3. Investigation methods

2.3.1. Theoretical framework for field observations

We studied the along-strike geometry of outcropping faults with increasing displacement from less than 1 cm to a few meters in order to reconstruct the initiation and early stages of faulting. Additionally, we studied a single fault with an apparent displacement (separation) of about 20 m to evaluate a more mature fault stage.

The mechanical characterization of the mapped faults is based on geometrical relationships between the slipping surfaces and the local stress field orientation. Fault initiation can be evaluated by using the Coulomb failure criterion (*Coulomb*, 1776):

$$\tau = c+\mu_i(\sigma_n - P_f) \quad (2.1)$$

where τ is the shear stress, σ_n is the normal stress on the failure plane, P_f is the fluid pressure, c is the cohesive strength and μ_i is the internal friction of the intact rock. The angle θ_i between the fault and the maximum principal stress σ_1 is defined as (e.g., *Anderson*, 1951; *Mandl*, 1988)

$$\theta_i = 45 - \frac{\varphi_i}{2} \quad (2.2)$$

where φ_i is the angle of internal friction, related to μ_i through the relation μ_i = tan φ_i. Amontons' law defines the shear stress necessary to reactivate a pre-existing, cohesionless fault (e.g., *Jaeger and Cook*, 1979) as follows:

$$\tau = \mu_s(\sigma_n - P_f) \quad (2.3)$$

where μ_s is the coefficient of sliding friction of the surface. The angle between the fault and the maximum principal stress σ_1 is defined as the angle of fault reactivation, θ_r.

We used both the geometry and the kinematics of the mapped faults to reconstruct the orientation of the stress field. The kinematic analysis was conducted through the linked Bingham distribution method (*Marrett and Allmendinger*, 1990), using all the calcite slickenfibers and striae with a strike-slip component (rakes <45°). Assuming a pure shear deformation, the resulting strain axes can be considered parallel to the stress axes. The pure shear assumption is reasonable for the studied outcrops since the fault system is characterized by small conjugate strike-slip faults occurring in a tectonic regime of shortening (e.g., *Sylvester*, 1988). We also reconstructed the local stress field for each single outcrop considering σ_3 perpendicular to extensional fractures, σ_2 parallel to the intersection of conjugate faults and σ_1 perpendicular to the plane containing σ_2 and σ_3. The direction of σ_2

was further constrained with the hinges of drag folds that, assuming a σ_1 perpendicular to the bedding (e.g., *Ramsay and Huber*, 1987), are parallel to the σ_2.

We used the local stress field of each outcrop to estimate the angle of fault initiation θ_i for small displacement faults, i.e., < 1 cm, whereas the reconstructed "regional" stress field resulting from the linked Bingham distribution method was used to estimate the angles of fault reactivation θ_r for large displacement faults, i.e., > 1 cm. We chose this threshold value because faults with displacement larger than ~1 cm are characterized by different geometry in respect to smaller faults.

2.3.2 Laboratory investigations

We performed rock deformation experiments on samples collected from the studied outcrops mentioned above, in exposures not affected by faulting. Marl cohesion is significantly lower than limestone cohesion (e.g., *Marinos and Hoek*, 2001) and foliation planes represent surfaces of almost zero cohesion. Thus, we designed experiments in different configurations (Table 2.1). Intact rock samples were collected from competent layers (~70-80 wt.% of $CaCO_3$, Table 2.1) to perform triaxial deformation experiments on cylindrical samples. Incohesive rock samples were collected from incompetent marly layers (59 wt.% of $CaCO_3$, Table 2.1) and powdered to perform biaxial friction experiments. We estimated a $CaCO_3$ content of ~80 wt.% in the competent limestone and ~60 wt.% in the incompetent marl (Table 2.1). Excluding the samples with chert nodules, the remaining weight reflects the amount of clay minerals, i.e., ~20% in competent limestone and ~40% in incompetent marl. Given the negligible cohesion, we assumed that the maximum shear strength of powdered marl represents a good proxy for strength of the parent intact rock.

Both triaxial and biaxial experiments were performed in a servo-controlled biaxial deformation apparatus installed in the High Pressure-High Temperature Laboratory at the INGV in Rome, Italy (Figure 2.2). This apparatus is equipped with a pressure vessel, that allows for the application of confining pressure and pore fluid pressure (Figure 2.2a) (*Collettini et al.*, 2014b). Vertical and horizontal loads are controlled and measured using load cells with 0.03 kN accuracy and positioned within the pressure vessel. Vertical and horizontal displacements are controlled and measured through Linear Variable Differential Transducers (LVDTs) sensors with 0.1 μm accuracy. The pressure vessel is equipped with two removable doors, both sealed with O-rings to prevent confining oil leakage. High-pressure ports allow

the communication between the sample assembly and up- and down- stream pressure intensifiers (Figure 2.2a).

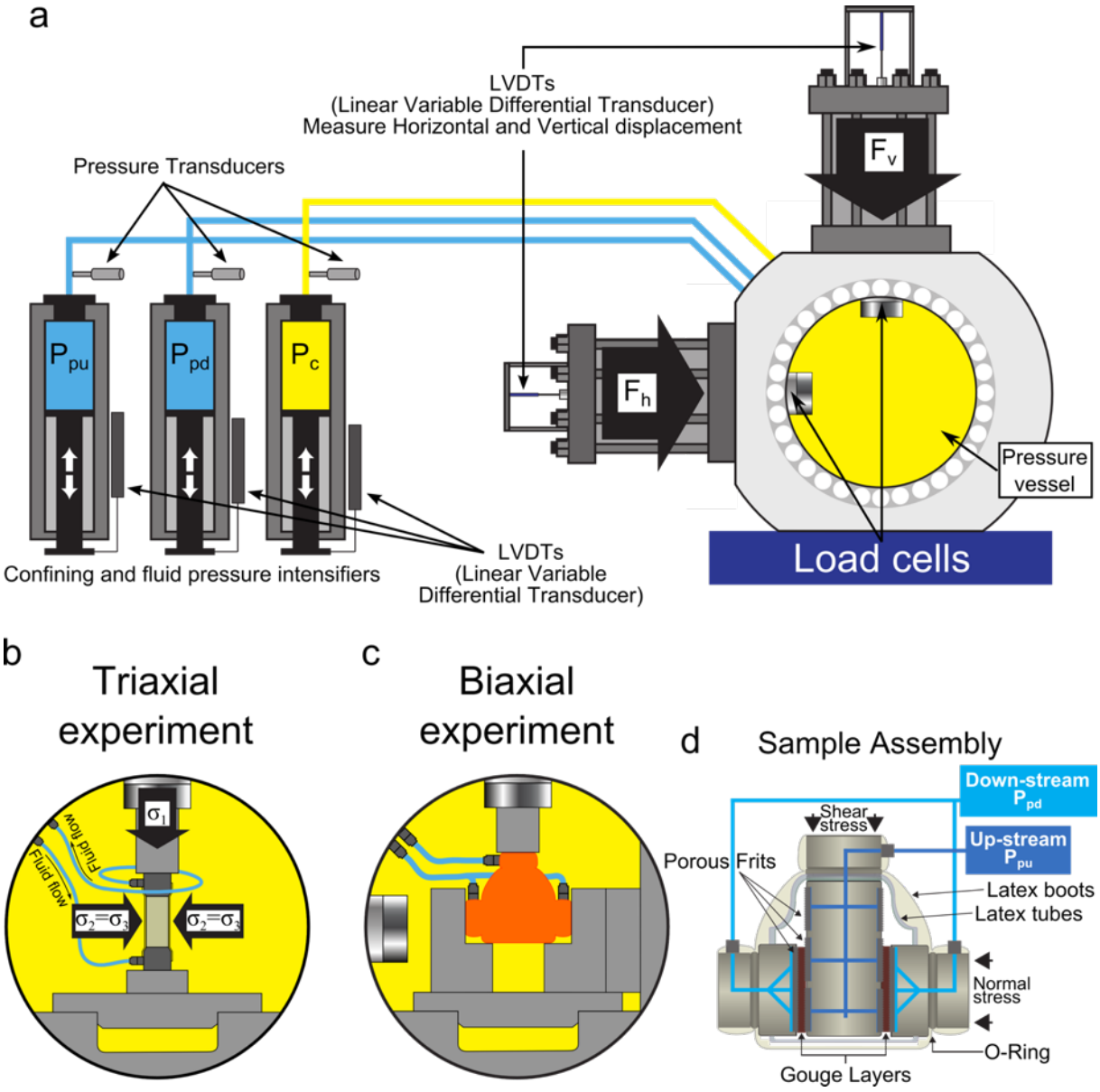

Figure 2.2. (a) The BRAVA rock deformation apparatus (after *Scuderi and Collettini*, 2016): two load cells, measuring vertical (F_v) and horizontal forces (F_h), are located within the pressure vessel designed to support the vertical and the horizontal pistons. Two high-pressure ports allow the communication between the sample assembly and the up- and down-stream pressure intensifiers. One high-pressure access port allows the communication between the pressure vessel and the confining oil intensifier. (b) Triaxial configuration within the pressure vessel. Confining oil is used to apply an isotropic pressure ($\sigma_3 = \sigma_2$) and the vertical loading frame applies a vertical force generating a differential stress. Pore pressure lines show the direction of the fluid flow during the experiment. (c) Double direct shear configuration within the pressure vessel and (d) a schematic representation of the configuration contained within the jacket (orange in figure c). In this configuration three stainless steel forcing blocks sandwich two identical layers of experimental fault gouge. The sample assembly consists of forcing blocks, equipped with internal channels for pore fluids, porous frits and rubber jacket (latex tubes and boots).

Similarly, a third pressure intensifier is connected to the pressure vessel to apply confining pressure. Pore fluid pressure is applied using tap water as a fluid and confining pressure via a

confining oil, i.e., 13,8660 VE 15–68 Vaselina Enologica (Green Star High Tech lubricant sand additives). Pressure values of the intensifiers are monitored through pressure transducers with 7 kPa accuracy. Displacement values of the intensifiers are monitored using LVDT sensors with 0.1 μm accuracy. Pore pressures and confining pressure are servo-controlled. During each experiment, forces, pressures and displacements were continuously acquired using a 24-bit analog to digital system and recorded at a frequency ranging between 1 - 10 Hz, depending on the loading velocity imposed on the vertical piston.

Table 2.1. Details of the experiments performed.

Experiment number	Material	$CaCO_3$ content[a] (wt.%)	Configuration	Applied stresses (MPa)	Deformation velocity[b] (μm/s)
i424	marly limestone	83	triaxial	P_c = 10	V_a = 0.1
i426	marly limestone	83	triaxial	P_c = 20	V_a = 0.1
i431	marly limestone	83	triaxial	P_c = 30	V_a = 0.1
i432	marly limestone with chert	72	triaxial	P_c = 10	V_a = 0.1
i435	marly limestone with chert	72	triaxial	P_c = 20	V_a = 0.1
i436	marly limestone with chert	72	triaxial	P_c = 30	V_a = 0.1
i469	marls	59	biaxial	P_c = 15 σ_n = 20	V_s = 10
i485	marls	59	biaxial	P_c = 15 σ_n = 30 - 40 -50	V_s = 10

[a] $CaCO_3$ content determined using a Dietrich-Fruhling calcimeter. [b] axial velocity (v_a) in triaxial experiments and sliding velocity (v_s) in biaxial experiments.

2.3.2.1 Triaxial deformation experiments

We conducted triaxial compression experiments on cylindrical samples 38 mm in diameter and 76 mm in length, which were cored from two intact blocks in an orientation perpendicular to the layering. The two intact blocks come from two different competent layers consisting of thinly-bedded marly limestone (72 wt.% and 83 wt.% of $CaCO_3$, Table 2.1). One of these two blocks contains a level enriched in small chert nodules. To estimate the porosity, our samples

were dried for 96 h at a temperature of 60° and then saturated with tap water under vacuum for one week. We calculated the porosity as follows:

$$\phi = \frac{V_p}{V_t} \tag{2.4}$$

where V_p is the volume of interconnected pores, calculated as the difference in weight between the saturated and dried sample multiplied by the density of water, and V_t is the sample's total volume.

The cylindrical sample was placed in-between two stainless steel end platens, equipped with internal channels for fluid flow (Figure 2.2b). The sample was jacketed with a poly-olefin heat-shrink tube and sealed with steel wires at the extremities to prevent oil from entering into the sample. The internal channels of the two end platens were connected to two access ports, through pore pressure lines, to allow the application of up- and down-stream pore pressures. We ran three experiments at different values of confining pressure and room temperature for each of the two tested lithologies (details in Table 2.1). We used the following procedure in all the triaxial experiments. We began by applying a constant confining pressure (P_c), with values of 10, 20 and 30 MPa. Then the differential stress was increased, imposing a constant axial strain rate of 1.3×10^{-6} s^{-1} by moving the vertical piston at a constant displacement rate of 0.1 μm/s. To evaluate fracture-enhanced permeability, we imposed different values of pore pressure between the up- and down- stream ends, i.e., 2 MPa and 1 MPa, respectively. Since the initial porosity of the tested samples was ~4%, as calculated from Equation 2.4, fluid flow through the samples was observed only after failure when fractures developed from the bottom to the top of the samples. Consequently, we considered pore pressure to be zero ($P_f = 0$) within the sample throughout the experiment.

The axial strain was evaluated after correcting the values of the vertical load point displacement for the machine stiffness on the vertical axis that, depending on the confining pressure, ranged between 791.1 kN/mm and 781.1 kN/mm. The resulting stress field acting on the sample during the experiment consisted of horizontal $\sigma_2 = \sigma_3 = P_c$ and vertical $\sigma_1 = P_c + \sigma_d$, where σ_d is the differential stress (Figure 2.2b). The effective mean stress, considering the pore pressure $P_f = 0$, acting on the sample is given by

$$\sigma_m = \frac{\sigma_1 + 2\sigma_3}{3} \tag{2.5}$$

In the framework of critical state soil mechanics (e.g., *Schofield and Wroth*, 1968), the peak differential stress shows a positive correlation with the effective mean stress, typical of

brittle failure described by a Mohr-Coulomb failure envelope (e.g., *Paterson and Wong*, 2005) that can be fitted by the following linear equation

$$\sigma_d = C + M\sigma_m \quad (2.6)$$

The parameters of equation 2.6 are related to the cohesion c and the friction μ_i of the Coulomb failure criterion (Equation 2.1) as follows (e.g., *Bolton*, 1979)

$$M = \frac{6\sin\varphi_i}{3-\sin\varphi_i};\ C = \frac{6c\cos\varphi_i}{3-\sin\varphi_i} \quad (2.7)$$

Following equations 2.6, 2.7 and 2.2 we estimated and compared the experimentally derived values of θ_i with the values of θ_i measured in the studied outcrops.

2.3.2.2 Biaxial deformation experiments

We conducted biaxial deformation experiments in a double-direct shear configuration on powders prepared from outcropping marls (59 wt.% of $CaCO_3$, Table 2.1) that were crushed and sieved to < 125 μm grain size. In this configuration, two layers of powdered marl were sandwiched in a three steel block assembly (Figure 2.2c). The experiments were run within the pressure vessel to apply confining pressure (*Scuderi and Collettini*, 2016 for additional details). Sintered stainless steel frits were placed within the blocks in contact with the gouge layers to allow homogeneous fluid distribution over the entire area of the sample. To isolate the gouge layers from the confining oil, the sample assembly was jacketed (Figure 2.2d) as described in the following procedure. First the assembly was covered and taped with a rubber sheet to protect the layers. Then the assembly was covered with two layers of latex tube in order to prevent frits of the central block from cutting the external jackets. Finally the sample assembly was encapsulated within two custom-made latex boots and sealed with steel wires placed where the forcing blocks are equipped with O-rings. The sample assembly, equipped with internal conduits for pore fluids (Figure 2.2d), was connected, through pore pressure lines, to three access ports to allow for the application of up- and down-stream pore pressures.

We ran two experiments at a confining pressure of 15 MPa (Table 2.1). One sample was sheared at a normal stress of 20 MPa for ~1.6 cm of displacement. Another experiment was performed shearing the layers at different normal stresses ranging from σ_n = 30 MPa to σ_n = 50 MPa, for a total displacement of ~1.4 cm. We used the same loading procedure in both the experiments, for comparison purposes. We applied and maintained constant confining pressure throughout the experiment. We then applied an additional horizontal force in order to reach the target value of the normal stress. We saturated the sample with tap water applying

10 MPa up-stream pore pressure, leaving the down-stream side open to the atmosphere until flow-through was established. At this stage, in order to achieve fully saturated boundary conditions but at zero pore pressure, for comparison purposes with the triaxial deformation tests, we decreased the upstream pore pressure to zero. We then opened the downstream pore pressure line to the atmosphere in order to perform the experiment in drained conditions. Additional details on the experimental procedure for the double direct shear configuration within the pressure vessel are reported in *Scuderi and Collettini* (2016). Marly powders were sheared at room temperature and at a constant velocity of 10 μm/s.

The displacement values of the vertical and horizontal load points were corrected for the elastic stretch of each load frame, taking into account that the machine stiffness is 1283 kN/mm on the horizontal axis and 928.5 kN/mm on the vertical axis. The average shear strain within the layer was calculated by progressively summing the shear displacement increments divided by the measured layer thickness.

The peak and steady state shear strength were measured for each normal stress and fitted with a linear regression in order to obtain the parameters in the Coulomb failure criterion and in the Amontons' law (Equation 2.1 and 2.3), thus obtaining the internal friction μ_i and the sliding friction μ_s.

2.4. Structural data

In order to characterize different stages of fault evolution and to reconstruct the related stress field, we studied in detail two outcrops. Outcrop A (Figure 2.3, 302690 N 4830479 E UTM coordinates 33T) is characterized by an overall marl-rich multilayer containing ~3-10 cm thick clay-rich layers with a strong primary foliation. These foliated layers alternate with competent limestone layers that are ~ 3-10 cm thick.

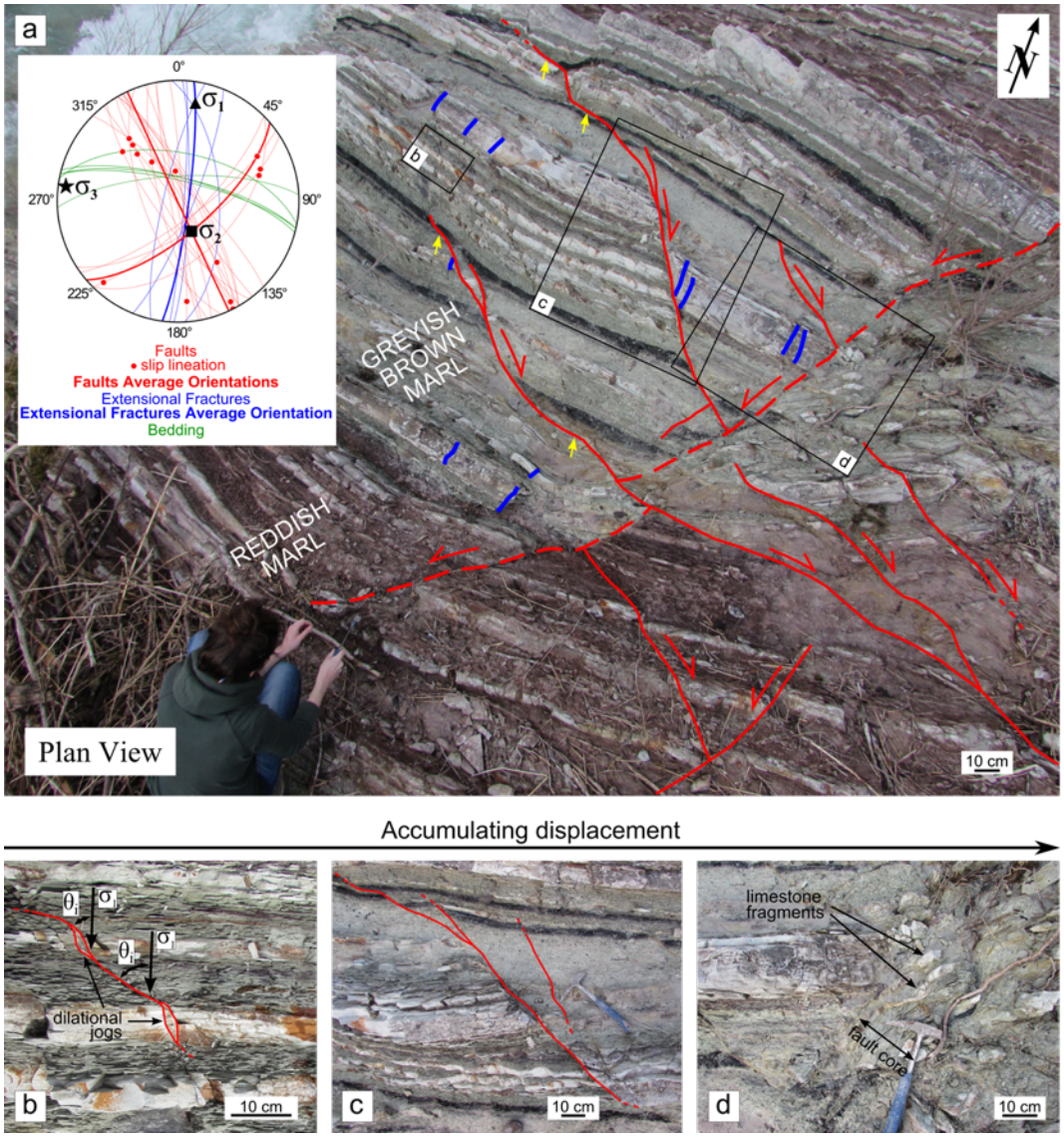

Figure 2.3. (a) Fault system in the marl-rich multilayer (outcrop A, 302690 N 4830479 E UTM coordinates 33T zone). Fault trajectories are complex especially for small displacements. Right-lateral faults, accumulating 1-10 cm of displacement, show undulate trajectories with segments propagating parallel to the layering in clay-rich layers (yellow arrows). The main left-lateral fault (dashed red line), showing 1-2 m of displacement, has an overall straight trajectory refracting at the boundary between the reddish and the greyish brown marly portion. Inset shows the orientation of the local stress field derived from the orientation of extensional fractures and conjugate faults. (b) Incipient fault displaying a staircase trajectory that results in dilational jogs within more competent limestone layers. (c) Fault with about 10 cm displacement displaying an almost straight trajectory in its lower portion; in the uppermost part of the fault, within clay-rich layers, the displacement is partitioned into different splays. (d) The main left-lateral fault in (a) does not refract at competence contrast between single layers and shows an approximately 10 cm wide fault core, characterized by duplexes of competent limestone surrounded by a foliated marly matrix.

Outcrop B (Figure 2.4, 302684 N 4830502 E UTM coordinates 33T zone) is characterized by an overall limestone-rich multilayer where competent limestone layers, ~2-5 cm thick, alternate with foliated marl layers, ~2-5 cm thick. In order to consider a more mature stage of fault evolution, we also studied the largest fault affecting our study area (outcrop C, Figure 2.7, 302628 N 4830455 E UTM coordinates 33T zone), a left-lateral strike-slip fault with a net displacement of about 20 m.

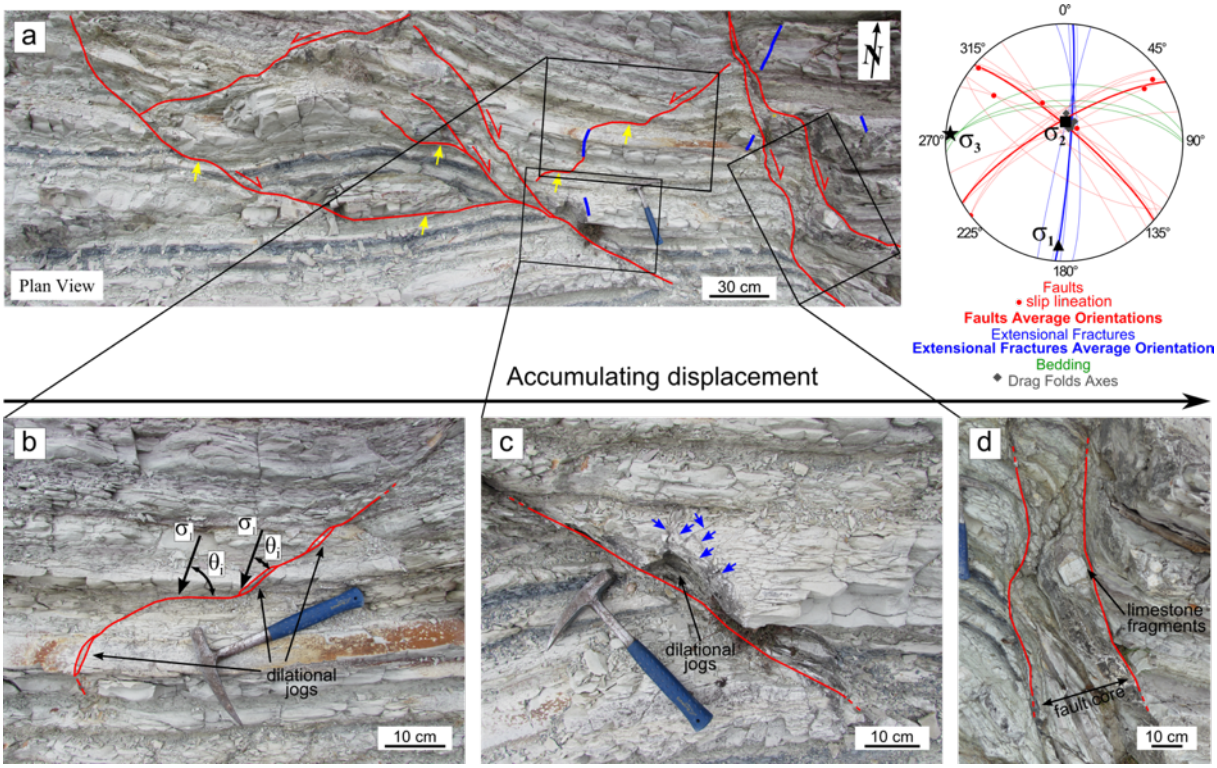

Figure 2.4. (a) Fault system in the limestone-rich multilayer (outcrop B, 302684 N 4830502 E UTM coordinates 33T zone). Fault trajectories are complex especially for small displacements. Faults with ~10 cm of displacement develop segments propagating parallel to the layering in clay-rich layers (yellow arrows). Inset shows the orientation of the local stress field derived from the orientation of extensional fractures and conjugate faults. (b) Fault with a few centimeters of displacement showing refraction at competence contrast with high θ_i values in clay-rich layers and small θ_i values in limestone layers. (c) Fault with displacement of a few decimeters showing a straight trajectory that results from the cutting and reworking of a dilational jog, developing an intensely fractured region (blue arrows). (d) Fault with metric displacement displaying a wide fault core with limestone fragments embedded in clay-rich matrix.

2.4.1. Fault architecture: from incipient to "mature" faults

Faults with displacement of ~1 cm or less develop a staircase trajectory with respect to the orientation of bedding, characterized by fault plane refraction at lithological contrasts (Figure 2.3a-b and 2.4a-b), as previously described in mechanical multilayers (e.g., *Peacock and Sanderson*, 1992; *Wilkins and Gross*, 2002; *Schöpfer et al.*, 2006; *Ferrill and Morris*, 2003;

Childs et al., 2009). Marly layers locally show widespread fractures characterized by conjugate planes with a dihedral angle of ~90° (Figure 2.5).

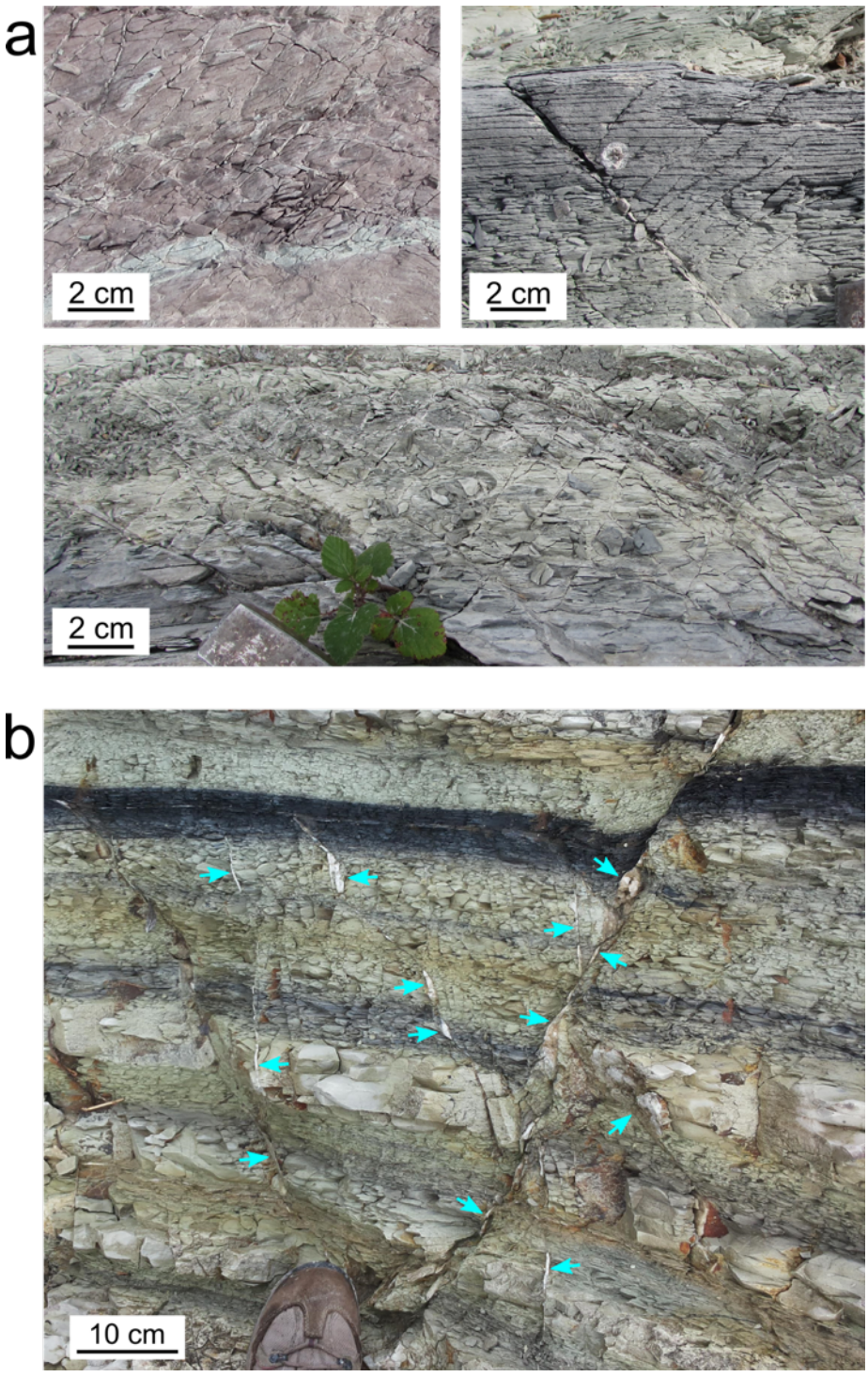

Figure 2.5. Fault initiation in the mechanical multilayer. (a) Local increase of fracturing within marly layers, showing dihedral angles of ~90° between conjugate fracture planes. (b) Fractures propagating throughout the multilayer. All the fractures are filled with calcite mineralization (light blue arrows).

These small shear fractures, with displacement of a few millimeters, are confined within incompetent layers and often do not show calcite mineralization. Contrastingly, all the faults that crosscut more than a single layer are characterized by calcite mineralization (Figure 2.5b

and 2.6). Faults across more competent layers develop a few centimeters thick dilational jogs filled with overlapping layers of calcite slickenfibers or blocky calcite (Figure 2.6a-c; e.g., *Sibson*, 1996; *Ferrill et al.*, 2014). Fault segments running through less competent layers are often marked by calcite veins with a thickness of few millimeters characterized by overlapping layers of slickenfibers (Figure 2.6d).

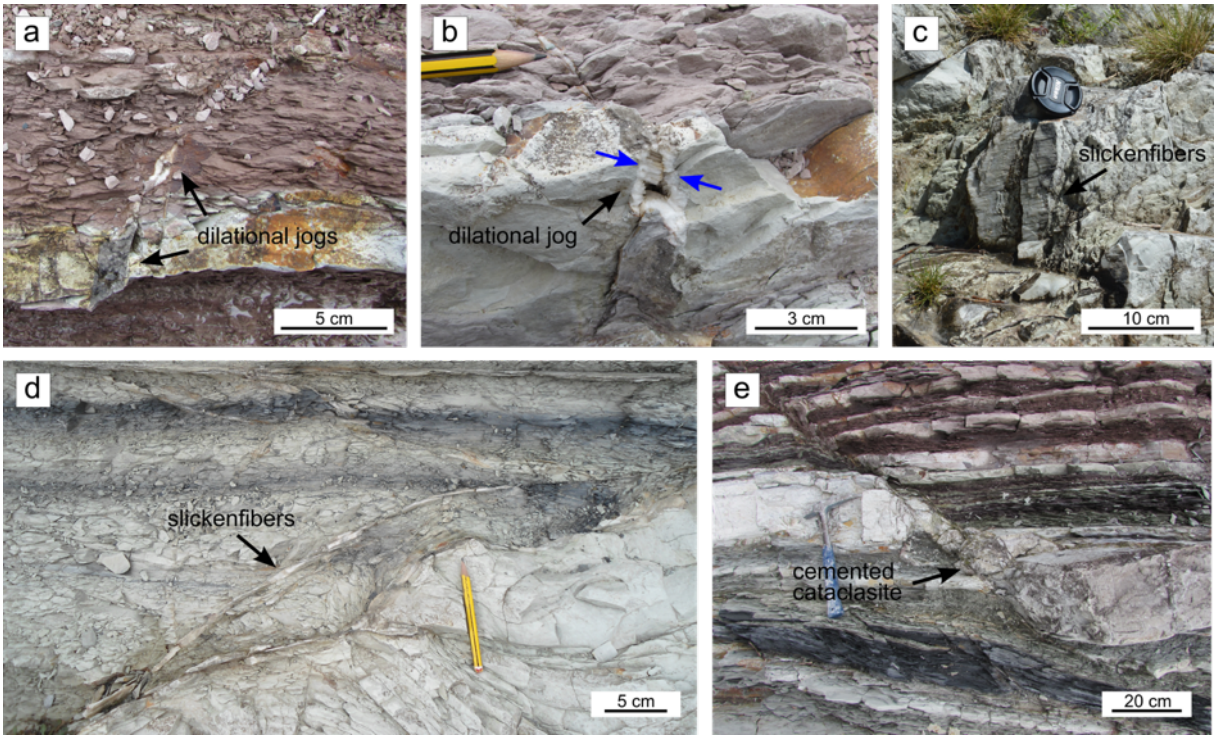

Figure 2.6. Types of calcite mineralization along faults. (a) Dilational jogs filled with blocky calcite. (b) Dilational jog filled with calcite having a growth direction (blue arrows) oblique to the wall of the fracture. (c) Slickenfibers of calcite along a fault cutting a competent layer. (d) Slickenfibers along faults developing in clay-rich layers. (e) Cataclastic fault rock developed from a competent layer, deeply reworked and cemented in a calcite matrix.

With increasing displacement from 1 cm up to 2 m, fault trajectories evolve toward a straighter geometry, with no refraction at competence contrasts at the level of the single bed. Moreover, the fault zones widen up to 10-20 cm in thickness (Figure 2.3c-d and 2.4c-d). Within clay-rich layers, faults tend to partition deformation through the development of numerous splays that ramp through the sedimentary succession (Figure 2.3a and 2.4a). Within competent layers, faults cut and rework dilational jogs (Figure 2.4c) and occasionally contain cataclastic breccias characterized by angular clasts of micritic limestone supported by calcite cement (Figure 2.6e). Faults with ~1-2 m of displacement develop foliated fault cores with a width of 10-20 cm, in which small sigmoidal duplexes of competent limestone are embedded in a marly matrix derived from incompetent layers (Figure 2.3d and 2.4d). Slipping surfaces occurring within fault cores are often marked by slickenfibers. The width of the fault cores varies along the fault structure depending on the displacement, lithology, spacing and

thickness of the competent layers. Where marly layers are predominant, the deformation appears localized within a thin fault core, i.e., ~1-2 cm thick; where thick competent layers are closely spaced, the fault core is 10-20 cm thick and well-developed. The main left-lateral fault in Figure 2.3a has a thin fault zone through the reddish marl, whereas it develops a thicker fault zone cutting across limestone layers (Figure 2.3d). Moreover, the straightness of fault trajectory depends on the amount of displacement and on the scale of the anisotropy: fault trajectory is insensitive to competence contrasts between layers whose thickness is well below the displacement, but it is still sensitive to competence contrasts between different groups of layers. As an example, the trajectory of the main left-lateral fault in Figure 2.3a, that accumulates ~1 m of displacement, is insensitive to anisotropy due to marl-limestone alternation but it is sensitive to the anisotropy of groups of layers since the fault plane refracts at the boundary between the reddish and the greyish brown group of layers resulting in a trajectory deflection of ~13°.

The more mature fault zone observed in the studied outcrops accumulated about 20 m of displacement (Figure 2.7). This fault shows an overall straight trajectory and a wide, up to 45 cm, well-organized foliated fault core, characterized by a SCC' fabric (*Koopman*, 1983) in which a well-developed marly foliation embeds sigmoidal fragments of limestone, up to ~10-20 cm long and a few centimeters thick (Figure 2.7b-c). Despite the slip surface trajectory is relatively straight, the boundaries of the fault zone preserve a staircase shape, likely inherited from the early stages of the fault activity. This structure results in a variable thickness of the fault rock, ranging from 5 to 45 cm (Figure 2.7c). The fault rock is not equally derived from the two blocks involved in the faulting processes. Most of the fault rock consists of reddish marl from the marl-rich group of layers in the hanging-wall (unit A, Figure 2.7), whereas only a thin layer of fault rock, ~ 1 cm thick, derives from the limestone-rich group of layers in the foot-wall block (unit B, Figure 2.7). This thin layer consists of an ultracataclasite mainly developed along boundary shear planes (C plane in Figure 2.7b). The rocks surrounding the fault are intensely deformed: in unit A the deformation is localized along antithetic faults that merge into the main fault zone, whereas unit B is mainly affected by a more distributed fracturing. The observed preservation of the staircase trajectory at the boundary of mature fault cores (Figure 2.4d and 2.7c) suggest a mechanism that deactivates the slipping surfaces in between the two steps developing a straight surface immediately next to them, causing progressive strain localization in the fault core. The strong asymmetry of deformation in Unit A and Unit B in proximity of the more mature fault zone (Figure 2.7) implies that, starting from a staircase trajectory in the more competent Unit B, where the boundary is sharp (Figure

2.7c), the fault growth propagates within the less competent Unit A producing a wide damage zone (e.g., *Ferrill et al.*, 2011; *Ferrill et al.*, 2012).

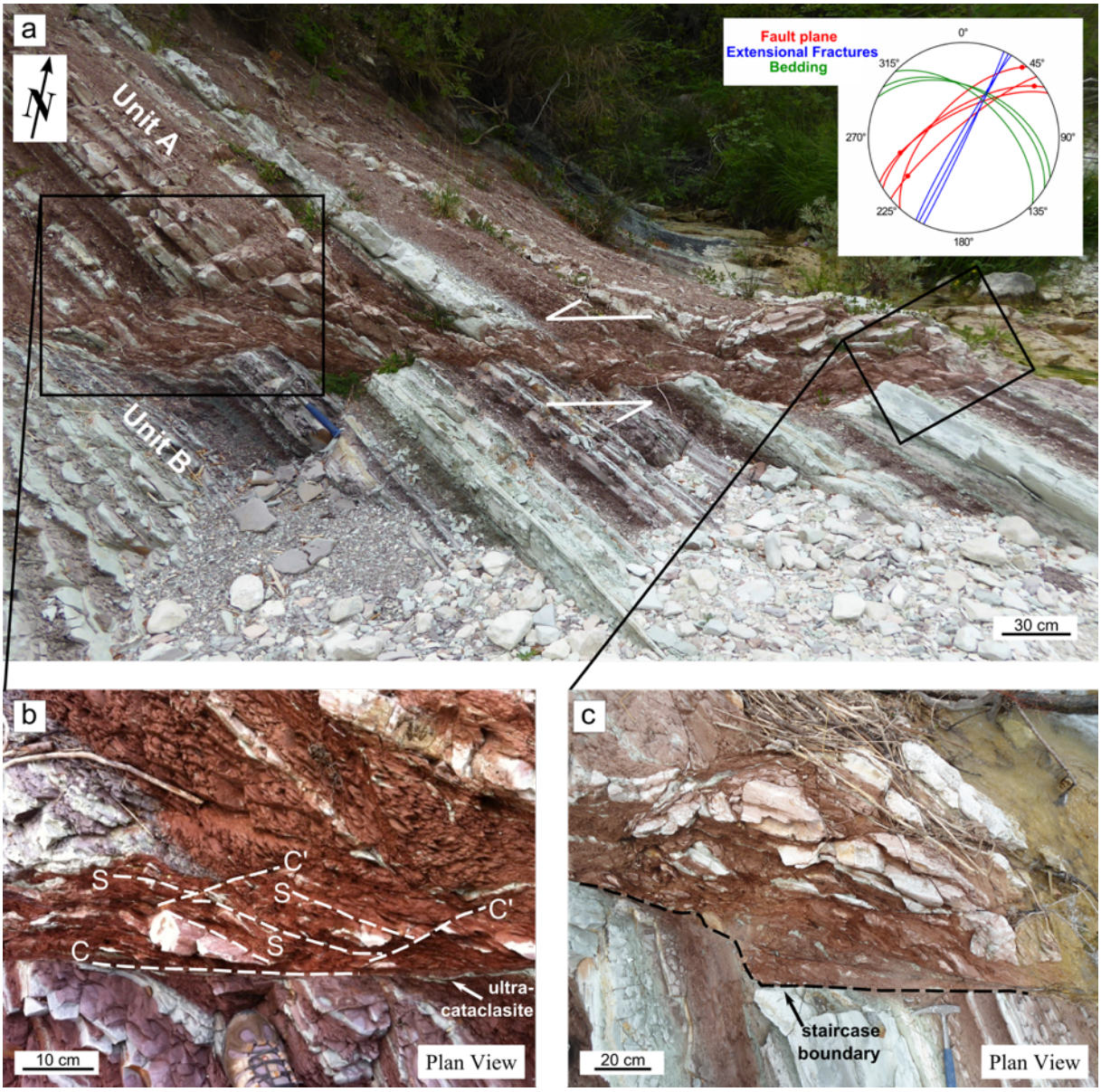

Figure 2.7. Fault with a large (20 m) displacement (Outcrop C, 302628 N 4830455 E UTM coordinates 33T zone), putting into contact a marl-rich group of layers (unit A, above) with a limestone-rich group of layers (unit B, below). (a) The mature fault develops a well-organized, foliated fault core, characterized by an SCC' fabric. The fault surface shows an overall straight trajectory, but its boundaries still maintain the original staircase shape, resulting in a variable thickness of the fault core, ranging from 5 cm to 45 cm. Inset shows the orientation of faults, extensional fractures and bedding. (b) Detail of the fault zone, mostly consisting of reddish marl from the marly unit A, where the SCC' fabric is evident; note the thin ultracataclasite layer at the lower boundary of the fault core, which is derived from the limestone-rich unit B. (c) The lower boundary of the fault core preserves well the initial staircase geometry.

2.4.2. Stress field orientation and angles of faulting

The reconstructed "regional" stress field results in a N-S trending subhorizontal σ_1, an E-W trending subhorizontal σ_3 and a subvertical σ_2 (Figure 2.8a). The resulting maximum principal stress σ_1 (N5°E) is slightly rotated with respect to the direction of maximum compression that

generated the compressional structures of the area (N22°E-N29°E, *Marshak* et al., 1982; *Engelde*r, 1984). The orientation of the local stress fields in general is consistent with the regional stress field obtained from slickenfibers and striae (Figure 2.8a).

The frequency of θ_i values is bimodal and controlled by lithology (Figure 2.8b). In limestone layers the angle of fault initiation ranges between θ_i = 5° and θ_i = 28°, whereas in marl layers it ranges between θ_i = 32° and θ_i = 86°. Most of the angles of fault initiation concentrate between θ_i = 20° and θ_i = 30° in competent layers and between θ_i = 40° and θ_i = 60° in incompetent layers. After the incipient stage, faults show reactivation angles ranging between θ_r = 17° and θ_r = 72°. The frequency of θ_r values shows a unimodal distribution centered at θ_r = 50°- 60° (Figure 2.8b).

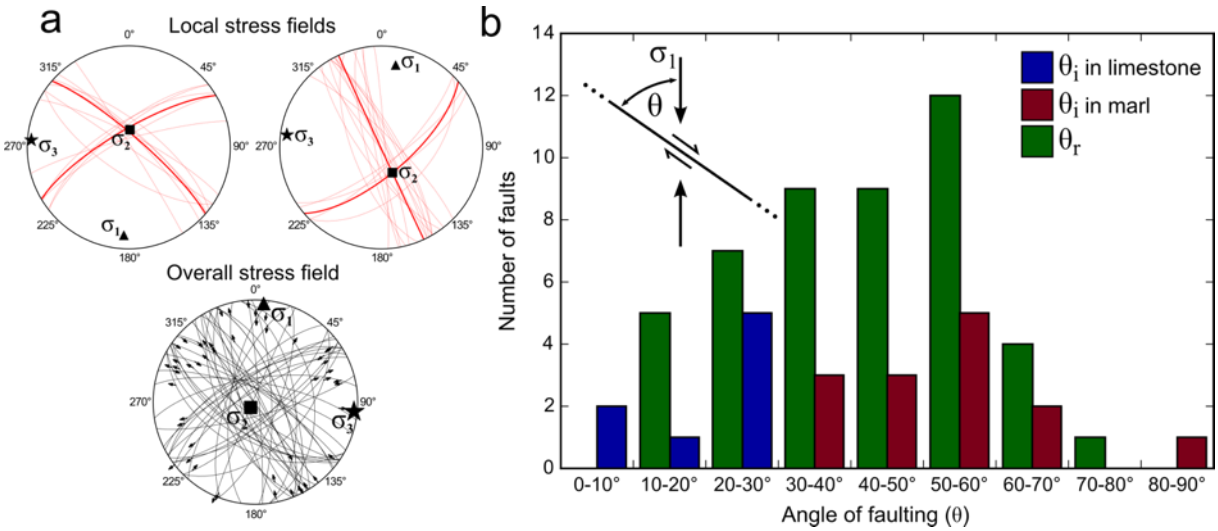

Figure 2.8. (a) Local stress fields determined using conjugate fault planes at outcrop A (right, Figure 2.3a) and B (left, Figure. 2.4a). Overall stress field: slickenfibers and striae orientation with kinematic tensors calculated using a linked Bingham distribution method (Marrett and Allmendinger, 1990; Allmendinger et al., 2012). The three diagrams show a consistent orientation of the stress field, with a nearly N-S trending maximum principal stress axis. (b) Frequency histograms showing the distribution of θ_i and θ_r angles. θ_i values are small in competent limestone layers, ranging from 5° to 28°, and large in incompetent marly layers, ranging from 32° to 86°. θ_r values show a bell-shaped distribution with values ranging between θ_r = 17° and θ_r = 72°.

2.5. Laboratory rock deformation data

2.5.1. Strength and fracture permeability of cohesive limestones

Figure 2.9a shows the evolution of differential stress, σ_d, with increasing axial strain ε_a. For each experiment, differential stress increases linearly until a peak stress, followed by a stress drop. This evolution is consistent with a brittle faulting regime (e.g., *Paterson and Wong*, 2005; *Wong at al*., 1997) and confirmed by the localization of deformation along crosscutting sharp fractures in the tested samples (e.g., Figure 2.10b). With increasing confining pressure from 10 to 30 MPa, both differential stress at failure and residual differential stress increase for all the tested samples. Conversely, the stress drop progressively decreases and requires more strain from the peak to the steady-state value. Samples with chert nodules show higher values of peak differential stress, σ_d, when the forming fracture cuts across the nodules, i.e., P_c = 10 and 20 MPa. At P_c = 30 MPa the values from different samples overlap. The analysis of the chert-rich sample deformed at P_c = 30 MPa show that the fracture does not pass through the nodules, suggesting that the resulting strength represents the marly limestone strength, and can be therefore compared with the strength of the chert-free samples. Thus, excluding samples whose fractures cut across chert nodules (chert-rich samples at P_c = 10 and 20 MPa), the peak stress values in a σ_d versus σ_m space (Figure 2.9b) are well fitted with a linear regression of the form of Equation 2.6 that results in M values of 1.54 and C values of 66 MPa. Following Equation 2.7, we obtain internal friction μ_i = 0.78 and cohesion c = 33 MPa and using Equation 2.2 we derive experimentally the angle of fault initiation θ_i = 26°.

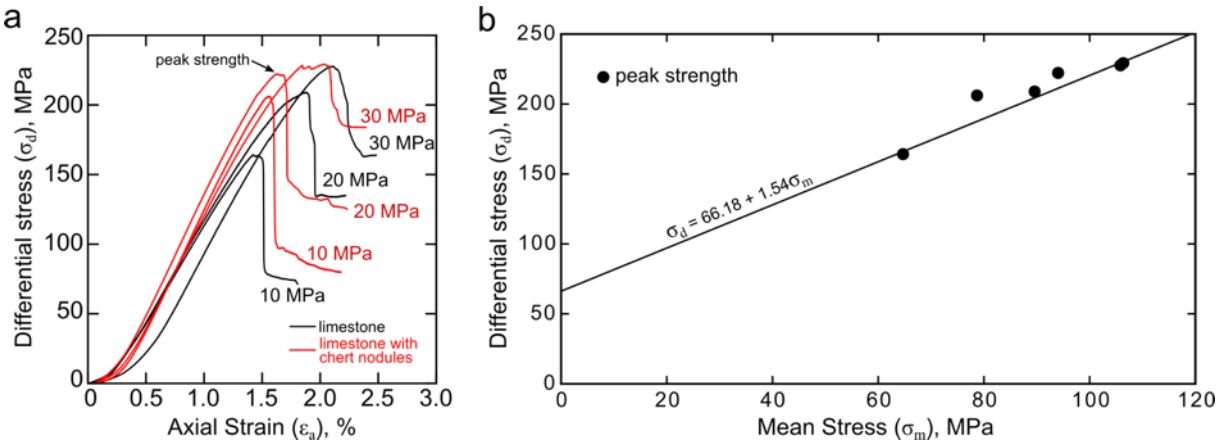

Figure 2.9. Results from triaxial loading experiments on marly limestones. (a) Evolution of differential stress with increasing axial strain for the tested samples (limestone and limestone with chert) at different confining pressures (P_c = 10-30 MPa). All the experiments show a stress drop after the attainment of a peak value of differential stress. With increasing confining pressure the stress drop is smaller and less sharp. (b) Differential stress at peak strength plotted against the mean stress. Linear regression of peak strength values, excluding the samples where nodules of chert are cut by fractures (10 and 20 MPa), shows M = 1.54 and C = 66.18 (Equation 2.7).

During the triaxial tests, although we imposed a pore fluid pressure gradient of 1 MPa, we did not observe any significant fluid flow during loading of the sample (Figure 2.10a). We observe significant fracture enhanced permeability in only one experiment at 10 MPa confining pressure (Figure 2.10). The analysis of the samples at the end of the experiments confirms that this is the only sample developing a through-going fracture, providing a path for fluid flow (Figure 2.10b). Since during failure the pore pressure at the bottom of the sample increases to re-equilibrate with the pore pressure at the top of the sample, we have a fluid flow controlled by a differential gradient of pore pressure changing with time. The permeability also varies with time due to the ongoing deformation. On the basis of this consideration, in order to estimate the enhanced fracture permeability k we applied Darcy's Law:

$$k = \frac{Q\,\eta\,dl}{A\,dP_p} \tag{2.8}$$

considering the current flow rate Q equal to the derivative of the fluid volume curve with time, the current length of the cylindrical sample dl, and the current differential pore pressure dP_p. A is the cross-sectional area of the cylindrical sample and η is the viscosity of the water, that is assumed to be 1.002×10^{-9} MPa s^{-1}. The estimated dynamic permeability, due to fracturing, ranges between $k = 2.7 \times 10^{-16}$ m^2 and $k = 5.6 \times 10^{-16}$ m^2.

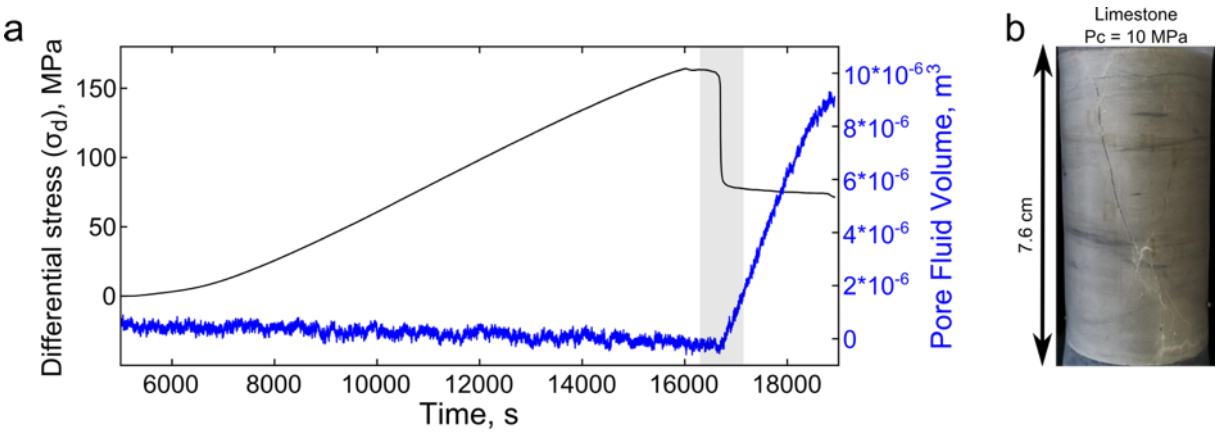

Figure 2.10. Fracture-enhanced permeability during triaxial experiments at 10 MPa confining pressure. (a) Pore fluid volume remains constant during loading and strongly increases immediately after the stress drop. (b) Failed sample displaying a through-going fracture from the bottom to the top of the rock cylinder, thus explaining the strong increase in pore fluid volume.

2.5.2. Strength of incohesive marls

The evolution of the shear stress, τ, with increasing shear strain, γ, during friction experiments (Figure 2.11a) shows an initial increase until the attainment of peak strength, followed by a decay to a steady-state strength. With increasing normal stresses from 20 to 50

MPa, the shear strength of marls increases, as well as the difference between the peak strength and the following steady state strength (Figure 2.11b). The values of peak and steady-state shear strength show a linear dependence with normal stress indicating brittle deformation. Assuming zero cohesion, the envelope of peak shear stresses results in friction μ_i = 0.42, whereas the envelope of steady-state strength results in lower friction μ_s = 0.39 (Figure 2.11b). We used these values of μ_i and μ_s to estimate the angle of fault initiation and the optimum angle for fault frictional reactivation respectively. Due to the small difference between μ_i and μ_s from Equation 2.2 results that the optimum angles for fault initiation, θ_i, and reactivation, θ_r, are similar, i.e., ~34°.

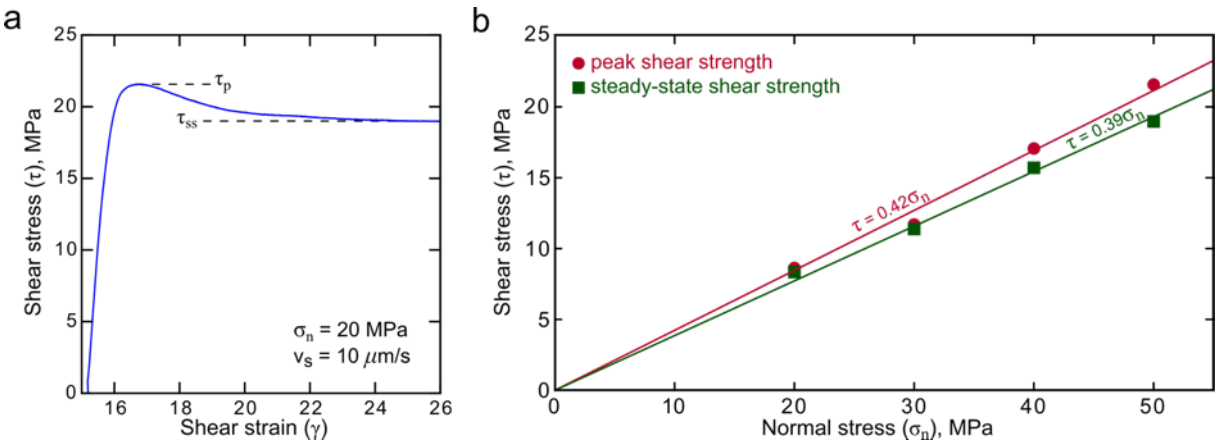

Figure 2.11. Results from biaxial loading experiments on marls. (a) Shear stress evolution with increasing shear strain. During the experiment, shear stress increases until the attainment of a peak value τ_p and then evolves to a steady-state value τ_{ss}. (b) Shear stress at peak and steady-state plotted against normal stress. The envelope of peak shear stresses results in friction μ_i = 0.42, whereas the envelope of steady-state stresses results in lower friction μ_s = 0.39.

2.6. Discussion

2.6.1. Fault initiation

2.6.1.1 Fault initiation in limestone

The angle of fault initiation derived from laboratory experiments on limestones, i.e., θ_i = 26°, is consistent with the peak of the distribution of faults within competent layers, i.e., 20° < θ_i < 30° (Figure 2.8b). This correspondence indicates that the geometry of faults developing at this θ_i is controlled by rock strength. In limestone layers, faults occasionally reactivate joints and extensional fractures formed almost parallel to σ_1, developing θ_i of 5° (e.g., histogram in Figure 2.8b). The propagation of fault segments through pre-existing fractures in limestone beds has been already well documented in mechanical multilayers (e.g., *Wilkins et al.*, 2001; *Crider and Peacock*, 2004; *Roche et al.*, 2012).

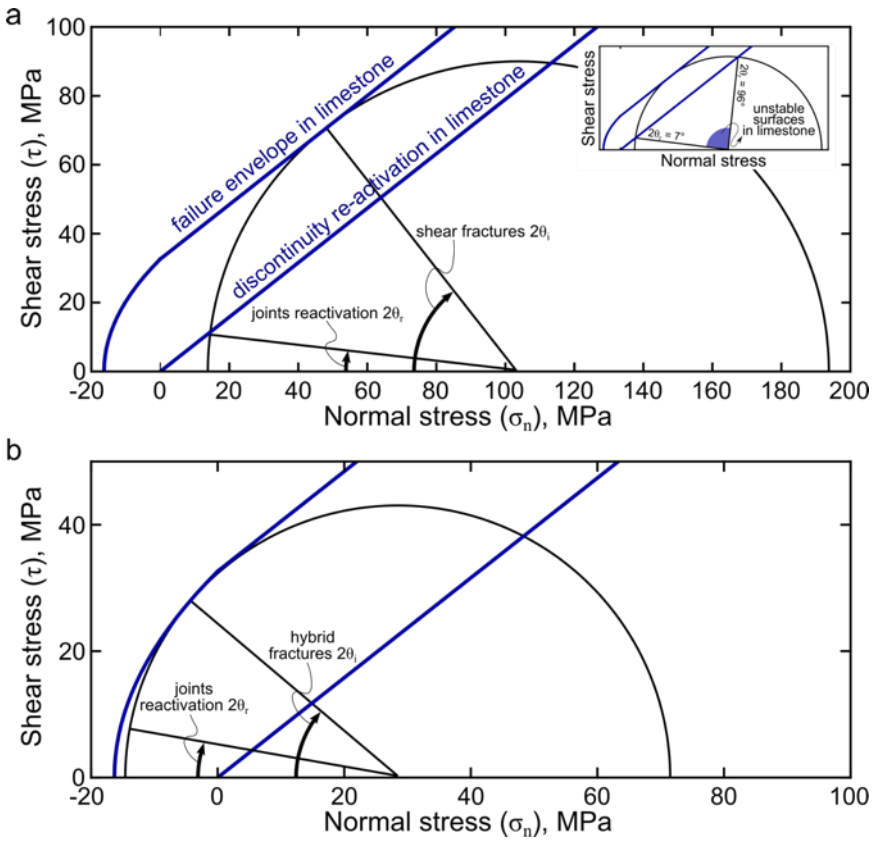

Figure 2.12. Fault initiation in limestones. We consider the Coulomb failure envelope derived from laboratory experiments for intact limestones and an envelope with the same friction but without cohesion for the reactivation of pre-existing surfaces within limestone. (a) Stress state able to explain the simultaneous initiation of shear fractures and reactivation of joints (discontinuities). In competent layers, when σ_1 and σ_3 are both positive, the initiation of faults with θ_i of ~26° and the reactivation of pre-existing surfaces with θ_r between 3° and 48° can simultaneously occur (cf. also the inset, showing the range of unstable orientations for pre-existing fractures, i.e., $2\theta_r$ = 7 - 96°). In the studied outcrops most of the pre-existing surfaces in calcite-rich layers are joints at low angles, 0 - 20° in Figure 2.8b, to σ_1. (b) Stress state able to explain the simultaneous initiation of hybrid fractures and reactivation of joints and foliation. In competent layers, when σ_3 is negative, and therefore under small differential stress and high fluid pressure conditions, the initiation of hybrid fractures with θ_i of ~20° and the reactivation of pre-existing surfaces with θ_r between 0° and 58° can simultaneously occur.

Considering pre-existing surfaces with no cohesion and on the grounds of our laboratory results, we suggest that the variability of θ_i observed in outcropping limestones likely result from the contemporaneous development of new shear fractures, i.e., θ_i ranging between 20° and 30°, and reactivation of pre-existing cohesionless surfaces, i.e., θ_i ranging between 0° and 20° (Figure 2.12a). An additional mechanism able to explain values of $\theta_i \approx 20°$ is the occurrence of hybrid extensional shear fractures (e.g., *Ramsey and Chester*, 2004) favored by fluid overpressure (Figure 2.12b). Assuming a low value of the minimum effective principal stress, local variations of the principal stresses, due possibly to the difference in elastic and poroelastic properties of the layers (e.g., *Gross*, 1995; *Healy*, 2009), can result in the simultaneous development of shear and hybrid fractures. Previous studies have proposed the occurrence of hybrid fractures as a key factor in controlling fault trajectory in mechanical multilayers (e.g., *Ferrill and Morris*, 2003; *Ferrill et al.*, 2012). In the studied faults the occurrence of hybrid fractures is supported by the field observation that re-precipitated calcite within some dilational jogs has a growth direction that is not perpendicular to the wall of the fracture (Figure 2.6b) (e.g., *Price and Cosgrove*, 1990). However, the limited evidences collected in the field suggest that this is not the dominant mechanism.

2.6.1.2 Fault initiation in marls

The strength of marls, $\mu_i = 0.42$, results in θ_i of 34°, that is at the bottom of the estimated range (32°-86°) of mapped faults (Figure 2.8b). Therefore, most of θ_i values cannot be explained by the Coulomb failure criterion for fault initiation (Equation 2.1 and 2.2). Indeed, through less competent clay-rich layers faults tend to form at high angles to σ_1, and even parallel to the layering (Figure 2.4a-b), due to the strong anisotropy of these clay-rich layers. Previous field observations have reported that fault segments propagate parallel to the layering in weak lithologies being discouraged to propagate within the bounding stronger layers (*Roche et al.*, 2012). However, fault initiation at angles higher than 45° requires not only a weak lithology but also the possibility to reactivate pre-existing discontinuities. We propose that the primary foliation of the marls, characterized by weak clay-rich layers, provides favorable horizons able to deviate fault trajectory, as in part suggested in previous studies (e.g., *Jaeger*, 1960; *Donath*, 1961; *Shea and Kronenberg*, 1993; *Bistacchi et al.*, 2012; *Misra et al.*, 2015). In the field we observe that the maximum value of θ_i is limited by the angle between foliation and σ_1. The maximum θ_i is ~86° in outcrop B where σ_1 is almost

perpendicular to the layering (Figure 2.4a) and ~46° in outcrop A where σ_1 is on average at 52° to the layering (Figure 2.3a).

2.6.1.3 Fault initiation in the mechanical multilayer

The intense fracturing that characterizes the marls, bounded by unbroken limestone beds, suggests that the onset of inelastic deformation occurs within incompetent layers (Figure 2.5a). At an incipient stage of deformation, before the localization along a fault plane crosscutting different layers, clay-rich layers achieve the yield strength and deform inelastically. At the same time, under the same stress field, limestone layers still have an elastic behavior. These limestone layers consist of micrite and have low porosity (~4%) and low permeability, as indicated by laboratory experiments (Figure 2.10). Moreover, we suggest that previous fractures related to folding do not significantly increase limestone permeability, since in the field we observe that extensional fractures are sealed by calcite cement. The inelastic deformation within marly layers thus occurs under undrained conditions (e.g., *Rice*, 1975; *Rudnicki and Rice*, 1975; *Rudnicki*, 1984). If the fluid and the rock are both considered incompressible, the undrained response is also incompressible and any stress increment is exactly compensated by changes in pore pressure, so that the strength is pressure insensitive (*Rudnicki*, 2002). The initial failure thus localizes at 45° to the maximum principal stress (*Runesson et al.*, 1996; *Rudnicki*, 2002), as supported by the strong fracturing confined within marly layers showing a pattern characterized by the development of conjugate shear fractures with a dihedral angle of 90° (Figure 2.5a). Because the marly layers are characterized by a pressure-insensitive behavior and do not allow for stress drop, any stress increments within the multilayer will result in an increase of differential stress within the limestone layers. The differential stress thus increases until the achievement of the limestone strength, resulting in the propagation of a fault within the multilayer and allowing for fluid drainage (Figure 2.5b).

2.6.2. Fault growth and angles of fault reactivation

With accumulating displacement the fault core progressively develops a well-organized marly foliation embedding fragments of limestone. With accumulating slip faults cut across dilational jogs causing fault straightening and rotation. Therefore the angle of fault reactivation, θ_r, in general increases with displacement. For example, in outcrop A (Figure 2.3) the asymmetry of the fault system with respect to σ_1 results from the different amount of displacement accumulated by the faults. Here, the main left-lateral fault has accumulated ~1

m of displacement and shows a θ_r angle of about 43°. The conjugate dextral faults, characterized by lower displacements, depict θ_r in the range of 30°-42° due to small-scale anisotropies produced by the limestone-marl alternation. Other structural anisotropies such us pre-existing joints and extensional veins control θ_r values during the very initial stages of faulting, whereas the influence of foliation is persistent up to higher displacement. For faults with displacement in the range of ~10 cm - ~1 m, the dihedral angle is high since the influence of marly foliation in flattening fault planes is more efficient. A representative example is depicted by the conjugate faults of outcrop B (Figure 2.4) showing high θ_r angles, i.e., $55° < \theta_r < 68°$, with frequent layer parallel fault segments. For further displacement (1 - 2 m) we document θ_r of about 42° in both marly and limestone-rich outcrops (Figure 2.3d and 2.4d). These faults display a foliated fault core, suggesting that the slip is mainly accommodated within the clay matrix, and therefore clay friction controls θ_r. The mature fault (Figure 2.7) characterized by a θ_r of about 50°, further supports the idea that after the achievement of a well-organized clay-rich fault structure, the orientation of the fault does not change significantly.

In summary, our field analysis suggests that the geometry of a fault is influenced by anisotropies having the same or higher scale than fault displacement: 1) a small fault, with ~1 cm of displacement, refracts at the competence contrasts between marly and limestone layers; 2) a fault, with ~1 - 2 m of displacement, refracts at competence contrast between different groups of layers and 3) a large displacement fault refracts due to the competent contrast of the different formations, i.e., between the Marne a Fucoidi Formation and the Maiolica Formation.

Based on the field observation that fault cores are foliated, localizing slip within the clay-rich matrix, we consider the steady-state friction value of the powdered marl (cf. paragraph 2.5.2 and Figure 2.11b) as a good approximation for the frictional strength of the outcropping faults. Experiments on natural fault rock samples indicate that the development of a through-going phyllosilicate-rich network is one of the primary mechanisms for fault weakening (e.g., *Holdsworth* 2004; *Collettini et al.*, 2009b; *Carpenter et al.*, 2011; *Tesei et al.*, 2014; 2015). The coefficients of sliding friction observed during our saturated experiments containing 40% of clay, $\mu_p = 0.39 - 0.43$ and $\mu_{ss} = 0.38 - 0.41$, are in good agreement with previous laboratory studies on mixtures of weak clay and strong minerals characterized by a similar percentage of clay (*Tembe et al.*, 2010).

We compare our values of θ_r measured in the field with frictional fault reactivation theory using the equation (*Sibson*, 1985):

$$R = \frac{\sigma_1}{\sigma_3} = \frac{1+\mu_s \cot \theta_r}{1-\mu_s \tan \theta_r} \quad (2.9)$$

where R is the stress ratio for reactivation and μ_s = 0.39 is our laboratory derived friction coefficient (Figure 2.11). Following equation 2.9, the optimum angle for fault reactivation is $\theta_r \approx 34°$ and the corresponding R value is 2.13. This optimum θ_r falls within the range of the most recorded θ_r values (Figure 2.13). Significant departures from the optimal orientation can be explained through the attainment of local fluid overpressures, as supported by calcite mineralization observed along fault planes.

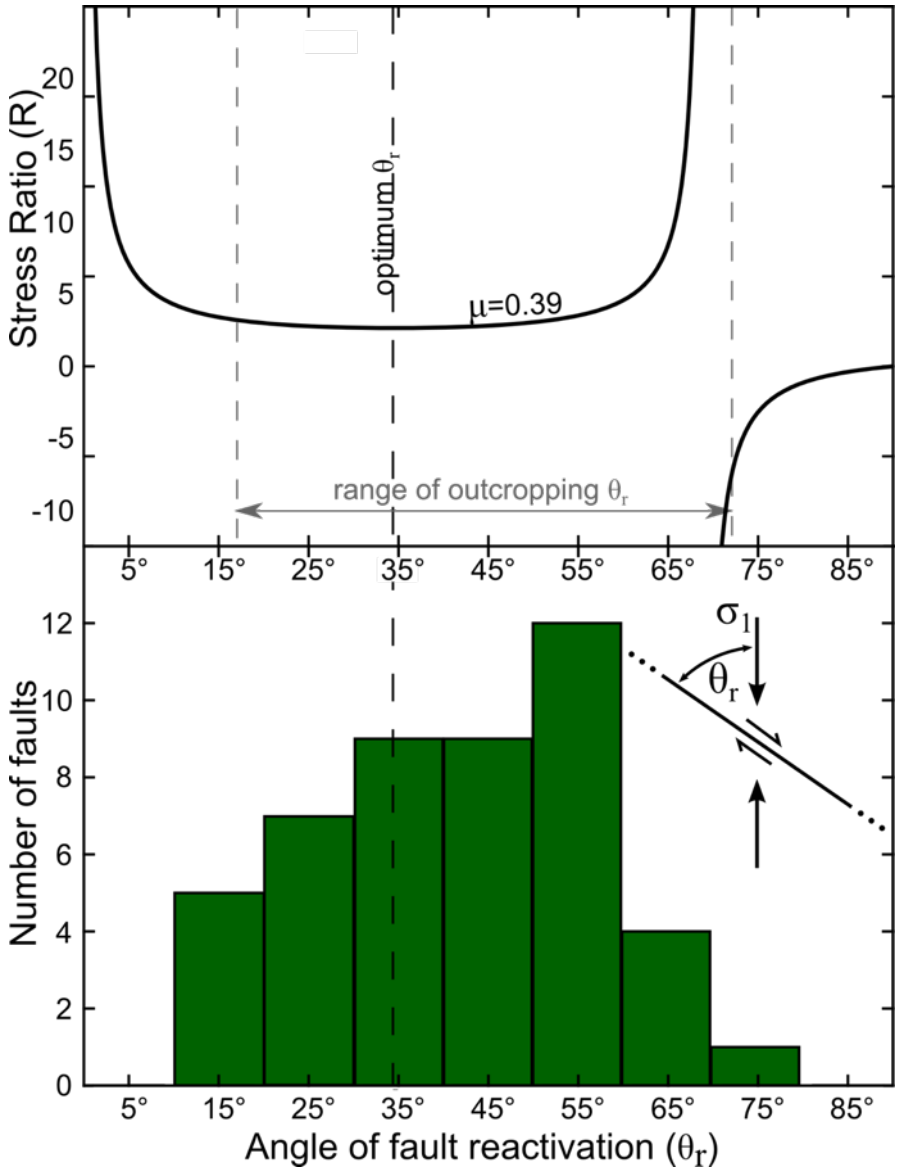

Figure 2.13. Stress ratio, $R = \sigma_1/\sigma_3$, for frictional reactivation of a cohesionless fault (e.g., *Sibson*, 1985) plotted against the reactivation angle, θ_r, for a friction value of μ_s = 0.39, that is the value obtained from biaxial experiments (see Figure 2.11b). The distribution of reactivation angles, θ_r, measured for outcropping faults is consistent with a friction value of μ_s = 0.39.

2.6.3. Fluid flow controlled by fracture and fault permeability

Within low-permeability lithologies, as in our case study, fracturing and faulting processes are the only mechanisms allowing for fluid flow (e.g., *Odling et al.*, 1999; *Aydin*, 2000; *Agosta and Kirschner*, 2003; *Ferrill et al.*, 2014). The faults observed in the field are characterized by calcite in the form of cement in cataclastic fault rocks, within dilational jogs and in the form of slickenfibers (Figure 2.6). This field observation suggests that fractures and faults act as conduits during slip events, as further supported by laboratory observations of fracture enhanced permeability (Figure 2.10). In the field we observe that fractures confined within a single layer (e.g., Figure 2.5a) do not often show calcite mineralization, whereas faults that cut through the multilayer are marked by calcite mineralization (e.g., Figure 2.5b). The initiation and reactivation of a fault trajectory that is not planar lead to the development of dilational jogs within the more competent lithology and consequently the opening of void space where fluids can circulate and calcite precipitate (e.g., *Sibson*, 1996). During the initial stages of faulting, fluid circulation can occur within dilational jogs, parallel to the intersection of the fault plane with the bedding, as suggested in previous field studies (e.g., *Sibson*, 1996; *Ferrill and Morris*, 2003). Here, fluid circulation is almost parallel to the bedding and confined within competent layers. However, the presence of calcite mineralization along slip surfaces also in clay-rich layers suggests that, at least during slip, the fault dilates and allows for fluid flow through different layers of the mechanical multilayer. The presence of calcite mineralization within the more mature and foliated fault core indicates that fluid circulation also occurs during fault growth, but the development of a low-permeability foliated fault rock allows for fluid flow only during fluid-assisted fault reactivation.

2.7. Conclusions

We have investigated the mechanics of fault initiation and evolution within a mechanical multilayer consisting of variously alternated limestones and clay-rich marls, integrating data from outcropping faults and rock deformation experiments on the involved lithologies. Our investigation sheds light on the influence of rock strength and pre-existing anisotropies on fault geometry, fault evolution and fluid assisted fracture permeability.

Fault initiation within the mechanical multilayer is characterized by the development of a staircase trajectory refracting at lithological contrasts. Through limestone layers, the small angles of fault initiation result from the interplay between the strength of intact limestones, responsible for $\theta_i \approx 20° - 30°$, and the reactivation of pre-existing joints at low angle to the maximum principal stress, responsible for $\theta_i \approx 0° - 10°$. Through weak marly layers, most of the angles of fault initiation are higher than predicted by the strength of marls, i.e., 34°, and fault segments often propagate parallel to the foliation in clay-rich layers, suggesting an important role played by the foliation in deflecting fault trajectory. During the incipient stages, marly layers locally develop a dense network of shear fractures, characterized by conjugate planes with dihedral angles of ~90°, suggesting a pressure-independent deformation of these weak layers before fault propagation throughout the multilayer.

With accumulating displacement faults evolve forming straighter trajectories and wider fault cores. At a few meters of displacement, the fault core progressively develops a well-organized marly foliation embedding fragments of limestone. Considering the laboratory-derived friction coefficient of marls, $\mu_s = 0.39$, most of the angles of fault reactivation lay in the field of optimal reactivation, indicating an important role exerted by clay minerals on fault strength.

The presence of different types of calcite mineralization in all the investigated faults (i.e., in cataclastic fault rocks, within dilational jogs and in form of slickenfibers) suggests that faulting is the main mechanism allowing for fluid flow within the sealing layer. Incipient faults promote fluid flow, confined within competent layers, through the opening of dilational jogs. With accumulating displacement, faults develop a low-permeability foliated fault core allowing for fluid flow only during fluid-assisted fault reactivation. This suggests that the sealing integrity of the mechanical multilayer can be affected only by the activity of larger faults cutting across the entire thickness of the sealing layer.

Acknowledgments

This research was carried out within the ERC Starting Grant GLASS (n° 259256). We thank Brett Carpenter and Eugenio Carminati for fruitful discussions and Giovanni Gaglianone for assistance in the laboratory. Reviews by R. Bullock and D. Ferrill significantly helped in improving the manuscript.

Chapter 3.
Fault reactivation:
insights from triaxial saw-cut experiments

Abstract

Fault zones in the brittle crust constitute planes of weakness that can be reactivated depending on their friction and the stress field magnitude and orientation. Analytical approach to evaluate the occurrence of fault reactivation is generally based on the assumption that faults are planes of weakness characterized by a certain friction. However, natural faults are complex structures of finite thickness. Here we aim to experimentally investigate the frictional reactivation of a fault of finite thickness. We simulated pre-existing faults by conducting triaxial experiments on sandstone cylinder containing a saw-cut, filled with clay-rich gouge, at various orientations to the maximum principal stress. Firstly, we have characterized the failure strength of the sandstone and the frictional properties of the clay-rich gouge via triaxial and biaxial experiments respectively. Then, triaxial saw-cut experiments on experimental faults, oriented from 30° to 80° with respect to the maximum compressive stress, were performed at a constant confining pressure of 10 MPa and a constant axial loading rate of 0.3 μm/s. Our results show that the reactivation of the experimental fault gouge follows the prediction of frictional fault reactivation theory. However, the differential stress for the reactivation of finite thickness faults differs from theoretical predictions. In particular, non-optimally oriented faults appear weaker than theoretically predicted and the thickness of the fault inversely relates with the apparent friction required for reactivation. Our findings suggest that theoretical predictions based on the assumption of zero-thickness constitute an upper bound on fault strength and that misoriented faults can be weaker than predicted. Moreover, the experimental fault reactivation occurs via stress drops, suggesting unstable fault reactivation. We tentatively propose that a gouge layer of finite thickness, loaded at any direction to the maximum principal stress, constitutes a compliant layer that can de-stiffen the overall loading system, matching the condition required for frictional instability. Further investigations are required to better characterize the role of stiffness in controlling stable vs. unstable reactivation of optimally and misoriented faults.

3.1. Introduction

Pre-existing faults in the brittle crust constitute zones of weakness, whose reactivation depends on stress state and fault friction (e.g., *Jaeger*, 1960; *Sibson*, 1985). Their frictional reactivation is often predicted based on the assumption that pre-existing faults are zero-thickness planes characterized by a given coefficient of friction (e.g., *Sibson*, 1985; *Morris et al.*, 1996; *Collettini et al.*, 2011). The simplest model used to predict frictional fault reactivation is the single planes of weakness theory (e.g., *Jaeger*, 1960), that is a generalization of the Coulomb failure criterion. In this theoretical framework, the minimum differential stress σ_d required for frictional reactivation of a pre-existing cohesion-less fault is defined as follows (e.g., *Sibson*, 1985):

$$\sigma_d = \frac{1+\mu_s \cot\theta}{1-\mu_s \tan\theta}\sigma_3' - \sigma_3' \tag{3.1}$$

where μ_s is the sliding friction of the pre-existing fault, θ is the frictional reactivation angle, that is the angle between the fault and the maximum principal stress, σ_1, and σ_3' is the effective minimum principal stress. Frictional reactivation occurs when the differential stress for reactivation (Equation 3.1) is lower than the differential stress required for surrounding rock failure. The differential stress σ_d required for failure depends on rock strength, i.e. internal friction φ_i and cohesion c, and the effective minimum principal stress σ_3' as follows:

$$\sigma_d = \frac{2c\cos\varphi_i + 2\sigma_3' \sin\varphi_i}{1-\sin\varphi_i} \tag{3.2}$$

The role of pre-existing planes of weakness on rock deformation has been experimentally investigated via conducting triaxial experiments on foliated anisotropic rocks (i.e. gneiss, schist, slate and shale) (e.g. *Jaeger*,1960; *Donath*, 1961; *McLamore and Gray*, 1967; *Jackson and Dunn*, 1974; *McCabe and Koerner*, 1975; *Shea and Kronenberg*, 1995) and triaxial saw-cut experiments on bare surfaces (e.g., *Jaeger*, 1959; *Jackson and Dunn*, 1974). This previous studies reported that the reactivation of weakness planes depends on their orientation to the maximum principal stress, showing general agreement with the single planes of weakness theory (e.g*., Donath*, 1961; *Hoek*, 1964; *Jackson and Dunn*, 1974).

However, natural faults are complex objects of finite thickness (e.g., *Caine et al.*, 1996; *Ben-Zion and Sammis*, 2003; *Faulkner et al.*, 2011). How does the presence of a finite thickness fault zone influence fault frictional reactivation? Previous experimental and theoretical studies suggest that the presence of a weak layer along a fault results in the rotation of the stress field in close proximity to the fault (e.g., *Byerlee and Savage*, 1992;

Rice, 1992; *Gu and Wong*, 1994), influencing fault reactivation by enhancing slip on unfavorably oriented faults (*Lecomte et al.*, 2012). Here we systematically investigate the reactivation of a finite-thickness fault as a function of frictional reactivation angle. We aim to experimentally validate the plane of weakness theory for faults of finite thickness by conducting triaxial experiments with gouge-filled saw-cuts oriented at different angles to the maximum principal stress, from favorable oriented to severely misoriented.

Moreover, once the differential stress for reactivation is achieved, does the reactivation occur via stable or unstable sliding? In natural faults, stability is controlled by the elastic interaction between the fault zone and the elastic surrounding (e.g., *Rice*, 1983; *Scholz*, 2002; *Kanamori and Brodsky*, 2004). In particular, when the decrease in fault frictional strength with displacement is faster than the elastic unloading of the surrounding, the condition for instability is matched. In faults deformed during laboratory experiments, frictional stability is evaluated in the framework of the rate- and state-dependent friction (e.g., *Dieterich*, 1979; *Ruina*, 1983; *Gu et al.*, 1984; *Marone*, 1998b). In this context, the experimental fault is loaded under constant normal stress conditions. However, a pre-existing fault can undergo a variety of loading path before reactivation, ranging from load-weakening to load-strengthening (e.g., *Sibson*, 1991). Here we tentatively analyze the slip behavior of the experimental faults upon reactivation, describing the elastic interaction between the fault gouge and the surrounding.

3.2. Methods

We conducted, three sets of experiments (Table 3.1). One set of triaxial experiments were conducted on cylindrical samples of Pietraserena sandstone (*Fratini et al.*, 2014). One set of biaxial friction experiments on fault gouge derived from Candigliano marl (59 wt% of $CaCO_3$ constrained by calcimetry and the remaining percentage consisting of a clay mineral assemblage of smectite, illite and mixed layer illite-smectite, *Giorgetti et al.*, 2016). The third set consists of triaxial experiments on Pietraserena sandstone containing a saw-cut filled with Candigliano marl gouge, with different orientation to the maximum principal stress, simulating a pre-existing fault within an intact rock volume.

Experiments were conducted using BRAVA (Brittle Rock deformAtion Versatile Apparatus), a servo-controlled biaxial apparatus equipped with pressure vessel situated in the High Pressure - High Temperature Laboratory at the INGV in Rome, Italy (*Collettini et al.*, 2014b, for further details) (Figure 3.1). Vertical and horizontal pistons apply vertical and horizontal forces, that are measured through load cells with 0.03 kN accuracy. Vertical and horizontal load point displacements are measured through Linear Variable Differential Transducers (LVDTs) sensors with 0.1 μm accuracy. A servo-hydraulic system is used to control alternatively the force applied by or the velocity imposed to the pistons. A pressure intensifier, connected to the pressure vessel, applies confining pressure via hydrogenated, paraffinic white oil. The pressure vessel is equipped with two doors sealed with O-rings to prevent confining oil leakage. Confining pressure is measured through pressure transducers with 7 kPa accuracy and controlled via a pressure-feedback control mode. Pressure intensifier displacement is measured through LVDT sensor with 0.1 μm accuracy.

3.2.1. Triaxial experiments

Triaxial experiments were conducted on cylindrical samples 38 mm in diameter and 82 mm in height (i.e. 2:1 aspect ratio, *Paterson and Wong*, 2005). The samples were placed in-between two stainless steel end platens, jacketed with one layer of poly-olefin heat-shrink tube and sealed with steel wires at the extremities to avoid confining oil leakage. Experiments were performed at room temperature and under dry conditions.

To evaluate the failure envelope, we performed experiments at different confining pressure P_c, in the range P_c = 10-30 MPa (Figure 3.1b). Confining pressure was first applied and maintained constant throughout the experiment. The differential stress was then applied

advancing the vertical piston at a constant velocity of 0.1 μm/s, corresponding to axial strain rates of $1.2*10^{-6}$ s^{-1}.

Table 3.1. Details of the experiments performed.

Experiment number	Configuration	Saw-cut angle to sample axis[a]	Layer thickness[b] (mm)	Material	Applied stress (MPa)	Deformation velocity[c] (μm/s)
b565	triaxial	-	-	Pietraserena Sandstone	$P_c = 10$	$v_a = 0.1$
b584	triaxial	-	-	Pietraserena Sandstone	$P_c = 20$	$v_a = 0.1$
b585	triaxial	-	-	Pietraserena Sandstone	$P_c = 30$	$v_a = 0.1$
b652	triaxial	-	-	Pietraserena Sandstone	$P_c = 15$	$v_a = 0.1$
b653	triaxial	-	-	Pietraserena Sandstone	$P_c = 25$	$v_a = 0.1$
b599	double-direct shear	-	3	Candigliano Marl	σ_n = 10-20-30	$v_s = 0.5$
b662	double-direct shear	-	3	Candigliano Marl	$\sigma_n = 30$	$v_s = 0.4$
b663	double-direct shear	-	3	Candigliano Marl	$\sigma_n = 30$	$v_s = 0.4$
b670	double-direct shear	-	3	Candigliano Marl	$\sigma_n = 50$	$v_s = 0.4$
b586	triaxial saw-cut	30°	3	Pietraserena Sandstone + Candigliano Marl	$P_c = 10$	$v_a = 0.3$
b587	triaxial saw-cut	30°	3	Pietraserena Sandstone + Candigliano Marl	$P_c = 20$	$v_a = 0.3$
b588	triaxial saw-cut	60°	3	Pietraserena Sandstone + Candigliano Marl	$P_c = 10$	$v_a = 0.3$
b596	triaxial saw-cut	50°	3	Pietraserena Sandstone + Candigliano Marl	$P_c = 10$	$v_a = 0.3$
b597	triaxial saw-cut	40°	3	Pietraserena Sandstone + Candigliano Marl	$P_c = 10$	$v_a = 0.3$
b598	triaxial saw-cut	70°	3	Pietraserena Sandstone + Candigliano Marl	$P_c = 10$	$v_a = 0.3$
b610	triaxial saw-cut	40°	3	Pietraserena Sandstone + Candigliano Marl	$P_c = 10$	$v_a = 0.3$
b611	triaxial saw-cut	50°	3	Pietraserena Sandstone + Candigliano Marl	$P_c = 10$	$v_a = 0.3$
b617[d]	triaxial saw-cut	50°	3	Pietraserena Sandstone + Candigliano Marl	$P_c = 10$	$v_a = 0.3$
b619[e]	triaxial saw-cut	50°	3	Pietraserena Sandstone + Candigliano Marl	$P_c = 10$	$v_a = 0.3$
b628	triaxial saw-cut	50°	1	Pietraserena Sandstone + Candigliano Marl	$P_c = 10$	$v_a = 0.3$
b629	triaxial saw-cut	50°	5	Pietraserena Sandstone + Candigliano Marl	$P_c = 10$	$v_a = 0.3$
b646	triaxial saw-cut	80°	3	Pietraserena Sandstone + Candigliano Marl	$P_c = 10$	$v_a = 0.3$
b648	triaxial saw-cut	70°	3	Pietraserena Sandstone + Candigliano Marl	$P_c = 10$	$v_a = 0.3$

[a] applicable only to triaxial saw-cut configuration.
[b] applicable only to double-direct shear and triaxial saw-cut configuration.
[c] axial velocity (v_a) in triaxial and triaxial saw-cut experiments and sliding velocity (v_s) in double-direct shear experiments.
[d] 2.75 mm total along saw-cut displacement to collect microstructures.
[e] 1.50 mm total along saw-cut displacement to collect microstructures.

Thus, the stress field acting on the sample is $\sigma_2 = \sigma_3 = P_c$, where σ_3 and σ_2 are the minimum and intermediate principal stresses respectively, and the maximum principal stress $\sigma_1 = P_c + \sigma_d$, where σ_d is the differential stress. The values of the vertical load point displacement were corrected for the machine stiffness on the vertical axis that, depending on the confining pressure, ranges between 757.7 kN/mm and 771.2 kN/mm.

In triaxial experiments, the maximum differential stress preceding a brittle shear failure linearly depends on the confining pressure (Figure 3.1b) (e.g., *Paterson and Wong*, 2005) and the linear correlation coefficients define the angle of internal friction φ_i and the cohesive strength c (e.g., *Wood*, 1990) as follows:

$$\sigma_d = \frac{4 \sin \varphi_i}{3-3 \sin \varphi_i} P_c + \frac{6 \cos \varphi_i}{3-3 \sin \varphi_i} c \tag{3.3}$$

From Equation 3.3, the failure strength is evaluated through the Coulomb failure criterion (*Coulomb*, 1776):

$$\tau = \mu_i \sigma_n + c \tag{3.4}$$

where τ is the shear stress, σ_n is the normal stress on the failure plane, $\mu_i = tan(\varphi_i)$ is the internal friction of the intact rock.

3.2.2. Friction experiments

Friction experiments were performed in double-direct shear configuration in which two layers of marly gouge were placed in between three grooved sliding blocks (Figure 3.1c) (e.g., *Dieterich*, 1972). Marly gouge was prepared from outcropping Candigliano marl (*Giorgetti et al.*, 2016) that were crushed and sieved to < 125 μm grain size. The two gouge layers, each with initial ~3 mm uniform thickness, were constructed in order to have a 5 cm × 5 cm uniform area, that is maintained constant throughout the experiment. Experiments were performed at room temperature and under dry conditions.

To evaluate the reactivation criterion, we conducted experiments at different normal stress σ_n ranging between 10 MPa and 50 MPa (Figure 3.1c). The normal stress was first applied and maintained constant throughout the experiment. Then, the shear stress was applied advancing the vertical piston at a constant velocity of 0.4-0.5 μm/s. The displacement values of the vertical and horizontal load points were corrected for the elastic stretch of each load frame, taking into account that the machine stiffness is 1283 kN/mm on the horizontal axis and 928.5 kN/mm on the vertical axis.

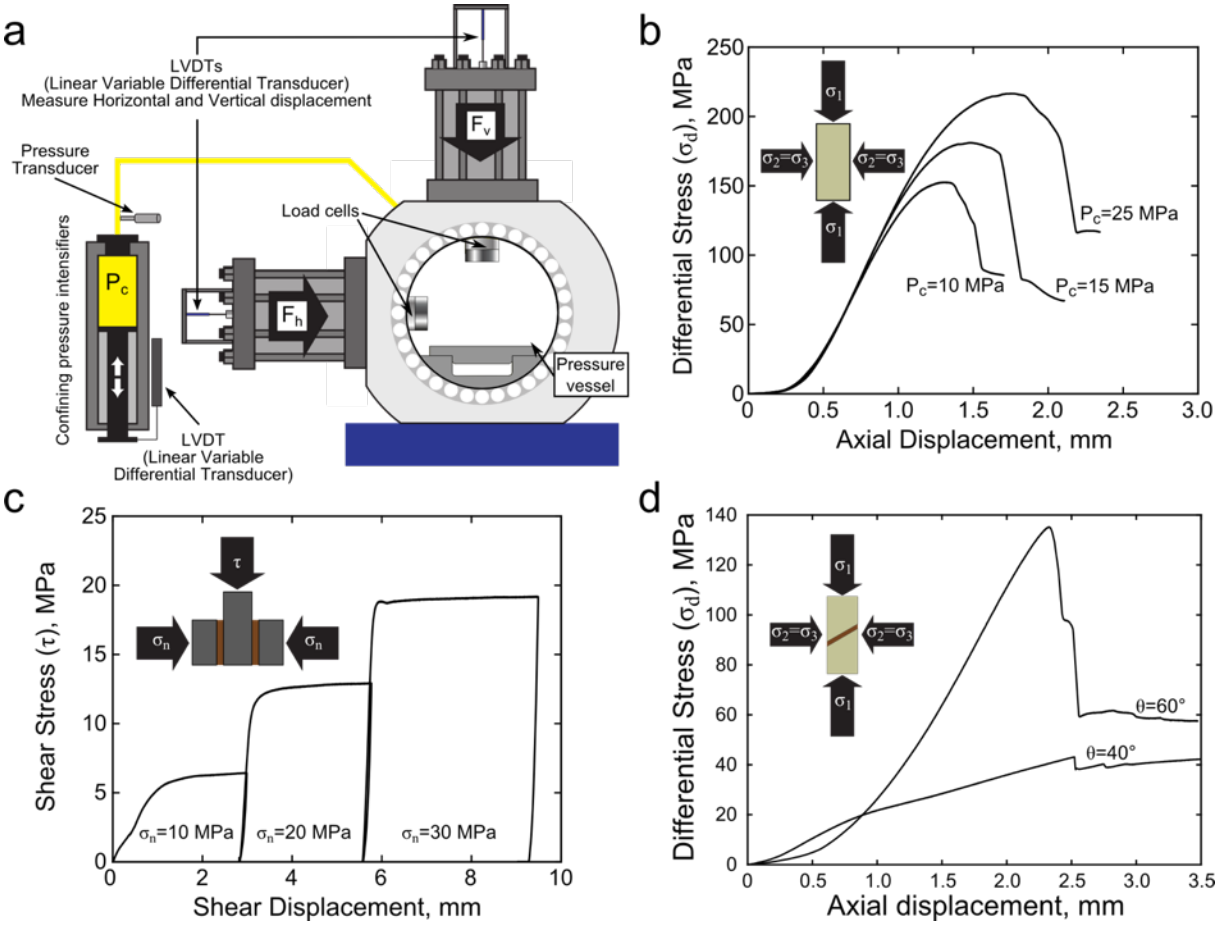

Figure 3.1. (a) The BRAVA rock deformation apparatus (after *Scuderi and Collettini*, 2016). Vertical and horizontal pistons apply vertical (F_V) and horizontal forces (F_H), that are measured through load cells located within the pressure vessel. Load point displacements are measured through Linear Variable Differential Transducers (LVDTs). Confining pressure (P_c) is applied by the pressure intensifier via confining oil and measured through a pressure transducer. Pressure intensifier displacement is measured through LVDT sensor. (b) Evolution of differential stress plotted versus axial displacement for selected triaxial experiments. Inset shows the triaxial configuration in which confining oil is used to apply an isotropic pressure ($\sigma_3 = \sigma_2$) and the vertical loading frame applies a vertical force generating a differential stress. (c) Evolution of shear stress plotted versus shear displacement during a friction experiment. Inset shows the double-direct shear configuration in which three stainless steel forcing blocks sandwich two identical layers of fault gouge. (d) Evolution of differential stress plotted versus axial displacement during triaxial saw-cut experiments. The uppermost curve shows the evolution of differential stress during an experiment in which the sample deformed through the development a new fracture, whereas the lowermost curve shows the evolution of differential stress during an experiment in which the sample deformed through the reactivation of the saw-cut. Inset shows the triaxial saw-cut configuration in which confining oil is used to apply an isotropic pressure ($\sigma_3 = \sigma_2$) and the vertical loading frame applies a vertical force generating a differential stress.

In brittle fault reactivation, the shear stress τ linearly depends on the applied normal stress σ_n (e.g., *Jaeger and Cook*, 1979) as follows:

$$\tau = \mu_s \sigma_n \tag{3.5}$$

where the sliding friction is a function of the angle of sliding friction, i.e. $\mu_s = tan(\varphi_s)$. The steady-state shear stress achieved during friction experiments at different normal stresses (Figure 3.1c) was measured to estimate the sliding friction of the marly gouge.

3.2.3. Triaxial saw-cut experiments

Triaxial saw-cut experiments were conducted systematically changing the orientation of the saw-cut, i.e. the angle θ between the experimental fault and the maximum principle stress, in the range θ = 30°-80°. The samples were prepared cutting Pietraserena sandstone cylinders 38 mm in diameter and ~2.2-2.3 in length to diameter ratio into two pieces at given θ angles. The saw-cut surfaces were roughened with #60 grit SiC abrasive paper (265 μm average abrasive grain size) to ensure frictional sliding to occur within the gouge layer. For all the tested orientations (Table 1), an initial ~3 mm thick layer of marly gouge was placed within the saw-cut surface. To test the effect of layer thickness on the mechanics of reactivation we performed two further experiments at θ = 50° with an initial layer thickness of ~1 mm and ~5 mm respectively. The marly gouge was the same sheared in friction experiments (see Section 2.2). The samples were placed in-between two stainless steel end platens, jacketed with two layers of poly-olefin heat-shrink tube and sealed with steel wires at the extremities to avoid confining oil leakage. Experiments were performed at room temperature and under dry conditions.

Confining pressure was first applied and maintained constant with values of P_c = 10 MPa (with the exception of one experiments at P_c = 20 MPa). The vertical piston was then advanced at a constant velocity of 0.3 μm/s and the evolution of the differential stress measured (Figure 3.1d). The values of the vertical load point displacement were corrected for the machine stiffness on the vertical axis, i.e. 771.2 kN/mm. Differential stress was corrected for jacket strength, i.e. 0.56 MPa/mm, and for reduction in contact area during saw-cut reactivation. When shear occurs within the saw-cut, the contact area continuously changes (e.g., *Scott et al.*, 1994a) as follows:

$$A = r^2(\Theta - \sin\Theta), \qquad \Theta = \pi - 2\sin^{-1}\left(\frac{\Delta l}{2r}\tan\theta\right) \tag{3.6}$$

where Δl is the axial displacement and r is the radius of the cylindrical sample. Θ is the angle subtended by the points of intersection of two overlapping circles of radius r and whose centers distance is $\Delta l \cdot \tan\theta$, at the centers of the circles. The normal stress acting on the gouge layer is function of the differential stress σ_d, the angle θ and the confining pressure P_c. The shear stress acting on the gouge layer is function of the differential stress σ_d and the angle θ. At constant P_c and θ, stress resolved on saw-cut evolved depending on the differential stress as follows:

$$\sigma_n = \frac{\sigma_d(1-\cos 2\theta)+2P_c}{2} \tag{3.7}$$

$$\tau = \frac{\sigma_d \sin 2\theta}{2} \tag{3.8}$$

Additional experiments with different amount of total displacement along a saw-cut with constant $\theta = 50°$, i.e. 1.5, 2.75 and 6 mm, were performed to provide a better insight into the stages of fault reactivation. Thin sections of sheared gouge were realized collecting and embedding in epoxy resin the gouge layer at the end of triaxial saw-cut experiments. Microstructural observations were performed with a Scanning Electron Microscope FEI Quanta 400 installed in the Scanning Electron Microscope Laboratory of the Earth Sciences Department at Sapienza University of Rome and a JEOL JSM-6500 F thermal field emission scanning electron microscope installed in the Electron Microscopy Laboratory at the INGV in Rome, Italy. All the microphotographs presented are backscattered electron images. The analyses were performed using acceleration voltage of 15 or 30 kV, working distance of 10 or 11 mm and carbon-coating.

3.3 Results

3.3.1. Sandstone strength and marl friction

In triaxial experiments the evolution of differential stress with progressive axial shortening (Δl) is characterized by an initial increase until the achievement of a peak value, a sudden stress drop and an almost constant residual stress (Figure 3.1b). This shape of the σ_d vs. Δl curves is typical of brittle deformation (e.g., *Paterson and Wong*, 2005; *Wong et al.*, 1997), as confirmed by localized shear fractures characterizing failed samples. The peak differential stress linearly increases with increasing confining pressure (Figure 3.2a), as a further indication of failure in brittle regime (e.g., *Paterson and Wong*, 2005). Fitting peak σ_d versus P_c data to Equation 3.3, we evaluated the failure criterion for Pietraserena sandstone. The resulting internal friction and cohesion are $\mu_i = 0.76$ and $c = 34.01$ MPa, respectively.

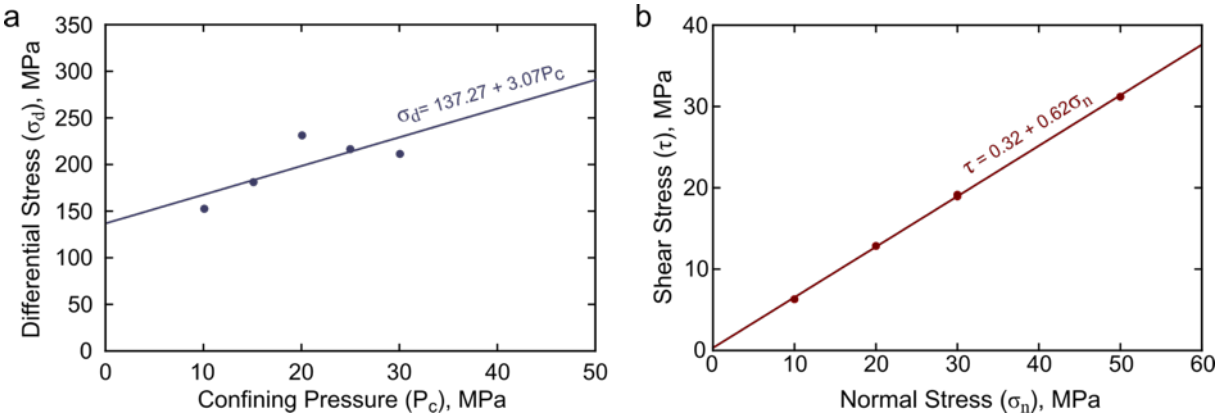

Figure 3.2. (a) Results from triaxial experiments on Pietraserena sandstone. Peak differential stress is plotted against confining pressure. Linear regression results in angular coefficient of 3.07 and intercept of 137.27 MPa (Equation 3.3). (b) Results from friction experiments on Candigliano marly gouge. Peak shear stress is plotted against normal stress. Linear regression results in sliding friction $\mu_s = 0.62$ and almost zero cohesion.

Friction experiments on Candigliano marly gouge are characterized by an increase in shear stress with displacement until the attainment of a steady-state value (Figure 3.1c). Increasing the normal stress from 10 to 50 MPa, the steady-state shear stress linearly increases (Figure 3.2b). The linear regression of τ measured during steady-state shearing versus σ_n data results in sliding friction $\mu_s = 0.62$ and almost zero cohesion.

3.3.2. Stress versus displacement evolution curves in triaxial saw-cut experiments: saw-cut reactivation versus new fracture development

Saw-cut reactivation occurs during the deformation of samples containing saw-cuts at θ = 30° - 40° - 50° (Figure 3.3a), whereas samples with saw-cuts at θ = 60° - 70° - 80° deformed through the development of new fractures (Figure 3.4).

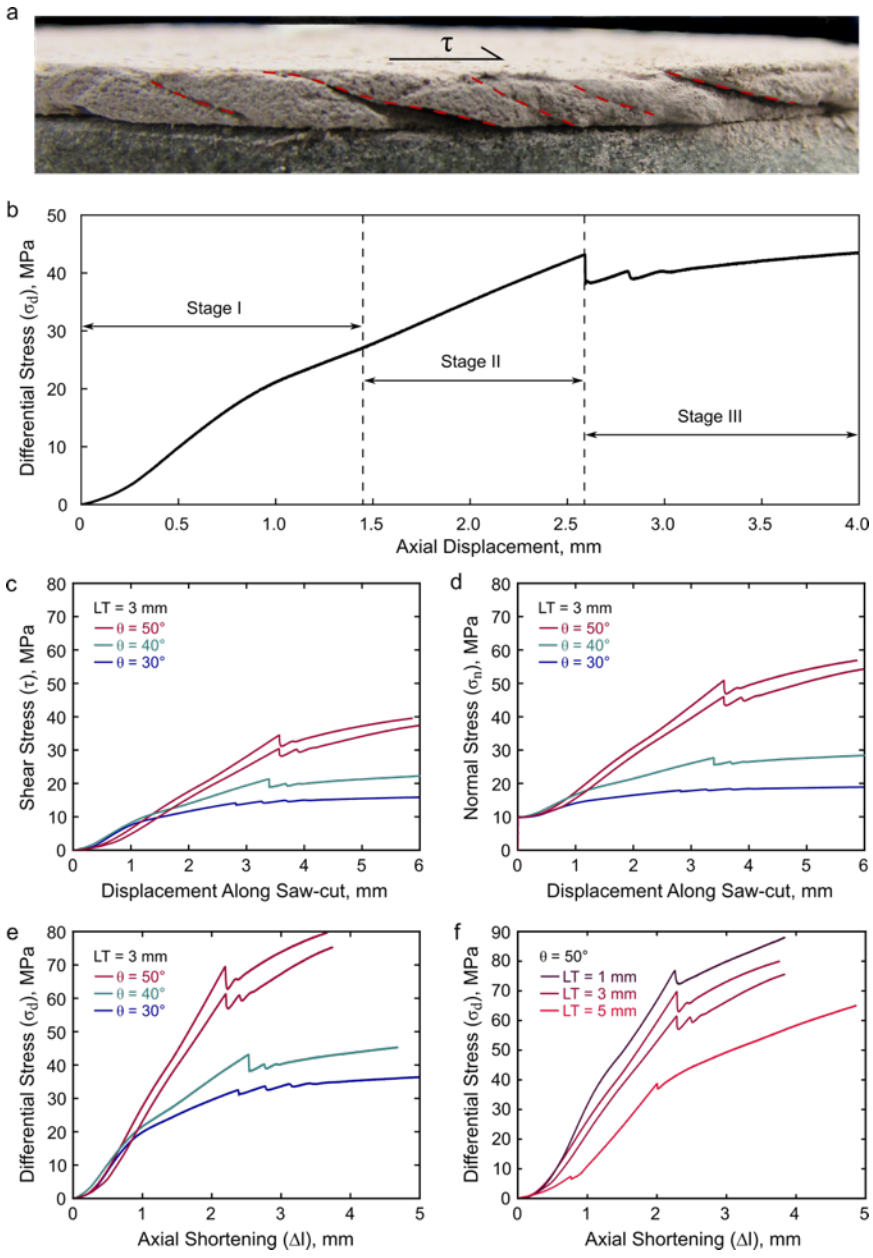

Figure 3.3. Results from triaxial saw-cut experiments with 3 mm-thick gouge layers in which deformation occurs via saw-cut reactivation. (a) Sheared gouge at the end of a triaxial saw-cut experiment showing Riedel shear planes (red dashed lines). (b) Characteristic evolution curve of differential stress versus axial displacement during saw-cut reactivation. During Stage I the stress increases non-linearly by initial progressive steepening and following progressive flattening of the curve. During Stage II the stress increases linearly. During Stage III the stress evolves through progressively dampened stress drops to stable sliding. Shear stress (c), normal stress (d) and differential stress (e) are characterized by the same evolution curve with increasing displacement. The slope of Stage II increases with increasing saw-cut angle. (e) Differential stress plotted versus axial displacement for saw-cut samples characterized by different layer thickness. The differential stress supported by the sample strongly decreases with increasing layer thickness.

Reactivation of samples with ~3 mm thick gouge layer show a characteristic evolution of the differential stress with increasing displacement (Figure 3.3b-e). The shear stress resolved on saw-cuts (Equation 3.8) shows the same evolution curve with displacement (Figure 3.3c). However, since the experiments were conducted at constant P_c, it is worth noting that shear and normal stresses are coupled via the shear zone in the saw cut and, consequently, normal stress evolves with displacement as well (Figure 3.3d). We identified three main stages in the stress-displacement evolution curve (Figure 3.3b): 1) an initial increase resembling the characteristic behavior of material that yields in compression (e.g., *Brace et al.*, 1966; *Jaeger and Cook,* 1979), comprising initial porosity closure, elastic loading and yielding (Stage I); 2) an almost linear strain-hardening (Stage II); 3) a stress drop indicating saw-cut reactivation followed by stress oscillations that are progressively dampened until stable sliding is achieved. With increasing θ from 30° to 50° the strain-hardening is progressively steeper, resulting in higher σ_d required for the reactivation of more misoriented anisotropies (Figure 3.3e). At $\theta = 30°$ the first stress drop is small, i.e. $\Delta\sigma_d \approx 1.5$ MPa, whereas at $\theta = 40°$-$50°$ the first stress drop is significantly larger, i.e. $\Delta\sigma_d \approx 4.5$ - 6.8 MPa (Figure 3.3e).

Figure 3.3f shows the effect of gouge layer thickness on saw-cut reactivation at $\theta = 50°$. The differential stress supported by the sample strongly decreases with increasing thickness of the weak layer. Indeed the reactivation of the 1-mm-thick weak layer occurs at a differential stress value, $\sigma_d = 77$ MPa, that is almost twice the value required for the reactivation of the 5-mm-thick weak layer, $\sigma_d = 39$ MPa. If compared to 3-mm-thick layer experiments, the evolution of σ_d with Δl during the reactivation of the 1-mm-thick layer is characterized by a more marked yielding in Stage I and a single stress drop of $\Delta\sigma_d \approx 4.5$ at the onset of Stage III. Differently, during the reactivation of a 5-mm-thick layer the previously described Stages I and II are not discernible. The σ_d vs. Δl curve of a 5-mm-thick layer is characterized by a more marked initial compaction, an almost linear increase and a small stress drop of 1.8 MPa followed by stable sliding.

The σ_d vs. Δl evolution curves in failed samples with saw-cut are typical of brittle deformation (Figure 3.4) (e.g., *Paterson and Wong*, 2005; *Wong et al.*, 1997). Samples with saw-cuts at $\theta = 60°$ - 70° - 80° failed at almost the same value of maximum differential stress, suggesting that saw-cut orientation does not affect sample failure strength. However, different rates of stress increase during the elastic loading portion of the curves suggest that saw-cut orientation influences overall sample elasticity. Particularly, the elastic loading of the sample steepens with increasing θ (Figure 3.4). Results from failed saw-cut samples mainly differ

from failed intact samples in how stress drops occur (Figure 3.4 vs. Figure 3.1b). Triaxial experiments are characterized by one stress drop followed by the residual strength, whereas triaxial saw-cut experiments are characterized by two or more stress drops separated by short strain-weakening portions of the stress curve (Figure 3.4). Failed samples at the end of the experiments show a localized, through-going fracture and conjugate antithetic fractures that end at the boundary of the weak layer (Figure 3.4b-c).

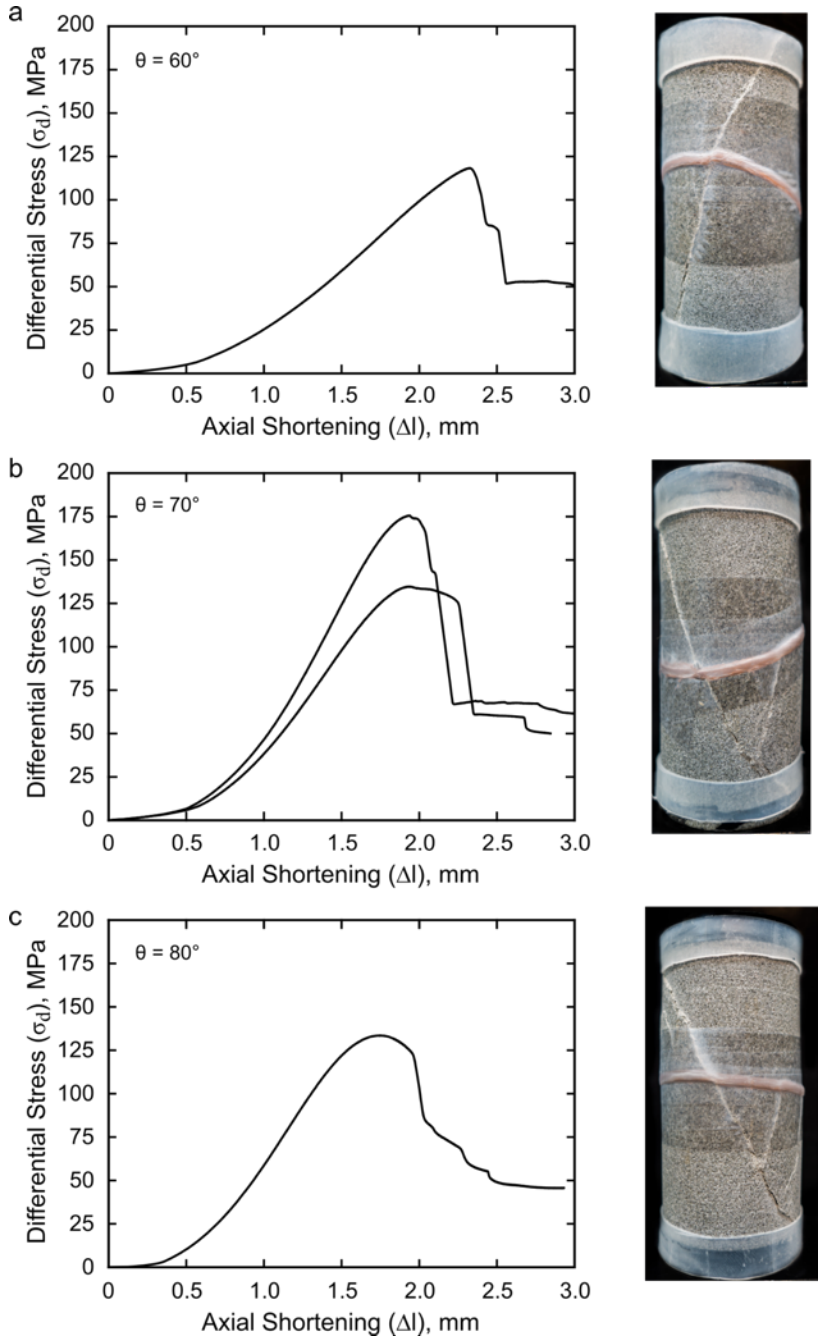

Figure 3.4. Evolution of differential stress plotted versus axial shortening during triaxial saw-cut experiments at θ = 60° (a), θ = 70° (b) and θ = 80° (c). The evolution curves of differential stress with displacement are characterized by an initial increase until the achievement of a peak value followed by stress drops and the development of localized shear fracture. Peak differential stress does not depend on θ angle. The slope of the linear elastic loading portion of the curve increasing with increasing θ, suggesting that saw-cut orientation influences overall sample elasticity.

3.3.3. Microstructural evolution during reactivation

Microstructural investigation on reactivated experimental faults give insights into their mechanical evolution curve (Figure 3.3b and 3.5).

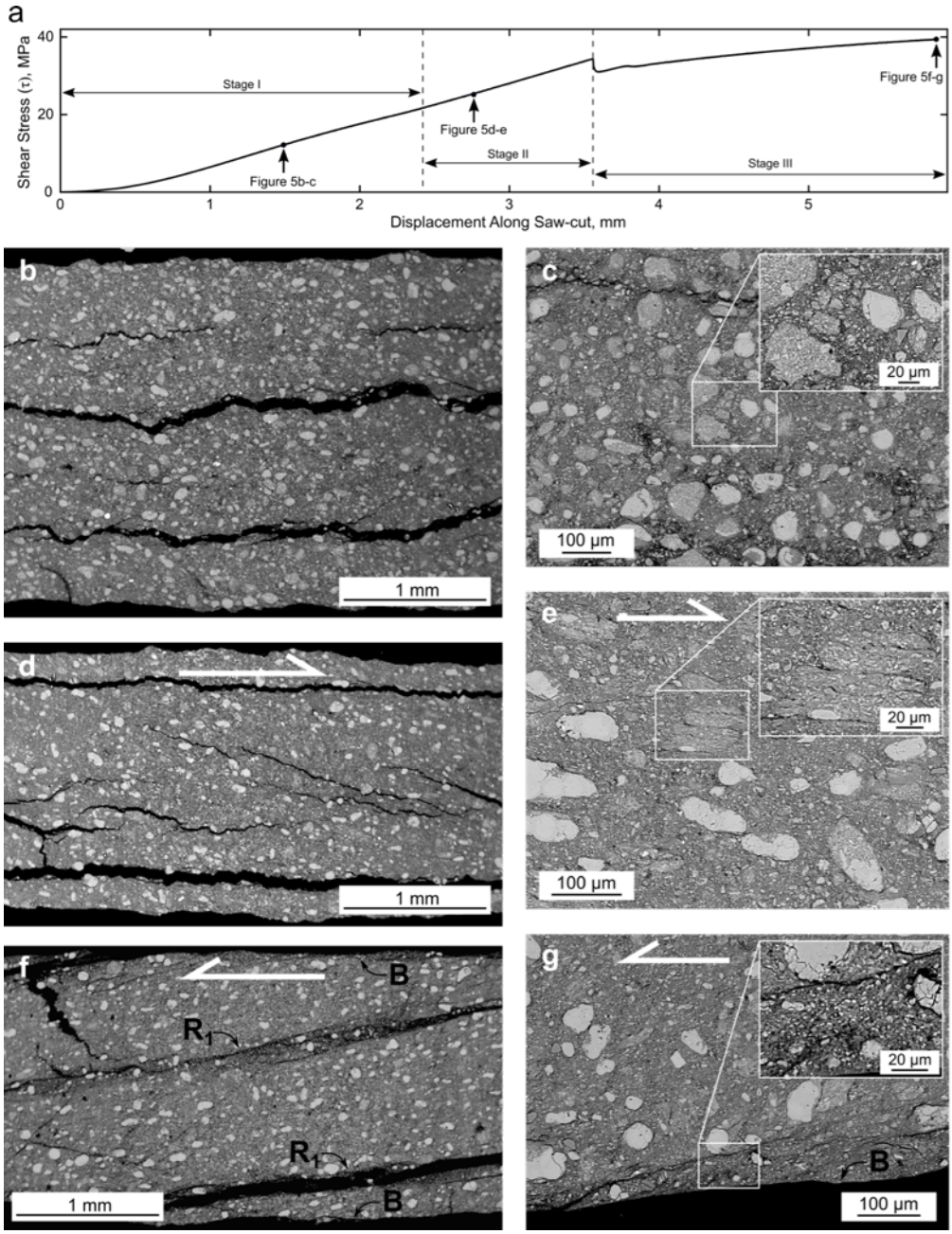

Figure 3.5. SEM micrograph showing microstructures developed in samples with different amount of total displacement. (a) Shear stress evolution with increasing displacement along saw-cut showing at which displacement and during which stage microstructures were collected. (b) Microstructure after 1.5 mm of displacement along saw-cut (experiment b619; Table 1) characterized by isotropically distributed clasts of marl. (c) Detail of microstructure after 1.5 mm of displacement in (b) showing marly clasts in a fine and loose matrix composed of clay flakes and calcite grains. Inset shows marly clasts that are angular and irregular in shape. (d) Microstructure after 2.75 mm of displacement along saw-cut (experiment b617; Table 1) characterized by elongated clasts oriented consistently with the shear direction and incipient Riedel shears. (e) Detail of microstructure after 2.75 mm of displacement in (d) showing elongated clasts oriented accordingly to the shear direction. Inset shows a rounded clast in a dense and well-packed matrix. (f) Microstructure after 6 mm of displacement along saw-cut (experiment b611; Table 1) characterized by localized Riedel (R_1) and boundary (B) shear planes (*Logan et al.*, 1992). (g) Details of a boundary shear planes in (f). Inset shows the concentration of fine clay and calcite fragments along the B shear planes.

After 1.5 mm of displacement along saw-cut, i.e. during Stage I, the microstructure is characterized by clasts of marl isotropically distributed in a fine and loose matrix composed of clay flakes and calcite grains (Figure 3.5b-c). The marly clasts are irregular in shape and characterized by jagged boundaries (Figure 3.5c). Increasing the amount of shear displacement up to 2.75 mm, i.e. during Stage II, marly clasts are more rounded and, if elongated, oriented accordingly to the shear direction (Figure 3.5d). With respect to gouge in Figure 3.5c, the matrix is denser and well-packed (Figure 3.5e). At the end of Stage III, after a shear displacement of 6 mm, the deformation is localized along shear planes parallel and at low angle to the saw-cut, i.e. respectively boundary and Riedel shear planes (Figure 3.5f-g) (*Logan et al.*, 1992). These shear planes are characterized by higher concentration of finer clay and calcite fragments with respect to the surrounding gouge (Figure 3.5f). Fine-grained gouge along boundary and Riedel shear planes derives from disaggregation of marly clasts and comminution of calcite grains.

3.4. Discussion

3.4.1. Integration of mechanical data and microstructures

Based on the integration of mechanical data and microstructures, we propose the following micromechanical evolution of fault reactivation during saw-cut experiments. During yielding in Stage I and strain-hardening in Stage II, the experimental fault evolves from a loosely packed and randomly oriented fabric to a densely packed fabric, as documented by the difference between microstructures after 1.5 (Stage I) and 2.75 mm of displacement (Stage II) (Figure 3.5b-c vs. Figure 3.5d-e). We infer that gouge compaction, documented during yielding and strain-hardening, occurs via distributed cataclastic flow. The linear strain-hardening characterizing Stage II ends with a stress drop that indicates fault frictional reactivation. Slip within the reactivated experimental fault is associated with localized deformation (Figure 3.5f-g). We infer that the transition from distributed deformation (Stage I and II) to slip localization along shear planes (onset of Stage III) results in and stress release and thus sudden fault slip, similarly to previous experimental studies indicating that localization promotes slip instability (e.g., *Moore et al., 1989*; *Logan et al.*, 1992; *Gu and Wong, 1994*; *Logan*, 2007; *Scuderi et al.*, 2017). Additionally, microstructures retrieved from Stage II characterized by Riedel and boundary incipient fractures (Figure 3.5d-e) suggest that incipient localization occurs before stress drops and fault frictional reactivation, as previously documented in experimental studies showing fault zone nucleation before dynamic failure (e.g., *Thompson et al.*, 2006; *Benson et al.*, 2007). Upon reactivation the experimental fault undergoes stress oscillations and strain-hardening (Figure 3.3), localizing the deformation along well-developed shear planes (Figure 3.5d-e).

3.4.2. Fault reactivation: theory versus experimental data

Assuming the experimentally constrained μ_i = 0.76 and c = 34.01 MPa for Pietraserena sandstone and μ_s = 0.62 for Candigliano marl, the mechanics of the samples with saw-cuts at different θ can be predicted by the single plane of weakness theory (Figure 3.6; Equations 3.1 and 3.2) (e.g., *Jaeger*, 1960). In Figure 3.6 we show the maximum σ_d supported by triaxial saw-cut samples before fault reactivation or new fracture development as a function of θ, comparing it with the plane of weakness theory. Theory predicts fault reactivation for $\theta <$ 55.9° and surrounding rock failure for $\theta >$ 55.9° (Figure 3.6). Accordingly, samples with saw-cuts oriented at θ = 30°-40°-50° accommodated the deformation sliding within the pre-

existing fault (Figure 3.3a), while samples with saw-cuts oriented at θ = 60°-70°-80° developed new fractures (Figure 3.4).

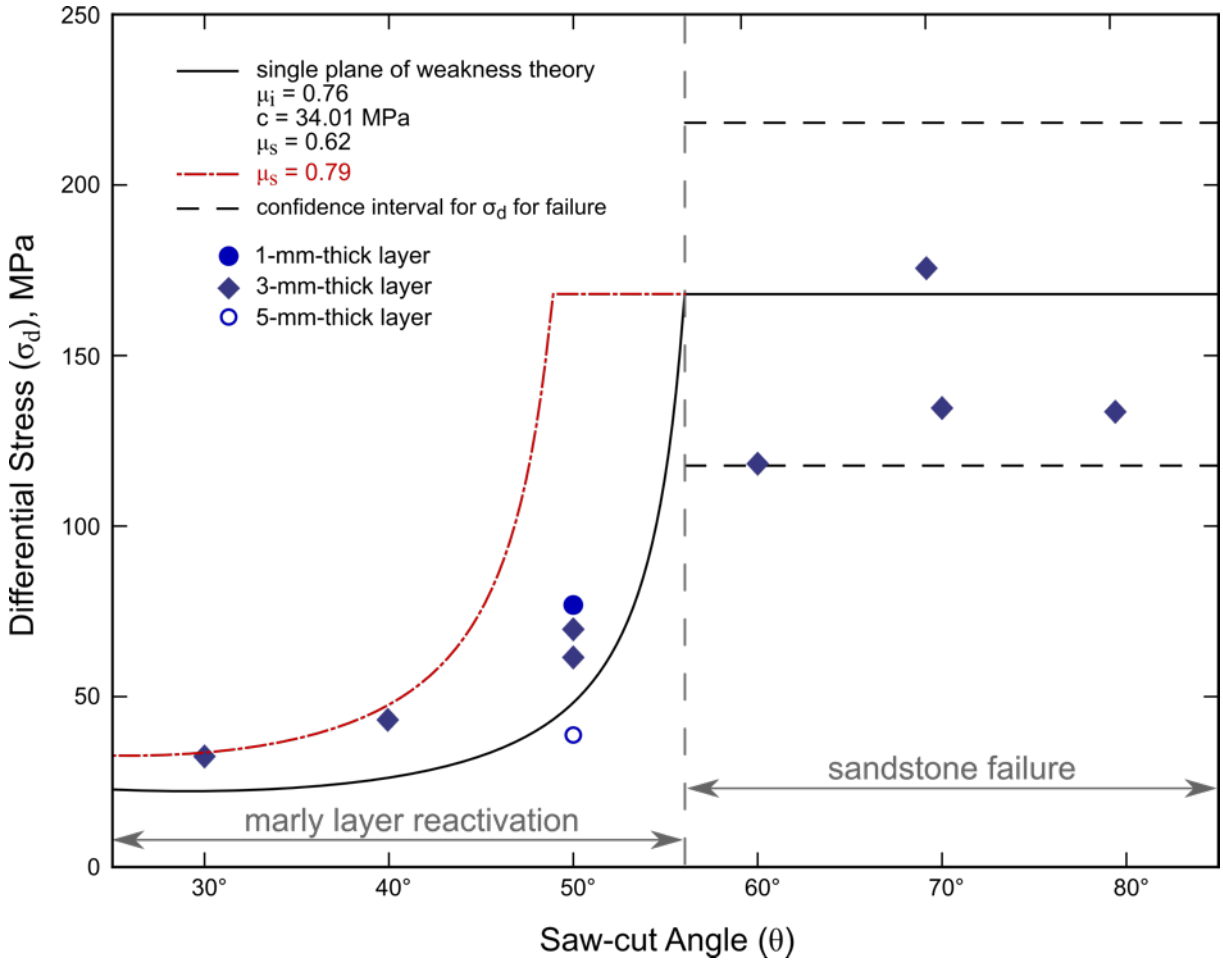

Figure 3.6. (c) Results from triaxial saw-cut experiments compared to the single plane of weakness theory (black line; see Equations 3.1 and 3.2) reconstructed on the grounds of the Pietraserena sandstone strength (μ_i = 0.76 and c = 34.01 MPa) (Figure 3.2a) and the Candigliano marl friction (μ_s = 0.62) (Figure 3.2b). The predicted sandstone strength is reported along with the confidence interval (two-sided, 95%) calculated on the base of the residuals of the linear regression (Figure 3.2a). The maximum σ_d supported by triaxial saw-cut samples before fault reactivation or new fracture development is plotted against the saw-cut angle. Slip within the fault occurs for θ = 30°-40°-50°, whereas the development of a new fracture occurs for θ = 60°-70°-80°, in agreement with theoretical predictions. The σ_d required for reactivation is systematically higher than the theoretical value predicted assuming $\mu_s = tan(\varphi_s)$. Conversely, considering $\mu_s = sin(\varphi_s)$ = 0.79 (red dashed line), i.e. the internal friction of marl, the σ_d required for reactivation of favorably oriented faults is well-predicted. Moreover, the σ_d required for reactivation at θ = 50° decreases with increasing gouge layer thickness.

Severely misoriented saw-cuts, i.e. θ = 60°-70°-80°, failed at σ_d values that are consistent with the failure strength of the sandstone (Figures 3.6). The σ_d required for reactivation of 3-mm-thick layers increases with increasing θ and strongly decreases with increasing layer thickness (Figures 3.3e-f and 3.6). Discrepancies between the model and the experimental data are marked in reactivated saw-cuts, i.e. θ = 30°-40°-50°. Particularly, reactivation of 3-mm-thick experimental fault requires σ_d that are higher than theoretically predicted. The apparent friction μ_a obtained dividing τ by σ_n values required for saw-cut reactivation is

higher than the sliding friction of marl from friction experiments, i.e. μ_a = 0.66-0.79 > μ_s = 0.62. Additionally, μ_a systematically decrease with increasing θ, as documented by previous triaxial experiments on gouge-filled saw-cut samples with variable θ (*Savage et al.*, 1996).

We interpret the discrepancy between saw-cut apparent friction and double-direct shear sliding friction as follow. In friction experiments in which the fault is loaded at constant normal stress (e.g., double-direct shear configuration), after the achievement of the steady-state, the maximum principal stress is oriented at 45° to the saw-cut (e.g., *Mandl*, 1977). It follows that the estimated friction from the linear envelope (Figure 3.2b) is an apparent value and the real internal friction of marly gouge, calculated by $\mu_i = sin(tan^{-1}(\mu_s))$ (e.g., *Marone et al.*, 1992; *Scott et al.*, 1994b; *Beeler et al.*, 2000), is μ_i = 0.79. During triaxial saw-cut experiments, well-oriented saw-cuts (θ = 30°) reactivate for apparent friction values μ_a = 0.79 - 0.78 that are consistent with the real internal value μ_i = 0.79. This observation is in agreement with previous studies suggesting that an optimally oriented gouge layer theoretically deforms at a friction value that corresponds to the internal friction of the gouge (e.g., *Byerlee and Savage*, 1992). Accordingly, considering the internal friction of the marly gouge μ_i = 0.79, the optimum θ for reactivation is 26° and almost coincides with well-oriented saw-cut (θ = 30°). The reactivation of progressively more misoriented saw-cuts occurs at progressively lower values, i.e. μ_a = 0.76 for θ = 40°and μ_a = 0.66 - 0.67 for θ = 50°. This decrease μ_a due to the departure from optimum θ possibly results from the re-orientation of the stress field within the gouge layer during the distributed cataclastic flow of Stage I and II (e.g., *Byerlee and Savage*, 1992; *Lockner and Byerlee*, 1993; *Gu and Wong*, 1994).

In addition, layer thickness drastically influences the differential stress required for misoriented fault reactivation. Indeed, the reactivation of the 1-mm-thick gouge layer occurred at $\sigma_d \approx$ 80 MPa, that is twice the σ_d required for the reactivation of the 5-mm-thick gouge layer, i.e. $\sigma_d \approx$ 40 MPa (Figure 3.3f and 3.5). Accordingly, the apparent friction decreases from μ_a = 0.69 to μ_a = 0.58 with increasing layer thickness, as also documented in previous studies (e.g., *Dieterich*, 1981; *Anthony and Marone*, 2005). Comparing our mechanical data with theory, slip within a thin gouge layer occurs accordingly to the frictional reactivation of a fault with μ_s = 0.79, i.e. the estimated internal friction of marl, while the behavior of a thick gouge layer strongly departs from theoretical predictions (Figure 3.6). Since the differential stress supported by the surrounding sandstone is not dependent upon layer thickness, differences in differential stress are thus carried by the clast-supported fabric

of the gouge layer. This clast-supported fabric contains a number of load-bearing contacts across the layer that depends on the layer thickness. Consequently, a thicker layer containing a higher number of contacts results in more points of potential failure and, since the force is distributed on a larger number of contacts, supports lower differential stress with respect to a thinner layer (e.g., *Anthony and Marone*, 2005).

3.4.3. The dynamics of fault reactivation

The reactivation of the experimental fault occurs via stress drops (Figure 3.3), suggesting that during Stage II the densely packed gouge (Figure 3.5d-e) accumulates at least part of the deformation elastically. Once the differential stress for reactivation is achieved, the slip mode, i.e. via stable vs. unstable sliding, depends on the elastic interactions between the fault and the loading system (e.g., *Rice*, 1983). Condition for instability is matched when the decrease of fault frictional strength with displacement exceeds the elastic unloading of the surrounding (e.g., *Rice*, 1983; *Kanamori and Brodsky*, 2004).

The strain-hardening of Stage II contains a linear portion whose slope represents in a first approximation the elasticity of the loading system (Figure 3.7a). In triaxial saw-cut experiments, the loading system coincides with the entire column sample resulting from the contribution of the sample and the vertical loading frame. The column and the sample can be considered an assembly of elastic members connected in series (e.g., *Shimamoto et al.*, 1980). Thus the inverse of the total stiffness of the loading system results from the stiffness of each elastic members as follow:

$$\frac{1}{k_{tot}} = \frac{1}{k'_{la}} + \frac{1}{k'_{ss}} + \frac{1}{k_g} \tag{3.11}$$

where k'_{la} is the stiffness of the vertical loading frame in the direction parallel to the saw-cut, k'_{ss} is the stiffness of the Pietraserena sandstone in the direction parallel to the saw-cut and k_g is the shear stiffness of the marly gouge. Knowing that the stiffness of the loading apparatus on the vertical axis from calibration tests is k_{la} = 771.2 kN/mm at P_c = 10 MPa and that the stiffness of the Pietraserena sandstone from triaxial experiments is k_{ss} = 240.5 kN/mm at P_c = 10, we evaluated k'_{la} and k'_{ss} as follows (e.g., *Goodman and Sundaram*, 1978; *He et al.*, 1998):

$$k'_{ss} = k_{ss}\,\mathrm{sen}^2(90-\theta)\cos(90-\theta)$$

$$k'_{la} = k_{la}\,\mathrm{sen}^2(90-\theta)\cos(90-\theta) \tag{3.12}$$

The resulting contributions parallel to the saw-cut are k'_{ss} = 67 - 78 - 81 MPa/mm and k'_{la} = 221 - 258 - 266 MPa/mm depending on θ. Following Equation 3.11 and 3.12, we evaluated the change in gouge stiffness as a function of the saw-cut angle (Figure 3.7). Since the gouge is the most compliant among the elastic members, gouge stiffness is systematically higher than the total stiffness of the loading system, i.e. $k_g > k_{tot}$. Upon reactivation, slip localizes along shear planes (Figure 3.5d-e vs. Figure 3.5f-g). The decrease of the frictional strength of the shear planes with displacement, that is assumed to be $-k_g$, is faster than the elastic unloading of the loading system $-k_{tot}$, resulting in force imbalance, fault acceleration and sudden stress drops (Figures 3.7b and 3.8). Moreover, gouge stiffness strongly increases with progressively misorienting the saw-cut (Figure 3.7b), similarly to theoretical simulations in which the stress state of a fault is perturbed with stress increments non-parallel to the fault (e.g., *Dieterich and Linker*, 1992).

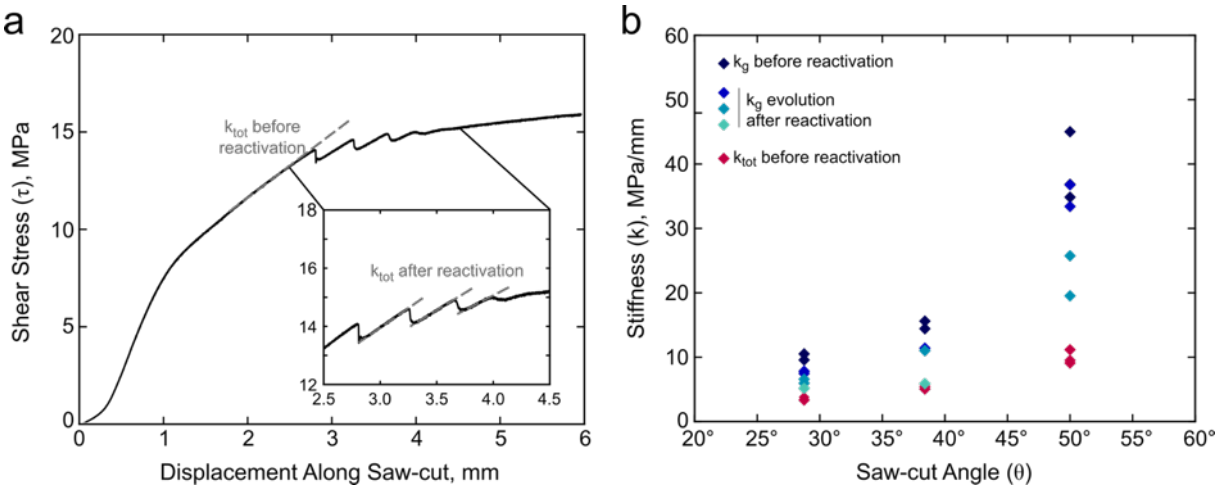

Figure 3.7. Shear stiffness evolution in reactivated saw-cuts. (a) Shear stress plotted versus displacement along saw-cut. The slope of the linear increase before the first stress drop represents the total shear stiffness (k_{tot}). Inset shows in detail the stress drops. This stress drops are preceded by linear loading phases that are progressively less steep with increasing displacement and that represent the evolution with increasing displacement of the total stiffness (k_{tot}). (b) Shear stiffness plotted against the saw-cut angle. Shear stiffness increases with progressively misoriented saw-cuts. Gouge stiffness before reactivation (k_g) is systematically higher than the total stiffness before reactivation (k_{tot}). Fault stiffness after reactivation is lower than gouge stiffness before reactivation (k_g) and decreases with increasing displacement approaching the initial total stiffness (k_{tot}).

Upon reactivation, the continuing deformation (Stage III) is characterized by few stick-slip events that are progressively dampened until stable sliding is achieved. Particularly, the elastic loading of these stick-slip events is progressively less steep with increasing displacement (Figure 3.7a). Assuming that the loading apparatus and the sandstone have the same stiffness throughout all the experiment and following Equations 3.9, we evaluated the evolution of the stiffness of the gouge layer from the elastic loading of the stick-slip events. Figure 3.7b shows that the gouge layer progressively de-stiffens approaching the total stiffness of the loading system. We suggest that the weakening rate of the experimental fault

with slip slows progressively until it exceeds the elastic unloading of the loading system, resulting in the observed transition from unstable to stable sliding (Figures 3.7b and 3.8).

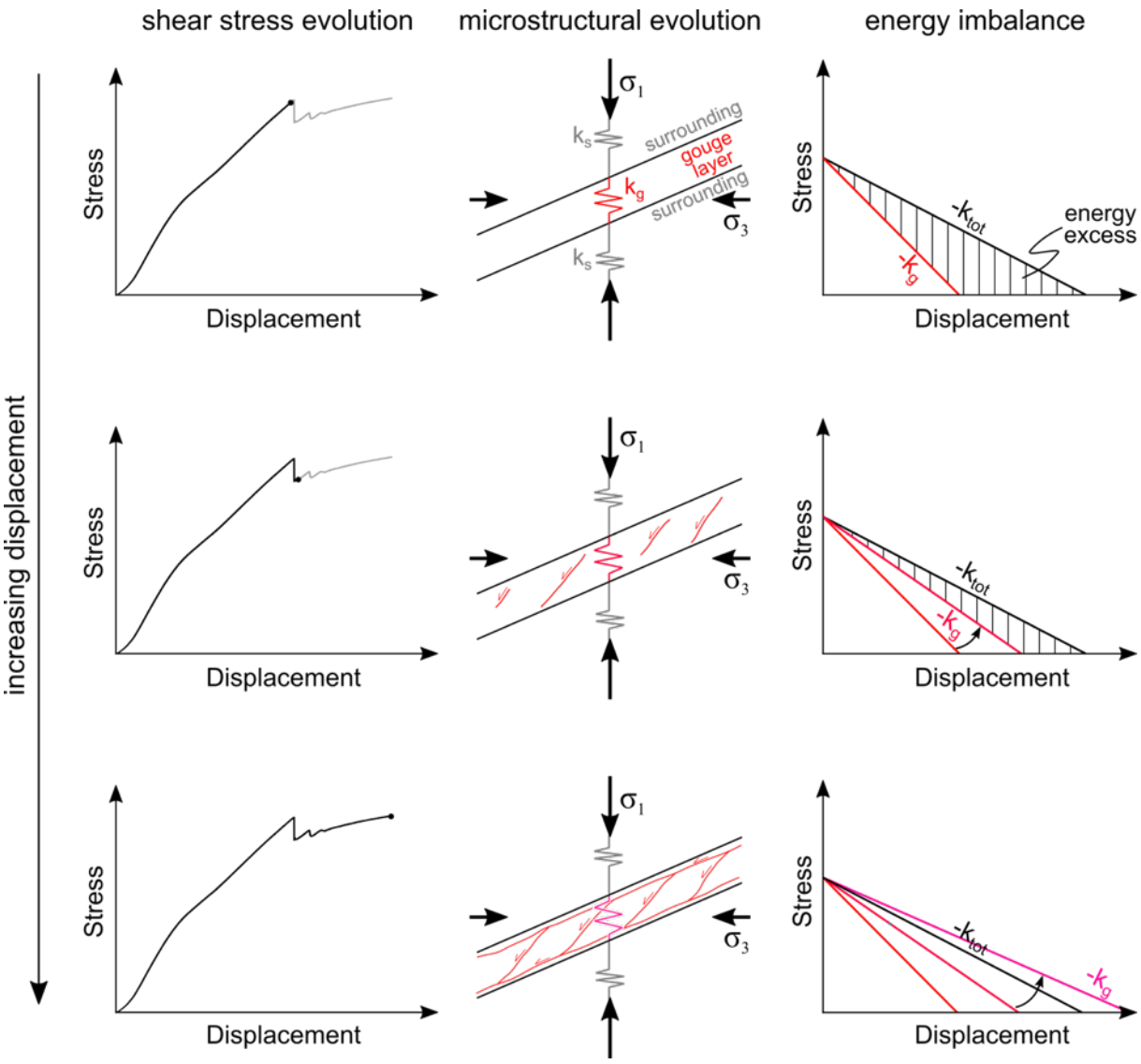

Figure 3.8. Conceptual micro-mechanical evolution of the experimental fault during reactivation. The experimental fault during Stage II accumulates at least part of the deformation elastically accordingly to gouge stiffness k_g. Gouge stiffness k_g is systematically higher than total stiffness k_{tot} (Equation 3.11). Upon reactivation, since the weakening rate of the fault is faster than the elastic unloading of the system, incipient shear planes within the fault zone suddenly slip, releasing the exceeding energy.

However, we acknowledge that further investigations are required to constrain seismic vs. aseismic reactivation of non-optimally oriented faults. To date, laboratory investigations on fault stability has been extensively conducted simulating experimental faults loaded under constant normal stress condition (e.g., *Dieterich*, 1979; *Ruina*, 1983; *Gu et al*., 1984; *Marone*, 1998b; *Leeman et al*., 2016; *Scuderi et al.,* 2016). However natural faults can be loaded under load-strengthening and load-weakening conditions and very little has known about the role that loading path has on fault stability, i.e. seismic vs. aseismic reactivation. Future work will build on these observations to constrain stable vs. unstable fault reactivation.

3.4.4. Implications for natural faults

Faults in nature are loaded by increasing the maximum principal stress, by reducing the minimum principal stress or by a combination of both (e.g., *Sibson*, 1993). Therefore, the tectonic loading direction is usually inclined to the fault plane, resulting in coupled shear and normal stress increase (e.g., *Sibson*, 1991). Dynamic slip is accompanied by both shear and normal stress drop whenever a fault is non-planar or the elastic is non-homogeneous. Experimentally simulating these conditions, we experimentally validate the single plane of weakness theory (*Jaeger*, 1960), showing that the reactivation is primarily controlled by the interplay between fault friction and surrounding rock strength. The occurrence or not of experimental fault reactivation is well constrained by theoretical predictions.

Analytical approaches to evaluate fault reactivation are generally based on the assumption that faults are planes of weakness characterized by a certain friction (e.g., *Sibson*, 1985; *Morris et al.*, 1996). However, natural faults are complex structures of finite thickness (e.g., *Caine et al.*, 1996; *Ben-Zion and Sammis*, 2003). Our findings point out that the presence of a finite thickness fault and its thickness strongly control the amount of stress required for reactivation. The presence of a finite thickness fault promotes the reorientation of the stress field within the fault zone and consequently the weakening of misoriented faults. In our experiments, fault gouge and boundary conditions being equal, misoriented faults appear to be weak when compared to favorably oriented faults, as documented in previous experimental studies (*Savage et al.*, 1996). We experimentally corroborate that the stress reorientation effectively contributes to enhancing slip along misoriented faults, as previously proposed by theoretical studies (e.g., *Byerlee and Savage*, 1992; *Gu and Wong*, 1994; *Faulkner et al.*, 2006). Moreover, our study shows that the thickness of the gouge layer strongly influences the maximum differential stress that a fault supports before reactivation. These observations suggest that the assumption of a zero-thickness, planar fault provides an upper bound on the stress required for reactivation. Thus, we conclude that natural faults characterized by fault zones of finite thickness, especially if misoriented, can appear weaker than theoretically predicted.

3.5 Conclusions

We investigated the reactivation of pre-existing faults of finite thickness at different orientation to the maximum principal stress. We simulated experimental faults from optimally oriented to severely misoriented for frictional reactivation by conducting triaxial experiments with gouge-filled saw-cuts at different angles to the maximum principal stress. Our results validate the single plane of weakness theory for experimental faults of finite thickness, showing that the reactivation is mainly controlled by the interplay between the friction of the marly layer and the strength of the surrounding sandstone. However, the differential stress and thus the apparent friction required for experimental fault reactivation decreases with increasingly misoriented layer from 30° to 50° to the maximum principal stress. We interpret this weakening as the evidence of the reorientation of the maximum principal stress within the misoriented weak layers. Concurrently, our results show that the thickness of the fault gouge influences the differential stress for reactivation. A thick layer of fault gouge contains a high number of load-bearing contacts resulting in reactivation at lower differential stress than a thin layer. Our study suggests that the assumption of a zero-thickness fault provides an upper bound on the stress required for reactivation and that misoriented natural faults of finite thickness appears weaker than theoretically predicted.

Moreover, the micro-mechanical evolution of experimental faults suggests that the reactivation, occurring via stress drops, results from the transition from distributed to localized deformation. We tentatively suggest that fault reactivation via stick-slips results from the interplay between the weakening rate with slip of the gouge and the elastic unloading of the loading system. In particular, we propose that a fault that undergoes any loading path, i.e. under variable normal stress, can constitute a compliant layer able to de-stiffen the overall loading system, matching the condition required for frictional instabilities. However, we propose that further investigations are required to constrain stable vs. unstable reactivation of finite-thickness faults that are variably oriented to the maximum principal stress and that thus undergoes variable loading paths.

Acknowledgments

The Authors thank D. Mannetta for high quality thin section preparation, M. Nazzari and M. Albano for assistance with the SEM and M. Mercuri for fruitful discussions. This research was funded by the ERC Starting Grant GLASS project (n° 259256) and Fondi Ateneo Sapienza 2015 to C. Collettini.

Conclusion

I investigated different aspects of the role of phyllosilicates in brittle rock deformation and in particular: 1) how the amount of talc influences the frictional properties of carbonate faults, 2) how the mechanical stratigraphy due to the alternation of clay-rich and calcite-rich layers influences the development and the growth of faults and 3) how the orientation of the stress field influences the reactivation of clay-rich faults.

I reported that the development of an interconnected talc network (20% wt. of talc) fully weakens experimental carbonate faults under water-saturated conditions. These results are in agreement with previous studies on phyllosilicates-bearing faults suggesting that the inherent weakness of phyllosilicates is related to their sheet structures. Interestingly, I documented that dispersed talc in the experimental fault (5% wt. of talc) strongly influences the velocity-dependence and the healing rate. This small amount of talc is capable of promoting an evolution from velocity-neutral to velocity-strengthening behavior and the halving of the healing rate. This mechanical behavior suggests that chemical processes may control frictional behavior of talc-bearing carbonate faults even at shallow crustal conditions. Thus the development of even minor amount of talc in carbonate faults possibly influences their slip behavior, promoting aseismic slip.

I showed that the complex trajectories characterizing incipient faults in clay-rich mechanical multilayers result from the interplay between the mechanical properties of the involved lithologies and the presence of pre-existing discontinuities. Particularly, pre-existing joints in calcite-rich layers and sedimentary foliation in clay-rich layers constitute pre-existing planes of weakness. Their reactivation explains severely misoriented fault segments. As a consequence, clay-rich layers appear extremely weak not only because of their intrinsic low friction but also because of their strong foliation. Moreover, with increasing displacement, faults develop fault cores characterized by clay-rich foliation. Their angles of reactivation are consistent with clay-rich marl friction, further underlining the key role exerted by clay minerals on fault strength.

I experimentally validated the single plane of weakness theory, that is a generalization of the Coulomb failure criterion, for a finite-thickness fault. In particular, I tested whether or not the reactivation of an experimental pre-existing fault occurs as a function of its orientation within the applied stress field. However, I suggest that the assumption of a zero-thickness fault provides an upper bound on the stress required for reactivation, because the differential stress for the reactivation of a finite-thickness misoriented fault is always lower than the

theoretical predictions. Microstructural and mechanical evolution of the experimental fault with increasing displacement suggests that the transition from distributed to localized shear and the occurrence of stress drops mark its reactivation. The unstable reactivation via stress drops is still not well constrained in the experiments of the present work, suggesting the need to better understand how the orientation of the stress field influences fault stability (seismic vs. aseismic reactivation). The evaluation of fault stability is theoretically based on the assumption that the normal stress clamping the fault is constant. However, natural faults can be also loaded under load-strengthening or load-weakening conditions. Based on these considerations, this study provides inputs and possible directions for future research.

Bibliography

Abbate, E., V. Bortolotti, P. Passerini, and M. Sagri (1970), Introduction to the geology of the Northern Apennines, *Sedimentary Geology*, *4*(3), 207-249, doi:10.1016/0037-0738(70)90017-5.

Agosta, F., and D. L. Kirschner (2003), Fluid conduits in carbonate-hosted seismogenic normal faults in central Italy, *J. Geophys. Res. Solid Earth*, *108*(B4), 2221-2234, doi:10.1029/2002JB002013.

Allmendinger, R.W., N.C Cardozo, D. Fisher (2012), *Structural Geology Algorithms: Vectors and Tensors*, Cambridge Univ. Press, Cambridge, U. K.

Alvarez, W. (1991), Tectonic evolution of the Corsica-Apennines-Alps region studied by the method of successive approximations, *Tectonics*, *10*, 936-947, doi:10.1029/91TC00232.

Anderson, E.M (1951), *The Dynamics of Faulting and Dyke Formation with Applications to Britain*, Oliver & Boyd, Edinburgh.

Anthony, J. L., and C. Marone (2005), Influence of particle characteristics on granular friction, *J. Geophys. Res.*, 110, B08409, doi:10.1029/2004JB003399.

Antonellini, M., E. Tondi, F. Agosta, A Aydin, and G. Cello (2008), Failure modes in deep-water carbonates and their impact for fault development: Majella Mountain, Central Apennines, Italy, *Marine and Petroleum Geology*, *25*(10), 1074-1096, doi:10.1016/j.marpetgeo.2007.10.008.

Atkinson, B. K., and P. G. Meredith (1989), The theory of sub-critical crack growth with application to minerals and rocks, in *Fracture Mechanics of Rocks*, edited by Atkinson, B. K., pp. 111-166, Academic, San Diego, Calif.

Aydin, A. (2000), Fractures, faults, and hydrocarbon entrapment, migration and flow. *Marine and petroleum geology*, *17*(7), 797-814, doi:10.1016/S0264-8172(00)00020-9.

Bally, A.W., L. Burbi, C. Cooper, and R. Ghelardoni (1986), Balanced sections and seismic reflection profiles across the Central Apennines, *Società Geologica Italiana*, *Memorie*, *35*, 257-310.

Barchi, M.R., A. Bernasconi, F. Brozzetti, G. Lavecchia, M. Menichetti, G. Minelli, S. Nardon, and G. Pialli (1993), Joint distribution in a Fractured Carbonate Reservoir in the Umbria-Marche Anticlines (Central Italy). in *Generation, Accumulation and Production of Europe's Hydrocarbons III*, *Special Publication of the European Association of Petroleum Geoscientists*, edited by A. M. Spencer, pp. 209-217, Springer, Berlin, doi:10.1007/978-3-642-77859-9_17.

Barchi, M.R., A. Landuzzi, G. Minelli, and G. Pialli (2001), Outer northern Apennines, in *Anatomy of an Orogen: the Apennines and Adjacent Mediterranean Basins*, edited by G. B. Vai and I. P. Martini, pp. 215-254, Kluwer Academic Publishers, Dordrecht, The Netherlands, doi:10.1007/978-94-015-9829-3_15.

Barchi, M.R., W. Alvarez, D. H. Shimabukuro (2012), The Umbria-Marche Apennines as a double orogen: observations and hypotheses, *Italian Journal of Geosciences*, *131*(2), 258-271, doi:10.3301/IJG.2012.17.

Bebout, G. E., and M. D. Barton (2002), Tectonic and metasomatic mixing in a high-T, subduction-zone mélange: Insights into the geochemical evolution of the slab-mantle interface, *Chem. Geol.*, *187*, 79-106, doi:10.1016/S0009-2541(02)00019-0.

Beeler, N. M., R. W. Simpson, S. H. Hickman, and D. A. Lockner (2000), Pore fluid pressure, apparent friction, and Coulomb failure, *J. Geophys. Res.*, 105(B11), 25533–25542, doi:10.1029/2000JB900119.

Beeler, N. M., T. E. Tullis, A. K. Kronenberg, and L. A. Reinen (2007), The instantaneous rate dependence in low temperature laboratory rock friction and rock deformation experiments, *J. Geophys. Res.*, *112*, B07310, doi:10.1029/2005JB003772.

Benson, P. M., B. D. Thompson, P. G. Meredith, S. Vinciguerra, and R. P. Young (2007), Imaging slow failure in triaxially deformed Etna basalt using 3D acoustic-emission location and X-ray computed tomography, *Geophys. Res. Lett.*, *34*, L03303, doi:10.1029/2006GL028721.

Ben-Zion, Y., and C. G. Sammis (2003), Characterization of fault zones, in *Seismic Motion, Lithospheric Structures, Earthquake and Volcanic Sources: The Keiiti Aki Volume*, edited by Y. Ben-Zion, pp. 677-715, Birkhäuser Basel.

Bernoulli, D., and H. Weissert (1985), Sedimentary fabrics in Alpine ophicalcites, South Pennine Arosa zone, Switzerland, *Geology*, *13*, 755-758, doi:10.1130/0091-7613(1985)13<755:SFIAOS>2.0.CO;2.

Billi, A. (2010), Microtectonics of low-P low-T carbonate fault rocks, *J. Struct. Geol.*, *32*, 1392-1402, doi:10.1016/j.jsg.2009.05.007.

Bistacchi, A., M. Massironi, L. Menegon, F. Bolognesi, and V. Donghi (2012), On the nucleation of non-Andersonian faults along phyllosilicate-rich mylonite belts, in *Faulting, Fracturing and Igneous Intrusion in the Earth's Crust*, vol. 367, edited by D. Healy et al., pp. 185-199, Geol. Soc., London, doi:10.1144/SP367.13.

Blanpied, M. L., C. J. Marone, D. A. Lockner, J. D. Byerlee, and D. P. King (1998), Quantitative measure of the variation in fault rheology due to fluid-rock interactions, *J. Geophys. Res.*, 103, 9691–9712, doi:10.1029/98JB00162.

Bolognesi, F., and A. Bistacchi (2016), Weakness and mechanical anisotropy of phyllosilicate-rich cataclasites developed after mylonites of a low-angle normal fault (Simplon Line, Western Alps), *J. Struct. Geol.*, *83*, 1-12, doi:10.1016/j.jsg.2015.11.009.

Bolton, M. (1979), *A Guide to Soil Mechanics*, John Wiley, New York.

Bos, B., and C. J. Spiers (2000), Effect of phyllosilicates on fluid-assisted healing of gouge-bearing faults, *Earth Planet. Sci. Lett.*, *184*, 199-210, doi:10.1016/S0012-821X(00)00304-6.

Bos, B., and C. J. Spiers (2001), Experimental investigation into the microstructural and mechanical evolution of phyllosilicate-bearing fault rock under conditions favouring pressure solution, *J. Struct. Geol*., *23*, 1187-1202, doi:10.1016/S0191-8141(00)00184-X.

Bos, B., and C. J. Spiers (2002), Fluid-assisted healing processes in gouge-bearing faults: Insights from experiments on a rock analogue system, *Pure Appl. Geophys.*, *159*, 2537-2566, doi:10.1007/s00024-002-8747-2.

Bos, B., C. J. Peach, and C. J. Spiers (2000), Slip behavior of simulated gouge-bearing faults under conditions favoring pressure solution, *J. Geophys. Res.*, *105*(B7), 16699-16717, doi:10.1029/2000JB900089.

Boschi, C., G. L. Früh-Green, and J. Escartín (2006), Occurrence and significance of serpentinite-hosted, talc- and amphibole-rich fault rocks in modern oceanic settings and ophiolite complexes: An overview, *Ofioliti*, *31*, 129-140.

Boutareaud, S., T. Hirose, M. Andréani, M. Pec, D.-G. Calugaru, A.-M. Boullier, and M.-L. Doan (2012), On the role of phyllosilicates on fault lubrication: Insight from micro- and nanostructural investigations on talc friction experiments, *J. Geophys. Res.*, *117*, B08408, doi:10.1029/2011JB009006.

Brace, W. F., and J. D. Byerlee (1966), Stick-Slip as a Mechanism for Earthquakes, *Science*, *153*(3739), 990-992, doi: 10.1126/science.153.3739.990.

Brace, W. F., B. W. Paulding Jr., and C. Scholz (1966), Dilatancy in the fracture of crystalline rocks, *J. Geophys. Res.*, *71*(16), 3939-3953, doi:10.1029/JZ071i016p03939.

Brown, K.M., A. Kopf, M. B. Underwood, and J. L. Weinberger (2003), Compositional and fluid pressure controls on the state of stress on the Nankai subduction thrust: a weak plate boundary, *Earth and Planetary Science Letters*, 214, 589–603.

Byerlee, J. D. (1978), Friction of rocks, *Pure Appl. Geophys.*, *116*, 615-626, doi:10.1007/BF00876528.

Byerlee, J. D., and J. C. Savage (1992), Coulomb plasticity within the fault zone. *Geophys. Res. Lett.*, 19(23), 2341-2344, doi:10.1029/92GL02370.

Caine, J. S., J. P. Evans, and C. B. Forster (1996), Fault zone architecture and permeability structure., *Geology*, *24*(11), 1025-1028, doi:10.1130/0091-7613(1996)024<1025:FZAAPS>2.3.CO;2.

Capuano, N., E. Levati, S. Merangola, G. Pappafico, M. Pera, G. Tonelli, S. Tosti, and M. Tramontana (2009), *Carta Geologica d'Italia alla scala 1:50.000*, F° 279 Urbino, Servizio Geologico D'Italia.

Carmignani, L., F. A. Decandia, L. Disperati, P. L. Fantozzi, R. Kligfield, A. Lazzarotto, D. Liotta, and M. Meccheri (2001), Inner Northern Apennines, in *Anatomy of an Orogen: the Apennines and Adjacent Mediterranean Basins*, edited by G. B. Vai and I. P. Martini, pp. 197-213, Kluwer Academic Publishers, Dordrecht, The Netherlands.

Carminati, E., and C. Doglioni (2012), Alps vs. Apennines: the paradigm of a tectonically asymmetric Earth, *Earth-Science Reviews*, *112*(1), 67-96, doi:10.1016/j.earscirev.2012.02.004.

Carpenter, B. M., C. Marone, and D. M. Saffer (2011), Weakness of the San Andreas Fault revealed by samples from the active fault zone, *Nat. Geosci.*, *4*, 251-254, doi:10.1038/ngeo1089.

Carpenter, B. M., M. M. Scuderi, C. Collettini, and C. Marone (2014), Frictional heterogeneities on carbonate-bearing normal faults: Insights from the Monte Maggio Fault, Italy, *J. Geophys. Res. Solid Earth*, *119*, 9062-9076, doi:10.1002/2014JB011337.

Carpenter, B. M., C. Collettini, C. Viti, and A. Cavallo (2016a), The influence of normal stress and sliding velocity on the frictional behaviour of calcite at room temperature: insights from laboratory experiments and microstructural observations, *Geophys. J. Int.*, *205*(1), 548-561, doi:10.1093/gji/ggw038.

Carpenter, B. M., M. J. Ikari, and C. Marone (2016b), Laboratory observations of time-dependent frictional strengthening and stress relaxation in natural and synthetic fault gouges, *J. Geophys. Res. Solid Earth*, *121*, 1183-1201, doi:10.1002/2015JB012136.

Centamore, E., A. Jacobacci, N. Malferrari, G. Martelli, and U. Pieruccini (1972), *Carta Geologica d'Italia alla scala 1:50.000*, F° 290 Cagli, Servizio Geologico D'Italia.

Chen, J., B. A. Verberne, and C. J. Spiers (2015), Interseismic re-strengthening and stabilization of carbonate faults by "non-Dieterich" healing under hydrothermal conditions, *Earth and Plan. Sci. Lett.*, *423*, 1-12, doi:10.1016/j.epsl.2015.03.044.

Chester, F. M., and J.M. Logan (1987), Composite planar fabric of gouge from the Punchbowl fault zone, California, *J. Struct. Geol.*, *9*, 621-634, doi:10.1016/0191-8141(87)90147-7.

Childs, C., T. Manzocchi, J. J. Walsh, C. G. Bonson, A. Nicol, and M. P. Schöpfer (2009), A geometric model of fault zone and fault rock thickness variations, *J. Struct. Geol.*, *31*(2), 117-127, doi:10.1016/j.jsg.2008.08.009.

Coccioni, R., R. Franchi, O. Nesci, N. Perilli, F. C. Wezel, and F. Battistini (1989), Stratigrafia, micropaleontologia e mineralogia delle Marne a Fucoidi (Aptiano inferiore-Albiano superiore) delle sezioni di Poggio le Guaine e del Fiume Bosso (Appennino umbro-marchigiano), *Evoluzione*, *Ambiente*, *Secondo Convegno Internazionale*: *Pergola*, *Italy*, *Atti*, 163-201.

Collettini, C., 2011. The mechanical paradox of low-angle normal faults: Current understanding and open questions. Tectonophysics, 510(3), 253-268.

Collettini, C., and R. H. Sibson (2001), Normal faults normal friction? *Geology*, *29*, 927-930, doi:10.1130/0091-7613(2001)029<0927:NFNF>2.0.CO;2.

Collettini, C., and R. E. Holdsworth (2004), Fault zone weakening and character of slip along low-angle normal faults: insights from the Zuccale fault, Elba, Italy, *J. Geol. Soc.*, *161*, 1039-1051, doi:10.1144/0016-764903-179.

Collettini, C., A. Niemeijer, C. Viti, and C. Marone (2009a), Fault zone fabric and fault zone weakness, *Nature*, *462*, 907-910, doi:10.1038/nature08585.

Collettini, C., C. Viti, S. A. F. Smith, and R. E. Holdsworth (2009b), Development of interconnected talc networks and weakening of continental low-angle normal faults, *Geology*, *37(6)*, 567-570, doi:10.1130/G25645A.1.

Collettini, C., A. Niemeijer, C. Viti, S. A. F. Smith, and C. Marone (2011), Fault structure, frictional properties and mixed-mode fault slip behavior, *Earth and Plan. Sci. Lett.*, *311*, 316-327, doi:10.1016/j.epsl.2011.09.020.

Collettini, C., B.M. Carpenter, C. Viti, F. Cruciani, S. Mollo, T. Tesei, F. Trippetta, L. Valoroso, L. Chiaraluce (2014a), Fault structure and slip localization in carbonate-bearing normal faults: An example from the Northern Apennines of Italy, *J. Struct. Geol.*, *67*, 154-166, doi: 10.1016/j.jsg.2014.07.017.

Collettini, C., G. Di Stefano, B. M. Carpenter, P. Scarlato, T. Tesei, S. Mollo, F. Trippetta, C. Marone, G. Romeo, and L. Chiaraluce (2014b), A novel and versatile apparatus for brittle rock deformation, *Int. J. Rock Mech. Min.*, *66*, 114-123, doi:10.1016/j.ijrmms.2013.12.005.

Corbett, K., M. Friedman, and J. Spang (1987), Fracture development and mechanical stratigraphy of Austin Chalk, Texas, *AAPG Bulletin*, *71*(1), 17-28.

Coulomb, C. A. (1776), Sur une application des règles de maximis et minimis à quèlques problèmes de statique relatifs à l'architecture, *Acad. Sci. Paris Mem. Math Phys.*, *7*, 343-382.

Crider, J. G., and D. C. P. Peacock (2004), Initiation of brittle faults in the upper crust: a review of field observations, *J. Struct. Geol*., *26*(4), 691-707, doi:10.1016/j.jsg.2003.07.007.

Davis, K. J., P. M. Dove, and J. J. De Yoreo (2000), The role of Mg^{2+} as an impurity in calcite growth, *Science*, *290*(5494), 1134-1137, *doi:*10.1126/science.290.5494.1134.

de Bresser, J. H. P., B. Evans, and J. Renner (2002), On estimating the strength of calcite rocks under natural conditions, in *Deformation mechanisms, rheology and tectonics: current status and future perspectives*, vol. 200, edited by S. de Meer et al., pp. 309-329, Geol. Soc., London, doi:10.1144/GSL.SP.2001.200.01.18.

den Hartog, S. A. M., C. J. Peach, D. A. M. De Winter, C. J. Spiers, and T. Shimamoto (2012), Frictional properties of megathrust fault gouges at low sliding velocities: new data on effects of normal stress and temperature, *J. Struct. Geol*., *38*, 156-171. doi:10.1016/j.jsg.2011.12.001.

den Hartog, S. A. M., D. M. Saffer, C. J. Spiers (2014), The roles of quartz and water in controlling unstable slip in phyllosilicate-rich megathrust fault gouges, *Earth, Planets and Space*, *66*, 78, doi:10.1186/1880-5981-66-78.

Dieterich, J. H. (1972), Time-dependent friction in rocks, *J. Geophys. Res*., *77*, 3690-3697, doi:10.1029/JB077i020p03690.

Dieterich, J. H. (1978), Preseismic fault slip and earthquake prediction, *J. Geophys. Res.*, *83*(B8), 3940-3948, doi:10.1029/JB083iB08p03940.

Dieterich, J. H. (1979), Modeling of rock friction: 1. Experimental results and constitutive equations, *J. Geophys. Res.*, *84*(B5), 2161-2168, doi:10.1029/JB084iB05p02161.

Dieterich, J. H. (1981), Constitutive properties of faults with simulated gouge, in *Mechanical behavior of crustal rocks: the Handin volume*, edited by N. L. Carter et al., pp. 103-120, AGU, Washington, D. C., doi: 10.1029/GM024p0103.

Dieterich, J. H., and M. F. Linker (1992), Fault stability under conditions of variable normal stress, *Geophys. Res. Lett.*, *19*(16), 1691-1694, doi:10.1029/92GL01821.

Dieterich, J. H., and B. D. Kilgore (1994), Direct observation of frictional contacts: New Insights for state-dependent properties, *Pure Appl. Geophys.*, *143*, 283-302, doi:10.1007/BF00874332.

Doglioni, C., F. Mongelli, and G. Pialli (1998), Appenninic back arc lithospheric boudinage on the former alpine belt, *Società Geologica Italiana*, *Memorie*, *52*, 457-468.

Donath, F. A. (1961), Experimental study of shear failure in anisotropic rocks, *Geol. Soc. Am. Bull.*, *72*(6), 985-989, doi:10.1130/0016-7606(1961)72[985:ESOSFI]2.0.CO;2.

d'Orazio, M., C. Boschi, and D. Brunelli (2004), Talc-rich hydrothermal rocks from the St. Paul and Conrad fracture zones in the Atlantic Ocean, *Eur. J. Mineral.*, *16*, 73-83, doi:10.1127/0935-1221/2004/0016-0073.

Engelder, T. (1984), The role of pore water circulation during the deformation of foreland fold and thrust belts, *J. Geophys. Res. Solid Earth*, *89*(B6), 4319-4325, doi:10.1029/JB089iB06p04319.

Escartín, J., G. Hirth, and B. Evans (2001), Strength of slightly serpentinized peridotites: Implications for the tectonics of oceanic lithosphere, *Geology*, *29*, 1023-1026, doi:10.1130/0091-7613(2001)029<1023:SOSSPI>2.0.CO;2.

Escartín, J., C. Mével, C. J. MacLeod, and A. M. McCaig (2003), Constrains on deformation conditions and the origin of oceanic detachments: the Mid-Atlantic Ridge core complex at 15°45'N, *Geochem. Geophys. Geosyst.*, *4*(8), 1067, doi:10.1029/2002GC000472.

Escartín, J., M. Andréani, G. Hirth, and B. Evans (2008), Relationship between the microstructural evolution and rheology of talc at elevated pressures and temperatures, *Earth Planet. Sci. Lett.*, *268*, 463-475, doi:10.1016/j.epsl.2008.02.004.

Evans, B., Y. Bernabé, and W. Zhu (1999), Evolution of pore structure and permeability of rocks in laboratory experiments, in *Growth, dissolution and pattern formation in geosystem*, edited by B. Jamteit and P. Meakin, pp. 327-344, Kluwer Academic Publishers, Dordrecht, The Netherlands.

Fagereng, Å., and R. H. Sibson (2010), Melange rheology and seismic style, *Geology*, *38*, 751-754, doi:10.1130/G30868.1.

Faulkner, D.R., A. C. Lewis, and E. H. Rutter (2003), On the internal structure and mechanics of large strike-slip fault zones: field observations of the Carboneras fault in southeastern Spain, *Tectonophysics*, *367*, 235-251, doi:10.1016/S0040-1951(03)00134-3.

Faulkner, D. R., T. M. Mitchell, D. Healy, and M. J. Heap (2006), Slip on 'weak' faults by the rotation of regional stress in the fracture damage zone, *Nature*, *444*, 922-925, doi:10.1038/nature05353.

Faulkner, D. R., T.M. Mitchell, E. Jensen, and J. Cembrano (2011), Scaling of fault damage zones with displacement and the implications for fault growth processes, *J. Geophys. Res. Solid Earth*, *116*(B5), B05403, doi:10.1029/2010JB007788.

Ferrill, D. A., and A. P. Morris (2003), Dilational normal fault, *Journal of Structural Geology*, *25*(2), 183-196, doi:10.1016/S0191-8141(02)00029-9.

Ferrill, D. A., and A. P. Morris (2008), Fault zone deformation controlled by carbonate mechanical stratigraphy, Balcones fault system, Texas, *AAPG Bulletin*, *92*(3), 359-380, doi:10.1306/10290707066

Ferrill, D. A., A. P. Morris, R. N. McGinnis, K. J. Smart, and W. C. Ward (2011), Fault zone deformation and displacement partitioning in mechanically layered carbonates: The Hidden Valley fault, central Texas, *AAPG Bulletin*, *95*, 1383-1397, doi:10.1306/12031010065.

Ferrill, D. A., R. N. McGinnis, A. P. Morris, and K. J. Smart (2012), Hybrid failure: Field evidence and influence on fault refraction, *J. Struct. Geol.*, *42*, 140-150, doi:10.1016/j.jsg.2012.05.012.

Ferrill, D.A., R. N. McGinnis, A. P. Morris, K. J. Smart, Z. T. Sickmann, M. Bentz, D. Lehrmann, and M. A. Evans (2014), Control of mechanical stratigraphy on bed-restricted jointing and normal faulting: Eagle Ford Formation, south-central Texas, U.S.A., *AAPG Bulletin*, *98*, 2477-2506, doi:10.1306/08191414053.

Floyd, J. S., J. C. Mutter, A. M. Goodliffe and B. Taylor (2001), Evidence for fault weakness and fluid flow within an active low-angle normal fault, *Nature*, *411*, 779-783, doi:10.1038/35081040.

Fratini, F., E. Pecchioni, E. Cantisani, S. Rescic, and S. Vettori (2014), Pietra Serena: the stone of the Renaissance, in *Geomechanics and Geology*, vol. 407, edited by J. P. Turner et al., pp. 173-186, Geol. Soc., London, doi:10.1144/SP407.11.

Frye, K. M., and C. Marone (2002), Effect of humidity on granular friction at room temperature, *J. Geophys. Res.*, *107*(B11), 2309, doi:10.1029/2001JB000654.

Giorgetti, C., C. Collettini, M. M. Scuderi, M. R. Barchi, and T. Tesei (2016), Fault geometry and mechanics of marly carbonate multilayers: An integrated field and laboratory study from the Northern Apennines, Italy, *J. Struct. Geol.*, *93*, 1-16, doi:10.1016/j.jsg.2016.10.001.

Giorgioni, M., D. Tiraboschi, E. Erba, Y. Hamann, and H. Weissert (2017), Sedimentary patterns and palaeoceanography of the Albian Marne a Fucoidi Formation (Central

Italy) revealed by high-resolution geochemical and nannofossil data, *Sedimentology*, *64*, 111-126, doi:10.1111/sed.12288doi:10.1111/sed.12288.

Goodman, R. E., and P. N. Sundaram (1978), Fault and system stiffnesses and stick-slip phenomena, *Pure Appl. Geophys.*, *116*(4), 873-887.

Grasemann, B., and C. Tschegg (2012), Localization of deformation triggered by chemo-mechanical feedback processes, *Geol. Soc. Am. Bull.*, *124*, 737-745, doi:10.1130/B30504.1.

Gross, M. R. (1995), Fracture partitioning: Failure mode as a function of lithology in the Monterey Formation of coastal California, *Geol. Soc. Am. Bull.*, *107*(7), 779-792, doi:10.1130/0016-7606(1995)107<0779:FPFMAA>2.3.CO;2.

Gross, M. R., G. Gutie, T. Bai, M. A. Wacker, K. B. Collinsworth, and R. J. Behl (1997) Influence of mechanical stratigraphy and kinematics on fault scaling relations, *J. Struct. Geol.*, *19*(2), 171-183, doi:10.1016/S0191-8141(96)00085-5.

Gu, J.-C., J. R. Rice, A. L. Ruina, and S. T. Tse (1984), Slip motion and stability of a single degree of freedom elastic system with rate and state dependent friction, *Journal of the Mechanics and Physics of Solids*, *32*(3), 167-196, doi:10.1016/0022-5096(84)90007-3.

Gu, Y., and T. F. Wong (1994), Development of shear localization in simulated quartz gouge: Effect of cumulative slip and gouge particle size, *Pure Appl. Geophys.*, *143*(1-3), 387-423.

He, C., S. Ma, and J. Huang (1998), Transition between stable sliding and stick-slip due to variation in slip rate under variable normal stress condition, *Geophys. Res. Lett.*, *25*(17), 3235-3238, doi:10.1029/98GL02518.

Healy, D. (2009), Anisotropy, pore fluid pressure and low angle normal faults, *J. Struct. Geol.*, *31*(6), 561-574, doi:10.1016/j.jsg.2009.03.001.

Hickman, S., and M. Zoback (2004), Stress orientations and magnitudes in the SAFOD pilot hole, *Geophys. Res. Lett.*, *31*, L15S12, doi:10.1029/2004GL020043.

Hindle, D., and M. Burkhard (1999), Strain, displacement and rotation associated with the formation of curvature in fold belts; the example of the Jura arc, *J. Struct. Geol.*, *21*(8), 1089-1101, doi:10.1016/S0191-8141(99)00021-8.

Hirauchi, K.-I., S. A. M. den Hartog, C. J. Spiers (2013), Weakening of the slab-mantle wedge interface induced by metasomatic growth of talc, *Geology*, *41*, 75-78, doi:10.1130/G33552.1.

Hoek, E. (1964), Fracture of anisotropic rock, *J. South Afr. Inst. Min. Metall.*, *64*, 501-523.

Holdsworth, R.E. (2004), Weak faults - rotten cores, *Science*, *303(5655)*, 181-182, doi:10.1126/science.1092491.

Ikari, M. J., D. M. Saffer, and C. Marone (2009a), Frictional and hydrologic properties of clay-rich fault gouge, *J. Geophys. Res.*, *114*, B05409, doi:10.1029/2008JB006089.

Ikari, M. J., D. M. Saffer, and C. Marone (2009b), Frictional and hydrologic properties of a major splay fault system, Nankai subduction zone, *Geophys. Res. Lett.*, *36*, L20313, doi:10.1029/2009GL040009.

Ikari, M. J., C. Marone, and D. M. Saffer (2011), On the relation between fault strength and frictional stability, *Geology*, *39*, 83-86, doi:10.1130/G31416.1.

Jackson, R. E., and D. E. Dunn (1974), Experimental sliding friction and cataclasis of foliated rocks, *Int. J. Rock Mech. Min. Sci*., *11*(6), 235-249, doi:10.1016/0148-9062(74)90130-2.

Jaeger, J. C. (1959), The frictional properties of joints in rock, *Geof. Pura Appl.*, *43*(1), 148-158.

Jaeger, J. C. (1960), Shear failure of anistropic rocks, *Geological Magazine*, *97*(01), 65-72, doi:10.1130/0016-7606(1961)72[985:ESOSFI]2.0.CO;2.

Jaeger, J. C., and N. G. W. Cook (1979), *Fundamentals of rock mechanics*, Chapman & Haii, London, U. K.

Jefferies, S. P., R. E. Holdsworth, C. A. J. Wibberley, T. Shimamoto, C. J. Spiers, A. R. Niemeijer, and G. E. Lloyd (2006), The nature and importance of phyllonite development in crustal-scale fault cores: an example from the Median Tectonic Line, Japan, *J. Struct. Geol.*, *28*, 220-235, doi:10.1016/j.jsg.2005.10.008

Kanagawa, K., S. F. Cox, and S. Zhang (2000), Effects of dissolution-precipitation processes on the strength and mechanical behavior of quartz gouge at high-temperature hydrothermal conditions, *J. Geophys. Res.*, *105*(B5), 11115-11126, doi:10.1029/2000JB900038.

Kanamori, H., and E. E. Brodsky (2004), The physics of earthquakes, *Reports on Progress in Physics*, *67*(8), 1429.

King, R. L., M. J. Kohn, and J. M. Eiler (2003), Constraints on the petrologic structure of the subduction slab-mantle interface from Franciscan Complex exotic ultramafic blocks, *Geol. Soc. Am. Bull.*, *115*, 1097-1109, doi:10.1130/B25255.1.

Koopman, A. (1983), Detachment tectonics in the Central Apennines, Italy, *Geologica Ultraiectina*, *30*, 155.

Kopf, A. (2001), Permeability variation across an active low-angle detachment fault, western Woodlark Basin (ODP Leg 180), and its implication for fault activation, in *The Nature and Tectonic Significance of Fault Zone Weakening*, vol. 186, edited by R. E. Holdsworth et al., pp. 23-41, Geol. Soc., London, doi:10.1144/GSL.SP.2001.186.01.03.

Kopf, A., and K. M. Brown (2003), Friction experiments on saturated sediments and their implications for the stress state of the Nankai and Barbados subduction thrusts, *Marine Geology*, *202*, 193-210, 10.1016/s0025-3227(03)00286-x.

Kristensen, M. B., C. Childs, N. Ø. Olesen, and J. A. Korstgård (2013), The microstructure and internal architecture of shear bands in sand–clay sequences, *J. Struct. Geol.*, *46*, 129-141, doi:10.1016/j.jsg.2012.09.015.

Lavecchia, G., G. Minelli, and G. Pialli (1988), The Umbria-Marche arcuate fold belt (Italy). *Tectonophysics*, *146*(1), 125-137, doi:10.1016/0040-1951(88)90086-8.

Lecomte, E., L. Le Pourhiet, and O. Lacombe (2012), Mechanical basis for slip along low-angle normal faults, *Geophys. Res. Lett.*, 39, L03307, doi:10.1029/2011GL050756.

Li, J., X. Hu, K. Zhao, Y. Cai, and T. Sun (2016), Paleoceanographic evolution and chronostratigraphy of the Aptian Oceanic Anoxic Event 1a (OAE1a) to oceanic red bed 1 (ORB1) in the Gorgo a Cerbara section (central Italy), *Cretaceous Research*, *66*, 115-128, doi:10.1016/j.cretres.2016.04.016.

Li, Y.-G., J. E. Vidale, S. M. Day, D. D. Oglesby, and E. Cochran (2003), Postseismic fault healing on the rupture zone of the 1999 M7.1 Hector Mine, California, earthquake, *Bull. Seismol. Soc. Am.*, *93*, 854–869, doi:10.1785/0120020131.

Leeman, J. R., D. M. Saffer, M. M. Scuderi, and C. Marone (2016), Laboratory observations of slow earthquakes and the spectrum of tectonic fault slip modes, *Nature Communications*, *7*, 11104, doi:10.1038/ncomms11104.

Lockner, D. A., and J. D. Byerlee (1993), How geometrical constraints contribute to the weakness of mature faults, *Nature*, *363*(6426), 250-252, doi:10.1038/363250a0.

Lockner, D. A., C. Morrow, D. E. Moore, and S. Hickman (2011), Low strength of deep San Andreas fault gouge from SAFOD core, *Nature*, *472*, 82-85, doi:101038/Nature09927.

Logan, J. M., C. A. Dengo, N. G. Higgs, and Z. Z. Wang (1992), Fabric of experimental fault zone: Their development and relationship to mechanical behavior, in *Fault Mechanics and Transport Properties of Rocks*, edited by B. Evans and T. Wong, pp. 33-67, Elsevier Academic, San Diego, Calif., doi:10.1016/S0074-6142(08)62814-4.

Logan, J. M. (2007), The progression from damage to localization of displacement observed in laboratory testing of porous rocks, in *The Relationship between Damage and Localization*, vol. 289, edited by H. Lewis and G. D. Couples, pp. 75-87, Geol. Soc., London, doi:10.1144/SP289.5.

Lupini, J. F., A. E. Skinner, and P. R. Vaughan (1981), The drained residual strength of cohesive soils, *Geotechnique*, *31*, 181-213, doi:10.1680/geot.1981.31.2.181.

Mair, K., and C. Marone (1999), Friction of simulated fault gouge for a wide range of velocities and normal stresses, *J. Geophys. Res.*, *104*(B12), 28899-28914, doi:10.1029/1999JB900279.

Mandl, G. G. (1988), *Mechanics of tectonic faulting: models and basic concepts*, Elsevier, New York.

Mandl, G., L. N. J. De Jong, and A. Maltha (1977), Shear zones in granular material, *Rock mechanics*, *9*(2-3), 95-144.

Manning, C.E. (1995), Phase-equilibrium controls on SiO_2 metasomatism by aqueous fluid in subduction zones: Reaction at constant pressure and temperature, *Int. Geol. Rev.*, *37*, 1039-1073, doi:10.1080/00206819509465440.

Manzocchi, T., A. E. Heath, B. Palananthakumar, C. Childs, and J. J. Walsh (2008), Faults in conventional flow simulation models: a consideration of representational assumptions and geological uncertainties, *Petroleum Geoscience*, *14*, 91–110, doi:10.1144/1354-079306-775.

Manzocchi, T., C. Childs, and J. J. Walsh (2010), Faults and fault properties in hydrocarbon flow models, *Geofluids*, *10*(1-2), 94-113, doi:10.1111/j.1468-8123.2010.00283.x.

Marinos, P., and E. Hoek (2001), Estimating the geotechnical properties of heterogeneous rock masses such as flysch, *Bulletin of the Engineering Geology & the Environment*, *60*, 85-92, doi:10.1007/s100640000090.

Marone, C. (1998a), The effect of loading rate on static friction and the rate of fault healing during the earthquake cycle, *Nature*, *391*(6662), 69-72.

Marone, C. (1998b), Laboratory-derived friction laws and their application to seismic faulting, *Annu. Rev. Earth Planet. Sci.*, *26*, 643-696, doi:10.1146/annurev.earth.26.1.643.

Marone, C., and B. Kilgore (1993), Scaling of the critical slip distance for seismic faulting with shear strain in fault zones, *Nature*, *362*, 618-621, doi:10.1038/362618a0.

Marone, C., C. B. Raleigh, and C. H. Scholz (1990), Frictional behavior and constitutive modeling of simulated fault gouge, *J. Geophys. Res*., *95*, 7007-7025, doi:10.1029/JB095iB05p07007.

Marone, C., B. E. Hobbs, and A. Ord (1992), Coulomb constitutive laws for friction: Contrasts in frictional behavior for distributed and localized shear, *Pure Appl. Geophys.*, *139*(2), 195-214.

Marrett, R., Allmendinger, R. W., 1990. Kinematic analysis of fault-slip data. Journal of Structural Geology, 12(8), 973-986, doi:10.1016/0191-8141(90)90093-E.

Marshak, S., P. A. Geiser, W. Alvarez, and T. Engelder (1982), Mesoscopic fault array of the northern Umbrian Apennine fold belt, Italy: Geometry of conjugate shear by pressure-solution slip, *Geological Society of America Bulletin*, *93*(10), 1013-1022, doi:10.1130/0016-7606(1982)93<1013:MFAOTN>2.0.CO;2.

Massironi, M., A. Bistacchi, and L. Menegon (2011), Misoriented faults in exhumed metamorphic complexes: Rule or exception? *Earth Planet. Sci. Lett*., *307*, 233-239, doi:10.1016/j.epsl.2011.04.041.

McCabe, W., and R. M. Koerner (1975), High pressure shear strength investigation of an anisotropic mica schist rock, *Int. J. Rock Mech. Min. Sci*., *12*(8), 219-228, doi:10.1016/0148-9062(75)91402-3.

McLamore, R., and K. E. Gray (1967), The mechanical behavior of anisotropic sedimentary rocks, *Journal of Engineering for Industry*, *89*(1), 62-73.

Misra, S., S. Boutareaud, and J.-P. Burg (2014), Rheology of talc sheared at high pressure and temperature: a case study for hot subduction zones, *Tectonophysics*, *610*, 51-62, doi:10.1016/j.tecto.2013.10.009.

Misra, S., S. Ellis, and N. Mandal (2015), Fault damage zones in mechanically layered rocks: The effects of planar anisotropy, *J. Geophys. Res. Solid Earth*, *120*(8), 5432-5452, doi:10.1002/2014JB011780.

Moore, D. E., and D. A. Lockner (2004), Crystallographic controls on the frictional behavior of dry and water-saturated sheet structure minerals, *J. Geophys. Res.*, *109*, B03401, doi:10.1029/2003JB002582.

Moore, D. E., and M. Rymer (2007), Talc-bearing serpentines and creeping section of San Andreas fault, *Nature*, *448*, 795-797, doi:10.1038/nature06064.

Moore, D. E., and D. A. Lockner (2008), Talc friction in the temperature range 25°-400°C: Relevance for fault-zone weakening, *Tectonophysics*, *449*, 120-132, doi:10.1016/j.tecto.2007.11.039.

Moore, D. E., and D. A. Lockner (2011), Frictional strengths of talc-serpentine and talc-quartz mixtures, *J. Geophys. Res.*, *116*, B01403, doi:10.1029/2010JB007881.

Moore, D. E., R. Summers, and J. Byerlee (1989), Sliding behavior and deformation textures of heated illite gouge, *J. Struct. Geol.*, *11*, 329-342.

Morris, A., D. A. Ferrill, and D. B. Henderson (1996), Slip-tendency analysis and fault reactivation. *Geology*, *24*(3), 275-278, doi:10.1130/0091-7613(1996)024<0275:STAAFR>2.3.CO;2.

Nicol, A., J. Watterson, J. J. Walsh, and C. Childs, (1996), The shapes, major axis orientations and displacement patterns of fault surfaces, *J. Struct. Geol.*, *18*(2), 235-248, doi:10.1016/S0191-8141(96)80047-2.

Niemeijer, A. R., and C. J. Spiers (2005), Influence of phyllosilicates on fault strength in the brittle-ductile transition: Insights from rock analogue experiments, in *High-Strain Zones: Structure and Physical Properties*, vol. 245, edited by D. Bruhn and L. Burlini, pp. 303-327, Geol. Soc., London, doi:10.1144/GSL.SP.2005.245.01.15.

Niemeijer, A. R., and C. J. Spiers (2006), Velocity dependence of strength and healing behavior in simulated phyllosilicate-bearing fault gouge, *Tectonophysics*, *427*, 231-253, doi:10.1016/j.tecto.2006.03.048.

Niemeijer, A., C. Marone, and D. Elsworth (2008), Healing of simulated fault gouges aided by pressure solution: Results from rock analogue experiments, *J. Geophys. Res.*, *113*, B04204, doi:10.1029/2007JB005376.

Niemeijer, A., C. Marone, and D. Elsworth (2010), Fabric induced weakness of tectonic faults, *Geophys. Res. Lett.*, *37*, L03304, doi:10.1029/2009GL041689.

Noda, H., and T. Shimamoto (2010), A rate- and state-dependent ductile flow law of polycrystalline halite under large shear strain and implications for transition to brittle deformation, *Geophys. Res. Lett.*, *37*, L09310, doi:10.1029/2010GL042512.

Numelin, T., C. Marone, and E. Kirby (2007), Frictional properties of natural fault gouge from a low-angle normal fault, Panamint Valley, California, *Tectonics*, *26*, TC2004, doi:10.1029/2005TC001916.

Odling, N.E., P. Gillespie, B. Bourgine, C. Castaing, J.-P. Chilés, N. P. Christensen, E. Fillion, A. Genter, C. Olsen, L. Thrane, R. Trice, E. Aarseth, J. J. Walsh, and J. Watterson (1999), Variations in fracture system geometry and their implications for fluid flow in fractured hydrocarbon reservoirs, *Petroleum Geoscience*, *5*, 373-384, doi:10.1144/petgeo.5.4.373.

Olsen, M., C. H. Scholz, and A. Léger (1998), Healing and sealing of a simulated fault gouge under hydrothermal conditions: Implications for fault healing, *J. Geophys. Res.*, *103*(B4), 7421-7430, doi:10.1029/97JB03402.

Paterson, M. S., and T.-F. Wong (2005), *Experimental rock deformation-the brittle field*, 2nd ed., Springer, New York.

Peacock, S. M. (1987), Serpentinization and infiltration metasomatism in the Trinity peridotite, Klamath province, northern California: implications for subduction zones, *Contrib. Mineral. Petrol.*, *95*, 55-70, doi:10.1007/BF00518030.

Peacock, D. C. P., and D. J. Sanderson (1992), Effects of layering and anisotropy on fault geometry, *Journal of the Geological Society*, *149*(5), 793-802, doi:10.1144/gsjgs.149.5.0793.

Price, N.J., and J. W. Cosgrove (1990), *Analysis of Geological Structures*, Cambridge Univ. Press, Cambridge, U. K.

Ramsay, J. G., and M. I. Huber (1987), *The techniques of modern structural geology: Folds and fractures* (Vol. 2), Academic Press., San Diego.

Ramsey, J. M., and F. M. Chester (2004), Hybrid fracture and the transition from extension fracture to shear fracture, *Nature*, *428*, 63-66, doi:10.1038/nature02333.

Reddy, M. M., and K. K. Wang (1980), Crystallization of calcium carbonate in the presence of metal ions: I. Inhibition of magnesium ion at pH 8.8 and 250°C, *J. Cryst. Growth*, *50*, 470-480, doi:10.1016/0022-0248(80)90095-0.

Reid, H. F. (1910), The mechanics of the earthquake, in *The California Earthquake of April 18, 1906, Report of the State Earthquake Investigation Commission*, vol. 2, pp. 16-28, Carnegie Institution, Washington, D. C.

Reinen, L. A.*, and* J. D. Weeks *(*1993*),* Determination of rock friction constitutive parameters using an iterative least squares inversion method*, J. Geophys. Res., 98(*B9*),* 15937-15950*,* doi:10.1029/93JB00780.

Reutter, K.-J., P. Giese, and H. Closs (1980), Lithospheric split in the descending plate: observations from the Northern Apennines, *Tectonophysics*, *64*, 1-9. doi:10.1016/0040-1951(80) 90254-1.

Rice, J. R. (1975), On the stability of dilatant hardening for saturated rock masses, *Journal of Geophysical Research*, *80*(11), 1531-1536, doi:10.1029/JB080i011p01531.

Rice, J. R. (1983), Constitutive relations for fault slip and earthquake instabilities, *Pure Appl. Geophys.*, *121*(3), 443-475.

Rice, J. R. (1992), Fault stress states, pore pressure distributions, and the weakness of the San Andreas fault, *International Geophysics*, *51*, 475-503, doi:10.1016/S0074-6142(08)62835-1.

Richardson, E., and C. Marone (1999), Effects of normal stress vibrations on frictional healing, *J. Geophys. Res.*, *104*(B12), 28859-28878, doi:10.1029/1999JB900320.

Rimstidt, J. D. (1997), Quartz solubility at low temperatures, *Geochim. Cosmochim. Acta*, *61*, 2553-2558, doi:10.1016/S0016-7037(97)00103-8.

Roche, V., C. Homberg, and M. Rocher (2012), Architecture and growth of normal fault zones in multilayer systems: A 3D field analysis in the South-Eastern Basin, France, *J. Struct. Geol.*, *37*, 19-35, doi:10.1016/j.jsg.2012.02.005.

Roller, S., J. H. Behrmann, and A. Kopf (2001), Deformation fabrics of faulted rocks, and some syntectonics stress estimates from the active Woodlark Basin detachment zone, in *Non-volcanic Rifting of Continental Margins: A Comparison of Evidence From Land and Sea*, vol. 187, edited by R. C. L. Wilson et al., pp. 319-334, Geol. Soc., London, doi:10.1144/GSL.SP.2001.187.01.16.

Rudnicki, J. W. (1984), Effects of dilatant hardening on the development of concentrated shear deformation in fissured rock masses, *Journal of Geophysical Research: Solid Earth*, *89*(B11), 9259-9270, doi:10.1029/JB089iB11p09259.

Rudnicki, J. W. (2002), Diffusive instabilities in dilating and compacting geomaterials. In *Multiscale Deformation and Fracture in Materials and Structures*, edited by T.-J. Chuang and J. W. Rudnicki, J.W., pp. 159-182, Kluwer Academic Publishers, Dordrecht, doi:10.1007/0-306-46952-9_10.

Rudnicki, J. W., and J. R. Rice (1975), Conditions for the localization of deformation in pressure-sensitive dilatant materials, *Journal of the Mechanics and Physics of Solids*, *23*(6), 371-394, doi:10.1016/0022-5096(75)90001-0.

Ruina, A. (1983), Slip instability and state variable friction laws, *J. Geophys. Res.*, *88*, 10359-10370, doi:10.1029/JB088iB12p10359.

Runesson, K., D. Perić, and S. Sture (1996), Effect of pore fluid compressibility on localization in elastic-plastic porous solids under undrained conditions, *International Journal of Solids and Structures*, *33*(10), 1501-1518, doi:10.1016/0020-7683(95)00104-2.

Saffer, D. M., and C. Marone (2003), Comparison of smectite- and illite-rich gouge frictional properties: Application to the updip limit of the seismogenic zone along subduction megathrusts, *Earth Planet. Sci. Lett.*, *215*, 219-235, doi:10.1016/S0012-821X(03)00424-2.

Saffer, D., K. Frye, C. Marone, and K. Mair (2001), Laboratory results indicating complex and potentially unstable frictional behavior of smectite clay, *Geophys. Res. Lett.*, *28*, 2297-2300, doi:10.1029/2001GL012869.

Sammis, C. G., and S. J. Steacy (1994), The micromechanics of friction in a granular layer, *Pure Appl. Geophys.*, *142*, 777-794.

Savage, J. C., D. A. Lockner, and J. D. Byerlee (1996), Failure in laboratory fault models in triaxial tests, J. *Geophys. Res.*, *101*(B10), 22215-22224, doi:10.1029/96JB02094.

Schleicher, A. M., B. A. van der Pluijm, and L. N. Warr (2010), Nanocoatings of clay and creep of the San Andreas fault at Parkfield, California, *Geology*, *38*, 667–670, doi:10.1130/G31091.1.

Schofield, A. N., and P. Wroth (1968), *Critical State Soil Mechanics*, McGraw-Hill, New York.

Scholz, C. H. (1998), Earthquakes and friction laws, *Nature*, *391*, 37-42, doi:10.1038/34097.

Scholz, C. H. (2002), *The Mechanics of Earthquakes and Faulting*, Cambridge Univ. Press, Cambridge, U. K.

Schöpfer, M. P., C. Childs, and J. J. Walsh (2006), Localisation of normal faults in multilayer sequences, *J. Struct. Geol.*, *28*(5), 816-833, doi:10.1016/j.jsg.2006.02.003.

Schöpfer, M. P., C. Childs, J. J. Walsh, T. Manzocchi, and H. A. Koyi (2007), Geometrical analysis of the refraction and segmentation of normal faults in periodically layered sequences, *J. Struct. Geol.*, 29(2), 318-335, doi:10.1016/j.jsg.2006.08.006.

Schroeder, T., and B. E. John (2004), Strain localization on an oceanic detachment fault system, Atlantis Massif, 30°N, Mid-Atlantic Ridge, *Geochem. Geophys. Geosyst.*, *5*, Q11007, doi:10.1029/2004GC000728.

Schubnel, A., E. Walker, B. D. Thompson, J. Fortin, Y. Guéguen, and R. P. Young (2006), Transient creep, aseismic damage and slow failure in Carrara marble deformed across the brittle-ductile transition, *Geophys. Res. Lett.*, *33*, L17301, doi:10.1029/2006GL026619.

Scott, D. R., D. A. Lockner, J. D. Byerlee, and C. G. Sammis (1994a), Triaxial testing of Lopez fault gouge at 150 MPa mean effective stress, *Pure Appl. Geophys.*, *142*(3), 749-775.

Scott, D. R., C. J. Marone, and C. G. Sammis (1994b), The apparent friction of granular fault gouge in sheared layers, *J. Geophys. Res.*, *99*(B4), 7231-7246, doi:10.1029/93JB03361.

Scuderi, M. M., and C. Collettini (2016), The role of fluid pressure in induced vs. triggered seismicity: insights from rock deformation experiments on carbonates, *Scientific Reports*, *6*, 24852, doi:10.1038/srep24852.

Scuderi, M. M., A. R. Niemeijer, C. Collettini, and C. Marone (2013), Frictional properties and slip stability of active faults within carbonate-evaporite sequences: The role of dolomite and anhydrite, *Earth Planet. Sci. Lett.*, *369*, 220-232, doi:10.1016/j.epsl.2013.03.24.

Scuderi, M. M., C. Marone, E. Tinti, G. Di Stefano, and C. Collettini (2016), Precursory changes in seismic velocity for the spectrum of earthquake failure modes, *Nature Geoscience*, *9*, 695-700, doi:10.1038/ngeo2775.

Scuderi, M. M., C. Collettini, C. Viti, E. Tinti, and C. Marone (2017), Evolution of shear fabric in granular fault gouge from stable sliding to stick slip and implications for fault slip mode, *Geology*, *45*(8), 731–734, doi:10.1130/G39033.1

Shea, W. T., and A. K. Kronenberg (1993), Strength and anisotropy of foliated rocks with varied mica contents, *J. Struct. Geol.*, *15*(9), 1097-1121, doi:10.1016/0191-8141(93)90158-7.

Shimamoto, T., and H. Noda (2014), A friction to flow constitutive law and its application to a 2-D modeling of earthquakes*, J. Geophys. Res. Solid Earth, 119,* 8089-8106*,* doi:10.1002/2014JB011170*.*

Shimamoto, T., J. Handin, and J. M. Logan (1980), Specimen-apparatus interaction during stick-slip in a triaxial compression machine: A decoupled two-degree-of-freedom model, *Tectonophysics*, *67*(3-4), 175-205, doi:10.1016/0040-1951(80)90234-6.

Sibson, R.H. (1977), Fault rocks and fault mechanics, *J. Geol. Soc. London*, *133,* 191-213.

Sibson, R. H. (1985), A note on fault reactivation, *J. Struct. Geol.*, *7*(6), 751-754, doi:10.1016/0191-8141(85)90150-6.

Sibson, R. H. (1991), Loading of faults to failure, *Bull. Seismol. Soc. Am.*, *81*(6), 2493-2497.

Sibson, R. H. (1993), Load-strengthening versus load-weakening faulting, *J. Struct. Geol.*, *15*(2), 123-128, doi:10.1016/0191-8141(93)90090-W.

Sibson, R. H. (1996), Structural permeability of fluid-driven fault-fracture meshes, *J. Struct. Geol.*, *18*(8), 1031-1042, doi:10.1016/0191-8141(96)00032-6.

Sibson, R. H. (2003), Thickness of the seismic slip zone, *Bull. Seismol. Soc. Am.*, *93*(3), 1169-1178.

Soliva, R., and A. Benedicto (2005), Geometry, scaling relations and spacing of vertically restricted normal faults, *J. Struct. Geol.*, *27*(2), 317-325, doi:10.1016/j.jsg.2004.08.010.

Sylvester, A. G. (1988), Strike-slip faults, *Geol. Soc. Am. Bull.*, *100*(11), 1666-1703, doi:10.1130/0016-7606(1988)100<1666:SSF>2.3.CO;2.

Tadokoro, K., and M. Ando (2012), Evidence for rapid fault healing derived from temporal changes in S wave splitting, *Geophys. Res. Lett.*, *29*, 4, doi:10.1029/2001GL013644.

Taylor, B., and P. Huchon (2002), Active continental extension in the western Woodlark Basin: A synthesis of Leg 180 results, *Proc. Ocean Drill. Program Sci. Results*, *180*, 1-36.

Tembe, S., D. A. Lockner, and T. -F. Wong (2010), Effect of clay content and mineralogy on frictional sliding behavior of simulated gouges: Binary and ternary mixtures of quartz, illite, and montmorillonite, *J. Geophys. Res.*, *115*, B03416, doi:10.1029/2009JB006383.

Tenthorey, E., S. F. Cox, and H. F. Todd (2003), Evolution of strength recovery and permeability during fluid-rock reaction in experimental fault zones, *Earth Planet. Sci. Lett.*, *206*(1-2), 161-172, doi:10.1016/S0012-821X(02)01082-8.

Tesei, T., C. Collettini, B. M. Carpenter, C. Viti, and C. Marone (2012), Frictional strength and healing behavior of phyllosilicate-rich faults, *J. Geophys. Res.*, *117*, B09402, doi:10.1029/2012JB009204.

Tesei, T., C. Collettini, C. Viti, and M. R. Barchi (2013), Fault architecture and deformation mechanisms in exhumed analogues of seismogenic carbonate-bearing thrusts, *J. Struct. Geol.*, *55*, 167-181.

Tesei, T., C. Collettini, M. R. Barchi, B. M. Carpenter, and G. Di Stefano (2014), Heterogeneous strength and fault zone complexity of carbonate-bearing thrusts with possible implications for seismicity, *Earth Planet. Sci. Lett.*, *408*, 307-318, doi:10.1016/j.epsl.2014.10.021.

Tesei, T., B. Lacroix, and C. Collettini (2015), Fault strength in thin-skinned tectonic wedges across the smectite-illite transition: Constraints from friction experiments and critical tapers, *Geology*, *43*(10), 923-926, doi:10.1130/G36978.1.

Thompson, B. D., R. P. Young, and D. A. Lockner (2006), Fracture in Westerly granite under AE feedback and constant strain rate loading: nucleation, quasi-static propagation, and the transition to unstable fracture propagation, *Pure Appl. Geophys.*, *163*(5-6), 995-1019.

Tornaghi, M.E., I. Premoli Silva, and M. Ripepe (1989), Lithostratigraphy and planktonic foraminiferal biostratigraphy of the aptian-albian "Scisti a Fucoidi" in the Piobbico core, Marche, Italy: background for cyclostratigraphy, *Rivista Italiana di Paleontologia e Stratigrafia*, *95*(3), 223-264.

Townend, J., and M. D. Zoback (2000), How faulting keeps the crust strong, *Geology*, *28*, 399-402, 10.1130/0091-7613(2000)28<399:HFKTCS>2.0.CO;2.

Verberne, B. A., C. J. Spiers, A. R. Niemeijer, J. H. De Bresser, D. A. M. De Winter, and O. Plümper (2014), Frictional properties and microstructure of calcite-rich fault gouges sheared at sub-seismic sliding velocities, *Pure Appl. Geophys.*, *171*, 2617-2640, doi:10.1007/s00024-013-0760-0.

Viti, C., and C. Collettini (2009), Growth and deformation mechanisms of talc along a natural fault: A micro/nanostructural investigation, *Contrib. Mineral. Petrol.*, *158*, 529-542, doi:10.1007/s00410-009-0395-4.

Vrolijk, P., and B. A. van der Pluijm (1999), Clay gouge, *J. Struct. Geol.*, *21*, 1039-1048, doi:10.1016/S0191-8141(99)00103-0.

Weeks, J. D., and T. E. Tullis (1985), Frictional sliding of dolomite: A variation in constitutive behavior, *J. Geophys. Res.*, *90*, 7821-7826, doi:10.1029/JB090iB09p07821.

Wilkins, S. J., and M. R. Gross (2002), Normal fault growth in layered rocks at Split Mountain, Utah: influence of mechanical stratigraphy on dip linkage, fault restriction and fault scaling, *J. Struct. Geol.*, *24*(9), 1413-1429, doi:10.1016/S0191-8141(01)00154-7.

Wilkins, S. J., M. R. Gross, M. Wacker, Y. Eyal, and T. Engelder (2001), Faulted joints: kinematics, displacement–length scaling relations and criteria for their identification, *J. Struct. Geol.*, *23*(2), 315-327, doi:10.1016/S0191-8141(00)00098-5.

Wintsch, R. P., R. Christoffersen, and A. K. Kronenberg (1995), Fluid-rock reaction weakening of fault zones, *J. Geophys. Res.*, *100*, 13021-13032, doi:10.1029/94JB02622.

Wong, T. F., C. David, and W. Zhu (1997), The transition from brittle faulting to cataclastic flow in porous sandstones: Mechanical deformation, *J. Geophys. Res. Solid Earth*, *102*(B2), 3009-3025, doi:10.1029/96JB03281.

Wood, D. M. (1990), *Soil behaviour and critical state soil mechanics*, Cambridge Univ. Press, New York.

Yasuhara, H., and D. Elsworth (2008), Compaction of a rock fracture moderated by competing roles of stress corrosion and pressure solution, *Pure Appl. Geophys.*, *165*, 1289-1306, doi:10.1007/s00024-008-0356-2.

Yasuhara, H., C. Marone, and D. Elsworth (2005), Fault zone restrengthening and frictional healing: The role of pressure solution, *J. Geophys. Res.*, *110*, B06310, doi:10.1029/2004JB00327.

Zhang, X., and C. J. Spiers (2005), Compaction of granular calcite by pressure solution at room temperature and effects of pore fluid chemistry, *Int. J. Rock Mech. Min. Sci.*, *42*(7-8), 950-960, doi:10.1016/j.ijrmms.2005.05.017.

Zhang, X., C. J. Spiers, and C. J. Peach (2010), Compaction creep of wet granular calcite by pressure solution at 28°C to 150°C, *J. Geophys. Res.*, *115*, B09217, doi:10.1029/2008JB005853.

Appendix A.
Technical corrections to mechanical data from triaxial and triaxial saw-cut experiments

A.1. Elastic stretch of the load frame on the vertical axis as a function of confining pressure

The vertical displacement is measured by a Linear Variable Displacement Transducer attached to the vertical piston of BRAVA (Collettini et al., 2014b). A minor contribution of the displacement imposed to the vertical piston to deform the experimental sample is accommodated by the elastic stretch of the load frame. The pressure vessel filled of pressurized confining oil influences the stiffness of the load frame. Different values of confining pressure result in different stiffnesses of the load frame on the vertical axis.

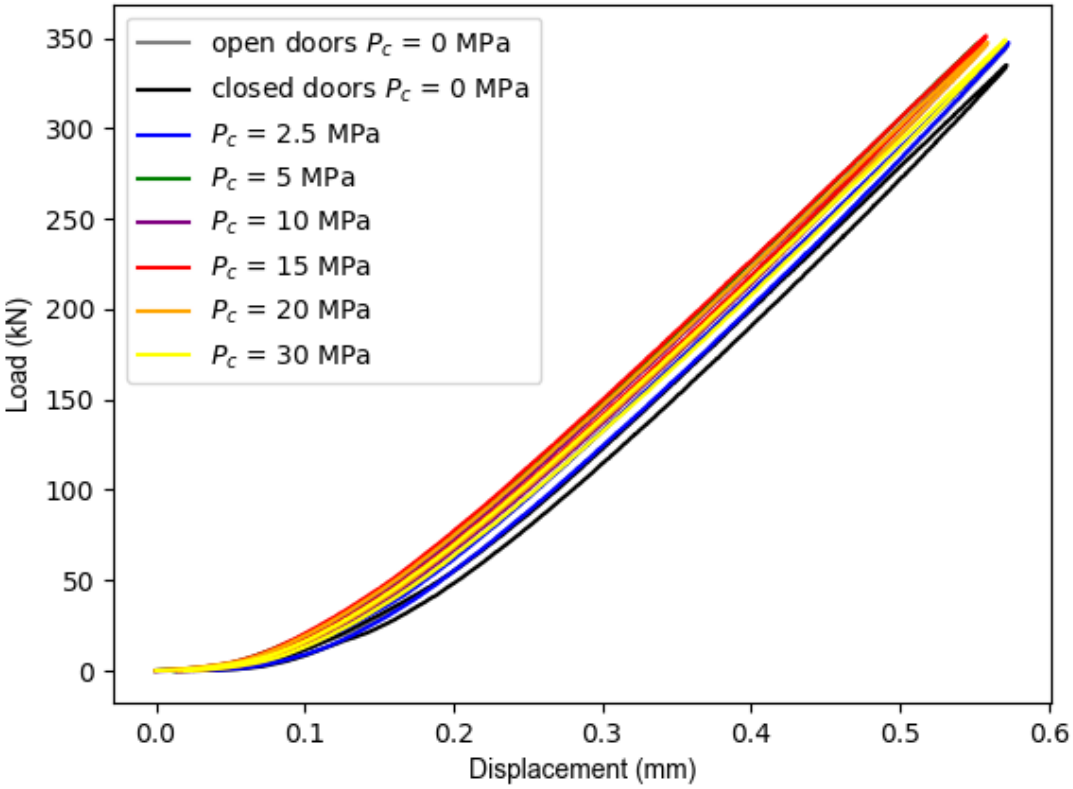

Figure A.1.1. Load versus displacement curve showing loading-unloading cycles performed to evaluate the stiffness of the loading frame on the vertical axis as a function of the confining pressure P_c.

To evaluate the real amount of displacement accommodated by the sample, the stiffness of the load frame on the vertical axis is determined at different values of confining pressure P_c. Loading-unloading cycles were applied to a stainless steel block at constant vertical displacement rate of 5 μm/s up to a maximum load of 350 kN. After a first cycle to compact

the vertical column, two cycles were performed at 0 MPa confining pressure. The doors of the vessel were open during one cycle and closed during the other cycle (empty vessel). Then, each cycle was performed at constant confining pressure, progressively increasing P_c from 2.5 MPa to 30 MPa. Figure A.1.1 shows the load vs. displacement curves during loading-unloading cycles. Load increases linearly with displacement at values higher than 50 kN. The average slope of the linear portions of the loading and unloading portions of the curve during one cycle performed at a given P_c constitutes the estimated stiffness at the given P_c. In Figure A.1.2 the stiffness of the vertical load frame at different confining pressure is reported. The stiffness values here estimated were used to evaluate the displacement experienced by the sample during triaxial and triaxial saw-cut experiments.

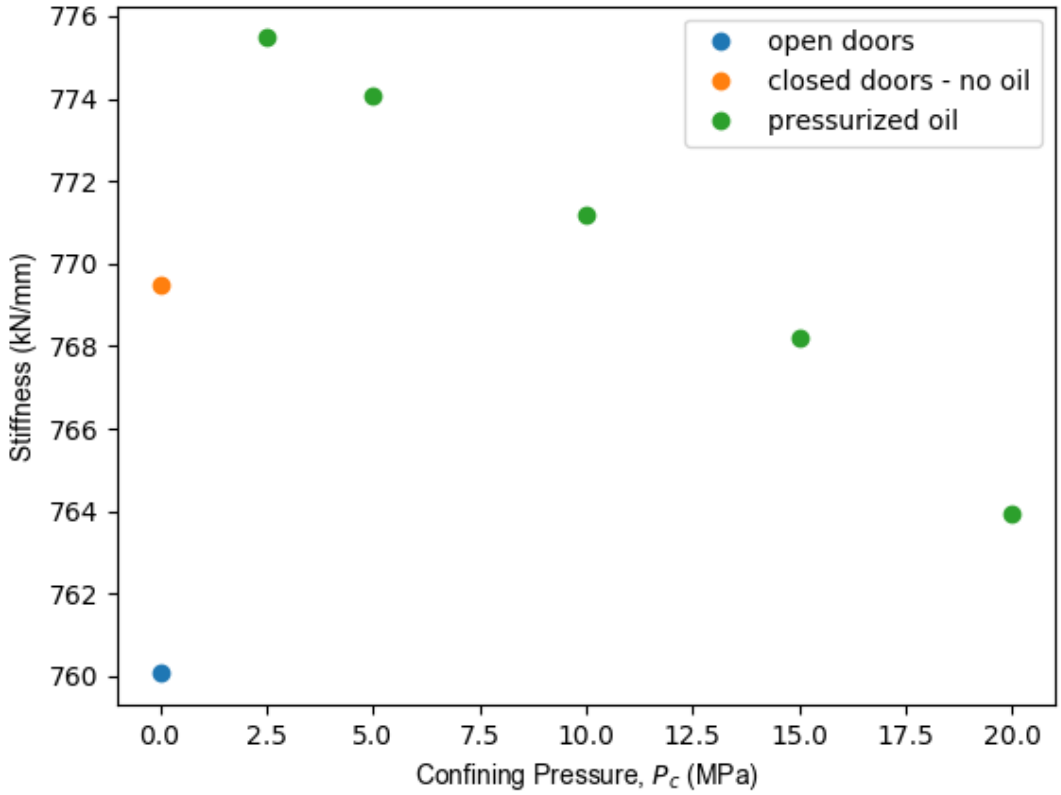

Figure A.1.2. Stiffness of the loading frame on the vertical axis at different values of confining pressure.

A.2. Strength of the polyolefin jacket used in triaxial saw-cut experiments

Cylindrical samples for triaxial saw-cut experiments were jacketed with two layers of poly-olefin heat-shrink tube to prevent confining oil to enter into the sample during the experiment. The stress required to deform the jacket as saw-cut shearing proceeds contributes to the total stress measured by the load cell. To determine the actual differential stress applied to the sample, the evaluation of the strength of the jacket is required. The strength of the jacket was

evaluated by shearing moly grade lubricant placed within a 40° polished saw-cut in a tonalite cylindrical sample jacketed with two layers of poly-olefin heat-shrink tube. Experiments were conducted at different values of constant confining pressure, i.e. P_c = 10 - 20 - 25 MPa, to evaluate jacket strength as a function of confining pressure. The slope of the linear portion of the differential stress vs. displacement curve (Figure A.2.1) represents the strength of the jacket. The strength of the jacket was used to correct the differential stress supported by the sampe.

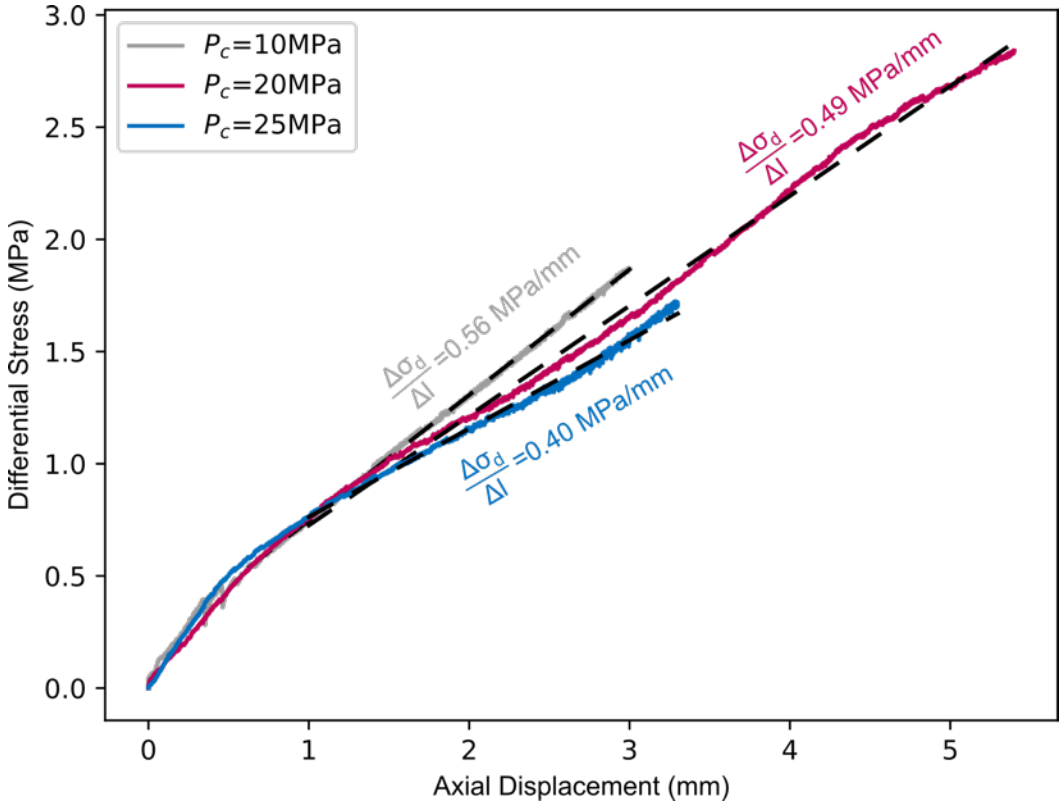

Figure A.2.1. Differential stress versus displacement curves of cylindrical samples with 40° saw-cuts polished and lubricated with moly grade lubricant to evaluate the strength of the poly-olefin heat-shrink tubes with which the samples were jacketed.

Appendix B.
Python scripts developed to analyze field and laboratory data

B.1. Local stress field and angle between faults and maximum principal stress from field data

This script was designed to evaluate the local stress field from field data. It is based on the assumption that the minimum principal stress is perpendicular to extensional fractures and that the intermediate principal stress is parallel to the intersection of conjugate shear planes.

```
"""
Local stress field and angle between faults and maximum principal stress
from field data

Author Carolina Giorgetti
Date:  05/07/2015

Description:

This program evaluates the local stress field from orientation (dip direction and
dip)
of extensional fractures and shear fractures.

Assuming that:
1) The minimum principal stress is perpendicular to extensional fractures;
2) The intermediate principal stress is parallel to the intersection of
   conjugate shear fractures;
3) The maximum principal stress is perpendicular to the plane containing the
   minimum and the intermediate principal stresses.

Then, this program evaluates angles between the maximum principal stress and the
fault plane.

mplstereonet provides stereonets for matplotlib

"""

# INPUT DATA

import numpy as np
import matplotlib.pyplot as plt
import mplstereonet as st

fid_df = open('filename_df.dat','r') # dextral faults
fid_sf = open('filename_sf.dat','r') # sinistral faults
fid_ef = open('filename_ef.dat','r') # extensional fractures

"""
They take .dat files containing field measurement.
The first line of the filenames consists of headers.
The filename_df and filename_sf consist of 3 columns:
Dip_Direction(degree) Dip(degree) Rake(degree).
```

```
The filename_ef consists of 2 columns:
Dip_Direction(degree) Dip(degree).
"""

# File headers
col_head_df = fid_df.readline()
col_head_sf = fid_sf.readline()
col_head_ef = fid_ef.readline()

# Structural data
dd_df, d_df = np.loadtxt(fid_df, unpack = True, usecols = [0,1]) # Dip direction
(°)
                                                                  # Dip (°)
dd_sf, d_sf = np.loadtxt(fid_sf, unpack = True, usecols = [0,1])
dd_ef, d_ef = np.loadtxt(fid_ef, unpack = True, usecols = [0,1])

s_df = dd_df - 90  # Strike (°)
s_sf = dd_sf - 90
s_ef = dd_ef – 90

# Mean vectors of poles
"""
If the poles are distributed across the primitive circle (i.e. subvertical
planes with opposite dips), the poles are first rotated in order to not cross
the primitive circle, the mean vector is calculated and then rotated
back to the original position.
"""

pl_df, b_df = st.pole2plunge_bearing(s_df, d_df)    # from strike and dip of a
                                                    # plane to plunge and
                                                    # bearing of its pole
lon_df, lat_df = st.line(pl_df,b_df)                # from stereographic to
                                                    # geographic
xdf,ydf,zdf = st.stereonet2xyz(lon_df, lat_df)      # from geographic to xyz

theta = np.radians(-90)                             # rotation angle

Xdf_r = xdf*np.cos(theta) + -zdf*np.sin(theta)      # rotation to 'y' axis
Ydf_r = ydf
Zdf_r = xdf*np.sin(theta) + zdf*np.cos(theta)

lon_df_r, lat_df_r = st.xyz2stereonet(Xdf_r,Ydf_r,Zdf_r)  # from xyz to geographic
pl_df_r,b_df_r = st.geographic2plunge_bearing(lon_df_r,lat_df_r)# from geographic
                                                              # to stereographic
mv_df_r, r_df_r = st.find_mean_vector(pl_df_r,b_df_r)     # meand vector (rotated)

lon_mdf_r, lat_mdf_r = st.line(mv_df_r[0],mv_df_r[1])
xdf_r,ydf_r,zdf_r = st.stereonet2xyz(lon_mdf_r, lat_mdf_r)

thetab = -theta

Xmdf = xdf_r*np.cos(thetab) + -zdf_r*np.sin(thetab)
Ymdf = ydf_r
Zmdf = xdf_r*np.sin(thetab) + zdf_r*np.cos(thetab)

lon_mdf, lat_mdf = st.xyz2stereonet(Xmdf,Ymdf,Zmdf)
pl_mdf,b_mdf = st.geographic2plunge_bearing(lon_mdf,lat_mdf) # plunge and bearing
                                                             # of mean dextral
                                                             # fault

pl_sf, b_sf = st.pole2plunge_bearing(s_sf, d_sf)
```

```
mv_sf, r_sf = st.find_mean_vector(pl_sf,b_sf)       # plunge and bearing of
                                                    # mean sinistral fault

pl_ef, b_ef = st.pole2plunge_bearing(s_ef, d_ef)

lon_ef, lat_ef = st.line(pl_ef,b_ef)
xef,yef,zef = st.stereonet2xyz(lon_ef, lat_ef)

Xef_r = xef*np.cos(theta) + -zef*np.sin(theta)
Yef_r = yef
Zef_r = xef*np.sin(theta) + zef*np.cos(theta)

lon_ef_r, lat_ef_r = st.xyz2stereonet(Xef_r,Yef_r,Zef_r)
pl_ef_r,b_ef_r = st.geographic2plunge_bearing(lon_ef_r,lat_ef_r)

mv_ef_r, r_ef_r = st.find_mean_vector(pl_ef_r,b_ef_r)

lon_mef_r, lat_mef_r = st.line(mv_ef_r[0],mv_ef_r[1])
xef_r,yef_r,zef_r = st.stereonet2xyz(lon_mef_r, lat_mef_r)

Xmef = xef_r*np.cos(thetab) + -zef_r*np.sin(thetab)
Ymef = yef_r
Zmef = xef_r*np.sin(thetab) + zef_r*np.cos(thetab)

lon_mef, lat_mef = st.xyz2stereonet(Xmef,Ymef,Zmef)
pl_mef,b_mef = st.geographic2plunge_bearing(lon_mef,lat_mef)


s_mdf, d_mdf = st.plunge_bearing2pole(pl_mdf,b_mdf)       # strike and dip of
                                                          # mean dextral fault
s_msf, d_msf = st.plunge_bearing2pole(mv_sf[0],mv_sf[1])  # strike and dip of
                                                          # mean sinistral fault

Sigm3 = [pl_mef,b_mef]                                    # plunge and bearing of
                                                          # minimum pricipal
                                                          stress
Sigm2 = st.plane_intersection(s_mdf,d_mdf,s_msf,d_msf)    # plunge and bearing of
                                                          # intermediate princ.
                                                    stress
lon_s3, lat_s3 = st.line(Sigm3[0],Sigm3[1])
Xs3, Ys3, Zs3 = st.stereonet2xyz(lon_s3, lat_s3)

lon_s2, lat_s2 = st.line(Sigm2[0],Sigm2[1])
Xs2, Ys2, Zs2 = st.stereonet2xyz(lon_s2, lat_s2)

Xs1 = Ys2*Zs3-Zs2*Ys3
Ys1 = Zs2*Xs3-Xs2*Zs3
Zs1 = Xs2*Ys3-Ys2*Xs3

lon_s1, lat_s1 = st.xyz2stereonet(Xs1, Ys1, Zs1)
Sigm1 = st.geographic2plunge_bearing(lon_s1, lat_s1)      # plunge and bearing of
the
                                                          # maximum principal
stress

# Angles between faults and maximum principal stress

Xdf = np.zeros(len(s_df))
Ydf = np.zeros(len(s_df))
Zdf = np.zeros(len(s_df))
Xi = np.zeros(len(s_df))
```

```
Yi = np.zeros(len(s_df))
Zi = np.zeros(len(s_df))

for i in range(len(s_df)):
    lon_df[i], lat_df[i] = st.line(pl_df[i],b_df[i])
    Xdf[i], Ydf[i], Zdf[i] = st.stereonet2xyz(lon_df[i], lat_df[i])
    Xi[i] = Ydf[i]*Zs1-Zdf[i]*Ys1
    Yi[i] = Zdf[i]*Xs1-Xdf[i]*Zs1
    Zi[i] = Xdf[i]*Ys1-Ydf[i]*Xs1

lon_i, lat_i = st.xyz2stereonet(Xi, Yi, Zi)
pl_i, b_i = st.geographic2plunge_bearing(lon_i, lat_i)
s_i, d_i = st.plunge_bearing2pole(pl_i,b_i)
pl_pi, b_pi = st.plane_intersection(s_i, d_i,s_df[1],d_df[1])
lon_pi, lat_pi = st.line(pl_pi,b_pi)
Xpi, Ypi, Zpi = st.stereonet2xyz(lon_pi, lat_pi)

angle = np.zeros(len(s_df))
vec1 = np.zeros((len(s_df),3))
vec2 = np.array([Xs1, Ys1, Zs1])
for i in range(len(s_df)):
    vec1[i]=[Xpi[i],Ypi[i],Zpi[i]]

angle[i]=np.arccos(np.dot(vec1[i],vec2)/(np.linalg.norm(vec1[i])*np.linalg.norm(ve
c2)))
    angle[i] = np.rad2deg(angle[i])
```

B.2. Data analysis of triaxial saw-cut experiments in which slip occurs within the saw-cut

This script was developed to analyze raw data of triaxial saw-cut experiments in which slip occurs within the saw-cut. It calculates differential, shear and normal stresses and it applies corrections to stresses and displacement for the strength of the polyolefin jacket and the elastic stretch of the load frame on the vertical axis (see Appendix A).

```
"""
Data analysis of triaxial saw-cut experiments in which slip occurs within the saw-
cut

Author: Carolina Giorgetti
Date:  28/02/2017

Description:
This program analyzes BRAVA data acquired during triaxial saw-cut experiments.
From the vertical force registered during the experiments results the
differential stress acting on the sample.
When slip occurs within the saw-cut, the differential stress depends on
the nominal contact area that changes through time with the axial displacement
(see e.g., Scott et al., 1994; Tembe et al., 2010).

Exp. number: b___
Saw-cut angle to the axial stress (maximum principal stress): __°
thickness of the gouge layer placed within the saw-cut: __ mm
sample height (on bench-top): ___ mm
sample height after confining pressure is applied: __ mm
```

```
"""

# INPUT DATA

import numpy as np
import math as math

fid = open('filename','r')

"""
It takes a filename containing the text output (with headers) from the tool
`XLook' (https://github.com/PennStateRockandSedimentM#echanics/xlook).

A series of zeroing corrections are previously applied to the experimental raw
data with XLook.

The first five lines of the filename are headers.
The filename consists of 6 columns: record number, vertical displacement,
vertical load, confining pressure, confining intensifier displacement, time.
"""

# File headers
num_recs = fid.readline() # number of records
num_cols = fid.readline() # column numbers
col_heads = fid.readline() # column headings
col_units = fid.readline() # column units
col_recs = fid.readline() # number of records per column

# Mechanical data
V_disp, V_load, Pc, Time = np.loadtxt(fid, unpack = True, usecols = [1,2,3,5])
"""
V_disp is vertical displacement [mm]
V_load is vertical load [kN]
Pc is confining pressure [MPa]
Time is time [s]
"""

# Sample geometrical parameters
theta = float( __ ) # theta is the angle between saw-cut and sample axis
                    # insert the value within the parentheses [degrees]
theta_rad = math.radians(theta)
d = float( __ ) # d is the diameter of the sample
                # insert the value within the parentheses [mm]
r = d / 2.0
shear_disp = V_disp / (math.cos(theta_rad)) # along saw-cut didplacement [mm]
dsd_dl = float( __ ) # jacket strength at the value of confining pressure at
                     # which the experiment is conducted
                     # insert the value within the parantheses [MPa/mm]
k_la = float( __ ) # stiffness of the loading apparatus on the vertical axis
[MPa/mm]

# CALCULATION OF DIFFERENTIAL STRESS FROM VERTICAL LOAD
"""
Nominal contact area changes through time with the axial displacement
and it is evaluated as follows (e.g. Scott et al., 1994):

A_corr = r ^ 2 * (THETA - sin(THETA))
THETA = pi – 2 * asin * (dl / (2 * r) * tan(theta))

where:
```

```
THETA is the angle subtended by the points of intersection of two overlapping
circles
at their centers (radius r and centers distance dl*tan(theta))
theta is the angle between saw-cut and sample axis
dl is the vertical (axial) displacement
r is the sample radius
"""

arg = np.zeros(len(V_load)) # argument of the arcsine in THETA equation
THETA = np.zeros(len(V_load))
A_corr = np.zeros(len(V_load)) # [mm^2]
SigmD = np.zeros(len(V_load)) # Differential stress [MPa]
SigmDNew = np.zeros(len(V_load)) # Differential stress corrected
                                 # for jacket strength [MPa]
V_dNew = np.zeros(len(V_disp)) # Vertical displacement corrected
                               # for apparatus stiffness

for i in range(len(V_load)):
    arg[i] = V_disp[i] / (2 * r) * math.tan(theta_rad)
    THETA[i] = math.pi – 2 * math.asin(arg[i])
    A_corr[i] = r**2 * (THETA[i] – math.sin(THETA[i]))

for i in range(len(V_load)):
    V_load[i] = V_load[i] / (10**3) # [MN]
    A_corr[i] = A_corr[i] * 10**(-6) # [m^2]
    SigmD[i] = V_load[i] / A_corr[i] # [MPa]

SigmDNew[0]=0
V_dNew[0]=0
for i in range(0,len(SigmDNew)-1,1):
    SigmDNew[i+1]=SigmDNew[i]+(SigmD[i+1]-SigmD[i])-(V_disp[i+1]-V_disp[i])*dsd_dl
    V_dNew[i+1]=V_dispNew[i]+(V_disp[i+1]-V_disp[i])-(SigmDNew[i+1]-
SigmDNew[i])/k_la

# CALCULATION OF NORMAL STRESS RESOLVED ON SAWCUT
# SigmN = 0.5 * (SigmD + 2*Pc) - 0.5 * SigmD * cos(2*theta)

SigmN = np.zeros(len(V_load)) # normal stress resolved on saw-cut [MPa]

for i in range(len(V_load)):
   SigmN[i] = 0.5 * (SigmDNew[i] + 2*Pc[i]) - 0.5 * SigmDNew[i] *
math.cos(2*theta_rad)

# CALCULATE OF SHEAR STRESS RESOLVED ON SAWCUT
# Tau = 0.5 * SigmD * sin(2*theta)

Tau = np.zeros(len(V_load)) # shear stress resolved on saw-cut [MPa]

for i in range(len(V_load)):
   Tau[i] = 0.5 * SigmDNew[i] * math.sin(2*theta_rad)
```

Appendix C.
Friction and scale-dependent deformation processes of large experimental carbonate faults

Appendix C. Frictional and scale-dependent deformation processes of large experimental carbonate faults

Journal of Structural Geology 100 (2017) 12–23

Contents lists available at ScienceDirect

Journal of Structural Geology

journal homepage: www.elsevier.com/locate/jsg

Friction and scale-dependent deformation processes of large experimental carbonate faults

Telemaco Tesei [a, *], Brett M. Carpenter [b], Carolina Giorgetti [a, c], Marco M. Scuderi [a, c], Amir Sagy [d], Piergiorgio Scarlato [a], Cristiano Collettini [a, c]

[a] Istituto Nazionale di Geofisica e Vulcanologia, Via di Vigna Murata 605, 00143, Roma, Italy
[b] School of Geology and Geophysics, University of Oklahoma, Norman, USA
[c] Dipartimento di Scienze della Terra, Università La Sapienza di Roma, Italy
[d] Geological Survey of Israel, Jerusalem, Israel

ARTICLE INFO

Article history:
Received 12 December 2016
Received in revised form
12 May 2017
Accepted 18 May 2017
Available online 19 May 2017

Keywords:
Fault
Carbonate
Friction
Nanoparticle
Deformation
Scale

ABSTRACT

We studied the frictional behaviour and deformation products of large (20 cm × 20 cm bare surfaces) experimental limestone faults. We sheared samples in a direct shear configuration, with an imposed normal force of 40–200 kN and shear velocity of 10 μm/s. The steady-state shearing of these surfaces yielded a coefficient of friction $0.7<\mu<1$ (average $\mu\sim0.9$), significantly higher than gouge friction of the same material, $\mu\sim0.6$. Frictional healing, studied via slide-hold-slide tests, is null ($\Delta\mu\leq0$ upon re-shear). Moreover, sliding of these surfaces is accompanied by dilatation and production of grooves, gouge striations and fault mirrors. These products are entirely analogous to slip surface phenomena found on natural limestone-bearing faults at both the macroscale and at the microscale. We infer that high friction, accompanied by dilatant deformation, and null frictional healing are the macroscopic effect of brittle damage on the sliding surface, constrained by the strength of the rock and by fast healing processes in the gouge. Simultaneously to brittle failure, plastic deformation occurs on the sliding surface and inside the intact rock via nanoparticle formation (mirrors) and twinning at the micron scale. Because of the similarity between experimental and natural structures, we suggest that sliding of carbonate-bearing faults in the uppermost crust could be characterized by high friction, fast healing and strongly dilatant deformation, which would help to explain shallow seismicity frequently documented in carbonatic terrains such as the Northern Apennines of Italy.

1. Introduction

In the uppermost crust, most of the displacement between rock masses is accommodated by brittle faults. The inner structure of fault zones can be complex as it is the result of complex geological histories and processes (e.g. Faulkner et al., 2010; Niemeijer et al., 2012 for recent reviews and references therein). However, a common characteristic of brittle fault zones is that they can be seen as a hierarchy of slip localization features, from large-scale fault systems to microscale fractures (Tchalenko, 1970; Ben Zion and Sammis, 2003). Individual fault zones are commonly characterized by damage zones and associated subsidiary faults, which host a "fault core" of more intensely deformed rocks (typically a few meters thick). In turn, the fault core hosts one or multiple throughgoing, "knife-edge" slip zones, commonly known as Principal Slip Zones (PSZ e.g. Sibson, 1986 and references therein) that accommodate most of the fault's displacement.

It is commonly assumed that the PSZ accommodate coseismic sliding (Sibson, 2003), which is corroborated by field and microstructural evidence, both in silicatic and carbonatic PSZ (e.g. Heesakkers et al., 2011; Rowe et al., 2012; Collettini et al., 2013). However, localized slip zones can also accommodate aseismic slip (e.g. Burford and Harsh, 1980; Scotti and Cornet, 1994). It is therefore crucial to study the deformation products and assess the mechanical properties of the PSZ, in order to understand fault motion and correlate field observations with slip dynamics.

In the field, PSZ are characterized by various slip surface phenomena (e.g. Stewart and Hancock, 1991). In particular, grooves and wear material are common products associated with fault slip (e.g. Engelder, 1974) and suggest directional and scale-dependent

* Corresponding author.
E-mail address: telemaco.tesei@ingv.it (T. Tesei).

http://dx.doi.org/10.1016/j.jsg.2017.05.008
0191-8141/

Appendix C. Frictional and scale-dependent deformation processes of large experimental carbonate faults

heterogeneity that may mirror equivalent heterogeneities in stress and slip behaviour along the PSZ (e.g. Dunham et al., 2011; Kirkpatrick and Brodsky, 2014).

The small thickness of typical PSZ, typically ranging from a few cm to a few microns (e.g. Sibson, 2003), enables the possibility to reproduce them during mm-size laboratory experiments (e.g. Brace and Byerlee, 1966; Barton, 1976; Sammis et al., 1987; Reches and Lockner, 2010 and many others). However, a number of outcrop-scale phenomena, and in particular those involving PSZ surrounded by cohesive fault materials or intact rocks (e.g. grooves and wear production), are not commonly captured in standard (mm-size) high-pressure rock friction experiments (but see e.g. McLaskey and Kilgore, 2013; Delle Piane et al., 2016). These features most likely depend on local stress heterogeneities imposed by the topography of the slip surfaces and/or competence contrasts between the hangingwall and footwall and remain poorly understood (e.g. Bistacchi et al., 2011; Brodsky et al., 2016).

To study the deformation of PSZ at different laboratory scales and to better understand the slip behaviour of carbonate-bearing faults, we performed biaxial experiments on limestone PSZ. We link the frictional properties with deformation mechanisms during slip and compare them with field observations. We performed direct shear experiments on large (20 cm × 20 cm) limestone bare surfaces simulating smooth carbonate PSZ surrounded by cemented fault rocks. With this experimental design, we are able to reproduce typical phenomena that affect PSZ such as grooves (toolmarks), fault mirrors and localized gouge formation. For comparison with previous experimental work and to test the reliability of our setup, we also performed experiments on standard synthetic fault gouge of the same limestone.

2. Characteristics of Principal Slip Zones in carbonatic faults

Carbonates frequently host intense seismicity (e.g. Ben-Menahem, 1991; Valoroso et al., 2014) and large carbonate-bearing fault zones are typically characterized by a complex interaction of brittle and ductile (mostly pressure-solution) processes (e.g. Koopman, 1983; Gratier et al., 2013; Tesei et al., 2013 and references therein). These processes may result in heterogeneous slip behaviour (i.e. seismic/aseismic) along these faults (e.g. Tesei et al., 2014). Still, fault displacement is generally localized along thin slip surfaces, albeit sometimes partitioned between several PSZ (e.g. Bussolotto et al., 2007; Collettini et al., 2014a).

Field observations in competent limestone formations show that PSZ of large faults (e.g. Fig. 1) are characterized by very fine-grained cataclastic rocks (e.g. Agosta and Aydin, 2006; Smith et al., 2011). These rocks are typically cohesive due to the lithification ("healing" s.l.) of the slip zone via compaction and cementation of the fault gouge after slip events (Fig. 1a–d). The slip zones are almost invariably decorated by slickenlines, slickenfibres and grooves (Fig. 1b and c), frequently filled with cemented cataclasites (Fig. 1d), or covered by unconsolidated gouge ("attrition gouge" *sensu* Sibson, 1986, Fig. 1e), depending on the fault's exhumation. Fig. 1 summarizes structures commonly found along PSZ in carbonates observable along the M. Maggio and Assergi fault system (Northern and Central Apennines, Italy), and in particular highlights deformation structures occurring at the outcrop scale that are rarely reproduced in the laboratory.

Moreover, unaltered carbonatic PSZ are frequently highly reflective ("fault mirrors", e.g. Fig. 1b) and are characterized, at the microscale, by smooth layers of nanoparticles and/or polygonal grains along the slip zone (Siman-Tov et al., 2013; Collettini et al., 2014a). Such nanoparticles still have unclear origin, and have been sometimes attributed to coseismic slip, in particular, when mirrors cover extensive fault portions and are associated with truncated clasts and shattered rocks. These features exhibit a striking similarity between natural and experimental faults (Boneh et al., 2013; Fondriest et al., 2015). Indeed, carbonate slip surfaces produced during high velocity friction experiments truncate gouge clasts and are characterized by nanoparticle formation and/or polygonal grains, showing evidence of crystal growth indicative of a thermal anomaly (Smith et al., 2012). However, nanoparticles can also form at sub-seismic slip rates in localized shear bands (e.g. Verberne et al., 2013, 2014; Tesei et al., 2014) and may not be indicative alone of co-seismic slip, even though they may be a prerequisite for efficient dynamic weakening (e.g. De Paola et al., 2015).

3. Methods

To study the friction of limestone surfaces at different laboratory scales, we designed sliding friction experiments in a "single direct" configuration (Fig. 2). Samples were cut into limestone blocks using a diamond saw. We cut slabs with dimensions of 20 cm × 20 cm x 3.5 cm and 25 cm × 20 cm x 3.5 cm to simulate slip zones embedded in a cemented (healed) fault rock (e.g. Fig. 1a–d). We simulated strongly cemented cataclastic fault rocks using a bioclastic limestone (Maljat® biomicrite/biosparite). The Maljat limestone is constituted by bioclasts, with heterogeneous size and shape and surrounded by sparite or a fine-grained matrix, similar to a cataclasite (Fig. S1). All of the experimental limestone blocks were cut from a single slab and show a mostly isotropic texture without stylolites. Block faces were ground flat with a precision grinder, better than 0.1 mm, and then ground along the edges to perfectly fit the sample holders (Fig. 2b). The sliding surfaces were then roughened with sandpaper to attain a similar starting roughness before the tests and to simulate the smoothness of natural PSZ. "Rough" surfaces, polished with #60 or #40 grit sandpaper (265 and 425 μm average abrasive grain size, respectively), and "smooth" surfaces, polished up to #3000 grit sandpaper (6 μm grain size), were used to study the effect of different initial roughness on the frictional properties of the experimental fault.

Experiments were performed using the BRAVA biaxial apparatus (INGV Rome, Collettini et al., 2014b) under conditions of room humidity (35–50% relative humidity) and ambient temperature (T 18–26 °C). In the single-direct configuration, two sliding blocks are sheared against each other (Fig. 2b). Alternatively a layer of rock powder can be built between the sample holders to study fault gouge-like materials. The sliding blocks, with area 20 cm × 20 cm and 20 cm × 25 cm respectively, are contained within two steel sample holders that act as a shear box (Fig. 2b). The side block is in contact with the horizontal ram, which applies the normal force to the samples, whereas the central block is pushed by the vertical piston to provide the shear force along the experimental surface. The central block in contact with a mirror-finished steel surface is lubricated with a MoS_2-based lubricant that ensures a very low friction contact ($\mu \ll 0.01$). The walls of the chamber act as the load frame. Forces are measured with stainless steel load cells (±0.03 kN precision) and displacements are measured with Linear Variable Displacement Transducers (LVDT, ±0.1 μm precision) attached to each piston (Fig. 2a). During data analysis, displacement measurements from LVDTs have been corrected for the elastic stretch of the steel chamber that acts as the load frame (1283 kN/mm and 928.5 kN/mm in the horizontal and vertical direction, respectively).

During each test on bare surfaces, normal force was kept constant during sliding, in the range 40–200 kN. These values are equivalent to ~1–5 MPa nominal normal stress on the surfaces, but are considered only as a reference value for the experiment given the uneven distribution of stress on the block surfaces. This uneven stress distribution is likely due to roughness and the progressive

Appendix C. Frictional and scale-dependent deformation processes of large experimental carbonate faults

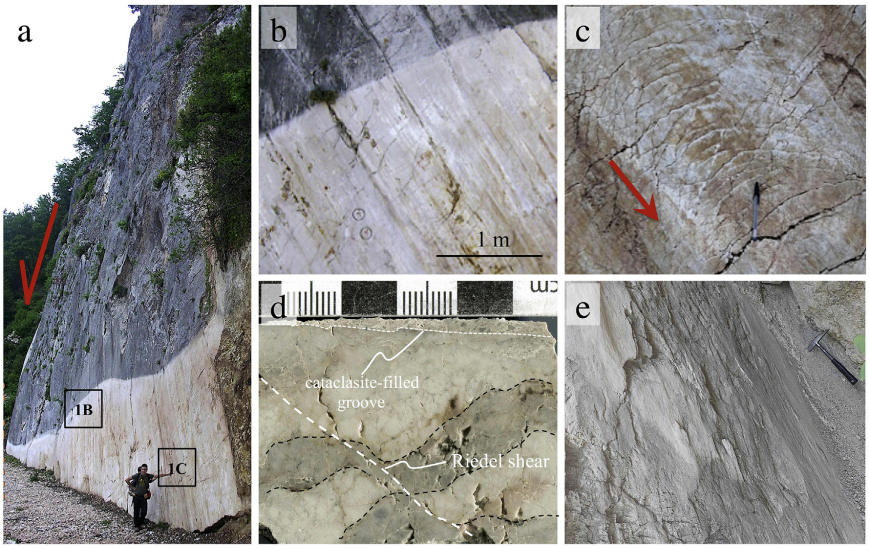

Fig. 1. Structural features of carbonatic Principal Slip Zones. A) Monte Maggio normal fault (Collettini et al., 2014a), striated PSZ accommodating ~50 m slip. B) Detail of the striated and polished Monte Maggio PSZ. C) Internal structure of a groove on the Monte Maggio PSZ displaying ring fractures with convexity opposed to the sense of shear (red arrow shows the movement of the hangingwall block). D) Cross-section of a PSZ characterized by synthetic Riedel shears (displacing a dark grey cataclastic horizon highlighted by black dashed lines) and grooves filled with cemented cataclasites (white dashed line, Assergi fault system, Central Apennines). E) Striated and incohesive fault gouge along the Assergi normal fault. (For interpretation of the references to colour in this figure legend, the reader is referred to the web version of this article.)

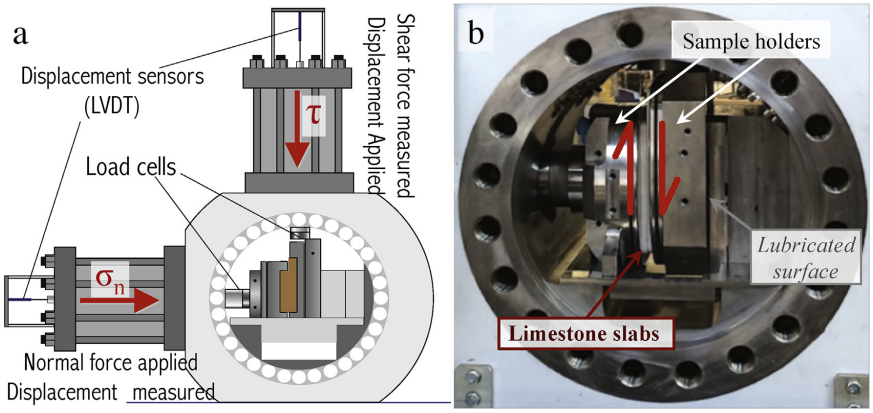

Fig. 2. A) Large single-direct shear configuration within the BRAVA biaxial apparatus. The steel chamber serves the loading frame of the apparatus. B) 20 cm × 20 cm limestone bare surfaces mounted in the sample holders during experiment b526.

stress concentration on small patches while sliding (see section 4). Sliding velocity was initially imposed at 10 μm/s and Fig. 3a shows typical friction vs. displacement and dilatation vs. displacement curves obtained during the shearing of both "rough" and "smooth" 20 cm × 20 cm bare surfaces (i366 and i332). Friction is computed as the ratio between the vertical force and the normal force applied by the vertical and horizontal pistons, respectively (F_τ/F_n). Friction and dilatation curves for all the experiments are illustrated in the Supplementary Material (Figs. S3–S15).

Initially, at slip distance values < 10 mm and usually less than 5 mm, the blocks show a non-linear slip hardening behaviour, which is attributed to a combination of adjustment of the sample assembly, the elastic loading of the limestone blocks, the yielding and unsteady sliding of the slip surfaces. After the initial phase, after a steady-state friction was reached, sliding velocity was varied in velocity-stepping sequences (not illustrated in the present study)

Appendix C. Frictional and scale-dependent deformation processes of large experimental carbonate faults

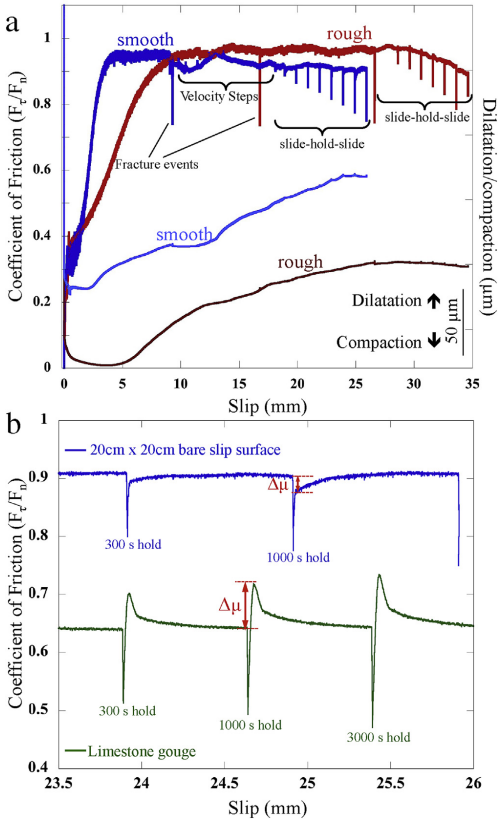

Fig. 3. A) Friction and dilatancy of large 20 × 20 cm bare surfaces. Typical friction curve during shearing of large bare surfaces: both smooth (blue, experiment i366) and rough (red, experiment i332) sliding surfaces yield high friction accompanied by dilatation and low frictional healing during slide-hold-slide tests. B) Zoom on typical slide-hold-slide sequences in both large bare surfaces (blue, i366) and gouge (green, i154, from Tesei et al., 2014). Frictional healing (Δμ) is measured as the difference between pre-hold steady state friction and peak friction upon reshear (red arrows). Note the lack of peak and slight weakening of 20 cm × 20 cm bare surfaces upon reshear. (For interpretation of the references to colour in this figure legend, the reader is referred to the web version of this article.)

and finally toggled for slide-hold-slide tests (SHS, e.g. Dieterich, 1972). Slide-hold-slide tests are used to study frictional strength recovery (frictional healing) due to variable periods of quasi-stationary contact between the surfaces (hold time t_h 3–3000 s). The frictional healing of both bare surfaces and gouge was measured as the difference, Δμ, between friction measured just before the sliding is halted and friction measured upon reshearing (Fig. 3b).

In addition, we performed sliding experiments on synthetic fault gouge obtained from the same Maljat® limestone under the same temperature and room-humidity conditions. The gouge was produced by crushing the rock in a disk mill and sieved to obtain the fraction with grain size <125 μm. Gouge experiments were carried out under constant normal stress, 1–10 MPa, using a 5 cm × 5 cm double-direct shear configuration and the large 20 cm × 20 cm single direct setup, with a sliding velocity of 10 μm/s and hold times of 3–3000s during SHS tests. In the double-direct experiments, we sandwiched 0.5 cm-thick gouge layers in between three steel forcing blocks. The forcing blocks are grooved with 2 mm-deep grooves to ensure that slip occurs in the gouge and not at the steel-gouge interface. The two side blocks are held stationary, and the central forcing block is driven downward causing shear to occur within the gouge layers. The layers were built with the help of a levelling jig and pre-compacted using a standard 6 kg weight. In the 20 cm × 20 cm single direct configuration, the same forcing blocks used in bare surface experiments, were filled with grooved steel plates (2 mm groove depth) and used as the base to build a 1 cm thick gouge layer. In all gouge experiments, the powder layer was held in place by adhesive tape attached to the sides of the sample assemblies. These tests were performed to compare frictional strength and healing of limestone surfaces with standard gouge experiments and to test the reliability of the large single-direct shear setup. Table 1 lists all the experiments and experimental conditions presented in this study.

After the experiments, we performed a visual inspection of the sheared surfaces/gouges. Moreover, to study slip surface phenomena and to estimate the real contact area of the blocks at the end of the experiment, most sliding surfaces were subject to high-resolution optical scanning (Epson PerfectionV300 scanner, 1200–2400 dpi). Scans were performed both before and after the experiment (Supplementary Material Figs. S23 and S24). We then used Optical Microscopy and Scanning Electron Microscopy (SEM) to study the products of deformation and the correlation between mechanical data and structural evolution of the sample. SEM analyses were performed with the Jeol 6005F Field Emission SEM hosted at the HP-HT Laboratory of the Istituto Nazionale di Geofisica e Vulcanologia, Rome (Italy), operated in secondary electron mode using an acceleration voltage of 6 kV.

4. Results

4.1. Friction and frictional healing properties

The sliding of the 20 × 20 cm bare surfaces is always associated with dilatation of the surfaces (Fig. 3a) and we observe the separation of the bare surfaces with progressive slip. Occasionally, small stress drops occurred in coincidence with minor failures of the limestone slabs, which in any case did not result in changes of slip behaviour during the experiments (Fig. 3a).

Fig. 4 reports the frictional strength of large 20 cm × 20 cm bare surfaces in comparison to experimental fault gouges of the same Maljat limestone and from fault zone limestone from Tesei et al. (2014) sheared under the same experimental conditions. Friction reported in Fig. 4 was measured at single points during steady-state shearing, in order to only compare the long-term evolution of friction vs. slip in different experiments, ignoring second order variations in friction.

The large bare surfaces have systematically high values of steady-state friction between $0.7<\mu<1$ (average $\mu\sim0.9$) and are generally independent from the initial roughness and imposed normal force acting on the blocks (Fig. 4). As a comparison, Maljat limestone gouges and similar calcite-bearing gouges (Tesei et al., 2014) show friction in the range $0.59<\mu<0.67$. Friction of gouges sheared in the small configuration (experiment i497) and large configuration (experiment b514) do not differ significantly, indicating that the experimental setup does not exert a significant effect on gouge friction (Fig. 4).

Frictional healing results, illustrated in Fig. 5, show a different evolution depending upon the tested boundary conditions. Large, bare surfaces show near zero re-strengthening after short periods

Appendix C. Frictional and scale-dependent deformation processes of large experimental carbonate faults

Table 1
List of experiments and experimental conditions.

Exp. #	Type of experiment	Surface finish sandpaper particle Ø	Normal Force (kN)	Velocity steps/Slide-hold-slide (yes/no)
i225	20 cm × 20 cm bare surfaces, single direct	265	120	y/y
i238	20 cm × 20 cm bare surfaces, single direct	265	40	n/y
i332	20 cm × 20 cm bare surfaces, single direct	265	40	n/y
i366	20 cm × 20 cm bare surfaces, single direct	6	40	y/y
i410	20 cm × 20 cm bare surfaces, single direct	6	40	n/n
i411	20 cm × 20 cm bare surfaces, single direct	6	40	n/n
i419	20 cm × 20 cm bare surfaces, single direct	6	60/80/120 160/200	y/n
i474	20 cm × 20 cm bare surfaces, single direct	265	40	y/y
i478	20 cm × 20 cm bare surfaces, single direct	6	40	n/n
i484	20 cm × 20 cm bare surfaces, single direct	6	40	n/n
i497	5 cm × 5 cm gouge, double direct	not applicable	2.5/25	n/n
b514	20 cm × 20 cm gouge, double direct	not applicable	40/80	n/n
b526	20 cm × 20 cm bare surfaces, single direct	6	200	n/n

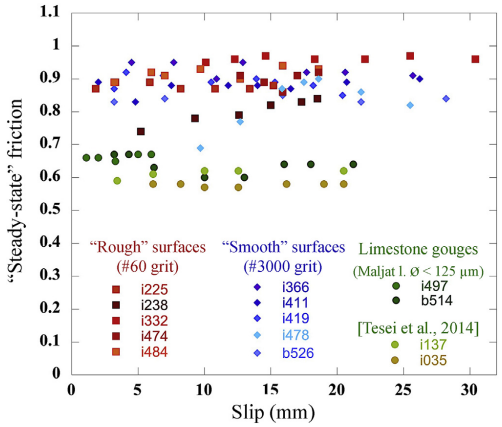

Fig. 4. Friction vs. displacement for all experiments on large bare surfaces, measured during steady-state sliding. Initially rough (lapped with sandpaper grit #60) are displayed in red tones and smooth surfaces (sandpaper grit #3000) are shown in blue tones. For comparison: friction of Maljat® limestone gouges and powders of natural cataclastic limestones (from Tesei et al., 2014). Room temperature and humidity conditions. (For interpretation of the references to colour in this figure legend, the reader is referred to the web version of this article.)

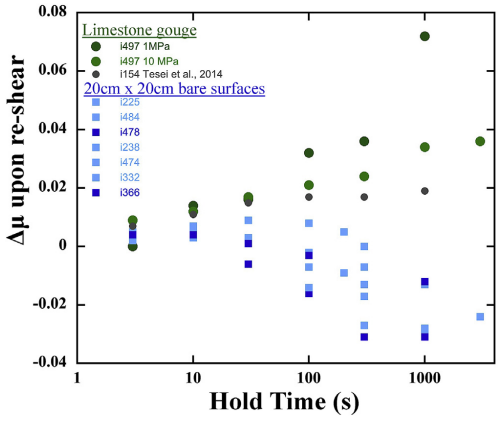

Fig. 5. Frictional healing (Δμ) vs. hold time of large bare surfaces (blue tones) and limestone gouges from this study (green tones) and Tesei et al., 2014 (grey), carried out at 1 and 10 MPa normal stress. (For interpretation of the references to colour in this figure legend, the reader is referred to the web version of this article.)

of quasi-stationary contact (hold time t_h < 300s) and negative values after hold times greater than 300s (Fig. 5). Indeed, after long hold times, the surfaces slid at slightly lower friction with respect to pre-hold levels (Fig. 3a). Conversely, experimental gouges of Maljat limestone always show positive Δμ, with a very high healing rate ($\beta = \Delta\mu/\log_{10}t_h$) in the range 0.009<β < 0.028 (Fig. 5). These frictional healing values are in the same range measured for Carrara Marble (0.008<β < 0.041, Chen et al., 2015; Carpenter et al., 2016a,b) and other limestone fault gouges (0.009<β < 0.027, Tesei et al., 2014, Fig. 5) sheared under a variety of normal stresses, temperature and saturation conditions.

4.2. Deformation structures

The macroscopic deformation structures observed on the 20 cm × 20 cm experimental surfaces were very similar at the end of each experiment, despite differences in sliding histories. The surfaces at the end of the experiments were always characterized by the presence of patches of wear material elongated in the direction of slip (Fig. 6a and b). The gouge patches always cover elongated grooves ploughed into the slip surfaces that are

Appendix C. Frictional and scale-dependent deformation processes of large experimental carbonate faults

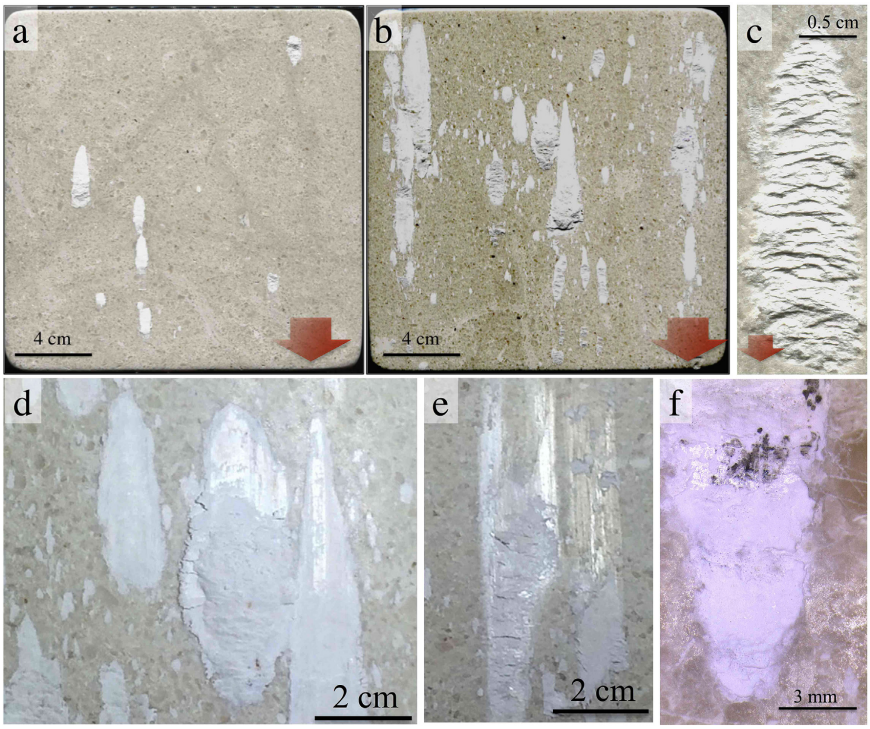

Fig. 6. Post-experimental structures on large bare surfaces. Red arrow indicates the movement of the hangingwall block (removed) A) Plane view of the surface of experiment i478 (F_N = 40 kN). Gouge patches (white) developed during the experiment. B) Plane view of the surface of experiment b526 (F_N = 200 kN). Note the abundance of wear products with respect to 6A. C) Typical groove developed under a gouge patch (removed), characterized by ring-shaped tensional fractures. D) Detail of gouge patch with relief, indicative of material transfer between the bare surfaces during the test. Reflective surfaces develop on the boundary shear plane of the gouge (mirrors). E) Reflective surfaces developed on the block bare surface (b526). F) Striated black material developed on top of a gouge patch (i478). (For interpretation of the references to colour in this figure legend, the reader is referred to the web version of this article.)

produced during the experiments (Fig. 6a–b). As expected, slip surfaces subjected to higher normal force produced more wear during slip (e.g. Fig. 6a vs. 6b and Fig. S16, see also Badt et al., 2016).

The length of isolated grooves and gouge patches typically ranges from a fraction of a millimeter to the length of total displacement imposed during the experiment (10–50 mm, Fig. 6a–b). In large bare surface experiments, we always observe a relatively large number (>10) of small wear patches distributed along the slip surface and a few longer grooves that are wider and host the majority of wear material (e.g. Fig. 6a–b, Fig. S26). This implies that small grooves accommodated only limited amount of slip, possibly during early stages of the experiments, with respect to longer grooves that were active through most of the sliding. These grooves effectively document a dynamic evolution of the real contact area between the blocks.

When the gouge is removed, the grooves have an elongated shape and show semi-circular en-enchelon cracks, in which the convexity is opposite to the sense of shear (Fig. 6c). Moreover, when the sliding surfaces are separated at the end of the experiment, it is commonly observed that some patches are characterized by striated surfaces and cohesive gouge with relief. These gouge masses overlie the slip surfaces and retain the shape of grooves observed on the opposite block, indicating a net mass transfer between the surfaces (Fig. 6d). Striated gouge streaks do not always correspond to grooves on the opposite block, highlighting a spreading of gouge material between the surfaces and frictional sliding at the gouge/block interface (Fig. 6e). In addition to the gouge and groove patches, in sliding experiments carried out with initially very smooth surfaces we observe the occurrence of reflective zones (Fig. 6d–f). These mirrors are usually distributed on areas much larger than the gouge patches. They occur both on the block and on top of gouge-rich zones and are striated in the slip direction (Fig. 6e). Furthermore, small (<1 mm long) patches of striated black material are sometimes observed in close association with the reflective zones (Fig. 6f).

In cross section, the grooves show ridges of cohesive rock and en echelon arrays of tensional open fractures dipping towards the leading edge of the groove, consistent with the shear sense (Fig. 7a). These structures develop above a “damage zone” of micro-fracturing appearing as white horizons marked by the obliteration of the original sedimentary fabric of the Malijat limestone (Fig. 7a).

The attrition gouge produced in our experiments is slightly cohesive and has angular, heterometric clasts (Fig. 7b, grain size distribution in Fig. S2). Thin sections highlight that the gouge is densely packed and characterized by slip localization along Riedel

Appendix C. Frictional and scale-dependent deformation processes of large experimental carbonate faults

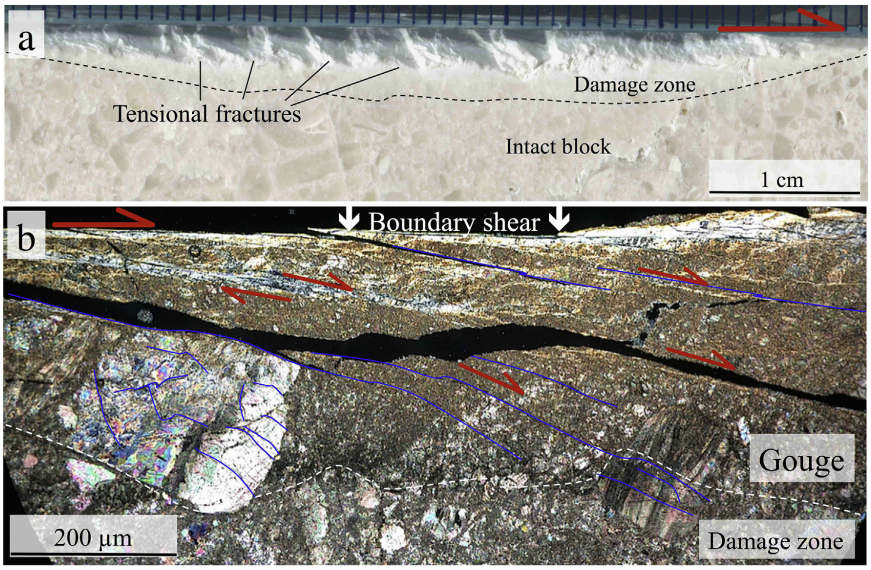

Fig. 7. A) Cross section of a typical experimental groove (experiment i410, gouge removed), characterized by en echelon tensional fractures developing from a cohesive "damage zone". B) Microphotograph (crossed polarizers) of a groove and wear material (experiment i419) characterized by en-enchelon tensional fractures in the block and within the gouge (highlighted by blue lines). Grain size reduction, highlighted by lighter colours in transmitted light, occurs in the gouge along Riedel (oblique) and boundary (horizontal) shears (highlighted by red shear arrows). (For interpretation of the references to colour in this figure legend, the reader is referred to the web version of this article.)

and boundary shears marked by bands of grain size reduction (Fig. 7b and Fig. S19). In particular, we note that Riedel shears are roughly parallel and directly linked to tensional fractures in the block that form the en enchelon fractures in the groove (Fig. 7b). Moreover, we observed drag folds in calcite crystals highlighted by the bending of the twins in the intact rock immediately beneath the groove and in larger clasts inside the cataclastic horizons, (Fig. S17).

Secondary electron SEM investigation of the sliding surfaces revealed that the slip surfaces at the top of the gouge patches (Y shears) are covered by a very fine grained material with micron and sub-micron scale striations (Fig. 8a–b). This ultrafine material is a thin (~1 μm) layer of rounded nanoparticles (grain size <50 nm) that lies on top of a coarser gouge (Fig. 8c). A similar analysis of the sliding surface was carried out in areas characterized by reflective surfaces (Fig. 8d). The reflective patches are smooth and striated zones, in contrast with the rough surface produced during sample preparation (Fig. 8d). The original sample surface is characterized by angular clasts of calcite with grain size similar to the sandpaper grit used to roughen the blocks (#3000 grit, 6 μm, Fig. 8e). Conversely, the reflective zones are constituted by layers of densely packed, sub-rounded nanoparticles similar to those found on the Y shears of the gouge (Fig. 8f).

5. Discussion

In the following section, we integrate mechanical data with microstructural investigations collected along carbonatic slip zones to discuss: a) the role of deformation processes and stress concentration on frictional strength; 2) the effect of fracturing and fault gouge development on frictional healing; 3) the development of plastic deformation along mirror-like slip surfaces; and d) faulting processes in carbonates.

5.1. Interpretation of frictional results & deformation products

Our experiments show that the frictional strength of carbonatic PSZ can be highly variable, ranging from the strength of the gouge (μ~0.6) to the strength of cohesive slip surfaces (μ~0.9–1), depending on the deformation processes, stress heterogeneity and slip history along the surfaces. In particular, our experiments carried out on larger samples allowed us to observe that during sliding on bare surfaces, deformation is typically dilatant (Fig. 3) and associated with the grooving of the slip surface and gouge production, as witnessed by post-experimental observations. Dilatation is caused by gouge formation from the intact block accumulating between the surfaces and/or riding of the blocks upon gouge materials, producing an actual separation of the blocks during the experiments. On the other end of the spectrum, the sliding of synthetic fault gouge is characterized by relatively lower friction and localization that causes shear-induced compaction (Fig. S14, e.g. Marone et al., 1992).

These observations have two main implications: 1) that high friction of bare surfaces is due to an excess energy needed to create penetrative brittle damage ("off-fault" damage) in the sliding surface where force concentrates (Figs. 2, 6 and 7) friction depends on the different deformation processes related to stress heterogeneity along the fault plane (e.g. Fig. 4). Over 11 experiments, the gouge patches are always distributed in different locations on the sliding surface, suggesting that heterogeneities on the sliding surface may not be due to the geometry of the experimental setup, which plays only a minor role on the location of gouge patches. The areas of force concentration were probably due to variability in the sample preparation and the 0.1 mm tolerance of the surface grinder, which may have imposed topographic variations higher than the nominal roughness of the blocks, attained by lapping with sandpaper.

Appendix C. Frictional and scale-dependent deformation processes of large experimental carbonate faults

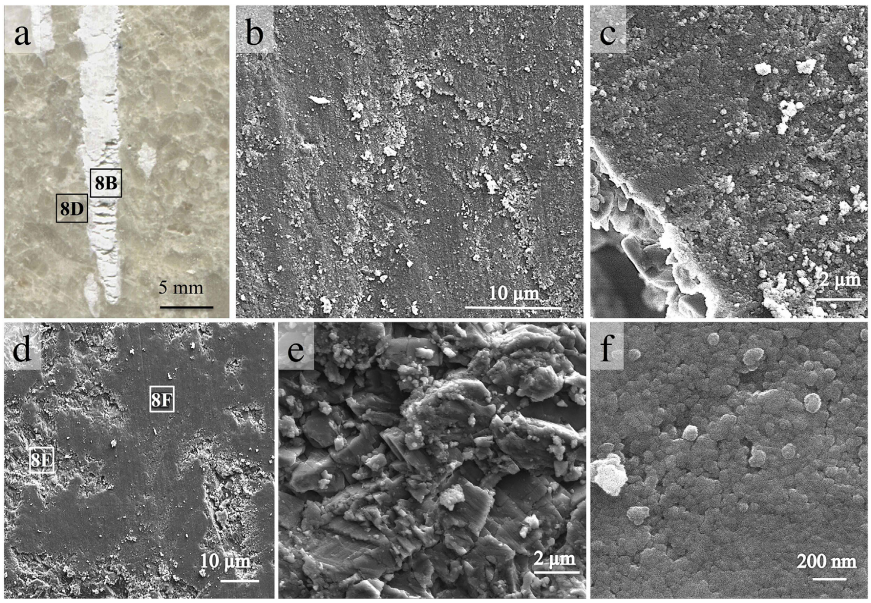

Fig. 8. A) Location of SEM investigation carried out on the post-experimental surface of i419. B) SEM microstructure of the boundary shear plane in the gouge characterized by striated patches of nanoparticles. C) Detail of rounded nanoparticles on the boundary shear forming a ~1 µm thick layer on top of µm-size clastic material (bottom left). D) Detail of the bare surface characterized by patches of smooth striated material. E) Detail of the rough portion of the bare surface, characterized by angular crystals of calcite. It is interpreted as the characteristic microstructure of a pre-experimental bare surface roughened with #3000 grit sandpaper. F) Detail of smooth area in D. The smooth surface is characterized by a layer of nanoparticles analogous to C.

However, during visual inspection of post-experimental surfaces we note that flattened areas, often characterized by mirror-like appearance, are evenly distributed along the surface and are present on both gouge patches and block surfaces. This observation indicates that large portions of the slip surface may be in contact at the beginning of the experiment before being separated by gouge formation occurring within more restricted areas. It also suggests that mirrors may have formed during slip at the gouge-block interface via processes that are similar (e.g. Fig. 8) to those occurring at the block-block interfaces. Moreover, we note that large grooves are typically carved a few millimetres into the intact rock (Fig. 7a), therefore much deeper than the ~0.1–0.2 mm asperity height we might expect to be induced by sample preparation. Consequently, after the initial phases of slip, friction and deformation processes along 20 cm × 20 cm bare surfaces become independent of the initial roughness and initial contact area while wear product and gouge patches develop and accumulate along the slip zone.

Experiments with large sliding blocks and synthetic gouges therefore represent two end-members of the friction and deformation processes along carbonate faults: 1) sliding on a cemented slip zone on which roughness imposes heterogeneous stress concentration and 2) sliding in zones with smooth stress distribution within an incohesive gouge layer.

In the case of cemented slip zones, the force concentrates at sites of small topographic irregularities, and the stress exceeded the brittle strength of the surface, producing the grooves and the associated gouge. At the tip and within the grooves, the stress field imposed by the topographic asperities and by the structure of the gouge is likely to be complex (e.g. Chester and Chester, 2000; Griffith et al., 2010), however, in case of dilatant slip, failure of the bare surface and grain size reduction in the gouge may be considered as laterally unconfined (Barton, 1976; Sammis et al., 1987). This interpretation is reinforced by the observation that, in cross section, the failure of the surface occurs via tensile fractures that are roughly parallel to Riedel shears in the gouge (Fig. 7a–b). Thus, we propose a conceptual model of deformation in which tensional cracks may form at/behind the tip of the groove that "propagates" into the intact block during slip, causing the initial fragmentation of the rock, at the location of asperities (Fig. 9a), in a similar way to what is observed during experiments of dynamic rupture propagation (e.g. Griffith et al., 2009). Subsequently, shear-induced compression behind the initial fracture zone causes localization and further grain size reduction along optimally oriented zones of localization (Riedels and boundary shears, Fig. 9b). Following the above considerations, we suggest that stress concentration during the ploughing of grooves should be at least as high as the uniaxial (laterally unconfined) strength of the intact rock. This model is based on the concept of unconfined strength of rock joints (Barton, 1976) and grain size reduction by uniaxial splitting (Sammis et al., 1987), incorporating the failure of relatively smooth slip surfaces and incorporating the effects of strength recovery.

The brittle processes occurring in our experiments are therefore qualitatively analogous to the abrasion process in ceramics (e.g. Buckley and Miyoshi, 1984; Buijs and Korpel van-Houten, 1993) and rocks (e.g. Spray, 1989) coupled with grain size reduction of the gouge observed in natural faults (e.g. Logan et al., 1992; Shipton and Cowie, 2001). If the friction of the surface is limited by the failure strength of the limestone, it implies that the real contact area and

Appendix C. Frictional and scale-dependent deformation processes of large experimental carbonate faults

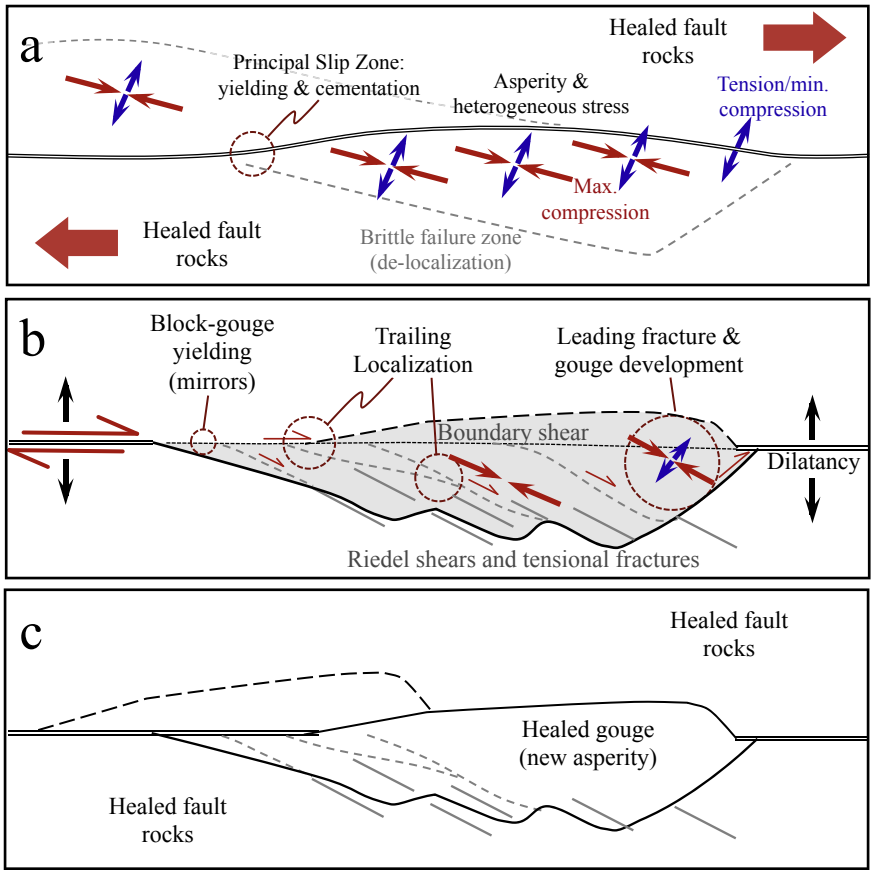

Fig. 9. Conceptual model proposed to explain the kinematics of deformation along a cohesive (healed) fault zone, either in natural (e.g. Fig. 1) or experimental (Figs. 6–8). A) The PSZ embedded in cohesive fault rocks and subject to shear is characterized by stress concentration (maximum principal stress shown by red arrows) in correspondence to topographic asperities, producing brittle failure and de-localization of the deformation. B) "Unclamped" shearing of the cohesive PSZ: grooving and progressive gouge formation occurs at the leading edge during incipient/slow slip, where stress concentrates. Within the trailing zone, further grain size reduction and displacement occur in the orientation of compression forming Riedel-type shears parallel to tensional fractures in the block. Outside the grooves and on top of gouge boundary shear, small asperities can yield by stress concentration, producing reflective, mirror-like surfaces. C) Healing of the newly-formed gouge under high heterogeneous stress leads to fault strength recovery and renewal of asperity populations. This results in an effective welding of the two fault walls. (For interpretation of the references to colour in this figure legend, the reader is referred to the web version of this article.)

amount of wear during the experiment will be directly proportional to the applied normal force. This is consistent with previous literature (Bowden and Tabor, 1950; Archard, 1953) and with the observation of grooved areas in our experiments (Fig. 6a–b and Fig. S16).

5.2. Fault gouge development and frictional healing of large bare surfaces

Grooving and fault gouge development, captured by experiments on large bare surfaces and associated with higher friction and dilatant faults, also influences the frictional healing behaviour. In fact, the healing behaviour of large surfaces differs dramatically from that of calcite-based gouges (Fig. 5). Carbonatic rocks have healing rates that are very high compared to other common rocks (Tesei et al., 2012; Carpenter et al., 2014, 2016b) and suggest that carbonatic rocks can effectively heal on laboratory timescales. This re-strengthening is potentially controlled by gouge compaction and asperity adhesion, which is particularly evident in experiments at low normal force (Fig. 5). This is apparently in contrast to the experiments on large slip surfaces showing negative or near-zero healing during re-shear (Fig. 5). This apparent paradox can be solved considering that the measure of $\Delta\mu$ yields only a relative difference between sliding and static strength of the rocks. As we discussed above, large slip surfaces have high friction because of the transient production of wear (Fig. 4). We suggest that, during the stationary contact, the newly formed gouge and/or highly stressed asperities effectively heal at a fast rate, similar to that

Appendix C. Frictional and scale-dependent deformation processes of large experimental carbonate faults

documented in gouges (Fig. 5) and in previous literature in smaller-scale experiments (e.g. Chen et al., 2015; Carpenter et al., 2014, 2016a,b). Fast healing may imply that gouge patches and/or asperities regain the strength of the intact rock during long hold times. As a consequence, the slip surfaces are substantially welded at the end of the holds and new fracturing of the blocks is required to initiate further slip. Thus, the stress needed to re-shear, i.e. re-fracture, the large experimental faults is essentially equal to the stress needed to fracture the block and form the gouge patches during steady-state sliding, resulting in the apparent null healing, $\Delta\mu \approx 0$. This process of adhesion and gouge healing is also clearly demonstrated by the common occurrence of cohesive gouge patches, in relief on one of the bare surfaces, highlighting a net transport of material from one surface to the other (Fig. 6d). Moreover, ring-shaped tensional fractures in the grooves (Fig. 6c) and in natural faults (Fig. 1c) further reinforce the interpretation that healed gouge may have an abrasive effect on the fault plane.

5.3. Plastic deformation along mirror surfaces

Whereas brittle failure is evident at the cm/mm scale and controls the macroscopic sliding strength, at small scales (μm), deformation is characterized by the occurrence of plastic deformation. The mirrors found on both the block surfaces and the gouge (Fig. 6d–e) suggest that they may form concurrently with brittle damage during the experiment. They are constituted by thin striated layers of rounded nanoparticles. Such particles are unlikely to form through brittle cracking, because of the comminution limit (e.g. Lowrison, 1974), or through subcritical crack growth and chemical precipitation (e.g. Atkinson, 1984), because of the relatively fast slip and substantially dry conditions of the experiments. Instead, their occurrence in thin shear bands and rounded shapes suggests plastic yielding of the surface asperities or the gouge due to large local stress concentrations. This yielding process could be similar to that observed during industrial milling processes in which grain size reduction is probably caused by accumulation of dislocations and subgrain/grain rotation (Koch, 1997). Indeed, striated mirrors are more evident on blocks that were polished with #3000 grit sandpaper, i.e. much smaller mean asperity size (Fig. 8d–e) even though small reflective patches have been occasionally observed after experiments with rough surfaces. Moreover, the occurrence of bent twins immediately beneath the grooves and inside large clasts in the newly-formed gouge suggests a plastic distortion of the intact rock (Fig. S25). The concomitant occurrence of active mirrors, twinning in the intact block and grooves filled with wear material are clear evidence of simultaneous plastic and brittle deformation along our experimental faults, each occurring at different scales (e.g. Brodsky et al., 2016, Fig. 9b).

Nanoparticles that form mirror-like slip surfaces in our experiments are morphologically very similar to those produced in numerous rotary shear experiments (e.g. Han et al., 2010; Chen et al., 2013). In these experiments the gouge is subjected to seismic slip velocity (typically >1 m/s) and nanoparticles are found along narrow slip zones in correlation with low-friction and high power dissipation (e.g. Boneh et al., 2013). For this reason, nanoparticles and mirror formation are commonly thought to form in case of coseismic slip. However, in our experiments mirrors are active at sub-seismic slip rates (10 μm/s) together with brittle deformation and high frictional strength. The mirrors we produced are less continuous and reflective than mirrors found in natural faults (e.g. Siman-Tov et al., 2013) or high-velocity experiments (Boneh et al., 2013; De Paola et al., 2015), although we also note that our experiments accommodated only a limited amount of displacement. As a consequence, we infer that the occurrence of these mirrors do not necessary imply an overall fault weakness or co-seismic slip, consistent with previous studies (e.g. Verberne et al., 2013).

5.4. Implications for faulting in carbonates

The experiments we conducted in large bare surfaces, with displacements in the range of 1–5 cm and a velocity of ~10 μm/s, can be considered representative of: 1) slip along an immature fault that due to the low displacement results in low gouge production, or 2) the pre-seismic phases of slip along a mature fault that experienced extensive consolidation and cementation of the fault rocks, i.e. fault healing. Shearing on "large" slip surfaces during our experiments reproduces a variety of phenomena typically observed on mature faults, including gouge production, striations, mirrors and fractures (e.g. Fig. 1 vs. Figs. 6 and 7; Fig. S19). Since we observe the same mechanisms of deformation, we suggest similar mechanics of sliding for experimental and natural faults, i.e. high friction accompanied by dilatation and wear production. However, we note that our experiments were performed under room dry-conditions and therefore, in spite of the striking similarity of the deformation products (Fig. S19), additional complications may arise in natural faults because of the physico-chemical effects induced by fluids.

Striations on healed fault planes are a characteristic of many faults exhumed from the uppermost crust, suggesting that, like in our experiments, large stress concentration and stress heterogeneities may occur. These concentrations arise from motion over or across asperities in the fault topography and lead to failure of the fault rock, formation of wear products and dilatation occurring in releasing bends (Fig. 9). Gouge-filled grooves retrieved from natural faults show internal structure very similar to those produced during our experiments, with en echelon tensional fractures and grain size reduction in the direction of maximum compression (e.g. Fig. 1 vs. Fig. 7). In particular, the structure of the gouge patches is similar to clusters of unconnected shear fractures that include rhombic zones of less deformed rock, which are thought to predate a through-going localization in the rock via Y shears (e.g. Tchalenko, 1970; Shipton and Cowie, 2003). Therefore, during the initial phases of slip, failure and grooving of the surface, occurring at the leading edge of the striation is followed by localization of slip within the gouge (Fig. 9b). The sliding strength of healed fault surfaces is then controlled by the fracture strength of the plane itself, rather than the friction of incohesive gouge, resulting in a very high "static" friction (e.g. Savage et al., 1996), as demonstrated in our tests ($0.8<\mu<1.0$, Fig. 3).

The condition of high friction and dilatation along the fault plane should continue as long as the motion stops, a continuous layer of gouge covers the fault patch, or dynamic weakening occurs (e.g. Di Toro et al., 2011). Incohesive and continuous gouge layers may significantly decrease the friction along the fault to $\mu \sim 0.6$ (Fig. 3), effectively providing powder lubrication (e.g. Reches and Lockner, 2010; Brodsky et al., 2011). If healing of the fault gouge is fast and/or the amount of slip is insufficient to complete the lubrication of the fault with a continuous and incohesive gouge horizon, fault strength is likely to remain high due to wear processes. In the case of stationary contact, healing promotes the strength recovery of the newly formed gouge (Fig. 9c), renewing the adhesion between the fault walls that can be envisioned either as a change in fault topography (e.g. Brodsky et al., 2011) or as intact rock bridges (e.g. Savage et al., 1996). The initial fracture and wear of the cohesive wall rock implies a local de-localization of deformation whereas localization in the gouge leads to a re-smoothing of the slip zone (Fig. 9a–b). Healing of the gouge thus positively correlates with high fault strength and this alternation of smoothing and re-roughening processes have been recently hypothesized to

Appendix C. Frictional and scale-dependent deformation processes of large experimental carbonate faults

explain the geometric evolution of natural faults (e.g. Shervais and Kirkpatrick, 2016). These conditions for heterogeneous stress distribution and high friction/dilatancy may be favoured by low confining pressures (e.g. Barton, 1976) and by rock types that show fast healing such as carbonates (e.g. Tesei et al., 2014).

We also suggest that these fault properties may favour earthquake slip in carbonates in the uppermost crust. In the Northern Apennines of Italy there are many examples of carbonate-bearing normal faults, considered exhumed analogues of seismogenic faults at depth: e.g. the Gubbio fault (Bussolotto et al., 2007), the Tre Monti and Venere faults (Agosta and Aydin, 2006; Smith et al., 2011), the Monte Maggio fault, (Collettini et al., 2014a), and the Assergi fault (Fig. 1). All of these faults are exhumed from depths less than 4 km and show fault planes with associated striations, slickenfibers and cohesive fault rocks. In particular, cohesive fault rocks and slickenfibers are the geological manifestation of healing of the PSZ and dilatant slip, respectively. As mentioned above, laboratory experiments show that also incohesive gouges may regain strength at a geologically fast rate, and even regain the strength of the original PSZ in a short time of days (e.g. Carpenter et al., 2014). Thus, there is compelling geological and experimental evidence that healing along these seismogenic faults is extremely efficient.

In principle, high fault strength and high healing rates would favour unstable fault slip and earthquake nucleation as they promote the accumulation of elastic strain energy in the crust (e.g. Dieterich, 1972; McLaskey et al., 2012). We note that high-resolution seismological observations from the Northern Apennines (e.g. Chiaraluce et al., 2005, 2017; Valoroso et al., 2014) show numerous aftershocks occurring in the first kilometres of the crust where carbonates are present and therefore we cannot rule out the seismic failure of strong and healed fault planes. In fact, there are several lines of microstructural evidence that suggest seismic slip occurring along cohesive carbonate PSZ, like fluidized cataclasites and shattered rocks (Rowe et al., 2012; Tesei et al., 2013; Fondriest et al., 2015), decarbonatation (Collettini et al., 2013) and continuous, sintered fault mirrors (Smith et al., 2012).

6. Conclusions

We performed slow friction experiments using a new biaxial apparatus, shearing 20 × 20 cm bare surfaces of limestone, and performed microstructural analysis to study the mechanics of incipient slip on large scale, cohesive fault planes in carbonates. Friction of these large surfaces is higher (μ~0.9) than the friction of limestone powders (μ~0.6), due to the additional fracture energy that is necessary to produce grooves and wear material during the sliding. Concurrently, frictional healing in our tests shows a complex behaviour, which coupled with structural/microstructural analyses, suggests fast fault healing and effective cementation of the Principal Slip Zones.

Our experiments produce striations, tensional fractures, gouge and fault mirrors identical to those found in natural carbonate-bearing faults. We also documented that plastic and brittle deformation processes can occur simultaneously during slip at subseismic rates: twinning and shiny surfaces coated with nanoparticles at small (μm) scales and pervasive brittle deformation and wear at a larger (mm) scale. We envision that carbonate-bearing faults in the uppermost crust can be very strong due to a combination of low effective stress and high healing rates of the fault gouge. In principle these properties may imply favourable conditions for earthquake generation and contribute to explaining the large occurrence of earthquakes hosted on carbonates at shallow crustal levels.

Acknowledgements

The Authors thank M. Nazzari ad D. Mannetta, for assistance with the SEM and high quality thin section preparation, respectively. Alfonso Tini (Mondial Marmi s.r.l.) is warmly acknowledged for providing the Maljat® limestone used in the experiments. B. Verberne and an anonymous reviewer provided constructive reviews that significantly helped to improve the clarity of the manuscript. Editor T. Takeshita is thanked for careful editorial handling. This research was funded by the ERC Starting Grant "GLASS" project (n° 259256) to CC.

Appendix A. Supplementary data

Supplementary data related to this article can be found at http://dx.doi.org/10.1016/j.jsg.2017.05.008.

References

Agosta, Fabrizio, Aydin, Atilla, 2006. Architecture and deformation mechanism of a basin-bounding normal fault in Mesozoic platform carbonates, central Italy. J. Struct. Geol. 28 (8), 1445–1467.
Archard, J.F., 1953. Contact and rubbing of flat surfaces. J. Appl. Phys. 24 (8), 981–988.
Atkinson, Barry Kean, 1984. Subcritical crack growth in geological materials. J. Geophys. Res. Solid Earth 89 (B6), 4077–4114.
Barton, N., 1976. The Shear Strength of Rock and Rock Joints. International Journal of Rock Mechanics and Mining Sciences & Geomechanics Abstracts, Vol. 13, No. 9. Pergamon, pp. 255–279.
Badt, Nir, Hatzor, Yossef H., Toussaint, Renaud, Sagy, Amir, 2016. Geometrical evolution of interlocked rough slip surfaces: the role of normal stress. Earth Planet. Sci. Lett. 443, 153–161.
Ben-Menahem, Ari, 1991. Four thousand years of seismicity along the dead sea rift. J. Geophys. Res. Solid Earth 96 (B12), 20195–20216.
Ben-Zion, Y., Sammis, C.G., 2003. Characterization of fault zones. Pure Appl. Geophys. 160 (3–4), 677–715.
Bistacchi, Andrea, Griffith, W. Ashley, Smith, Steven A.F., Di Toro, Giulio, Jones, Richard, Nielsen, Stefan, 2011. Fault roughness at seismogenic depths from LIDAR and photogrammetric analysis. Pure Appl. Geophys. 168 (12), 2345–2363.
Boneh, Yuval, Sagy, Amir, Reches, Ze'ev, 2013. Frictional strength and wear-rate of carbonate faults during high-velocity, steady-state sliding. Earth Planet. Sci. Lett. 381, 127–137.
Bowden, F.P., Tabor, D., 1950. The Friction and Lubrication of Solids. Oxford University Press.
Brace, W.F., Byerlee, J.D., 1966. Stick-slip as a mechanism for earthquakes. Science 153 (3739), 990–992.
Brodsky, Emily E., Gilchrist, Jacquelyn J., Sagy, Amir, Collettini, Cristiano, 2011. Faults smooth gradually as a function of slip. Earth Planet. Sci. Lett. 302 (1–2), 185–193.
Brodsky, Emily E., Kirkpatrick, James D., Candela, Thibault, 2016. Constraints from fault roughness on the scale-dependent strength of rocks. Geology 44 (1), 19–22.
Buckley, Donald H., Miyoshi, Kazuhisa, 1984. Friction and wear of ceramics. Wear 100 (1–3), 333–353.
Buijs, M., Korpel-van Houten, K., 1993. Three-body abrasion of brittle materials as studied by lapping. Wear 166 (2), 237–245.
Burford, R.O., Harsh, P.W., 1980. Slip on the San Andreas fault in central California from alinement array surveys. Bull. Seismol. Soc. Am. 70 (4), 1233–1261.
Bussolotto, M., Benedicto, A., Invernizzi, C., Micarelli, L., Plagnes, V., Deiana, G., 2007. Deformation features within an active normal fault zone in carbonate rocks: the Gubbio fault (Central Apennines, Italy). J. Struct. Geol. 29 (12), 2017–2037.
Carpenter, B.M., Scuderi, M.M., Collettini, C., Marone, C., 2014. Frictional heterogeneities on carbonate-bearing normal faults: insights from the Monte Maggio fault, Italy. J. Geophys. Res. Solid Earth 119 (12), 9062–9076.
Carpenter, B.M., Collettini, C., Viti, C., Cavallo, A., 2016a. The influence of normal stress and sliding velocity on the frictional behaviour of calcite at room temperature: insights from laboratory experiments and microstructural observations. Geophys. J. Int. 205 (1), 548–561.
Carpenter, B.M., Ikari, M.J., Marone, C., 2016b. Laboratory observations of time-dependent frictional strengthening and stress relaxation in natural and synthetic fault gouges. J. Geophys. Res. Solid Earth 121 (2), 1183–1201.
Chen, X., Madden, A.S., Bickmore, B.R., Reches, Z., 2013. Dynamic weakening by nanoscale smoothing during high-velocity fault slip. Geology 41 (7), 739–742.
Chen, Jianye, Verberne, Berend A., Spiers, Christopher J., 2015. Effects of healing on the seismogenic potential of carbonate fault rocks: experiments on samples from the Longmenshan Fault, Sichuan, China. J. Geophys. Res. Solid Earth 120 (8), 5479–5506.
Chester, Frederick M., Chester, Judith S., 2000. Stress and deformation along wavy

Appendix C. Frictional and scale-dependent deformation processes of large experimental carbonate faults

frictional faults. J. Geophys. Res. Solid Earth 105 (B10), 23421–23430.
Chiaraluce, L., Barchi, M., Collettini, C., Mirabella, F., Pucci, S., 2005. Connecting seismically active normal faults with Quaternary geological structures in a complex extensional environment: the Colfiorito 1997 case history (northern Apennines, Italy). Tectonics 24 (1) n/a-n/a.
Chiaraluce, L., Di Stefano, R., Tinti, E., Scognamiglio, L., Michele, M., Casarotti, E., Cattaneo, M., De Gori, P., Chiarabba, C., Monachesi, G., Lombardi, A., Valoroso, L., Latorre, D., Marzorati, S., 2017. The 2016 Central Italy seismic sequence: a first look at the mainshocks, aftershocks, and source models. Seismol. Res. Lett. 88 (3), 757–771.
Collettini, C., Viti, C., Tesei, T., Mollo, S., 2013. Thermal decomposition along natural carbonate faults during earthquakes. Geology 41 (8), 927–930.
Collettini, C., Carpenter, B.M., Viti, C., Cruciani, F., Mollo, S., Tesei, T., Trippetta, F., Valoroso, L., Chiaraluce, L., 2014. Fault structure and slip localization in carbonate-bearing normal faults: an example from the Northern Apennines of Italy. J. Struct. Geol. 67, 154–166.
Collettini, Cristiano, Di Stefano, Giuseppe, Carpenter, Brett, Scarlato, Piergiorgio, Tesei, Telemaco, Mollo, Silvio, Trippetta, Fabio, Marone, Chris, Romeo, Gianni, Chiaraluce, Lauro, 2014. A novel and versatile apparatus for brittle rock deformation. Int. J. Rock Mech. Min. Sci. 66, 114–123.
Delle Piane, Claudio, Giwelli, Ausama, Clennell, M. Ben, Esteban, Lionel, Nogueira Kiewiet, Melissa Cristina D., Kiewiet, Leigh, Kager, Shane, Raimon, John, 2016. Frictional and hydraulic behaviour of carbonate fault gouge during fault reactivation — an experimental study. Tectonophysics 690, 21–34.
De Paola, Nicola, Holdsworth, Robert E., Viti, Cecilia, Collettini, Cristiano, Bullock, Rachael, 2015. Can grain size sensitive flow lubricate faults during the initial stages of earthquake propagation? Earth Planet. Sci. Lett. 431, 48–58.
Dieterich, James H., 1972. Time-dependent friction as a possible mechanism for aftershocks. J. Geophys. Res. 77 (20), 3771–3781.
Di Toro, G., Han, R., Hirose, T., De Paola, N., Nielsen, S., Mizoguchi, K., Ferri, F., Cocco, M., Shimamoto, T., 2011. Fault lubrication during earthquakes. Nature 471 (7339), 494–498.
Dunham, E.M., Kozdon, J.E., Belanger, D., Cong, L., 2011. Earthquake ruptures on rough faults. In: Multiscale and Multiphysics Processes in Geomechanics. Springer Berlin Heidelberg, pp. 145–148.
Engelder, James T., 1974. Microscopic wear grooves on slickensides: indicators of paleoseismicity. J. Geophys. Res. 79 (29), 4387–4392.
Faulkner, D.R., Jackson, C.A.L., Lunn, R.J., Schlische, R.W., Shipton, Z.K., Wibberley, C.A.J., Withjack, M.O., 2010. A review of recent developments concerning the structure, mechanics and fluid flow properties of fault zones. J. Struct. Geol. 32 (11), 1557–1575.
Fondriest, Michele, Aretusini, Stefano, Di Toro, Giulio, Smith, Steven A.F., 2015. Fracturing and rock pulverization along an exhumed seismogenic fault zone in dolostones: the Foiana Fault Zone (Southern Alps, Italy). Tectonophysics 654, 56–74.
Gratier, J.P., Thouvenot, F., Jenatton, L., Tourette, A., Doan, M.L., Renard, F., 2013. Geological control of the partitioning between seismic and aseismic sliding behaviours in active faults: Evidence from the Western Alps, France. Tectonophysics 600, 226–242.
Griffith, W.A., Rosakis, A., Pollard, D.D., Ko, C.W., 2009. Dynamic rupture experiments elucidate tensile crack development during propagating earthquake ruptures. Geology 37 (9), 795–798.
Griffith, W. Ashley, Nielsen, Stefan, Di Toro, Giulio, Smith, Steven A.F., 2010. Rough faults, distributed weakening, and off-fault deformation. J. Geophys. Res. 115 (B8).
Han, Raehee, Hirose, Takehiro, Shimamoto, Toshihiko, 2010. Strong velocity weakening and powder lubrication of simulated carbonate faults at seismic slip rates. J. Geophys. Res. 115 (B3).
Heesakkers, V., Murphy, S., Reches, Z., 2011. Earthquake rupture at focal depth, Part I: structure and rupture of the Pretorius fault, TauTona mine, South Africa. Pure Appl. Geophys. 168 (12), 2395–2425.
Kirkpatrick, James D., Brodsky, Emily E., 2014. Slickenline orientations as a record of fault rock rheology. Earth Planet. Sci. Lett. 408, 24–34.
Koch, C.C., 1997. Synthesis of nanostructured materials by mechanical milling: problems and opportunities. Nanostruct. Mater. 9 (1), 13–22.
Koopman, A., 1983. Detachment tectonics in the central Apennines, Italy (Doctoral dissertation, Instituut voor Aardwetenschappen RUU).
Logan, J.M., Dengo, C.A., Higgs, N.G., Wang, Z.Z., 1992. Fabrics of experimental fault zones: their development and relationship to mechanical behavior. Int. Geophys. 51, 33–67.
Lowrison, G.C., 1974. Crushing and Grinding. The Size Reduction of Solid Materials (London).
McLaskey, Gregory C., Thomas, Amanda M., Glaser, Steven D., Nadeau, Robert M., 2012. Fault healing promotes high-frequency earthquakes in laboratory experiments and on natural faults. Nature 491 (7422), 101–104.
Marone, Chris, Hobbs, B.E., Ord, A., 1992. Coulomb constitutive laws for friction: contrasts in frictional behavior for distributed and localized shear. Pure Appl. Geophys. PAGEOPH 139 (2), 195–214.
McLaskey, Gregory C., Kilgore, Brian D., 2013. Foreshocks during the nucleation of stick-slip instability. J. Geophys. Res. Solid Earth 118 (6), 2982–2997.
Niemeijer, André, Di Toro, Giulio, Griffith, W. Ashley, Bistacchi, Andrea, Smith, Steven A.F., Nielsen, Stefan, 2012. Inferring earthquake physics and chemistry using an integrated field and laboratory approach. J. Struct. Geol. 39, 2–36.
Reches, Z.E., Lockner, D.A., 2010. Fault weakening and earthquake instability by powder lubrication. Nature 467 (7314), 452–455.
Rowe, Christie D., Fagereng, Åke, Miller, Jodie A., Mapani, Ben, 2012. Signature of coseismic decarbonation in dolomitic fault rocks of the Naukluft Thrust, Namibia. Earth Planet. Sci. Lett. 333–334, 200–210.
Sammis, Charles, King, Geoffrey, Biegel, Ronald, 1987. The kinematics of gouge deformation. Pure Appl. Geophys. PAGEOPH 125 (5), 777–812.
Savage, J.C., Byerlee, J.D., Lockner, D.A., 1996. Is internal friction friction? Geophys. Res. Lett. 23 (5), 487–490.
Scotti, O., Cornet, F.H., 1994. August. In situ evidence for fluid-induced aseismic slip events along fault zones. In: International Journal of Rock Mechanics and Mining Sciences & Geomechanics Abstracts, Vol. 31, No. 4. Pergamon, pp. 347–358.
Shervais, Katherine A.H., Kirkpatrick, James D., 2016. Smoothing and re-roughening processes: the geometric evolution of a single fault zone. J. Struct. Geol. 91, 130–143.
Shipton, Z.K., Cowie, P.A., 2001. Analysis of three-dimensional damage zone development over a micron to km scale range in the high-porosity Navajo sandstone, Utah. J. Struct. Geol. 23, 1825–1844.
Shipton, Z.K., Cowie, P.A., 2003. A conceptual model for the origin of fault damage zone structures in high-porosity sandstone. J. Struct. Geol. 25 (3), 333–344.
Sibson, R.H., 1986. Brecciation processes in fault zones: inferences from earthquake rupturing. Pure Appl. Geophys. 124 (1–2), 159–175.
Sibson, R.H., 2003. Thickness of the seismic slip zone. Bull. Seismol. Soc. Am. 93 (3), 1169–1178.
Siman-Tov, S., Aharonov, E., Sagy, A., Emmanuel, S., 2013. Nanograins form carbonate fault mirrors. Geology 41 (6), 703–706.
Smith, Steven A.F., Billi, Andrea, Toro, Giulio Di, Spiess, Richard, 2011. Principal slip zones in limestone: microstructural characterization and implications for the seismic cycle (Tre Monti fault, central Apennines, Italy). Pure Appl. Geophys. 168 (12), 2365–2393.
Smith, S.A.F., Di Toro, G., Kim, S., Ree, J.-H., Nielsen, S., Billi, A., Spiess, R., 2012. Coseismic recrystallization during shallow earthquake slip. Geology 41 (1), 63–66.
Spray, John G., 1989. Slickenside formation by surface melting during the mechanical excavation of rock. J. Struct. Geol. 11 (7), 895–905.
Stewart, I.S., Hancock, P.L., 1991. Scales of structural heterogeneity within neotectonic normal fault zones in the Aegean region. J. Struct. Geol. 13 (2), 191–204.
Tchalenko, J.S., 1970. Similarities between shear zones of different magnitudes. Geol. Soc. Am. Bull. 81 (6), 1625–1640.
Tesei, Telemaco, Collettini, Cristiano, Carpenter, Brett M., Viti, Cecilia, Marone, Chris, 2012. Frictional strength and healing behavior of phyllosilicate-rich faults. J. Geophys. Res. Solid Earth 117 (B9).
Tesei, Telemaco, Collettini, Cristiano, Viti, Cecilia, Barchi, Massimiliano R., 2013. Fault architecture and deformation mechanisms in exhumed analogues of seismogenic carbonate-bearing thrusts. J. Struct. Geol. 55, 167–181.
Tesei, Telemaco, Collettini, Cristiano, Barchi, Massimiliano R., Carpenter, Brett M., Di Stefano, Giuseppe, 2014. Heterogeneous strength and fault zone complexity of carbonate-bearing thrusts with possible implications for seismicity. Earth Planet. Sci. Lett. 408, 307–318.
Valoroso, L., Chiaraluce, L., Collettini, C., 2014. Earthquakes and fault zone structure. Geology 42 (4), 343–346.
Verberne, B.A., de Bresser, J.H., Niemeijer, A.R., Spiers, C.J., de Winter, D.M., Plümper, O., 2013. Nanocrystalline slip zones in calcite fault gouge show intense crystallographic preferred orientation: crystal plasticity at sub-seismic slip rates at 18–150 C. Geology 41 (8), 863–866.
Verberne, B.A., Plumper, O., Matthijs de Winter, D.A., Spiers, C.J., 2014. Superplastic nanofibrous slip zones control seismogenic fault friction. Science 346 (6215), 1342–1344.

Appendix D.
Structural Disorder of Graphite and Implications for Graphite Thermometry

Solid Earth Discuss., https://doi.org/10.5194/se-2017-74
Manuscript under review for journal Solid Earth
Discussion started: 20 July 2017

Solid Earth Discussions

Structural Disorder of Graphite and Implications for Graphite Thermometry

Martina Kirilova[1], Virginia Toy[1], Jeremy S. Rooney[2], Carolina Giorgetti[3], Keith C. Gordon[2], Cristiano Collettini[3]

[1] Department of Geology, University of Otago, PO Box 56, Dunedin 9054, New Zealand

[2] Department of Chemistry, University of Otago, PO Box 56, Dunedin 9054, New Zealand

[3] Dipartimento di Scienze della Terra, Università degli Studi La Sapienza, Rome, Italy

Correspondence to: Martina Kirilova (martina.a.kirilova@gmail.com)

Key Points:

- graphite, disorder, thermometry, Raman

Abstract

Graphitization, or the progressive maturation of carbonaceous material, is considered an irreversible process. Thus, the degree of graphite crystallinity has been calibrated as an indicator of the peak metamorphic temperatures experienced by the host rocks. However, discrepancies between temperatures indicated by graphite crystallinity versus other thermometers have been documented in deformed rocks. To examine the possibility of mechanical modifications of graphite structure and the potential impacts on graphite 'thermometry' we performed laboratory deformation experiments. We sheared highly crystalline graphite powder at normal stresses of 5 and 25 MPa and aseismic slow sliding velocities of 1 µm/s, 10 µm/s and 100 µm/s. The degree of graphite crystallinity both in the starting and resulting materials was analyzed by Raman microspectroscopy. Our results demonstrate consistent decrease of graphite crystallinity with increasing shear strain. We conclude that the calibrated graphite 'thermometer' is ambiguous in active tectonic settings and we suggest that a calibration that accounts for shear strain is needed.

Appendix D. Structural disorder of graphite and implications for graphite thermometry

Solid Earth Discuss., https://doi.org/10.5194/se-2017-74
Manuscript under review for journal Solid Earth
Discussion started: 20 July 2017

Solid Earth Discussions

1 Introduction

Organic matter, preserved in sedimentary rocks, can be transformed into crystalline graphite due to structural and compositional changes during diagenesis and metamorphism, a process known as graphitization (Beyssac et al., 2002a; Bonijoly et al., 1982; Buseck and Beyssac, 2014; Wopenka and Pasteris, 1993; etc.). Graphitization is thought to be an irreversible process and graphite is known to remain stable to the highest temperatures of granulite facies and the highest pressures of coesite-eclogite facies (Buseck and Beyssac, 2014). It is generally accepted that the degree of graphite crystallinity, or its structural order, is determined mainly by the maximum temperature conditions experienced by the host rocks, whereas lithostatic pressure and shear strain are considered to have only minor influence on graphitization (Bonijoly et al., 1982; Wopenka and Pasteris, 1993; Bustin et al, 1995). Therefore, graphite crystallinity has been calibrated as an indicator of the peak temperatures reached during progressive metamorphism (Beyssac et al., 2002a; Reitmeijer and McKinnon, 1985). However, in strained rocks discrepancies between temperatures indicated by the crystallinity of graphite vs. other thermometers have been reported (Barzoi, 2015; Nakamura et al., 2015; Kirilova et al., in review). Thus, numerous authors have speculated that tectonic deformation results in graphite structural modifications that challenge the validity of the existing graphite thermometers (Large et al., 1994; Bustin et al, 1995; Crespo et al., 2006; Barzoi, 2015; Nakamura et al., 2015).

Furthermore, graphite occurrence and enrichment have been documented in several fault zones in the world, e. g. the Alpine Fault zone, New Zealand (Kirilova, et al., in review), the Hidaka metamorphic belt, Hokkaido, Japan (Nakamura et al., 2015), the Atotsugawa fault system, Japan (Oohashi, et al., 2012), the Tanakura Tectonic Line, Japan (Oohashi et al., 2011), the Err nappe detachment fault, Switzerland (Manatschal, 1999), and the KTB borehole, Germany (Zulauf et al., 1990). In these intensely deformed rocks its presence is of particular interest because its low friction at $\mu \sim 0.1$ (Morrow et al., 2000) allows graphite to act as a natural solid lubricant (Savage, 1948). The mechanical behavior of graphite has been broadly investigated in both natural and experimental specimens, where it manifests with the lowest μ among sheet structure minerals (Moore and Lockner, 2004; Oohashi et al., 2011, 2013; Rutter, et al., 2013; Kuo et al., 2014, etc.) confirming it could have a significant impact on fault mechanics. It has been experimentally proven that even a small fraction of graphite has disproportionally large effect on frictional strength due to concentration of smeared graphite layers (Rutter, et al., 2013).

However, structural changes in crystalline graphite caused by tectonic deformation have not been explained until now. To examine this aspect and to investigate the potential impacts of structural disordering of graphite on the graphite 'thermometer', we have carried out laboratory deformation experiments on highly crystalline graphite powder.

Solid Earth Discuss., https://doi.org/10.5194/se-2017-74
Manuscript under review for journal Solid Earth
Discussion started: 20 July 2017

Solid Earth Discussions

50 **2 2 Experimental methods**

51 **2.1 Sample description**

52 As a starting material in the current study we used synthetic (or commercially synthesized) graphitic carbon to avoid
53 complexities arising from variable degree of crystallinity in natural carbon materials. Initially, the material was crushed to
54 160 µm in a RockLabs Swing (TEMA) mill. The resulting fine graphitic powder was 'cooked' at 700˚C for two hours in a
55 Lindberg Blue M Muffle Furnace to achieve full graphitization, which is known to occur at this temperature in the absence
56 of other variations in physical conditions (Buseck and Beyssac, 2014). This was used as the starting material for the
57 deformation experiments.

58 **2.2 Experimental procedure**

59 In total, 10 deformation experiments were performed at room temperature and room humidity in the Brittle Rock
60 Deformation Versatile Apparatus BRAVA (Collettini et al., 2014), at INGV, Rome. For each experiment two 3-mm thick
61 layers of synthetic graphite gouges were placed in between three grooved forcing blocks in a double-direct shear
62 configuration (e.g. Dieterich, 1972). The two side blocks are held stationary, and the central forcing block is driven
63 downward causing shear to occur within the graphite gouge layers. Normal stress is applied by the horizontal piston in load-
64 feedback control mode and shear displacement accomplished by the vertical piston in displacement-feedback control mode.
65 Forces are measured with stainless steel load cells (± 0.03 kN) and displacements are measured with LVDTs (± 0.1 µm)
66 attached to each piston. Experiments have been conducted at normal stresses of 5 MPa or 25 MPa and aseismic sliding
67 velocities of 1 µm/s, 10 µm/s and 100 µm/s. The experiments were carried out to total displacements of 20 mm. In addition,
68 some experiments were stopped at 5 mm and 10 mm and the specimens were then recovered to reveal graphite structural
69 changes that took place during different amounts of total deformation. The coefficient of friction (µ) was calculated as the
70 ratio of measured shear load to measured normal load ($\mu = \tau / \sigma_n$, where τ is shear stress and σ_n is effective normal stress).
71 The average shear strain (**γ**) within the layer was calculated by dividing shear displacement increments by the measured layer
72 thickness and summing. The displacement values of the vertical and horizontal load points were corrected for the elastic
73 stretch of each load frame, taking into account that the machine stiffness is 1283 kN/mm on the horizontal axis and 928.5
74 kN/mm on the vertical axis.

75 **2.3 Raman microspectroscopy**

76 The degree of graphite crystallinity was measured by an Alpha 300R+ confocal Raman microscope (WITec, Ulm, Germany)
77 with a 532 nm laser (Coherent, Santa Clara, California), located at the Department of Chemistry, University of Otago, New
78 Zealand. The laser (3.0 mW) was focused on the samples with a 50× Zeiss objective. The scattered light was dispersed with

Solid Earth Discuss., https://doi.org/10.5194/se-2017-74
Manuscript under review for journal Solid Earth
Discussion started: 20 July 2017

a 1200 g/mm grating. The combination of the 50× objective and 532 nm laser wavelength produced a laser spot size of approximately 412 nm in diameter. The integration time of each spectrum was 2 seconds with 50 co-additions (100 seconds in total). The spectra were calibrated using the Raman band from a silicon wafer prior to each set of measurements.

The collected spectra were pre-processed in GRAMS AI 9.1 (Thermo Fisher Scientific Inc.), where cosmic spikes were removed and a multi-point linear baseline offset was performed. This was followed by peak fitting three Lorentzian-Gaussian functions to each spectrum with a linear baseline over 1000 - 1700 cm^{-1}. For each spectrum, the area ratio was calculated (R2 = AD1 / (AG + AD1 +AD2), where A*i* = area of the *i*th peak) (Beyssac et al.., 2002a; Wopenka and Pasteris, 1993).

2.4 Scanning electron microscopy

Microstructural analyses of the graphite gouge recovered from the biaxial apparatus were carried out using a scanning electron microscope (SEM). Some SEM images were acquired from the shiny surfaces of the graphite layers that had been parallel to the center and or side forcing blocks (Y-Z sections), with a Zeiss Sigma field emission scanning electron microscope (VP FEG SEM) at the Otago Centre for Electron Microscopy (OCEM), University of Otago, New Zealand. The instrument was operated in variable pressure mode (VP) at 15 kV using a working distance (WD) of 7 – 8 mm and a VPSE (VP-mode secondary electrons) detector. In addition, polished thin sections cut perpendicular to the surface of contact with the center and side forcing blocks (X-Z sections) were imaged on a JEOL JSM-6510 SEM at the University of Potsdam, Germany, where high-resolution secondary electron images were collected at 20 kV and a WD of 10 mm.

3 Results

3.1 Mechanical data

Our experiments allowed us to investigate graphite mechanical behavior and structural modifications under various sliding velocities, normal stresses and shear strain. These conditions are summarized in Table 1.

3.1.2 Friction variations

Over several mm of displacement, the friction coefficient shows a similar evolution trend in all experiments. On a plot of friction vs. displacement (Fig. 1a), the friction coefficient (μ) delineates a curve characterized by a rapid increase to an initial peak friction (μ_{peak}), followed by a subsequent exponential decay towards a steady-state friction (μ_{ss}) over a slip weakening distance. The shapes of the friction-displacement curves vary with the normal stress applied and are steeper for the experiments conducted at 25 MPa than the ones at 5 MPa (Fig. 1a) i.e. the displacement required to achieve steady-state decreases at higher normal stress. In addition, the values of both μ_{peak} and μ_{ss} (Fig. 1a; Table 1) are significantly lower in the experiments at 25 MPa (μ_{peak} = ~0.4; μ_{ss} = ~ 0.1) than in the experiments at 5 MPa (μ_{peak} = ~0.5; μ_{ss} = ~ 0.2). Plots of μ at all

Solid Earth Discuss., https://doi.org/10.5194/se-2017-74
Manuscript under review for journal Solid Earth
Discussion started: 20 July 2017

Solid Earth Discussions

slip rates (Fig. 1a) indicate a gradual decrease of μ_{peak} with increasing shear velocity at high normal stress (Table 1). In the experiments at 5 MPa subtle variations in μ_{peak} also occur but a velocity-related trend is not observed. μ_{ss} does not depend in any experiment on slip rates, and μ_{ss} remains constant for experiments at both low and high normal stress (Fig. 1a; Table 1).

3.1.3 Shear strain variations

Plots of friction vs. shear strain (Fig. 1b) show significant variations in shear strain (γ) attained over equivalent sliding displacements. The estimated shear strain values are a geometric consequence of different thickness changes. Consideration of the shear strain at equivalent sliding velocities but different normal stresses demonstrates that shear strains achieved during the 5 MPa experiments are approximately half of those at 25 MPa (Fig. 1b; Table 1). In addition, the experiments at 25 MPa demonstrate a dramatic increase in shear strain with increasing slip velocity (Fig. 1b; Table 1), whereas at low normal stress we do not observe any systematic variations associated with changes in sliding velocities (Fig. 1b, c and d). Fig. 1c and d show the experiments at low shear strain used to characterize graphite structural changes in the early stages of deformation (Table 1).

3.2 Graphite crystallinity

All the experiments resulted in the development of shiny smooth surfaces with gentle slickenlines (macroscopic fine grooves, parallel to the slip direction as defined by Toy et al., in press). Raman spectra obtained on the top of these surfaces, that had accommodated most of the induced deformation, are compared to Raman spectra from the starting material to identify the effects of mechanical deformation on graphite crystallinity.

Raman data from 20 spectra per sample are presented in Supplementary material 1 (S1). Representative spectra for each sample are illustrated in Fig. 2, which shows spectra displaying the least (left column) and the most (right column) disordered graphite within a sample (i. e. lowest and highest R2 values respectively). Spectra that were typical of the average for each sample are also presented (middle column). Experiments 3 and 7 were stopped at only 5 mm displacement and resulted in extremely fragile deformed surfaces, which were unable to be extracted without them breaking into pieces too small to obtain spectra from. Thus, graphite crystallinity was not measured in these experiments.

All the acquired spectra show typical G, D1 and D2 bands, respectively at ~1580 cm^{-1}, ~1350 cm^{-1} and ~1620 cm^{-1} (S1). The degree of graphite crystallinity in each sample could thus be calculated by using the area ratio R2 (Fig. 2; S1). Raman spectra collected from the starting material show R2 values ranging from 0 to 0.327 (Fig. 2), corresponding respectively to fully crystalline and highly organized graphite. Spectra acquired from the deformed surfaces show higher R2 values (Fig. 2; S1). The most crystalline graphite with R2=0.330 was produced in Exp. 2 (Fig. 2) while the most disordered graphite with R2=0.661 resulted from Exp. 10 (Fig. 2).

Solid Earth Discuss., https://doi.org/10.5194/se-2017-74
Manuscript under review for journal Solid Earth
Discussion started: 20 July 2017

Solid Earth Discussions

As graphite crystallinity vary within a sample (Fig. 2; S1), we examine average R2 values for each one and compare them with applied normal stress, sliding velocity and shear strain (Table 2). The starting material has average $R2_{pre\text{-}shear\ graphite}$ = 0.173, whereas all deformed samples have higher average R2 values (Table 2). Analyzing the average R2 values for deformed samples reveals that graphite is more disordered in the high-pressure experiments (Table 2) than in the experiments at 5 MPa. Furthermore, in the experiments at 25 MPa the average graphite crystallinity decreases with increasing sliding velocities (Table 2). In contrast, at low normal stress, we do not observe any dependence of the degree of graphite crystallinity on the applied sliding velocities (Table 2). Overall graphite appears as most disordered in the experiments where the highest shear strain was achieved (Table 2). This relationship is illustrated in Fig. 3 by fitting a power function with a correlation coefficient $R^2 = 0.96$. The experiments 2 and 6 at low normal stress, which were stopped at 10 mm displacement and accommodated the least amount of shear strain, contain the least disordered graphite (Fig. 3; Table 2).

3.3 Microstructural characteristics

Similar microstructural features were observed in all the deformed samples. SEM images obtained from the sample deformed during experiment 8 are presented to demonstrate our observations (Fig. 4).

These high-resolution images in Y-Z sections reveal that the shiny surfaces are decorated by closely spaced (from < 5 to 10 micrometers) slickenlines (Fig. 4a), on top of a smooth continuous layer. In places, the continuity of this layer is interrupted by fine (~1 to 2 micrometers in width) fractures (Fig. 4a), with random orientation compared to the slip direction. Occasionally, the deformed surface appears as completely disrupted, comprising of platy graphite crystals 10 to 50 micrometers in size, oriented nearly parallel to the shear direction (Fig. 4b). In X-Z sections this highly deformed surface is observed as a thin slip-localized zone, composed of well-compacted layer of aligned graphite grains (Fig. 4c). This localized shear surface is underlain by a zone of randomly oriented, inequigranular, irregular graphite grains (Fig. 4d). In places, most of the graphite grains are aligned with their basal (001) planes parallel to the slip direction, and form compacted layers, defining a weak fabric development (Fig. 4e). There has been some dilation along these cleavage planes, and the spaces thus created are filled with smaller graphite grains with their (001) planes sub-perpendicular to the shear direction (Fig. 4e). Locally, intensely fractured grains are also observed (Fig. 4f).

4 Discussion

4.1 Mechanical behavior

Graphite in our experiments shows mechanical behavior consistent with other mechanical studies of pure graphite gouges. Our results display low μ_{ss} values (from ~0.1 to ~0.2; Table 1) as did the low-pressure deformation experiments of carbonaceous material performed by Morrow et al. (2000), Moore & Lockner (2004), Oohashi et al. (2011, 2013), Kuo et al.

Solid Earth Discuss., https://doi.org/10.5194/se-2017-74
Manuscript under review for journal Solid Earth
Discussion started: 20 July 2017

Solid Earth Discussions

(2014), and Rutter et al. (2016). The low frictional strength of graphite is well known and has been attributed to its sheet structure composed of covalently bonded carbon atoms held together only by van der Waals forces. These weak interlayer bonds along (001) planes are easily broken during shear (Moore & Lockner, 2004; Rutter, et al., 2016). Initial μ_{peak} followed by strain weakening during deformation experiments of graphite gouges has been previously explained with the work involved in rotating the grains with their (001) planes sub-parallel to the shear surfaces, which puts them in the optimal position for shearing along the weak interlayer bonds (Morrow et al., 2000; Moore & Lockner, 2004; Rutter, et al., 2016).

Controversially, Oohashi et al. (2011) reported an absence of μ_{peak} in pure graphite gouges sheared at $\leq$ 2 MPa with sliding velocities of 1.3 m/s. Instead shearing started and continued at a similar μ throughout their experiments. Our data indicate that μ_{peak} tends to increase with decreasing normal stresses (see experiments at 25 MPa vs. 5 MPa: Fig. 1a; Table 1), therefore, we attribute the discrepancies in graphite frictional strength to the effect of sliding velocity on graphite friction. We hypothesize that higher velocities result in more efficient reorientation of graphite grains, and therefore, μ_{peak} is not present in experiments carried out at seismic rates. This hypothesis is also consistent with the observations from our experiments at 25 MPa that clearly indicate a trend of decreasing μ_{peak} with increasing sliding velocity (Fig. 1a, b; Table 1). We also acknowledge that the imposed velocities in the experiments by Oohashi et al. (2011) were substantially different to ours, and shearing at those seismic rates may cause partial frictional heating. Therefore, graphite frictional strength in their experiments may be related to thermally-activated weakening mechanisms (Nakatani, 2001) that are only significant at these high velocities.

We also observed shear strain variations in the various samples (Fig. 1b, c and d) that are systematically related to the conditions of the experiments. The calculated shear strain (or the ratio of shear displacement to measured layer thickness) is linearly dependent on the applied normal stress, and shear strains are significantly higher in the experiments performed at 25 MPa than the ones at 5 MPa due to better compaction and thinning of the sheared graphite gouges. Furthermore, slip rates also play a role in the accommodated total shear strain, and shear strain increases with increase in the applied sliding velocities but only in the high-pressure experiments (Fig. 1b). As we previously suggested, higher velocities may result in more efficient reorganization of graphite grains, and thus further progressive thinning of the graphite gouges occurred. However, we cannot explain the absence of similar trend at the 5 MPa experiments by our results. There are too few of these relationships to fully characterize the effect of sliding velocity on shear strain accumulation in graphite gouges, and more mechanical data of this sort need to be collected in future.

4.2 Structural disorder of graphite

Our experimental study clearly demonstrates transformation of fully/highly crystalline graphite (with R2 ratios ranging from 0 to 0.327; Fig. 2; S1) into comparatively poorly organized graphitic carbon (with R2 ratios up to 0.661; Fig. 2; S1), which indicates significant graphite disorder with increasing strain at the tested aseismic sliding velocities (Fig. 3). We also

Solid Earth Discuss., https://doi.org/10.5194/se-2017-74
Manuscript under review for journal Solid Earth
Discussion started: 20 July 2017

Solid Earth Discussions

acknowledge that the slickenlined surfaces that were produced experimentally contain some graphite that yield spectra comparable to those acquired from the starting material i.e. there is highly crystalline graphite that appears as unaffected by the deformation. However, at least some of these spectra are derived from undeformed graphite powder that underlies the shear surfaces and could not be entirely removed during sample preparation due to the fragile nature of the samples. It is also possible that some non-deformed graphite powder was accidently measured through the fractures that are cross-cutting the accumulated shear surfaces (Fig. 4a). But even if some graphite did not undergo mechanical modification during the experiments, the results overall validate that structural disorder of graphite can result from shear deformation subsequent to the graphitization process.

Our findings contradict the paradigm that the degree of graphite crystallinity is determined by an irreversible maturation of carbonaceous material (Beyssac et al., 2002a; Bonijoly et al., 1982; Buseck and Beyssac, 2014; Wopenka and Pasteris, 1993). Therefore, graphite should not be considered as a stable mineral, especially in active tectonic settings, where mechanical motions, such as fault creep, may cause disordering of the structure of carbonaceous material that formed during typical graphitization processes. Similar assumptions have been made on graphite in intensely deformed cataclasites (comprising crushed mylonitic chips floating in a fine-grained matrix) that is significantly disordered in comparison with graphite in the spatially associated mylonitic rocks (Kirilova et al, in review; Nakamura et al., 2015).

We have experimentally proven that shear strain can not only affect the final structural order of graphite but also manifests as a controlling parameter in the transformation process (Fig. 3; Table 2). Previous authors have suspected that shear strain may play an important role for graphite modifications, and evidence for this has been found in graphite crystallinity variations in natural samples from active fault zones (Kirilova et al, in review; Nakamura et al., 2015), and strained rocks in metamorphic terrains (Barzoi, 2015; Large et al., 1994). Thus, we conclude that the previously proposed model of progressive graphitization due to increase of temperature (Bonijoly et al., 1982) does not completely reflect the graphite formation mechanisms.

Furthermore, graphite can form or be transported at various depths by tectonic processes, and therefore, it can be exposed to different lithostatic pressures. We demonstrated that during shearing higher normal stress results in an increase of shear strain (Fig. 1b), and thus causes a higher degree of graphite disorder (Fig. 3; Table 2). This outlines the significant effect of lithostatic pressure on graphite crystallinity that has been undervalued until now (Bonijoly et al., 1982; Wopenka and Pasteris, 1993; Bustin et al, 1995; Beyssac et al. 2002b). Previous experimental studies have identified initiation and enhancement of graphitization under pressure (i. e. increase in graphite crystallinity) but only at nanometer scale (Bonijoly et al., 1982; Beyssac et al., 2003). Nevertheless, we speculate pressure should be also considered as a factor that can determine the degree of graphite crystallinity during both graphitization and graphite structural modifications.

Solid Earth Discuss., https://doi.org/10.5194/se-2017-74
Manuscript under review for journal Solid Earth
Discussion started: 20 July 2017

Solid Earth Discussions

We have investigated the effects of shear strain and pressure on graphite crystallinity during shear deformation with aseismic velocities, using a starting material with uniform properties (i.e. highly crystalline graphite powder). In contrast, Kuo et al. (2014) and Oohashi et al. (2011) simulated fault motions in synthetic and natural carbonaceous material with variable degree of maturity at the start of the experiments (ranging from amorphous carbonaceous material to crystalline graphite). Both studies reported graphitization of carbonaceous material due to localized frictional heating rather than structural disordering. These experiments reveal the impact of seismic velocities on graphite structural order and the fact their findings differ so markedly from ours highlights the complexity of graphite transformations in fault zones.

Our microstructural observations provide some indications of the deformation processes that affected graphite structural order. They reveal a thin slip-localized zone (Fig. 4d), underlined by a less deformed zone with typical cataclastic fabric (random fabric (Fig. 4d), affected by occasional fractures (Fig. 4f)). These observations demonstrate that brittle processes operated during shearing and we infer these processes resulted in the structural disorder of graphite, manifested as changes in the Raman spectra. However, crustal fault zones do not only accommodate brittle deformation; at `higher temperatures, confining pressures, and lower strain rates, localised shearing may be accommodated by plastic mechanisms (White et al., 1980). We hypothesize that graphite crystallinity can also be influenced by plastic deformation as also suggested in previous studies by Large et al. (1994), Bustin et al. (1995), Barzoi et al. (2015). Investigating this hypothesis and identifying the exact effects of strain on graphite crystallinity during ductile deformation remain goals for future research.

4.3 Implications for graphite thermometry

The crystallographic structure of graphite measured by Raman spectroscopy has been applied as a thermometer that relies on progressive maturation of originally-organic carbonaceous material during diagenesis and metamorphism. Previous studies have focused on calibrating this thermometer. The current best calibration is described by the following equation T (ºC) = -445 * R2 + 641 ± 50 (Beyssac et al. 2002) by inferring a linear correlation between R2 ratio and peak metamorphic temperatures. However, this thermometer disregards the effects of mechanical modifications of the graphite structure, which this study has identified as having a substantial influence on graphite crystallinity in deformed rocks at sub-seismic velocities.

Our experiments demonstrate a shear strain-dependent increase of the R2 ratio of initially highly crystalline graphite powder due to shear deformation (Fig. 3; Table 2). In natural analogues, the pre-shear graphite would yield temperatures up to 641 ± 50 ºC (S1), which is the upper limit of the calibrated thermometer (Beyssac et al. 2002). Whereas, the sheared samples would indicate peak metamorphic temperatures as low as 347 ± 50 ºC (estimated from the most strained samples; S1). Thus, we experimentally prove that in active tectonic settings graphite thermometers may underestimate the peak metamorphic temperatures by < 300 ºC. In cataclasites from the Alpine Fault zone, New Zealand (Kirilova et al., in review) and fault zones of the Hidaka metamorphic belt, Japan (Nakamura, et al., 2015), the graphite thermometer yields temperature

Solid Earth Discuss., https://doi.org/10.5194/se-2017-74
Manuscript under review for journal Solid Earth
Discussion started: 20 July 2017

Solid Earth Discussions

discrepancies of more than 100 ºC compared to temperature estimates derived both from the surrounding high-grade amphibolite facies mylonites and the lower grade equilibrium cataclastic phases (marked by chlorite alteration). Barzoi (2015) also described differences of ~ 150 ºC in graphite temperatures between strained and less strained low grade metamorphic rocks from Parang Mountains, South Carpathians.

We conclude that shear strain calibration of the current graphite thermometer is needed and we propose an appropriate adjustment based on our dataset. Fig. 3 illustrates good correlation between the average R2 and the shear strain measured within a sample, which can be described by the following equation (1):

$$y = 495.9 * \gamma^{4.875} + 1.117 \text{ with a correlation coefficient } R^2 = 0.96 \quad (1)$$

where γ = shear strain.

However, a calibration of the existing graphite thermometer could be still insufficient to permit reliable temperature estimates in active tectonic settings because of the variable slip rates likely to be encountered in fault zones.

5 Conclusions

We have experimentally demonstrated that graphite crystallinity is not irreversible by performing shear deformation experiments at aseismic sliding velocities on graphite gouges composed of powdered highly-organized graphite. Our results clearly demonstrate significant decrease in graphite structural order, which is a function of the total shear strain attained during the various experiments. We also observed a trend of increasing shear strain within a sample with increase in the applied normal stresses and sliding velocities. This reveals the complexity of graphite structural modifications and highlights the significance of the various parameters that can affect the graphitization process. Furthermore, our findings compromise the validity of the calibrated graphite thermometers as they may underestimate the peak metamorphic temperatures in active tectonic settings. Thus, we tentatively suggest a shear strain calibration of these thermometers.

Acknowledgments

The research was funded by the Department of Geology, University of Otago, New Zealand, and Rutherford Discovery Fellowship RDF-UOO0612 awarded to Virginia Toy. We also acknowledge the 'Tectonics and Structure of Zealandia' subcontract to the University of Otago by GNS Science. We thank our colleagues Gemma Kerr and Brent Pooley for assistance in sample preparation, and Hamish Bowman for helping with data visualization. We also wish to express our gratitude to Laura Halliday for generously offering to perform grain size analysis on our samples at the Department of Geography, University of Otago, New Zealand. And last but not least, we thank Marco Scuderi for valuable discussions and assistance throughout the experimental procedures.

Solid Earth Discuss., https://doi.org/10.5194/se-2017-74
Manuscript under review for journal Solid Earth
Discussion started: 20 July 2017

Solid Earth Discussions

286 **References**

287 Barzoi, S. C.: Shear stress in the graphitization of carbonaceous matter during the low-grade metamorphism from the
288 northern Parang Mountains (South Carpathians)—Implications to graphite geothermometry, International Journal of Coal
289 Geology, 146, 179-187, 2015.

290 Beyssac, O., Goffé, B., Chopin, C. and Rouzaud, J. N.: Raman spectra of carbonaceous material in metasediments: a new
291 geothermometer, Journal of metamorphic Geology 20.9: 859-871, 2002a

292 Beyssac, O., Rouzaud, J. N., Goffé, B., Brunet, F., and Chopin, C.: Graphitization in a high-pressure, low-temperature
293 metamorphic gradient: a Raman microspectroscopy and HRTEM study. Contributions to Mineralogy and Petrology, 143(1),
294 19-31, 2002b

295 Beyssac, O., Brunet, F., Petitet, J. P., Goffé, B., and Rouzand, J. N.: Experimental study of the microtextural and structural
296 transformations of carbonaceous materials under pressure and temperature. European Journal of Mineralogy, 15(6), 937-951,
297 2003.

298 Bonijoly, M., Oberlin, M. and Oberlin, A.: A possible mechanism for natural graphite formation. International Journal of
299 Coal Geology 1.4: 283-312, 1982.

300 Buseck, P. R. and Beyssac, O.: From organic matter to graphite: Graphitization, Elements 10.6: 421-426, 2014.

301 Bustin, R. M., Ross, J. V., and Rouzaud, J. N.: Mechanisms of graphite formation from kerogen: experimental evidence,
302 International Journal of Coal Geology, 28(1), 1-36, 1995.

303 Collettini, C., Di Stefano, G., Carpenter, B., Scarlato, P., Tesei, T., Mollo, S., Trippetta, F., Marone, C., Romeo, G. and
304 Chiaraluce, L.: A novel and versatile apparatus for brittle rock deformation, International journal of rock mechanics and
305 mining sciences, 66, 114-123, 2014.

306 Crespo, E., Luque, F. J., Barrenechea, J. F., and Rodas, M.: Influence of grinding on graphite crystallinity from experimental
307 and natural data: implications for graphite thermometry and sample preparation, Mineralogical magazine, 70(6), 697-707,
308 2006.

309 Kirilova, M., Toy, V., Timms, N., Little, T., Halfpenny, A., Menzies. C., Craw, D., DFDP-1 Science Team, and DFDP-2
310 Science Team: Transformation of graphite by tectonic and hydrothermal processes in an active plate boundary fault zone,
311 Alpine Fault, New Zealand, in review.

Solid Earth Discuss., https://doi.org/10.5194/se-2017-74
Manuscript under review for journal Solid Earth
Discussion started: 20 July 2017

312 Kuo, L. W., Li, H., Smith, S. A., Di Toro, G., Suppe, J., Song, S. R., and Si, J.: Gouge graphitization and dynamic fault
313 weakening during the 2008 Mw 7.9 Wenchuan earthquake. Geology, 42(1), 47-50, 2014.

314 Large, D. J., Christy, A. G., and Fallick, A. E.: Poorly crystalline carbonaceous matter in high grade metasediments:
315 implications for graphitisation and metamorphic fluid compositions, Contributions to Mineralogy and Petrology, 116(1-2),
316 108-116, 1994.

317 Manatschal, G.: Fluid-and reaction-assisted low-angle normal faulting: evidence from rift-related brittle fault rocks in the
318 Alps (Err Nappe, eastern Switzerland), Journal of structural geology, 21(7), 777-793, 1999.

319 Moore, D. E., and Lockner, D. A.: Crystallographic controls on the frictional behavior of dry and water-saturated sheet
320 structure minerals, Journal of Geophysical Research: Solid Earth, 109(B3), 2004.

321 Morrow, C. A., Moore, D. E., and Lockner, D. A.: The effect of mineral bond strength and adsorbed water on fault gouge
322 frictional strength, Geophysical research letters, 27(6), 815-818, 2000.

323 Nakamura, Y., Oohashi, K., Toyoshima, T., Satish-Kumar, M., and Akai, J.: Strain-induced amorphization of graphite in
324 fault zones of the Hidaka metamorphic belt, Hokkaido, Japan, Journal of Structural Geology 72: 142 – 161, 2015.

325 Nakatani, M.: Conceptual and physical clarification of rate and state friction: Frictional sliding as a thermally activated
326 rheology, Journal of Geophysical Research: Solid Earth, 106(B7), 13347-13380, 2001.

327 Oohashi, K., Hiros, T. and Shimamoto, T.: Shear-induced graphitization of carbonaceous materials during seismic fault
328 motion: experiments and possible implications for fault mechanics, Journal of Structural Geology 33.6: 1122-1134, 2011.

329 Oohashi, K., Hirose, T. and Shimamoto, T.: The occurrence of graphite-bearing fault rocks in the Atotsugawa fault system,
330 Japan: origins and implications for fault creep, Journal of Structural Geology 38: 39-50, 2012.

331 Rietmeijer, F. J., and Mackinnon, I. D.: Poorly graphitized carbon as a new cosmothermometer for primitive extraterrestrial
332 materials. Nature, 315(6022), 733-736, 1985.

333 Savage, R. H.: Graphite lubrication, Journal of Applied Physics 19.1: 1-10, 1948.

334 Toy, V.G., Niemeijer, A.R., Renard, F. Wirth, R., and Morales, L.: Striation and slickenline development on quartz fault
335 surfaces at crustal conditions: origin and effect on friction. Journal of Geophysical Research, doi: 10.1002/2016JB013498, in
336 press.

Solid Earth Discuss., https://doi.org/10.5194/se-2017-74
Manuscript under review for journal Solid Earth
Discussion started: 20 July 2017

White, S. H., Burrows, S. E., Carreras, J., Shaw, N. D., & Humphreys, F. J.: On mylonites in ductile shear zones, Journal of Structural Geology, 2(1-2), 175-187, 1980.

Wopenka, B., and Pasteris, J. D.: Structural characterization of kerogens to granulite-facies graphite: applicability of Raman microprobe spectroscopy, The American Mineralogist, 78(5-6), 533-557, 1993.

Zulauf, G., Kleinschmidt, G., and Oncken, O.: Brittle deformation and graphitic cataclasites in the pilot research well KTB-VB (Oberpfalz, FRG), Geological Society, London, Special Publications, 54(1), 97-103, 1990.

Table 1. Summary of the conditions at which experiments were carried out and results.

Table 2. Summary of the relationship between shear strain and average R2 within a sample. The conditions of each experiment are also given as follows: applied normal stress in MPa, slip rates in µm/s and sliding displacement in mm.

Figure 1. Plots of mechanical data (a) friction coefficient, µ vs. displacement (b), (c), (d) friction coefficient, µ vs. shear strain.

Figure 2. Representative Raman spectra illustrating: (i) the most crystalline graphite (left column) within a sample; (ii) graphite with approximate average crystallinity per sample (middle column); and (iii) the most disordered graphite (right column) encountered in each sample. The R2 ratio for each spectrum is also noted in italic font.

Figure 3. Plot of the average R2 ratio vs shear strain accumulated during each experiment.

Figure 4. SEM images, obtained from the deformed graphite gouge during experiment 8 (normal stress at 25 MPa with 1 µm/s sliding velocity), show: (a) Slickenlines ornamenting the shear surface; (b), (c) A well-compacted layer of aligned graphite grains, which make up the shear surface. Bright patches due to a differential charging effect; (d) A less deformed zone with typical cataclastic fabric, underlying the shear surface; (e) Dilated cleavage planes in large graphite grains filled with smaller platy graphite grains oriented sub-perpendicular to the shear direction; (f) Fractured graphite grains.

Supplementary material 1 (S1). Raman data from 20 spectra per sample together with calculated R2 ratio and average R2 value for each sample. The last column represents temperature estimated by the current best calibration of a Raman-based thermometer: T (ºC) = - 445 * R2 + 641 ± 50.

Solid Earth Discuss., https://doi.org/10.5194/se-2017-74
Manuscript under review for journal Solid Earth
Discussion started: 20 July 2017

Solid Earth Discussions

Experiment number	Normal stress (MPa)	Sliding velocity (μm/s)	Displacement (mm)	Peak friction (μ_{peak})	Steady state friction (μ_{ss})	Shear strain maximum (γ)
1	5	1	20	0.53	*0.22*	17.70
2	5	1	10	0.53	0.22	8.17
3	5	1	5	0.52	*not reached*	4.23
4	5	10	20	0.53	0.24	20.45
5	5	100	20	0.57	0.22	16.89
6	5	100	10	0.55	0.22	9.80
7	5	100	5	0.57	*not reached*	3.87
8	25	1	20	0.43	0.17	21.45
9	25	10	20	0.43	0.17	31.86
10	25	100	20	0.41	0.14	46.77

Table 1. Summary of the conditions at which experiments were carried out and results.

Solid Earth Discuss., https://doi.org/10.5194/se-2017-74
Manuscript under review for journal Solid Earth
Discussion started: 20 July 2017

Solid Earth Discussions

Sample	Experimental conditions	Shear strain (γ)	Average R2
Pre-shear graphite	N/A	N/A	0.173
Exp. 2	5 MPa, 1 μm/s, 10 mm	8.17	0.438
Exp. 6	5 MPa, 100 μm/s, 10 mm	9.80	0.430
Exp. 5	5 MPa, 100 μm/s, 20 mm	16.89	0.454
Exp. 1	5 MPa, 1μm/s, 20 mm	17.70	0.506
Exp. 4	5 MPa, 10 μm/s, 20 mm	20.45	0.517
Exp. 8	25 MPa, 1 μm/s, 20 mm	21.45	0.520
Exp. 9	25 MPa, 10 μm/s, 20 mm	31.86	0.580
Exp. 10	25 MPa, 100 μm/s, 20 mm	46.77	0.604

Table 2. Summary of the relationship between shear strain and average R2 within a sample. The conditions of each experiment are also given as follows: applied normal stress in MPa, slip rates in μm/s and sliding displacement in mm.

Solid Earth Discuss., https://doi.org/10.5194/se-2017-74
Manuscript under review for journal Solid Earth
Discussion started: 20 July 2017

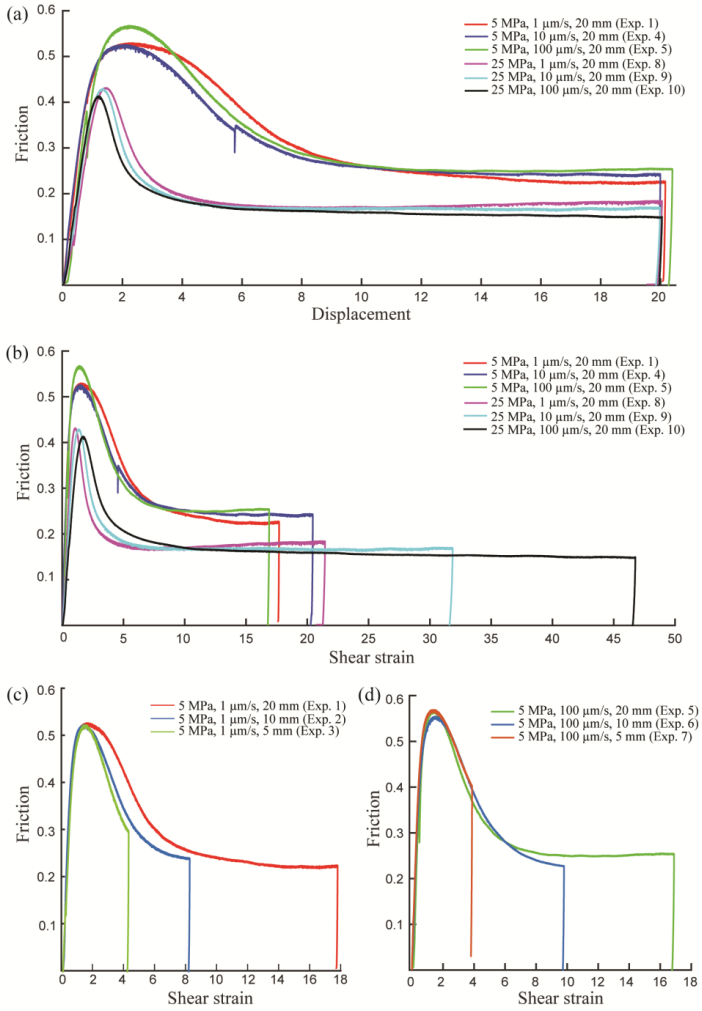

Figure 1. Plots of mechanical data (a) friction coefficient, µ vs. displacement (b), (c), (d) friction coefficient, µ vs. shear strain.

Solid Earth Discuss., https://doi.org/10.5194/se-2017-74
Manuscript under review for journal Solid Earth
Discussion started: 20 July 2017

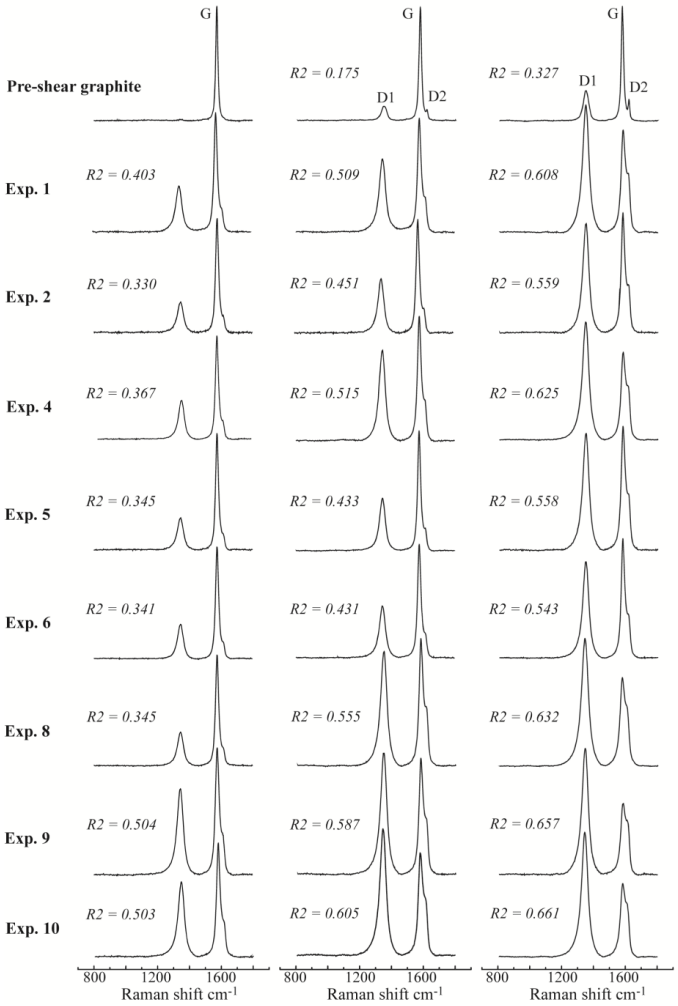

394

395 **Figure 2.** Representative Raman spectra illustrating: (i) the most crystalline graphite (left column) within a sample; (ii)
396 graphite with approximate average crystallinity per sample (middle column); and (iii) the most disordered graphite (right
397 column) encountered in each sample. The R2 ratio for each spectrum is also noted in italic font.

Solid Earth Discuss., https://doi.org/10.5194/se-2017-74
Manuscript under review for journal Solid Earth
Discussion started: 20 July 2017

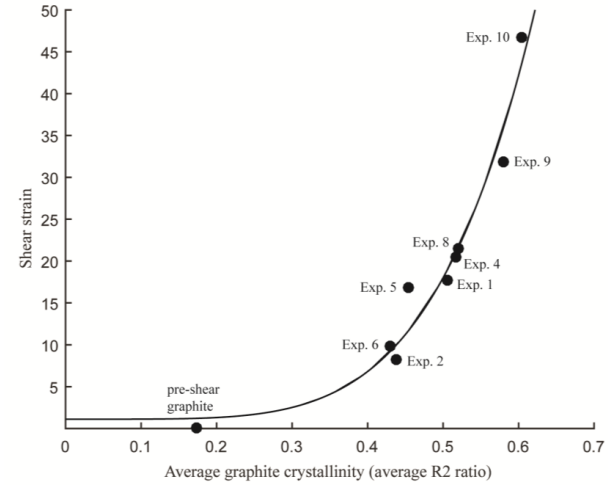

Figure 3. Plot of the average R2 ratio vs shear strain accumulated during each experiment.

Solid Earth Discuss., https://doi.org/10.5194/se-2017-74
Manuscript under review for journal Solid Earth
Discussion started: 20 July 2017

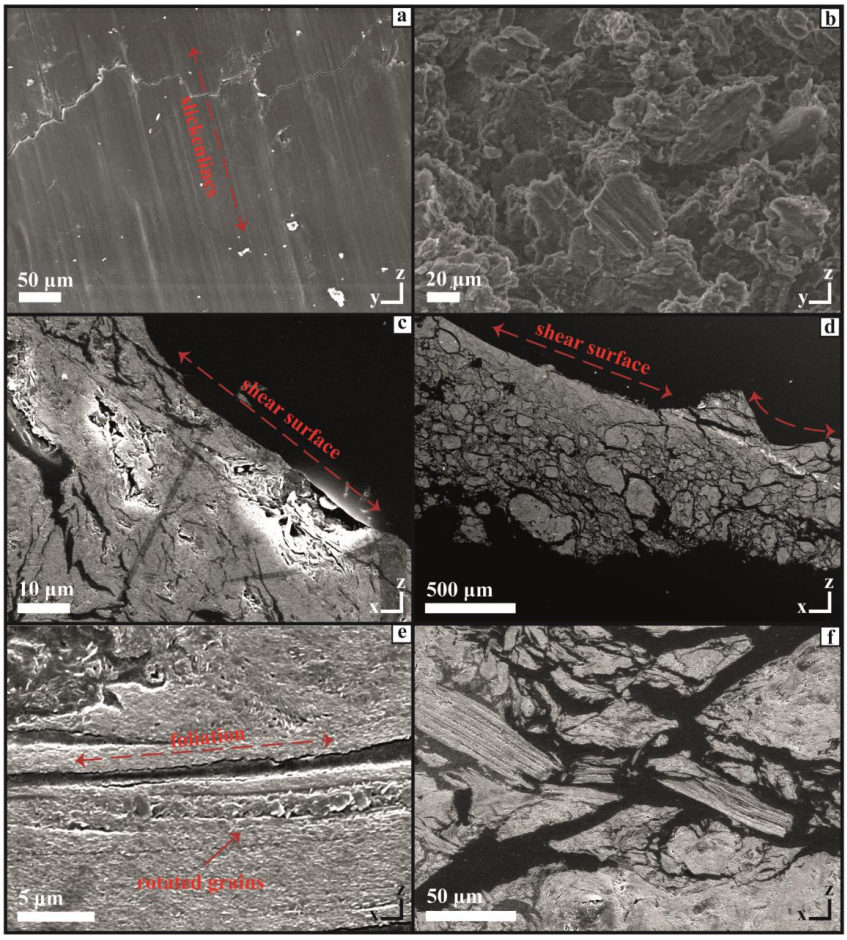

408

409 **Figure 4.** SEM images, obtained from the deformed graphite gouge during experiment 8 (normal stress at 25 MPa with 1
410 µm/s sliding velocity), show: (a) Slickenlines ornamenting the shear surface; (b), (c) A well-compacted layer of aligned
411 graphite grains, which make up the shear surface. Bright patches due to a differential charging effect; (d) A less deformed
412 zone with typical cataclastic fabric, underlying the shear surface; (e) Dilated cleavage planes in large graphite grains filled
413 with smaller platy graphite grains oriented sub-perpendicular to the shear direction; (f) Fractured graphite grains.

Appendix E.
Dynamics of fault slip near the stability transition combining laboratory and numerical experiments

Deepa Mele Veedu[1], Carolina Giorgetti[2], Marco Maria Scuderi[2], Sylvain Barbot[4], Chris Marone[5] and Cristiano Collettini[2,3]

[1]Nanyang Technological University, Singapore, Singapore

[2]Sapienza University of Rome, Rome, Italy

[3]Pennsylvania State University, University Park, PA, United States

[4]Earth Observatory of Singapore, Nanyang Technological University, Singapore, Singapore

[5]Penn State University, Department of Geosciences, University Park, PA, United States

Frictional stability controls the seismogenic potential of faults. Laboratory and theoretical studies document and predict the conditions under which fault slip is seismic or aseismic. However, the full gamut of fault slip behavior near the stable/unstable boundary is still poorly known. Here, we combine insight from laboratory and numerical experiments to identify the wide spectrum of frictional instabilities around that transition, including slow-slip events, period-multiplying events, and chaos. We present a synoptic picture of the dynamics of fault slip in a bifurcation diagram obtained from a series of laboratory and numerical experiments. We compare the laboratory observations with spring-slider and finite-fault numerical models. In the laboratory, we vary the stiffness of the system by modulating the stress field around the experimental fault. In the numerical experiments, we vary the characteristic weakening distance to explore a range of critical nucleation sizes. Contrarily to previously found, complex fault dynamics can be obtained with a rate-and-state constitutive law with a single state variable. While the dynamics of fault slip is complicated on large faults by the presence of morphological and rheological heterogeneities, the range of instabilities identified in the laboratory is reminiscent of the variety of slow and fast earthquakes found along subduction zones. The accord between laboratory data and theoretical models affords more realistic predictions of fault behavior at slow slip speeds.

Appendix F.
List of experiments

Experiment number	Configuration Description	Related Project
i173	double direct shear on gouge (5 cm x 5 cm nominal contact area)	Giorgetti, C., B. M. Carpenter, and C. Collettini (2015), Frictional behavior of talc-calcite mixtures, Journal of Geophysical Research Solid Earth, 120, 6614-6633, doi:10.1002/2015JB011970.
i174	double direct shear on gouge (5 cm x 5 cm nominal contact area)	
i175	double direct shear on gouge (5 cm x 5 cm nominal contact area)	
i176	double direct shear on gouge (5 cm x 5 cm nominal contact area)	
i179	double direct shear on gouge (5 cm x 5 cm nominal contact area)	
i181	double direct shear on gouge (5 cm x 5 cm nominal contact area)	
i183	double direct shear on gouge (5 cm x 5 cm nominal contact area)	
i184	double direct shear on gouge (5 cm x 5 cm nominal contact area)	
i186	double direct shear on gouge (5 cm x 5 cm nominal contact area)	
i234	double direct shear on gouge (5 cm x 5 cm nominal contact area)	
i235	double direct shear on gouge (5 cm x 5 cm nominal contact area)	
i236	double direct shear on gouge (5 cm x 5 cm nominal contact area)	
i237	double direct shear on gouge (5 cm x 5 cm nominal contact area)	
i262	double direct shear on gouge (5 cm x 5 cm nominal contact area)	
i339	double direct shear on gouge (5 cm x 5 cm nominal contact area)	
i421	triaxial on cylindrical sample (38 mm diameter)	Giorgetti, C., C. Collettini, M. M. Scuderi, M. R. Barchi, and T. Tesei (2016), Fault geometry and mechanics of marly carbonate multilayers: An integrated field and laboratory study from the Northern Apennines, Italy, Journal of Structural Geology, 93, 1-16, doi:10.1016/j.jsg.2016.10.001.
i422	triaxial on cylindrical sample (38 mm diameter)	
i424	triaxial on cylindrical sample (38 mm diameter)	
i426	triaxial on cylindrical sample (38 mm diameter)	
i431	triaxial on cylindrical sample (38 mm diameter)	
i432	triaxial on cylindrical sample (38 mm diameter)	

i435	triaxial on cylindrical sample (38 mm diameter)	Giorgetti, C., C. Collettini, M. M. Scuderi, M. R. Barchi, and T. Tesei (2016), Fault geometry and mechanics of marly carbonate multilayers: An integrated field and laboratory study from the Northern Apennines, Italy, Journal of Structural Geology, 93, 1-16, doi:10.1016/j.jsg.2016.10.001.
i436	triaxial on cylindrical sample (38 mm diameter)	
i469	duoble direct shear on gouge within the pressure vessel (5.54 cm × 5.55 cm nominal contact area)	
i485	duoble direct shear on gouge within the pressure vessel (5.54 cm × 5.55 cm nominal contact area)	
b515	double direct shear on gouge (5 cm x 5 cm nominal contact area)	
b506	triaxial on cylindrical sample (38 mm diameter)	Trippetta et al. (2016), Variations of the petrophysical properties of rocks with increasing hydrocarbons content and their implications at larger scale: insights from the Majella reservoir (Italy), EGU General Assembly 2016, Vienna, Austria, 17 – 22 April 2016.
b507	uniaxial on cylindrical sample (38 mm diameter)	
b508	uniaxial on cylindrical sample (38 mm diameter)	
b523	uniaxial on cylindrical sample (38 mm diameter)	
b524	uniaxial on cylindrical sample (38 mm diameter)	
b525	uniaxial on cylindrical sample (38 mm diameter)	
b558	uniaxial on cylindrical sample (38 mm diameter)	
b559	uniaxial on cylindrical sample (38 mm diameter)	
b514	single direct shear on gouge (20 cm x 20 cm nominal contact area)	Tesei, T., B. M. Carpenter, C. Giorgetti, M. M. Scuderi, A. Sagy, P. Scarlato, and C. Collettini (2017), Friction and scale-dependent deformation processes of large experimental carbonate faults, J. Struct. Geol., 100, 12-23, doi: 10.1016/j.jsg.2017.05.008.
b526	single direct shear on bare surfaces (20 cm x 20 cm nominal contact area)	
b569	double direct shear on gouge (5 cm x 5 cm nominal contact area)	Kirilova. M., V. Toy, J. S. Rooney, C. Giorgetti, K. C. Gordon, and C. Collettini, Structural Disorder of Graphite and Implications for Graphite Thermometry, Solid Earth, under review.
b570	double direct shear on gouge (5 cm x 5 cm nominal contact area)	
b571	double direct shear on gouge (5 cm x 5 cm nominal contact area)	
b572	double direct shear on gouge (5 cm x 5 cm nominal contact area)	

b573	double direct shear on gouge (5 cm x 5 cm nominal contact area)	Kirilova. M., V. Toy, J. S. Rooney, C. Giorgetti, K. C. Gordon, and C. Collettini, Structural Disorder of Graphite and Implications for Graphite Thermometry, Solid Earth, under review.
b574	double direct shear on gouge (5 cm x 5 cm nominal contact area)	
b575	double direct shear on gouge (5 cm x 5 cm nominal contact area)	
b576	double direct shear on gouge (5 cm x 5 cm nominal contact area)	
b577	double direct shear on gouge (5 cm x 5 cm nominal contact area)	
b578	double direct shear on gouge (5 cm x 5 cm nominal contact area)	
b550	triaxial on cylindrcal sample with saw-cut at 40° to sample axis (38 mm diameter)	Giorgetti, C., T. Tesei, M. M. Scuderi and C. Collettini, Fault reactivation: insights from triaxial saw-cut experiments, in preparation.
b551	triaxial on cylindrcal sample with saw-cut at 40° to sample axis (38 mm diameter)	
b552	triaxial on cylindrcal sample with saw-cut at 40° to sample axis (38 mm diameter)	
b554	triaxial on cylindrcal sample with gouge-filled saw-cut at 30° to sample axis (38 mm diameter)	
b557	triaxial on cylindrcal sample with saw-cut at 30° to sample axis (38 mm diameter)	
b565	triaxial on cylindrical sample (38 mm diameter)	
b584	triaxial on cylindrical sample (38 mm diameter)	
b585	triaxial on cylindrical sample (38 mm diameter)	
b586	triaxial on cylindrcal sample with gouge-filled saw-cut at 30° to sample axis (38 mm diameter)	
b587	triaxial on cylindrcal sample with gouge-filled saw-cut at 30° to sample axis (38 mm diameter)	
b588	triaxial on cylindrcal sample with gouhge-filled saw-cut at 60° to sample axis (38 mm diameter)	
b596	triaxial on cylindrcal sample with gouge-filled saw-cut at 50° to sample axis (38 mm diameter)	

b597	triaxial on cylindrcal sample with gouge-filled saw-cut at 40° to sample axis (38 mm diameter)	Giorgetti, C., T. Tesei, M. M. Scuderi and C. Collettini, Fault reactivation: insights from triaxial saw-cut experiments, in preparation.
b598	triaxial on cylindrcal sample with gouge-filled saw-cut at 70° to sample axis (38 mm diameter)	
b599	double direct shear on gouge (5 cm x 5 cm nominal contact area)	
b610	triaxial on cylindrcal sample with gouge-filled saw-cut at 40° to sample axis (38 mm diameter)	
b611	triaxial on cylindrcal sample with gouge-filled saw-cut at 50° to sample axis (38 mm diameter)	
b613	triaxial on cylindrcal sample with gouge-filled saw-cut at 50° to sample axis (38 mm diameter)	
b617	triaxial on cylindrcal sample with gouge-filled saw-cut at 50° to sample axis (38 mm diameter)	
b619	triaxial on cylindrcal sample with gouge-filled saw-cut at 50° to sample axis (38 mm diameter)	
b628	triaxial on cylindrcal sample with gouge-filled saw-cut at 50° to sample axis (38 mm diameter)	
b629	triaxial on cylindrcal sample with gouge-filled saw-cut at 50° to sample axis (38 mm diameter)	
b645	triaxial on cylindrcal sample with saw-cut at 70° to sample axis (38 mm diameter)	
b646	triaxial on cylindrcal sample with gouge-filled saw-cut at 80° to sample axis (38 mm diameter)	
b648	triaxial on cylindrcal sample with gouge-filled saw-cut at 70° to sample axis (38 mm diameter)	
b652	triaxial on cylindrical sample (38 mm diameter)	
b653	triaxial on cylindrical sample (38 mm diameter)	
b654	uniaxial on cylindrical sample (38 mm diameter)	

b655	uniaxial on cylindrical sample (38 mm diameter)	Giorgetti, C., T. Tesei, M. M. Scuderi and C. Collettini, Fault reactivation: insights from triaxial saw-cut experiments, in preparation.
b662	double direct shear on gouge (5 cm x 5 cm nominal contact area)	
b663	double direct shear on gouge (5 cm x 5 cm nominal contact area)	
b665	triaxial on cylindrcal sample with saw-cut at 40° to sample axis (38 mm diameter)	
b634	double direct shear on gouge (5 cm x 5 cm nominal contact area)	Preliminary data from ongoing project.
b635	double direct shear on gouge (5 cm x 5 cm nominal contact area)	
b636	double direct shear on gouge (5 cm x 5 cm nominal contact area)	
b637	double direct shear on gouge (5 cm x 5 cm nominal contact area)	
b670	double direct shear on gouge (5 cm x 5 cm nominal contact area)	Mele Veedu, D., Giorgetti C., Scuderi M.M., Barbot S., Marone C. and Collettini C., 2017. Dynamics of fault slip near the stability transition combining laboratory and numerical experiments. Fall Meeting, AGU, New Orleans, 11 - 15 December 2017.
b686	double direct shear on gouge (5 cm x 5 cm nominal contact area)	
b687	double direct shear on gouge (5 cm x 5 cm nominal contact area)	
b693	double direct shear on gouge (5 cm x 5 cm nominal contact area)	
b694	double direct shear on gouge (5 cm x 5 cm nominal contact area)	
b695	double direct shear on gouge (5 cm x 5 cm nominal contact area)	
b696	double direct shear on gouge (5 cm x 5 cm nominal contact area)	
b697	double direct shear on gouge (5 cm x 5 cm nominal contact area)	
b698	double direct shear on gouge (5 cm x 5 cm nominal contact area)	
b721	double direct shear on gouge (5 cm x 5 cm nominal contact area)	
b722	double direct shear on gouge (5 cm x 5 cm nominal contact area)	
b723	double direct shear on gouge (5 cm x 5 cm nominal contact area)	
b724	double direct shear on gouge (5 cm x 5 cm nominal contact area)	
b725	double direct shear on gouge (5 cm x 5 cm nominal contact area)	

b726	double direct shear on gouge (5 cm x 5 cm nominal contact area)	Mele Veedu, D., Giorgetti C., Scuderi M.M., Barbot S., Marone C. and Collettini C., 2017. Dynamics of fault slip near the stability transition combining laboratory and numerical experiments. Fall Meeting, AGU, New Orleans, 11 - 15 December 2017.
b727	double direct shear on gouge (5 cm x 5 cm nominal contact area)	
b728	double direct shear on gouge (5 cm x 5 cm nominal contact area)	